# Low temperature methanol steam reforming for HT-PEMFC

**Paulo António Alves Ribeirinha**

**Dissertation presented for the degree of**

Doctor in Chemical and Biological Engineering

**By the**

University of Porto

**Supervisors**

Professor Adélio Miguel Magalhães Mendes

Professor José Manuel Ribeiro de Sousa

Doctor Marta Ferreira da Silva Boaventura

**LEPABE – Laboratory for Process Engineering, Environment, Biotechnology and Energy**

Chemical Engineering Department

Faculty of Engineering – University of Porto

Porto, 2017

UNIÃO EUROPEIA

Fundo Europeu de Desenvolvimento Regional

## Statement of originality

I certify that this work does not contain any material that has been used nor will be for the award of any other degree or diploma in my name or anyone, in any university or institution. In addition, I certify that, to the best of my knowledge, this work does not contain any material previously published or written by another person, expect where due reference has been made in the text.

_____

Paulo António Alves Ribeirinha

## Statement

In order to fulfil the Rules of Ethics of the Doctoral Program of Chemical and Biological Engineering (PDEQB), we hereby declare that all the contents of the thesis presented by Paulo António Alves Ribeirinha, entitled “Low temperature methanol steam reforming for HT-PEMFC”, is exclusively from the author with the collaborations mentioned in the thesis.

| | |
|---|---|
| _____ | _____ |
| Adélio Miguel Magalhães Mendes | Marta Ferreira da Silva Boaventura |
| Full Professor | Assistant Researcher |

_____

José Manuel Ribeiro de Sousa

Assistant Professor

## Acknowledgments

I would like to express my sincere gratitude to my supervisors Professor Adélio Mendes, Dr. Marta Boaventura and Professor José Sousa for their guidance, continuous support, patience, motivation, shared knowledge and above all, friendship. I would like to emphasise my gratitude for the privilege of having Professor Mendes as supervisor.

My thankful words also go to all my lab mates: thank you for the good moments and friendship. A special word to my friend Dr. Mahdi Abdollahzadeh for the fruitful coffee breaks and teaching me so much about numeric simulation.

I want to thank my family, my mother Maria and my sister Teresa, for the unconditional love, never-ending support and for always believing in me. To my beautiful wife Silvia, I would like express my deepest gratitude for the kindness and generosity, for the optimism and motivation. Thank you, for listen to me and appreciate my small successes; thank you, for standing by my side, thank you for your love and making me happy.

I would like to acknowledge, the financial support of the Portuguese Foundation for Science and Technology (FCT) for my PhD grant (Grants PD/BD/52621/2014) and the European Union's Seventh Framework Programme (FP7/2007-2013) for the FCH JU under GA 303476 due to the funding received for part of this work (www.beingenergy.eu). As well as the financial support of the Projects:

(i) POCI–01–0145-FEDER -006939 (Laboratory for Process Engineering, Environment, Biotechnology and Energy – UID/EQU/00511/2013) funded by the European Regional Development Fund (ERDF), through COMPETE2020 - Programa Operacional Competitividade e Internacionalização (POCI) and with financial support from FCT/MCTES through national funds (PIDDAC);

(ii) NORTE-01-0145-FEDER-000005 – LEPABE-2-ECO-INNOVATION, supported by North Portugal Regional Operational Programme (NORTE 2020), under the Portugal 2020 Partnership Agreement, through the European Regional Development Fund (ERDF).

*“But I, being poor, have only my dreams;*
*I have spread my dreams under your feet;*
*Tread softly because you tread on my dreams.”*
***W. B. Yeats***

## Contents



### Chapter 1. Introduction



### Chapter 2. A novel catalyst for low temperature MSR reaction

## Chapter 3. Designing a methanol steam reformer



## Chapter 4. Integration of a reformer with a HT-PEMFC – Part A

## Chapter 5. Integration of a reformer with a HT-PEMFC – Part B



## Chapter 6. Integration of a reformer with a HT-PEMFC – Part C (modelling)

## Chapter 7. H2 production with low carbon content using PBMRs



## Chapter 8. Integration of a PBMR with a HT-PMFC (modelling)

## Chapter 9. Conclusions and future work

## Abstract

The present thesis embraces the hydrogen production via low temperature methanol steam reforming (MSR) and its integration with a high temperature polymer electrolyte membrane fuel cell (HT-PEMFC). It covers the catalyst preparation for methanol steam reforming, kinetic modelling, design of reformers and bipolar plates, experimentally and simulated integration of MSR with HT-PEMFCs and strategies for hydrogen purification.

A novel and very active MSR catalyst, a gallium-promoted copper-based ($CuO/ZnO/Ga_2O_3$) prepared by the hosting research team, was characterized concerning the morphology, structure, composition and catalytic activity. The developed catalyst was 2.2 times more active at 453 K than two tested commercial catalysts ($CuO/ZnO/Al_2O_3$). Two kinetic models, one empirical and one mechanistic, were used to describe the MSR reaction over the novel catalyst. After proper kinetic parameter estimation, the two models showed a good agreement with experimental methanol conversions.

The effect of pressure drop, temperature and flow distribution on the methanol conversion using different reformer designs (tubular, multi-channel and radial) was thoroughly studied experimentally and by CFD simulation. The simulation results showed that the multi-channel design assures similar flow velocity between channels, low-pressure drop and low temperature sink due to narrow channels, resulting in high methanol conversions. Reformers with multi-channel designs demonstrated to be a good solution for the thermal integration with HT-PEMFC.

The thermal integration of a methanol steam reformer cell (MSR-C) with a HT-PEMFC, operating at the same temperature, was studied experimentally and by simulation. To that purpose, a bipolar plate made of carbon/PPS (polyphenylenesulfide) composite was produced, featuring the fuel cell anode flow field in one side and the reformer flow field in the other. Equipped with a 25 $cm^2$ membrane electrode assembly (MEA) from ADVENT TPS and using commercial BASF RP-60 catalyst, the combined unit MSR-C/HT-PEMFC showed a high performance at 453 K. After several hours of operation, the degradation of the MEA was noticeable, due to low methanol conversion at the reformer (<90 %). Electrochemical impedance spectroscopy (EIS) analysis showed that the cath-

ode resistance increased, when reformate was used as fuel, due to the methanol cross-over from the anode to the cathode, especially at lower operating temperatures where the methanol conversion was also lower. The self-thermal sustainability of the combined device was only reached for > 0.75 $A \cdot cm^{-2}$ due to the poor thermal insulation of the combined reactor. In a second attempt, the combined MSR-C/HT-PEMFC unit was modified and an optimized bipolar plate made of gold plated aluminium was developed. Equipped with a 45 $cm^2$ Celtec P2200N MEA from BASF and using commercial BASF RP-60 catalyst the combined unit displayed a remarkable performance at 453 K and the highest reported in the literature for similar devices. The device demonstrated a good stability in a durability test of *ca*. 700 h at 0.2 $A \cdot cm^{-2}$. The EIS analysis also demonstrated that using directly the produced reformate as fuel had no significant influence in MEA degradation process. The thermal integration of the combined MSR-C/HT-PEMFC was also assessed by simulation. A 3D non-isothermal model was developed and validated. The simulation results show self-thermal sustainability of the device at low current densities (0.1 $A \cdot cm^{-2}$) using a thermal insulation of 3 cm thick glass wool. Based on the combined unit a 10 cell stack was proposed; results showed that the stack operates without any external heat source for current between 4.5 A (0.1 $A \cdot cm^{-2}$) and 54 A (1.2 $A \cdot cm^{-2}$).

The production and purification of a reformate stream for HT-PEMFC applications was also investigated. A 3D non-isothermal model of packed bed membrane reactor (PBMR) was developed considering two types of membranes, a Pd-Ag membrane selective to hydrogen and a supported ionic liquids (ILs) membrane selective to carbon dioxide. Simulation results showed that the selective hydrogen removal from the reaction bulk enhances methanol conversion and produces a pure hydrogen stream, despite the low efficiency and high complexity of the process. The selective carbon dioxide removal showed to be more energy efficient than hydrogen removal especially for high hydrogen recoveries; however, the selective carbon dioxide removal has a smaller effect on the methanol conversion and requires very selective and fast membranes, which are not currently available. The integration of a cellular packed bed membrane reactor (PBMR-C) with a HT-PEMFC was also assessed by simulation at 473 K, considering a very thin Pd-Ag membrane between the reforming catalyst and the MEA. The PBMR-C/HT-PEMFC showed high performance, similar to the one obtained with a HT-PEMFC fed with hydrogen, moreover, it demonstrated to be compact and thermally efficient. The performance

of the combined unit depends on the permeability, selectivity and stability of Pd-Ag membrane at 473 K.

## Sumário

A presente tese visa os principais tópicos referentes à produção de hidrogénio através de reformação a baixa temperatura de metanol por vapor de água (MSR), e integração com uma célula de combustível de membrana de eletrólito polímerica de alta temperatura (HT-PEMFC). Inclui, preparação de um catalisador para reformação de metanol e respectivos modelos cinéticos, desenvolvimento de novos reformadores e pratos bipolares, integração experimental e por simulação de reformadores com HT-PEMFCs, e ainda, estratégias para a purificação de hidrogénio a partir de uma corrente de reformado.

Esta tese inicia-se com a preparação de um novo catalisador de cobre-gálio ($CuO/ZnO/Ga_2O_3$) para reformação de metanol pelo grupo de investigação. O catalisador foi caracterizado quanto à morfologia, estrutura e composição. A sua actividade catalitica foi ainda comparada com dois catalisadores comerciais ($CuO/ZnO/Al_2O_3$) e mostrou ser cerca de 2,2 vezes mais elevada. A reacção de MSR com o novo catalisador foi ainda descrita através de dois modelos cinéticos, um empírico e outro mecanistico. Os modelos, após determinação adequada dos parametros cinéticos, permitiram um bom ajuste entre os dados simulados e os experimentais.

Foi estudada experimentalmente e por simulação a influência da queda de pressão, perfis de temperatura e distribuiçao dos reagentes na conversão de methanol, usando para tal reformadores com diferentes geometrias. Os resultados mostraram que a geometria em multi-canal assegura velocidades de fluxo semelhantes entre canais, baixa queda de pressão e temperatura homogénea no leito de catalisador, o que resulta em altas conversões de methanol. Concluiu-se, ainda, que reformadores com geometria em multi-canal são uma boa opção para a integração térmica com HT-PEMFCs.

A integração térmica de um reformador celular (MSR-C) com uma HT-PEMFC foi estudada experimentalmente e por simulação. Para tal, desenvolveu-se uma placa bipolar em compósito de carbono/PPS (polifenileno-sulfureto), em que, num dos lados foram desenhados os canais de escoamento para o MSR e, do outro, os canais de escoamento para ânodo da HT-PEMFC. A unidade integrada MSR-C/HT-PEMFC foi montada utilizando um conjunto de eléctrodos/membrana (MEA) da ADVENT TPS com área ativa de 25 $cm^2$ e demonstrou elevado desempenho a 453 K. A operação em contínuo resultou na degradação acentuada da MEA devido a uma baixa conversão de metanol (<90%). A análise por espectroscopia de impedância eletroquímica (EIS)

mostrou aumento da resistência no cátodo devido à utilização de reformado. Este facto deveu-se à presença de metanol no ânodo e consequente permeação para o cátodo, especialmente a temperaturas mais baixas onde a conversão do metanol era menor. Devido ao mau isolamento térmico, a sustentabilidade térmica da unidade integrada só foi atingida a 0,75 $A \cdot cm^{-2}$. Num segundo estudo, a unidade MSR-C/HT-PEMFC foi modificada e usou-se uma nova placa bipolar de alumínio banhada a ouro. A unidade combinada foi montada com uma MEA Celtec P2200N de 45 $cm^2$ e, demonstrou um desempenho notável a 453 K, sendo o mais alto já reportado na literatura para dispositivos semelhantes. O dispositivo demonstrou boa estabilidade num ensaio de durabilidade de 700 h e à densidade de corrente de 0,2 $A \cdot cm^{-2}$. A análise de EIS demonstrou que o uso de reformado como combustível, durante o período estudado, não teve influência significativa na degradação da MEA. A integração térmica do MSR-C/HT-PEMFC foi ainda analisada por simulação e, para tal, foi desenvolvido um modelo tri-dimensional não-isotérmico em CFD. Os resultados da simulação mostram sustentabilidade térmica do dispositivo a baixas densidades de corrente (0,1 $A \cdot cm^{-2}$) utilizando um isolamento térmico de lã de vidro de 3 cm de espessura. Foi ainda proposta uma pilha de 10 células, a qual demonstrou elevado desempenho sem qualquer fonte externa de calor, para densidades de corrente entre 4,5 A (0,1 $A \cdot cm^{-2}$) e 54 A (1,2 $A \cdot cm^{-2}$).

Foi ainda investigada a produção e purificação e de uma corrente de reformado para aplicações em HT-PEMFC. Foi desenvolvido um modelo tri-dimensional não-isotérmico em CFD de um reator de membrana (PBMR), com remoção selectiva de hidrogénio através do uso de membranas de Pd-Ag ou remoção seletiva de dióxido de carbono através de membranas com líquidos iónicos suportados (ILs). O uso de membranas de Pd-Ag, apesar da baixa eficiência e complexidade do processo, permitiu ober uma corrente pura de hidrogénio, e aumentar a conversão devido à remoção de hidrogénio do meio reacional. A remoção seletiva de dióxido de carbono do meio reacional revela-se energeticamente mais eficiente que a remoção de hidrogénio, apesar de se refletir num pequeno aumento da conversão de methanol. Para a purificação de hidrogénio com PMBRs, as membranas com líquidos iónicos suportados necessitam de ser muito seletivas e rápidas, as quais ainda não foram desenvolvidas. A integração de um reator de membrana celular (PBMR-C) com um HT-PEMFC foi ainda avaliada por simulação a 473 K. No modelo considerou-se uma membrana fina de Pd-Ag

entre o catalisador de reformação e o MEA. A unidade combinada (PBMR-C/HT-PEMFC) demonstrou ser compacta, termicamente eficiente e com desempenho elevado e semelhante ao obtido com uma HT-PEMFC alimentada diretamente com hidrogénio. Conclui-se, ainda, que o desempenho da unidade combinada está dependente da permeabilidade, seletividade e estabilidade da membrana de Pd-Ag a 473 K.

## 摘要

本论文涵盖如下主题：通过低温甲醇蒸汽重整（MSR）的制氢、以及与高温聚合物电解质膜燃料电池（HT-PEMFC）的一体化。它覆盖MSR的催化剂制备、动力学建模、重整器和双极板的设计、MSR与HT-PEMFC实验和模拟的集成、以及氢气净化策略。本论文首先合成了一种新型且高活性的MSR催化剂。该催化剂是一种掺杂镓的铜基（$CuO/ZnO/Ga_2O_3$），对其形貌、结构和组成进行了分析。在453 K，其催化活性是商业催化剂（$CuO/ZnO/Al_2O_3$）的2.2倍。采用两种动力学模型：一种是通过经验，另一种是通过机理，来描述新型催化剂的MSR反应。 在合适的动力学参数评估之后，两个模型显示了预测和实验两方面的甲醇转化率之间的良好一致性。

通过实验和CFD模拟，透彻研究了压降、温度和流量分布对使用不同重整器设计的甲醇转化的影响。结果表明，由于窄通道和高金属表面积，多通道设计保证了通道之间近似的流速、低的压降和低的温度下降，由此导致高甲醇转化率。这表明，具有多通道设计的重整器是与HT-PEMFC热集成的一个良好解决方案。

通过实验和模拟研究了甲醇重整装置（MSR-C）与HT-PEMFC的热集成。为此，制造了由碳/PPS（聚苯硫醚）复合材料制成的双极板，其特征在于燃料电池的阳极流场在一侧，而重整器的流场在另一侧。装配有ADVENT TPS公司面积为25 $cm^2$ 的膜电极组件（MEA）的MSR-C/HT-PEMFC，在453 K下显示出高的性能。经过几个小时的操作，由于甲醇转化率低（<90 %），MEA的降解是显着的。电化学阻抗谱（EIS）分析显示，阴极阻抗随着作为燃料的重整产物而增加，这是由于从阳极到阴极有甲醇渗透现象，特别是在较低温度下甲醇转化率更低而导致的。，仅在> 0.75 $A \cdot cm^{-2}$时，组合装置的自热可持续性才能获得，这是由于组合反应器的隔热性差。在第二次尝试中，进一步改进了MSR-C/HT-PEMFC组合单元，制备了

一种新的、且优化的镀金的铝双极板。装配了来自BASF的面积为45 $cm^2$的 Celtec P2200N MEA的组合单元，在453 K下显示出了卓越的电池性能，并且在相比于使用类似装置的文献报道中具有最高性能。该装置在0.2 $A \cdot cm^{-2}$下，700小时短时耐久性测试中表现出良好的稳定性。EIS分析还表明，直接使用生产的甲醇重整气作为燃料对MEA的降解没有显著影响。同时也通过模拟评估了组合的MSR-C/HT-PEMFC的热集成。开发了一种3D非等温模型，并通过先前获得的实验结果进行了验证。仿真结果显示了使用3厘米厚的玻璃棉保温的低电流密度（0.1 $A \cdot cm^{-2}$）的装置的自热可持续性。基于组合单元，提出了一个具有10个单体的电堆; 结果表明，该电堆在4.5 A（0.1 $A \cdot cm^{-2}$）和54 A（1.2 $A \cdot cm^{-2}$）之间的电流下的电池性能不需要任何外部热源。

本文还研究了面向HT-PEMFC应用的重整气的生产和净化。考虑两种类型膜，即对氢气选择性透过的Pd-Ag膜和对二氧化碳选择性透过的支撑的离子液体（ILs）膜，开发了固定床膜反应器（PBMR）的3D非等温模型。模拟结果表明，尽管效率低，工艺复杂程度高，但从反应体中的选择氢气排出可提高甲醇转化率，产生纯氢气流。选择性二氧化碳去除的膜，相比除氢的膜，具有更好的能量效率性，特别是对于高氢回收时；然而，它对甲醇转化率有一个小的影响，而且需要具有非常高的选择性和高速度的膜，而这种膜是难以获得的。考虑重整催化剂和MEA之间非常薄的Pd-Ag膜，通过在473K下的模拟评估了单体固定床膜反应器（PBMR-C）与HT-PEMFC的集成，。PBMR-C/HT-PEMFC显示出高性能，其性能可媲美使用氢气的HT-PEMFC，而且，展示出它是紧凑的、和高热效性。 组合单元的性能依赖于Pd-Ag膜在473K的渗透性、选择性和稳定性。

# Chapter 1

# Introduction

## 1.1. Changing environmental policies

The continuing growth of urban areas is likely to be one of the most significant factors affecting society over the next 50 years, according to United Nations Agency [1]. The large cities in the world will be overcrowded and characterised by poverty and pollution. Moreover, the International Energy Agency (IEA) predicted a world energy consumption growth of 56% between 2010 and 2040 [2], mostly from non-Organization for Economic Cooperation and Development countries, where demand is driven by strong economic growth and reliant on fossil fuels.

Presently, an estimated 90% of European Union (EU) citizens are exposed to some of the most harmful atmospheric pollutants, namely $NO_2$, at levels judged dangerous by the World Health Organisation [3, 4]. 70 000 premature deaths in 2013 were attributed to the $NO_2$ high levels, where diesel-powered vehicles are pointed out as the main sources of these gas emissions in EU. The European Commission identified possible measures to lower polluting emissions, which includes reducing overall traffic volumes, adapting driving behaviour, replacing the type of fuels used, or switching to electric cars.

The Paris Agreement entered into effect on 4 November of 2016 and is the global response to the threat of climate change caused by the greenhouse gases emissions. The goals of this agreement [5], described in Article 2 of the United Nation Framework Convention of Climate Change Agreement, are the following:

(a) Holding the increase in the global average temperature to well below 2 $^{\circ}$C above pre-industrial levels, but preferably no more than 1.5 $^{\circ}$C above pre-industrial levels.

(b) Increasing the ability to adapt to the adverse impacts of climate change and foster climate resilience and low greenhouse gas emissions development, in a manner that does not threaten food production.

(c) Making finance flows consistent with a pathway towards low greenhouse gas emissions and climate resilient development.

The climate goals of the Paris Agreement are extremely challenging to meet, requiring policies that help to accelerate low carbon technologies and energy efficiency in all sectors. According to IEA[6], more than 700 million of electric cars by 2040 will be needed, wind and solar should replace coal growing in importance in the energy sector, renewables need to expand their use in the industrial, building and transportation sectors instead of being confined to electricity generation. Environmentally friendly technologies are being developed and implemented, but government policies will determine the future of global energy.

## 1.2. The role of hydrogen in the new economy

In 1970, John Bockris foresaw the hydrogen economy, but only in recent years hydrogen has gained a considerable interest as an energy carrier, mostly due to fuel cells technology. Hydrogen is the smallest of all atoms and most common chemical element on the planet Earth; it is eight times lighter than methane, so light that it escapes the Earth gravity and consequently does not exist in nature in its pure form. Hydrogen can be produced by water electrolysis or by chemical processes from hydrocarbons or even other hydrogen carriers (*e.g.* $NH_3$) and when burned in the presence of oxygen, only water is produced, which can be returned to nature in its original form. The hydrogen obtained by water electrolysis produces no pollutants in all the production/consumption cycle and renewable energy sources such as solar, wind, water, or geothermal heat can supply the electrical power needed. Producing hydrogen from water splitting using electrical energy is however one of the most energy-intensive ways to produce this fuel [7]. A high over-potential is required to overcome polarization and ohmic losses caused by the electric current flow, making the efficiency of the process low. Therefore, hydrogen is produced mostly from natural gas steam reforming over supported nickel catalysts in packed-bed reactors with an efficiency of *ca.* 90% [8]. The hydrogen-rich stream is further upgraded through several steps of purification, which includes water-gas-shift

(WGS), preferential oxidation (PROX) and pressure-swing-adsorption process [8]. The purification process comprehends several individual process units running at different temperatures and pressures, which influences negatively the overall efficiency [9]. Methane reforming with respect to *well-to-wheel* efficiency analysis and overall $CO_2$ emissions, does not show significant advantages since most of the practical applications, *e.g.* engines propulsion, can use directly natural gas instead of hydrogen. Moreover, hydrogen gas is difficult to store, transport, deliver and has a low energy density by volume. Gas compression, liquefaction or chemisorption using metal hydrides are some of the techniques used to store hydrogen [10]. Typically, hydrogen is stored at high pressure (700 bar) in multilayers carbon fibre-reinforced tanks, providing an energy density of 4.4 $MJ \cdot dm^{-3}$ [10, 11]. The hydrogen compression to 700 bar results, however, in an energy consumption of *ca.* 13 % of the stored hydrogen high heating value (HHV) [12]. Liquid hydrogen can increase the energy density to 9.4 $MJ \cdot dm^{-3}$ [10, 11], but the energy cost for the liquefaction is above 30 % HHV. Storing hydrogen in spongy matrices of alloys such as, $LaNi_5$, $LiBH_4$ or $NaBH_4$ by physical/chemical sorption provides an energy density by volume of *ca.* 7.7 – 8.4 $MJ \cdot dm^{-3}$, but by mass only 1.2 $MJ \cdot kg^{-1}$, making metal hydrides yet impractical for mobile applications [13].

### 1.3. Fuel cells

Fuel cells (FCs), by definition, are electrochemical devices that convert chemical energy of a fuel into electrical energy. The first references to Fuel Cells appeared in 1838 by William Grove, who reported an improved wet-cell battery called the 'Grove cell', based on reversing the electrolysis of water [14]. FCs are essentially composed by an electrolyte (membrane), two electrodes and two gas diffusion layers for the anode and cathode, as depicted in Fig. 1.1. The fuel, typically hydrogen, is fed to the anodic compartment and oxidant, typically air, is fed to the cathodic compartment. The potential difference between the two half-cells creates an electric field that ionizes the adsorbed atomic hydrogen (Volmer – Tafel mechanism) [15]. The electrons flow through the external circuit, while protons (in acid electrolytes) migrate through the electrolyte in order to maintain the electroneutrality of the medium. In the cathode, the proton and electrons react catalytically with the adsorbed oxygen to form water vapour (Damjanovic – Brusic mechanism) [16]. In the last years, FCs gained a renewed attention because they

represent an environmental friendly technology with high efficiency, low noise pollution and has water vapour as the only gas emission.

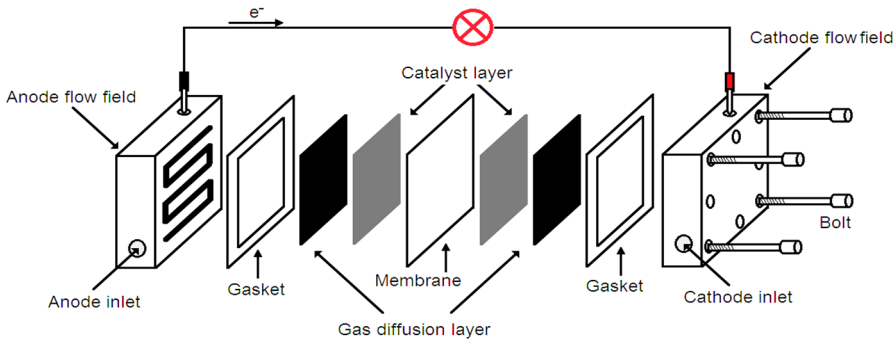


**Fig. 1.1** Fuel cell scheme.

### 1.3.1. Types of fuel cells

Fuel cells are primarily classified according to the nature of the electrolyte. The electrolyte determines the type of chemical reactions, the operating temperature and most suitable applications for the fuel cell. A brief description of the most common FCs is presented below.

*Alkaline fuel cell (AFCs)*

Alkaline fuel cells (AFCs), also known as the Bacon fuel cell, were invented in 1940 by Francis Thomas Bacon [17]: They became famous after being employed in the Nasa Apollo Space Program in the 1960s. AFCs use an aqueous solution of potassium hydroxide (KOH) supported in a porous material as electrolyte and operate at low temperature between 298 and 343 K, reaching efficiencies of *ca*. 60–70% [18]. The electrochemical reactions are the following:

$$\text{Anode: } 2H_2 + 4OH^- \rightarrow 4H_2O + 4e^- \quad (1.1)$$

$$\text{Cathode: } O_2 + 2H_2O + 4e^- \rightarrow 4OH^- \quad (1.2)$$

The electrodes can be made of different cheap materials, but the efficiency increases when platinum and noble metal catalysts are used, increasing also the costs [19]. The AFCs are cheap, compared to other FCs, and have a quick start-up; the major disadvantages relates to the use of corrosive electrolytes, that reduce the life span, and the

sensitivity towards $CO_2$, which reacts with the electrolyte forming carbonates that precipitate on the pores of the electrodes, blocking them [20]. Therefore, AFCs require both anode and cathode gas stream purification making them inadequate for commercialization. The control of the electrolyte level is critical, since the excess leads to electrode flooding and the insufficiency to the electrode drying [21].

*Phosphoric acid fuel cell (PAFC)*

Phosphoric acid fuel (PAFC) cells were developed in the 1960s and were the first fuel cells to be commercialized. Since the 1970s, more than 500 PAFC power plants were built, being the largest operated in Japan between 1991 and 1997 with a capacity of 11 MW [22]. This type of FCs uses phosphoric acid ($H_3PO_4$) retained in a 0.1–0.2 mm thick SiC matrix as an electrolyte. The protonic conductivity of electrolyte is high, due to the low thickness, but the mechanical properties are limited, allowing a maximum pressure difference between anode and cathode of 200 mbar [23]. The PAFC operates above the melting point of $H_3PO_4$, more precisely between 423K and 473 K [24]. The electrochemical reactions are the following:

$$\text{Anode: } 2H_2 \rightarrow 4H^+ + 4e^- \quad (1.3)$$

$$\text{Cathode: } O_2 + 4H^+ + 4e^- \rightarrow 2H_2O \quad (1.4)$$

The electrodes are made of carbon supported platinum- and uses Pt loading ranging between 0.25 - 0.5 $mg \cdot cm^{-2}$ [25]. The use of carbon support at high temperatures and acid conditions limit the potential to less than 0.8 V [26], due to the corrosion of the electrodes and Pt agglomeration. The PAFC are very stable [27], very tolerant to impurities (reformed hydrocarbons can be used as fuel) and can be used for cogeneration and hot water supply due to their high operating temperature [19,27]. The main drawback of PAFC are the high costs related to the platinum catalyst.

*Molten carbonate fuel cell (MCFC)*

Molten carbonate fuel cells were invented by G.H.J. Broers and J.A.A. Ketelaar in 1960 [28]. The device employed an electrolyte comprising a mixture of alkali metal carbonates constrained within a disc of magnesium oxide. The high operating temperatures of MCFC, between *ca.* 873–973 K, allow the carbonate ions to be transported through the melted electrolyte. The electrochemical reactions are the following:

$$\text{Anode: } 2H_2 + 2CO_3^{2-} \rightarrow 2H_2O + 2CO_2 + 4e^- \quad (1.5)$$

$$\text{Cathode: } O_2 + 2CO_2 + 4e^- \rightarrow 2CO_3^{2-} \quad (1.6)$$

The high operating temperature allows the use of non-precious metals as electrodes that are in contact with a molten carbonate electrolyte [19]. MCFCs use two nickel based porous electrodes with good electric conductivity, nickel in the metal form in the anode and nickel oxide in the cathode [29, 30]. The electrolyte is typically a eutectic mixture of lithium and potassium carbonates (62 wt. % $Li_2CO_3$ and 38 wt. % $K_2CO_3$) with melting point of *ca*. 823 K [31]. The major advantages of MCFC are the high efficiency, between 50–60%, low cost and the possibility of internal reforming in the anode [19, 28]. The degradation of materials associated with high operating temperature results in a poor lifespan. The MCFC are intolerant to sulphur and have a slow start-up making these devices interesting only for large plants applications [32].

*Solid oxide fuel cell (SOFC)*

Solid oxide fuel cells (SOFCs) were proposed for the first time by Emil Baur and H. Preis in the late 1930s, while working with solid oxide electrolytes such as zirconium, yttrium, cerium, lanthanum and tungsten oxide. However, the first operative ceramic fuel cell was only reported in 1937 by Baur and Preis [33]. SOFC relies on oxygen ion ($O^{2-}$) transport in a stabilised zirconia such as yttria-stabilised zirconia (YSZ, $(ZrO_2)_{0.92}(Y_2O_3)_{0.08}$) electrolyte [34]. The high operating temperatures of SOFC, between ca. 973–1273 K, allow the use of different fuels besides hydrogen, such as methane and carbon monoxide. Depending on the type of fuel used, the electrochemical reactions can occur according to the following equations:

$$\text{Anode: } 8H_2 + 4O^{2-} \rightarrow 4H_2O + 8e^- \quad (1.7)$$

$$\text{Anode: } 4CO + 4O^{2-} \rightarrow 4CO_2 + 8e^- \quad (1.8)$$

$$\text{Anode: } CH_4 + 4O^{2-} \rightarrow 2H_2O + CO_2 + 8e^- \quad (1.9)$$

$$\text{Cathode: } 2O_2 + 8e^- \rightarrow 4O^{2-} \quad (1.10)$$

The anode electrode is a composite powder mixture of electrolyte material and nickel oxide (NiO), reduced to metal during operation [35]. Perovskite-type lanthanum strontium manganite, ($La_{1-x}Sr_xMnO_3$, LSM) and lanthanum calcium manganite ($La_{0.66}Ca_{0.33}MnO_3$, LCM) can offer good performances as cathode electrodes at temperatures above 1073 K [34, 35]. SOFCs are the most promising FC technology for stationary

and large power plants applications. It is the most efficient fuel to electricity converter (ca. 50–60 %) and presents flexibility in the choice of fuel. The heat released can be used for co-generation or for combined cycle applications [36]. The electrodes are made of non-precious metals and have potential for long life expectancy (40 000–80 000 h) [34]. The slow start up, high cost, material degradation, low variation in the load demand and intolerance to sulphur content of the fuel cell are some of SOFCs drawbacks [19].

*Polymer electrolyte membrane fuel cell (PEMFC)*

Polymer electrolyte membrane fuel cells (PEMFC) are the most developed technology among FCs. They were invented in 1958 by Willard Thomas Grubb and Leonard Niedrach when using sulfonated polystyrene membranes as electrolytes [37]. In 1966, the company Dupont produced sulfonated tetrafluoroethylene, known by the commercial name of Nafion™ [38]. The high proton conductivity and mechanical stability at temperatures of 313 K – 363 K under fully hydrated conditions, makes Nafion™ the most used electrolyte in PEMFCs. The electrochemical reactions in PEMFCs are the following:

$$\text{Anode: } 2H_2 \rightarrow 4H^+ + 4e^- \quad (1.11)$$

$$\text{Cathode: } O_2 + 4H^+ + 4e^- \rightarrow 2H_2O \quad (1.12)$$

A new type of membranes for PEMFCs was developed in 1995 by Robert F. Savinell and Jesse S. Wainright [39], using (poly[2,2'-(*m*-phenylene)-5,5'-bibenzimidazole]), more commonly referred as polybenzimidazole (PBI), doped with phosphoric acid. These membranes are capable to operate efficiently without humidification at temperatures between 393 K and 453 K. The proton transport is assured by the phosphoric acid groups, with a mechanism similar to one observed in PAFCs. Savinell and Wainright predicted that a proton conducting polymer membrane operating at 473 K would be an opportunity to overcome the activity and stability problems of the Pt catalyst due to fuel impurities [40]. A more detailed description of the PEMFCs will be presented in the subchapter 1.4.

### 1.3.2. Fuel cell efficiency

In a fuel cell, the hydrogen oxidization by oxygen to form water is an exothermic reaction and is described as follows:

$$2H_2(g) + O_2(g) \rightarrow 2H_2O(l) \quad (1.13)$$

The Gibbs energy ($\Delta G$), as defined by J. Gibbs [41], is the greatest amount of mechanical work, which can be obtained from a given quantity of a certain substance in a given initial state. In the previous reaction (Eq. 1.13), a spontaneous process, the standard Gibbs energy of formation ($\Delta_f G^0$) of the products is less than that of the reactants (Eq. 1.14).

$$\Delta_r G^0_{H_2O_{(l)}} = \Delta_f G^0_{(\text{products})} - \Delta_f G^0_{(\text{reactants})} = -237.13\ \text{kJ}\cdot\text{mol}^{-1} \quad (1.14)$$

Standard Gibbs energies of formation of the elements ($H_2$ and $O_2$) in their reference states are zero; therefore, the standard Gibbs energy of reaction value (Eq. 1.14) is equal to the standard Gibbs energy of water formation. For reversible electrochemical processes, all the Gibbs energy can be converted into electrical energy. The standard potential ($E^0$) or the reversible open cell voltage (OCV) for a fuel cell, is defined as:

$$E^0 = -\frac{\Delta_f G^0_{(H_2O_{(l)})}}{nF} = 1.229\ \text{V} \quad (1.15)$$

The fuel cell potential ($E$) is described by the Nernst equation and depends on the reactants temperature and partial pressures. Considering also the effect of temperature on $E^0$, $E$ is calculated according to the following expression:

$$E = E^0 - (T - T_0)\left(\frac{\Delta S^0}{nF}\right) + \frac{RT}{nF}\ln\frac{P_{H_2}P_{O_2}^{1/2}}{P_{H_2O}} \quad (1.16)$$

where $R$ is the ideal gas constant, $T$ is the temperature, $P$ is the partial pressure, $n$ is the mole number of electrons involved in the reaction and $F$ is the Faraday constant (96 485.309 $C\cdot mol^{-1}$) and $\Delta S$ is the entropy variation. Rearranging Eq. 1.16 and using the standard thermodynamic values, it can be written as:

$$E = 1.229 - 0.85\times10^{-3}(T - 298) + 4.3\times10^{-5}T\left(\ln P_{H_2} + 0.5P_{O_2}\right) \quad (1.17)$$

The thermodynamic efficiency is described as the ratio between the energy output and the energy input. The efficiency in fuel cells can be expressed as the ratio between the electrical work produced and the heat released by burning the fuel (Eq. 1. 18).

$$\eta = \frac{\Delta_f G^0_{H_2O_{(l)}}}{\Delta_d H^0_{H_2O_{(l)}}}\times100 = \frac{-237.13}{-285.83}\times100 = 83\ \% \quad (1.18)$$

Considering that all Gibbs energy of formation ($\Delta G_f$) is converted to electric energy, the maximum efficiency of a fuel cell at standard conditions is 83 %. However, not all the Gibbs energy of formation is converted to electric energy, some of it is lost in the form of heat due to cell polarization and the ohmic losses. The fuel cell energy conversion efficiency can be expressed as the ratio between electric potential output ($V_{FC}$) and the thermoneutral electric potential (the electric potential if all the enthalpy of hydrogen is converted in electric energy):

$$\eta == \frac{\text{Power output}}{\text{Power input}} \times 100 = \frac{V_{FC} I}{\frac{\Delta_f H^0_{H_2O_{(l)}}}{2F} I} \times 100 = \frac{V_{FC}}{1.482} \times 100 = 67 V_{FC}\% \qquad (1.19)$$

Fuel cells do not necessarily have a higher efficiency than heat engines. A fuel cell operating at 0.6 V has a maximum efficiency of 40 %. Low speed diesel marine engines, can reach an overall energy conversion efficiency above 50% [42] and gas turbines in combined-cycle for power generation applications can reach thermal efficiencies above 60 % [43]. Fuel cells are thermodynamically more efficient at lower temperatures ($E$ decreases with temperature increase, Eq. 1.17), but the potential losses (kinetic losses, namely activation and ohmic) are lower at higher temperatures. It is more advantageous to run a fuel cell at higher temperatures, yet with lower thermodynamic efficiency, and produce higher operating currents. Moreover, the heat produced by fuel cells at higher operating temperatures can be used more efficiently, than the heat produced at low operating temperatures.

### 1.3.3. Potential losses

The electric potential difference ($\Delta V$) of the fuel cell decreases with the electric load due mostly to potential losses, which are classified as activation, ohmic and concentration/diffusion losses. Each of these terms are important at different electric loads, as shown in the potential difference-current density curve (Fig. 1.2).

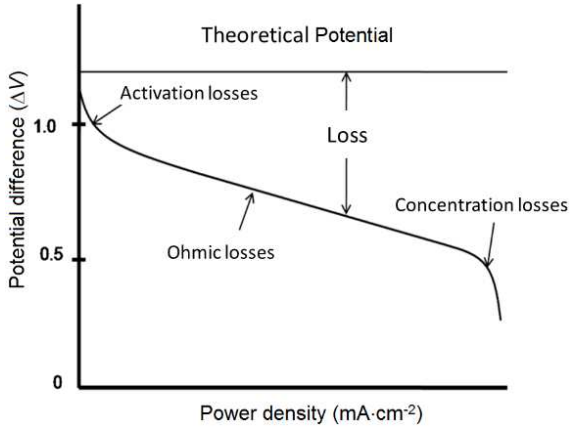


**Fig. 1.2** Typical potential-current density curve.

*Activation losses*

Activation losses reflect a loss of overall potential for driving the reaction in the desired products direction, which includes the hydrogen split into electrons and protons and the water formation. The losses are often referred as overpotential and are the difference between thermodynamic potential and the observed potential. The relationship between activation losses ($V_{act}$) and current density ($j$) can be mathematically described by the Tafel equation:

$$V_{act} = A\ln\left(\frac{j}{j^0}\right), \qquad A = \frac{RT}{2\alpha F} \tag{1.20}$$

Where, $j^0$ is the exchange current density (ranging between $10^{-2}$ and $10^{-8}$ A·cm$^{-2}$ [44]) and α is the charge transfer coefficient (ranging between 0 and 1 and has no units [44]). The exchange current density is the current density at the equilibrium, where the overpotential is zero (reversible potential). The charge transfer coefficient is the fraction of electrostatic potential at the electrode-electrolyte interface that affects the rate in an electrode reaction by lowering the free energy barrier [45]. The Tafel equation is applied to each electrode separately, assumes that the reverse reaction rate is negligible compared to the forward reaction rate and is only valid for $j > j^0$.

*Ohmic losses*

Ohmic losses are due to the proton transport resistance in the electrolyte, electrical resistance in the electrodes and current collectors and interface resistances. Ohmic losses are calculated by the Ohm's law:

$$V_{ohmic} = R_{ohm} j \tag{1.21}$$

*Concentration losses*

Concentration losses reflect changes in the local concentration of reactants at the neighbourhood of the catalyst. This effect occurs at high current densities, when the reactants are consumed faster than they can be transport from the bulk to the catalyst active sites. The mass transport mechanisms within the fuel cell include convection and diffusion. This effect is responsible for an important voltage drop and can be calculated using the semi-empirical equation:

$$V_{conc} = b \ln\left(1 - \frac{j}{j_{\lim}}\right) \tag{1.22}$$

where $b$ is empirical coefficient and $j_{lim}$ is the current density when the concentration of reactants in the catalyst active site is zero. [14].

The quantification of losses based on the polarization curve is a difficult task, since contributions from the different processes are overlapped. Considering all the losses, namely activation, ohmic and mass transport losses, the fuel cell effective potential ($V_{Fc}$) becomes:

$$V_{Fc} = E - V_{Act} - V_{ohmic} - V_{conc} \tag{1.23}$$

## 1.4. Polymer electrolyte membrane fuel cell

PEMFCs are divided accordingly to the operating temperature; those that operate below the water vaporization temperature, named low temperate PEMFC (LT-PEMFC or, more generally, just PEMFC) and those that operates above the water vaporization temperature, named high-temperature PEMFC (HT-PEMFC).

### 1.4.1.Low-temperature PEMFC

*Nafion™ membranes, electrolyte*

Despite the efforts of the scientific community to develop more efficient and stable electrolytes, LT-PEMFCs still rely mostly on Nafion™ membranes and similar polymers. Nafion™ presents a proton conductivity of *ca*. 10 – 20 $S \cdot m^{-1}$ under fully hydrated conditions at low-to-medium temperatures (343-363 K) [46]. The proton transport occurs through hydrated ionic clusters originated in the hydrophilic sulfonic acid group attached to the hydrophobic backbone of Nafion™ (Fig. 1.3).

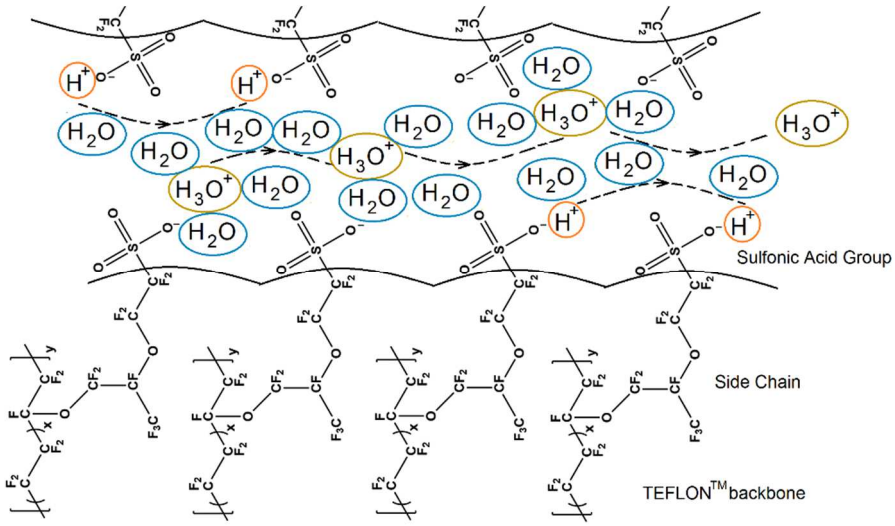


**Fig. 1.3** Illustration of the Nafion™ polymer chains self-align into a micro channel structure and proton-conduction along the channel through the sulfonic acid functional groups.

Microstructured percolated channels are formed in the ionic clusters and to them is attributed the high proton conductivity of Nafion™ membranes [46, 47]. The operating temperature is generally limited to *ca.* 363 K; a further increase in the temperature diminishes significantly the water content in the membrane, which results in a sharp decrease in the proton conductivity [48]. Nafion™, can also be used as electrolyte in direct formic acid fuel cell (DFAFC), direct ethanol fuel cell (DEFC) and direct methanol fuel cell (DMFC). These types of fuel cells show poor performances, despite the great efforts for

their development, due to a slow oxidation kinetics and fuel crossover through the membrane [49].

*Pt based electrodes*

The critical component in LT-PEMFCs, in terms of costs, is the electro catalytic system based on platinum (Pt). LT-PEMFCs use Pt nanoparticles dispersed on carbon black support. The Pt loadings typically used in the anode and cathode are *ca.* 0.4 $mg_{Pt} \cdot cm^{-2}$. Since the oxygen reduction reaction is more than six orders of magnitude slower than the hydrogen oxidation reaction, higher Pt loadings are typically used in the cathode [50]. The high price and loadings of Pt precious metal have a significant impact on the final price, making the spreading of this technology challenging. The US DOE 2017 targets for vehicles applications a Pt loading for the sum of both electrodes of 0.125 $mg_{Pt} \cdot cm^{-2}$ capable to produce power densities of 8.0 $kW \cdot g_{Pt}^{-1}$. To achieve such power density, it is required a membrane electrode assembly (MEA) producing at 0.6 V at least 1.5 - 2 $A \cdot cm^{-2}$ of current density [51]. The strategies to achieve such low loading includes producing very small and highly dispersed Pt nanoparticles [52], development and optimization of the carbon supports [53] and producing core-shell catalysts where a Pt shell is surrounding a particle core of a non-precious metal such as copper or nickel [54].

*Fuel contaminants*

The electro catalytic systems based on Pt can be easily poisoned, especially by CO, at the operating temperature of LT-PEMFCs. According to the International Organization for Standardization (ISO 14687), the hydrogen for LT-PEMFCs in automotive applications should have a CO concentration lower than 0.2 ppm [55]. To obtain such purity, hydrogen can be produced directly from water electrolysis, which is an expensive process, or can be produced from methane by steam reforming, followed by an expensive and complex purification process. Some strategies can be implemented to suppress the catalyst poisoning due to high CO levels (< 50ppm) namely internal/external air bleed or/and introducing a second metal, such as ruthenium (Ru), in the catalyst system [56]. In short, the high purity of hydrogen required for LT-PEMFCs is a critical issue for this technology.

*Long-term stability*

The life span and the long-term performance, especially considering start-stop cycles, is an important concern in LT-PEMFCs. According to US DOE, the lifetime target in 2020 for LT-PEMFCs is 5000 h for vehicle applications (with cycling, Table 1.1) [57]. Often the lifetime for mobile applications is measured in terms of service life until 10 % performance degradation is reached. For portable applications (<1 kW) the lifetime target is usually defined when 20 % of performance degradation is reached. Currently, these targets can only be met under controlled laboratory conditions [58]. The performance degradation is attributed generally to poor water management, fuel and oxidant starvation, corrosion and chemical reactions of cell components. Operation under dehydrated condition can damage the membrane while flooding facilitates corrosion of the electrodes, gas diffusion media and the membrane. Impurities present in the fuels can also poison the electrodes or damage the membrane.

*Vehicle applications*

LT-PEMFCs are the most adequate technology for vehicles and mobile applications. In 2014, LT-PEMFCs have finally been implemented in automobile for mass production; the Toyota Miray (Fig. 1.4) nowadays in commercialization is equipped with a 370-cell stack, which after a DC-DC converter, deliveries 650 V with a maximum output of 114 kW and power output density of 3.1 kW/L, the highest value ever reported for a stack [59]. The hydrogen is fed to the stack using two carbon fibre-reinforced tanks that store up to 5 kg of hydrogen pressurized at 70MPa. In collaboration with Toyota Motor Corp, BMW is developing PEM stacks and hydrogen tanks for implementation in future automobiles. BMW already presented its first prototype using the 5-series Gran Turismo platform but its commercialization will only occur in the next decade. After Toyota announcing that would freely share almost 6 000 patents related to hydrogen FC technology, several other car manufactures joined Toyota in developing furthermore this FC technology.

**Fig. 1.4** Toyota Miray (未来, 'mirai' Japanese word for 'future') is the first mass production hydrogen fuel cell vehicle. Adapted from [59].

### 1.4.2.High-temperature PEMFC

*Doped polybenzimidazole, electrolyte*

PBI membranes doped with phosphoric acid, after being developed by Robert F. Savinell and Jesse S. Wainright became the most common electrolyte for HT-PEMFC [39, 60]. PBI is an aromatic heterocyclic polymer (Fig. 1.5) with high mechanical strength, good chemical resistance and glass transition temperature of 703 K. The proton conductivity of PBI is low (*ca.* 3.82 mS·cm$^{-1}$ at 473 K); to increase it above 50 mS·cm$^{-1}$ and become suitable for fuel cell applications, PBI has to be doped with an acid [61]. However, the proton conductivity of PBI acid doped electrolyte systems is one order of magnitude lower than the free protic acids [62].

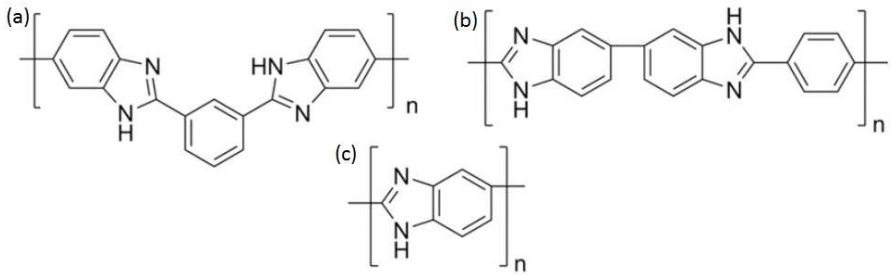


**Fig. 1.5** Chemical structure of mPBI (a), pPBI (b) and AB-PBI (c).

Other polymers can also be used as electrolyte, such as: the regioisomer poly[2,2 -*p* -(phenylene)- 5,5 -bibenzimidazole], or the most simple polymer of the polybenzimidazole family, poly(2,5-benzimidazole). Sulfonated poly-ether-ether-ketone (S-PEEK) blended with poly-benzimidazole (PBI), S-PEEK derived membranes such as sulfonated

poly-ether-ether-ketone with cardo group (S-PEEK-WC) [63] or pyridine based aromatic polyether doped with phosphoric acid electrolyte (Advent®) have also been used successfully as electrolyte.

*Phosphoric acid, transport mechanism, and permeability*

Phosphoric acid exhibits the highest proton conductivity amongst other simple inorganic and organic electrolytes (acids or bases), due to a strong autoprotolysis. The phosphoric acid, as other strong protic acids, is chemisorbed at PBI-type polymers. The chemisorption occurs through reaction between the acid and the alkaline imidazole structural units of the PBI polymer originating coulombic interactions and hydrogen bonds [64]. The phosphoric acid as doping electrolyte acts as a monoprotonic acid, despite being a triprotonic acid, because only the first dissociation exceeds the acidity of the protonated benzimidazole groups ($K_{A(H3PO4)} = 10^{-2.16}$ and $K_{A(H2PO4^-)} = 10^{-7.21}$) [65].

Grotthuss mechanism (also known as structure diffusion) is the dominant elementary process for the proton transport in PBI acid doped electrolyte systems [66]. The Grotthuss mechanism for proton conduction comprises a network of hydrogen bonds; the formation and breaking of these bonds, due to low bond strength, can be initiated by the thermal energy released locally during acid–base reactions [67]. Phosphoric acid-doped PBI presents a zero water electro-osmotic drag coefficient, meaning that water molecules are not transported together with protons. However, increasing the partial pressure of water vapour generally increases the proton conductivity of the membrane [68]. Without humidification, the orthophosphoric acid ($H_3PO_4$) is converted to pyrophosphoric acid ($H_4P_2O_7$) or higher oligomers at temperatures around 433 – 443 K, which have lower proton conductivity [69].

In the un-doped form, PBI membranes present a permeability towards hydrogen and oxygen at standard temperature and pressure of $1.9 \times 10^{-11}$ mol·m$^{-1}$·s$^{-1}$·bar$^{-1}$ and $4.5 \times 10^{-13}$ mol·m$^{-1}$·s$^{-1}$·bar$^{-1}$, respectively [70]. PBI membranes doped with phosphoric acid at temperatures between 423 K and 473 K show a hydrogen and oxygen permeability 2 to 3 orders of magnitude higher compared to the un-doped form at standard conditions [70, 71]. The presence of permeated oxygen in the anode side leads to the corrosion of the carbon supported catalyst, reducing the life span of the electrodes.

*Pt based electrodes*

HT-PEMFCs use Pt nanoparticles supported on high surface area carbon (graphitized or non-graphitized) held together by a high temperature stable polymer binder, *e.g.* PTFE, to form the catalyst layer. Phosphoric acid is added or transferred during the assembly from the doped membrane, to allow the proton transport to and from the catalyst layer. The HT-PEMFCs, typically use reformate gases as a fuel, requiring Pt loadings, of *ca.* 1.0 $mg_{Pt}·cm^{-2}$ in the anode and cathode, which is 2.5 times higher than in LT-PEMFCs and represents 45 % of the HT-PEM stack cost [72]. Despite having higher Pt loadings HT-PEMFCs have similar cost per kW of LT-PEMFCs; *e.g.* small power supplies (<1kW) has a cost of 6000 €·$kW^{-1}$[72]. The same approaches used in LT-PEMFCs can be adopted for HT-PEMFCs to reduce the electrode costs such as avoiding a catalyst support using platinum black, sputtered electrodes [73], Pt-based aerogels [74] or carbon-free multi/bimetallic materials in the form of meso/nanostructured thin films [75, 76].

The Pt based catalyst tolerance to fuel impurities increases with the temperature [77–79]. Long-term stability studies (>3500 h) of HT-PEMFC at 453 K with a reformate stream as fuel (60 % $H_2$, 2% CO, 5 ppm $H_2S$, 21 % $H_2O$, and 17 % CO) showed a degradation of 20 μV·$h^{-1}$, similar to the observed with pure hydrogen [80]. HT-PEMFCs can tolerate up to 3 % of CO concentration [81], allowing the use of methanol/ethanol reformate as fuel without earlier purification.

*Long term stability*

The required stability for automotive fuel cell systems is 5000 h (Table 1.1), which is equivalent to 200 000 driven kilometres. A dynamic study using HT-PEMFCs considering 240 start-up/shutdown cycles of 12 h of operation at 433 K and 0.2 A·$cm^{-2}$ followed by 12 h of shutdown, after 6 000 h showed an average potential drop of 200 μV·$cycle^{-1}$ and 11 μV·$h^{-1}$. A more extensive study considering 860 start-up/shutdown cycles of 7 h of operation at 423 K and 0.5 V followed by 17 h of shutdown, after 3.5 years showed an average potential drop of 300 μV·$cycle^{-1}$ and 40 μV·$h^{-1}$. Steady state operation during 17 500h, at temperatures between 423 – 433 K and 0.2 A·$cm^{-2}$, showed performance losses < 6 μV·$h^{-1}$. The experimental results, so far reported, for long-term durability tests with HT-PEMFCs at steady state and dynamic are very encouraging, but still nearly halfway of the DOE targets.

**Table 1.1** DOE durability targets for PEMFCs for automotive systems of 80-kWe (net) [57].

| Characteristic | Units | 2015 Status | 2020 Targets | Ultimate Targets |
|---|---|---|---|---|
| Stack power density | $W \cdot L^{-1}$ | 3 000 | 2 250 | 2 500 |
| Stack specific power | $W \cdot kg^{-1}$ | 2 000 | 2 000 | 2 000 |
| Performance 0.8 V | $mA \cdot cm^{-2}$ | – | 300 | 300 |
| Cost | $\$ \cdot kW^{-1}_{net}$ | 26 | 20 | 15 |
| Durability in automotive drive cycle | hours | 3 900 | 5 000 | 8 000 |
| Start-up/shutdown durability | cycles | – | 5 000 | 5 000 |
| $Q/\Delta T_i$ | $kW \cdot °C^{-1}$ | 1.9 | 1.45 | 1.45 |
| Pt (both electrodes) | $g \cdot kW^{-1}$ | 0.16 | 0.125 | - |
| Pt (both electrodes) | $mg_{PGM} \cdot cm^{-2}$ | 0.13 | 0.125 | - |
| Loss in initial activity (mass activity loss) | % | 66c | <40 | - |
| Loss in performance at 0.8 $A \cdot cm^{-2}$ | mV | 13 | <30 | - |
| Electrocatalyst support stability (mass activity loss) | % | 41 | <40 | - |
| Loss in performance at 1.5 $A \cdot cm^{-2}$ | mV | 65 | <30 | - |

*Degradation mechanisms*

Several components contribute for the fuel cell performance degradation. Accelerated aging test with Fenton agent indicated that benzenoid rings of the polybenzimidazole polymers could be oxidized by peroxide radicals producing significant degradation of the membrane physicochemical properties [82, 83]. Covalently crosslinking and ionic blending of the polymers demonstrate to improve the materials durability; however, the effect in the HT-PEMFC performance and degradation was not yet assessed [84]. The phosphoric acid loss is a critical factor in the fuel cell performance degradation [39]. The phosphoric acid loss via evaporation is the main mechanism for acid loss, but acid leaching by liquid water can also occur during cold starts or shutdowns. The acid loss in steady state, via evaporation at 423 K, is *ca.* 2.1 $\mu g \cdot m^{-2} \cdot s^{-1}$ and can increase more than one order of magnitude when the temperature increases to 473 K [85]. The acid evaporation increases at high current densities; the generated water converts pyrophosphoric acid to orthophosphoric acid, which has higher vapour pressure [86].

Carbon corrosion and platinum dissolution in the acidic electrolyte also contribute to the HT-PEMFC performance degradation. High operating temperatures and high electrode potentials enhance these phenomena. Studies have shown a platinum mass loss of 80 % at 478 K and 0.9 V after 100 h of operation [87, 88]; fortunately, the metal dis-

solution rate decreases by more than 8 orders of magnitude when the cell potential decreases from values close to the open circuit voltage to 0.6 V [88]. The carbon support corrosion leads to the detachment of platinum, triggering the agglomeration of nanoparticles and the reduction of hydrophilicity of the catalyst layer. The mechanism for carbon corrosion in acid electrolytes considers a three-step process [89]: the carbon oxidation, the formation of carbon surface oxides and the formation of carbon dioxide from the hydrolysis of the carbon surface oxides. The hydrolysis of the carbon surface oxides is thermodynamically favourable at potentials higher than 0.207 V [90], but the low kinetics makes the use of carbon as support feasible. Increasing the operating temperature increases the carbon corrosion kinetics making this issue more critical in HT-PEMFCs than in LT-PEMFCs. The degradation of bipolar plates and gas diffusion layers are assumed to be of significance, but only limited information is available.

### 1.5. Methanol steam reforming*

As mentioned previously, hydrogen is the most suitable fuel for PEMFC applications but has a very low volume energy density and shows limitations regarding storage and transportation. Methanol has been pointed out as an important energy carrier [91,92]; It can be produced from renewable sources, has a high hydrogen/carbon ratio and has no carbon to carbon bonds, which allows low reforming temperature (513 K – 533 K), making it attractive for *in-situ* hydrogen production. Methanol can be also used directly in PEMFC, but displays low energy performance due to poor oxidation kinetics and methanol crossover from the anode to the cathode [93].

Methanol steam reforming (MSR) is a more attractive reaction than auto-thermal reforming or partial oxidation due to higher hydrogen production and low CO content in the product stream. Methanol steam reforming reaction (Eq. 1.24) is an endothermic reaction that occurs simultaneously with two side reactions that produce CO, reverse water-gas-shift (RWGS, Eq. 1.25) and methanol decomposition (MD, Eq. 1.26) [94,95].

---

* The content of this subchapter is adapted from: A. Iulianelli, P. Ribeirinha, A. Mendes, A. Basile, Methanol steam reforming for hydrogen generation via conventional and membrane reactors: A review, Renewable and Sustainable Energy Reviews 29 (2014) 355–368.

$$CH_3OH+H_2O \rightleftarrows CO_2+3H_2 \ , \ \Delta H°_{298K}=+49.40 \ kJ \cdot mol^{-1} \quad (1.24)$$

$$CO_2+H_2 \rightleftarrows CO+H_2O \ , \ \Delta H°_{298K}=+41.14 \ kJ \cdot mol^{-1} \quad (1.25)$$

$$CH_3OH \rightleftarrows CO+2H_2 \ , \ \Delta H°_{298K}=+90.54 \ kJ \cdot mol^{-1} \quad (1.26)$$

### 1.5.1.Catalysts

The state of the art of commercial catalysts for MSR are copper-based catalysts such as $CuO/ZnO/Al_2O_3$, due to their low cost and considerably high activity at temperatures of *ca.* 523 K [96]. They present a pyrophoric nature, originate significant amounts of carbon monoxide and show low stability; *e.g.* after 60 h of operation at 523 K the methanol conversion drops *ca*. 40 % [97]. Sintering, coke deposition, catalyst poisoning (chloride, sulphur) and change in oxidation state, have been pointed out in the literature as possible reasons for the catalyst deactivation [98,99]. The coke formation can be prevented using a water molar fraction above the stoichiometric value [100]; the sintering of the copper nanoparticles and change in oxidation state can be minimized by decreasing the operating temperature. Thermodynamically, almost complete methanol conversion can be achieved at 453 K [101], with only traces of carbon monoxide being produced. More active and stable at low temperatures catalysts for MSR are strongly desired and apparently conceivable. Two approaches can be followed to prepare and improve the characteristics of copper-based catalysts: a) adding promoters [102-105] or/and b) changing the preparation method [106, 107]. Both approaches are used to increase the metal dispersion and surface area, and to decrease the particle size. The most used promoters for copper-based catalysts are ZnO [102], $ZrO_2$ [108], Mn [109], $CeO_2$ [110] or $Al_2O_3$ [111]. Some materials can affect the CO selectivity such as $ZrO_2$ [102] or change the surface area where copper is dispersed such as alumina or chromium (III) oxide [112]. Alumina is also used as catalyst support, but there are others such as carbon nanotubes that are being investigated with promising results [113]. The catalyst preparation method is the second tool available for improving the catalytic activity of copper-based catalysts; co-precipitation and wet-impregnation based methods are the most used. Depending on the promoters or the supports, a more active catalyst of a specific type can be obtained by one or other method or even by a derivation of the previous (*e.g.* to produce $CuZrO_2$, the best synthesis method is a derivation from co-precipitation

[114]). The family of gallium-promoted copper-based catalyst, produced by co-precipitation, demonstrated one of the highest activities, stabilities and selectivities reported in the literature at temperatures lower than 473 K [115]. The high activity of this catalyst family was attributed to the Ga incorporation into the Cu–Zn oxide. A non-stoichiometric cubic spinel phase containing interstitial $Cu^{1+}$ ions is originated, resulting in extremely small copper clusters (< 5 Å [115]) highly dispersed on a defective oxide surface. Other catalyst families, besides copper-based catalysts, are being studied for MSR reaction, in particular those containing metals from the group VIII-X, such as palladium. $Pd/ZnO/Al_2O_3$ catalyst presents higher stability than $Cu/ZnO/Al_2O_3$ [97]; when compared with other metals (Ni, Pt, Ru, Ir) supported on ZnO, Pd catalysts present lower CO production and a higher methanol conversion [116-119]. The application of a second metal to form bimetallic alloy, can also improve the catalyst activity and selectivity. The best activity reported for Pd-based catalysts was obtained with Pd/Zn and Pd/Ga and the best selectivity with Pd/Cd [119]. Pd-based catalysts are drawing the attention of many researchers that are investigating the role of the preparation methods [120], the effect of support surface area [121] and the particle size [122]. Pt-based catalysts also demonstrated very high activity; *e.g.* $Pt/In_2O_3/Al_2O_3$ showed an activity 10 times higher than commercial Cu-based [123,124]. This high activity of $Pt/In_2O_3/Al_2O_3$ has been assigned to the contact regions between the metallic Pt with partially reduced $In_2O_3$ [125]. The major challenges of implementing commercially noble metals for MSR is the prohibitive high noble metal loadings (typical ranging from 5.0 to 15 wt.%), which limits their economic viability.

### 1.5.2. Reaction mechanisms

The MSR reaction mechanism over copper-based catalysts has been intensively discussed in the literature [126-129]. The first reported mechanisms assumed that hydrogen was produced by the methanol decomposition followed by water gas shift reaction [126,127]. Later, a mechanism involving the methyl formate as an intermediate, was suggested as follows [128]:

$$2CH_3OH \rightleftarrows HCOOCH_3 + 2H_2 \quad (1.27)$$

$$HCOOCH_3 + H_2O \rightleftarrows CH_3OH + HCOOH \quad (1.28)$$

$$HCOOH \rightleftarrows H_2 + CO_2 \quad (1.29)$$

Several Langmuir–Hinshelwood kinetic models have been presented to predict the evolution of the MSR reaction [94,129]. These models proposed the methanol dehydrogenation to produce methyl formate and hydrogen, followed by the methyl formate hydrolysis to form formic acid and methanol and then the decomposition of formic acid to form carbon dioxide. The CO formation has been attributed to the reverse water gas shift reaction since the methanol decomposition reaction only occurs at higher temperatures [129]. The methanol decomposition reaction, if occurs, should use a second type of active sites (Type 2), different from the ones used by MSR and water-gas shift reaction (Type 1) [94, 95]. Most of the elementary reactions are catalysed by both types of active sites (Type 1 and Type 2) (Table 1.2, Eq. 1.30 – 1.41), with different adsorption entropies and enthalpies. The reaction between hydroxyls and methyl formate in the methanol decomposition (Type 2) follows a different path, with decarbonylation via a formyl, instead of hydroxylation as occurs in MSR (Type 1, Eq. 1.42 –1.53, Table 1.2).

**Table 1.2** Reaction mechanisms occurring on active sites type 1 and 2 [94, 95].

| Reactions on active sites Type 1 and Type 1a | | Reactions on active sites Type 2 and Type 2a | |
|---|---|---|---|
| $S_1+S_{1a}+CH_3OH\ (g) \underset{k_{-CH_3O^{(1)}}}{\overset{k_{CH_3O^{(1)}}}{\rightleftarrows}} CH_3O^{(1)}+H^{(1a)}$ | (1.30) | $S_2+S_{2a}+CH_3OH\ (g) \underset{k_{-CH_3O^{(2)}}}{\overset{k_{CH_3O^{(2)}}}{\rightleftarrows}} CH_3O^{(2)}+H^{(2a)}$ | (1.42) |
| $S_1+S_{1a}+H_2O\ (g) \underset{k_{-OH^{(1)}}}{\overset{k_{OH^{(1)}}}{\rightleftarrows}} OH^{(1)}+H^{(1a)}$ | (1.31) | $S_2+CO(g) \underset{k_{-CO^{(2)}}}{\overset{k_{CO^{(2)}}}{\rightleftarrows}} CO^{(2)}$ | (1.43) |
| $S_1+CO_2(g) \underset{k_{-CO_2^{(1)}}}{\overset{k_{CO_2^{(1)}}}{\rightleftarrows}} CO_2{}^{(1)}$ | (1.32) | $2S_{2a}+H_2\ (g) \underset{k_{-H^{(2a)}}}{\overset{k_{H^{(2a)}}}{\rightleftarrows}} 2H^{(2a)}$ | (1.44) |
| $S_1+CO(g) \underset{k_{-CO^{(1)}}}{\overset{k_{CO^{(1)}}}{\rightleftarrows}} CO^{(1)}$ | (1.33) | $CH_3O^{(2)}+S_{2a} \underset{k_{-CH_2O^{(2)}}}{\overset{k_{CH_2O^{(2)}}}{\rightleftarrows}} CH_2O^{(2)}+H^{(2a)}$ | (1.45) |
| $2S_{1a}+H_2\ (g) \underset{k_{-H^{(1a)}}}{\overset{k_{H^{(1a)}}}{\rightleftarrows}} 2H^{(1a)}$ | (1.34) | $CH_3O^{(2)}+CH_2O^{(2)} \underset{k_{-C_2H_5O_2^{(2)}}}{\overset{k_{C_2H_5O_2^{(2)}}}{\rightleftarrows}} CH_3OCH_2O^{(2)}+S_2$ | (1.46) |
| $CH_3O^{(1)}+S_{1a} \underset{k_{-CH_2O^{(1)}}}{\overset{k_{CH_2O^{(1)}}}{\rightleftarrows}} CH_2O^{(1)}+H^{(1a)}$ | (1.35) | $CH_3OCH_2O^{(2)}+S_{2a} \underset{k_{-CH_3OCHO^{(2)}}}{\overset{k_{CH_3OCHO^{(2)}}}{\rightleftarrows}} CH_3OCHO^{(2)}+H^{(2a)}$ | (1.47) |

$$CH_3O^{(1)}+CH_2O^{(1)} \underset{k_{-C_2H_5O_2^{(1)}}}{\overset{k_{C_2H_5O_2^{(1)}}}{\rightleftarrows}} CH_3OCH_2O^{(1)} + S_1 \quad (1.36)$$

$$CH_3OCH_2O^{(1)}+S_{1a} \underset{k_{-C_2H_4O_2^{(1)}}}{\overset{k_{C_2H_4O_2^{(1)}}}{\rightleftarrows}} CH_3OCHO^{(1)} + H^{(1a)} \quad (1.37)$$

$$CH_3OCHO^{(1)}+OH^{(1)} \underset{k_{-HCOOH^{(1)}}}{\overset{k_{HCOOH^{(1)}}}{\rightleftarrows}} HCOOH^{(1)} + CH_3O^{(1)} \quad (1.38)$$

$$HCOOH^{(1)}+S_{1a} \underset{k_{-HCOO^{(1)}}}{\overset{k_{HCOO^{(1)}}}{\rightleftarrows}} HCOO^{(1)} + H^{(1a)} \quad (1.39)$$

$$OH^{(1)}+CO^{(1)} \underset{k_{-HCOO^{(1),b}}}{\overset{k_{HCOO^{(1),b}}}{\rightleftarrows}} HCOO^{(1)} + S_1 \quad (1.40)$$

$$HCOO^{(1)}+S_{1a} \underset{k_{-CO_2^{(1),a}}}{\overset{k_{CO_2^{(1),a}}}{\rightleftarrows}} H^{(1a)} + CO_2{}^{(1)} \quad (1.41)$$

$$CH_3OCHO^{(2)} \underset{k_{-HCOOH^{(2)}}}{\overset{k_{HCOOH^{(2)}}}{\rightleftarrows}} CH_3OCHO + S_2 \quad (1.48)$$

$$CH_3OCHO^{(2)} + S_2 \underset{k_{-CHO^{(2)}}}{\overset{k_{CHO^{(2)}}}{\rightleftarrows}} CH_3O^{(2)}+CHO^{(2)} \quad (1.49)$$

$$CHO^{(2)}+S_{2a} \underset{k_{-CO^{(2)},b}}{\overset{k_{CO^{(2)},b}}{\rightleftarrows}} H^{(2a)} + CO^{(2)} \quad (1.50)$$

$$S_2+S_{2a}+H_2O\,(g) \underset{k_{-OH^{(2)}}}{\overset{k_{OH^{(2)}}}{\rightleftarrows}} OH^{(2)}+H^{(2a)} \quad (1.51)$$

$$S_2+CO_2(g) \underset{k_{-CO_2{}^{(2)}}}{\overset{k_{CO_2{}^{(2)}}}{\rightleftarrows}} CO_2{}^{(2)} \quad (1.52)$$

$$HCOO^{(2)}+S_{2a} \underset{k_{-CO_2^{(2),a}}}{\overset{k_{CO_2^{(2),a}}}{\rightleftarrows}} H^{(2a)} + CO_2{}^{(2)} \quad (1.53)$$

### 1.5.3. Reformer designs

The reformer design has direct impact on the reaction conversion, but due to higher technical complexity and manufacturing costs of other designs, the reformers are normally tubular. Recent efforts in the area of micro-processing made possible and easier to manufacture other reactor designs and namely well-structured flat micro-reactors (Fig. 1.6). A micro-reactor is defined as a device that contains micro structured features, with a sub-millimeter dimension, in which chemical reactions are performed in a continuous manner [130]. They present advantages compared to conventional ones, such as: higher surface-to-volume ratio, smaller mean distance of the specific fluid volume to the reactor walls, better heat and mass transfer properties and flow patterns that fit with the reaction needs [130,131]. Packed-bed micro-reactors require catalyst particles with regular shape and a size smaller than the internal dimensions of the micro-channels. Most of micro-reactors use the catalyst applied as a coating, to prevent high pressure drop created by very small packed catalyst particles [130]. Micro-reactors range in area from 0.1 $cm^2$ to 10 $cm^2$ [130], while mini-reactors range between 10 $cm^2$ and 200 $cm^2$.

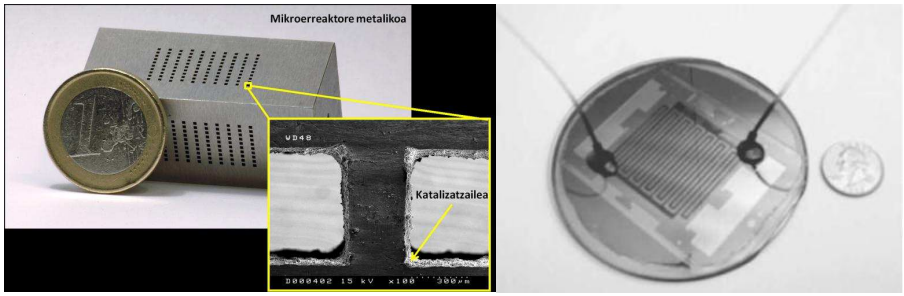


**Fig. 1.6** Micro reactors for methanol steam reforming. Adapted from [132,133].

The design of a reactor targets the maximization of the conversion and selectivity at the lowest cost; the reactor performance is influenced by the flow pattern, velocity profile, pressure drop and heat transfer, so all these aspects must be considered in the design. For conducting the methanol steam reforming reaction, the designs of most of reactors are parallel channels, pin-hole, coil-based and radial based (Fig. 1.7).

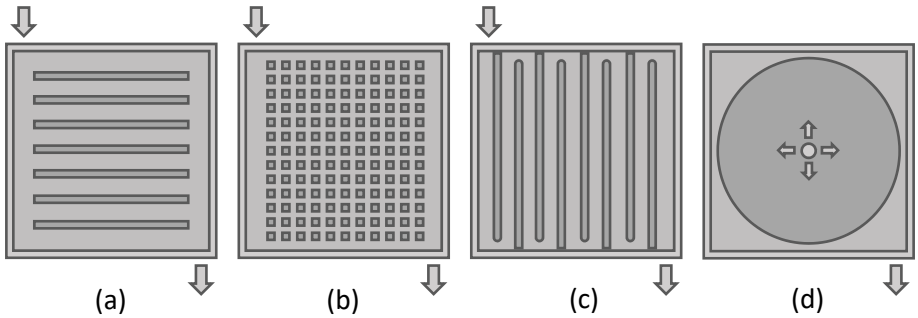


**Fig. 1.7** Different types of reformers; (a) parallel channels, (b) pin-hole, (c) coil/ serpentine and (d) radial.

Coil-based reactor designs allow high conversions, but impose a significant pressure drop penalty, which may be a limitation for compact applications [134]. On the other hand, the parallel channel designs exhibit a small-pressure drop, but the conversion is low due to uneven mass distribution and is affected by the Reynolds number [134]. By adjusting the channels width or by imposing a pressure drop at the channels entrance even distributions on parallel channel designs can be obtained, improving the methanol conversion [134,135]. The pinhole design displays a methanol conversion comparable to coil-based designs, but originates lower pressure drop. The pinhole de-

sign, however, exhibits a mass distribution that depends on the Reynolds number, representing an important limitation, since the reactor should be operated at different flow rates. Typically, the molar flowrate of reformate stream is almost twice the feed flowrate (Eq. 1.24), originating a significant surface velocity increase as the reaction conversion progresses along a constant cross-section reactor. Moreover, since the pressure decreases towards the exit of the reactor, the surface velocity increases even more [136]. For a diffusion-limited or close to diffusion-limited reaction, this large variation of surface velocity can be very detrimental for the reaction conversion [137].

To minimize temperature gradients, some strategies have been considered such as high metallic surface, internal heating [138] or wall coated reformers [139-140]. Wall-coated compared to packed-bed reformers, show low-pressure drop and high heat transfer, providing near-isothermal conditions but having lower specific catalyst load. Several studies indicated that wall-coated perform better than packed bed reformers, while others claim similar performances [141-143]. These different conclusions might be related to differences in catalyst-layer packing or coating methods, catalyst weight, channel width and operating conditions. Inside the catalyst layer, heat transfer is dominated by heat conduction (*e.g.* $\lambda_{cat} = 0.17$ $W \cdot m^{-1} \cdot K^{-1}$ [144]), thus using glass beads or other inert particles with higher heat conductivity should improve the temperature distribution.

### 1.6. Combining devices (MSR/HT-PMFC)*

HT-PEMFCs based on PBI membranes, can be directly fed with methanol reformate, since these devices can tolerate CO concentrations up to 3 % [68]. *In-situ* hydrogen production is already commercially used by Ultracell [145], and Serenergy [146,147] combined with HT-PEMFCs (Fig. 1.8).

---

* The content of this subchapter is adapted from: A. Iulianelli, P. Ribeirinha, A. Mendes, A. Basile, Methanol steam reforming for hydrogen generation via conventional and membrane reactors: A review, Renewable and Sustainable Energy Reviews 29 (2014) 355–368.


(a) (b)

**Fig. 1.8** Commercial HT-PEM reformed methanol fuel cell system, (a) Ultracell UC25; (b) Serenergy H3-350. Adapted from [145,146]

### 1.6.1. External reforming

UC25 [145] and H3-350 [146,147] power supplies use a similar arrangement for combining a fuel processor and HT-PEMFC. The fuel processor consists of a combustor, which burns the hydrogen of the anode vent, a vaporizer to heat and vaporize the fuel (molar water/methanol ratio of 1.5:1) and a reformer loaded with $CuO/ZnO/Al_2O_3$ catalyst (as depicted in Fig. 1.9). Since the fuel processor operates as a stand-alone process, this approach is typically designated as external reforming [148]. During the start-up period, which takes *ca.* 10- 15 minutes, a lithium battery provides the energy to electrical heaters until the operating temperature is reached. The reforming temperature is kept controlling the oxidant flow rate supplied to the burner. The heat transfer between the combustor and reformer requires high heat conductive materials, since it has a significant impact on the temperature distribution and consequently on the methanol conversion [149].

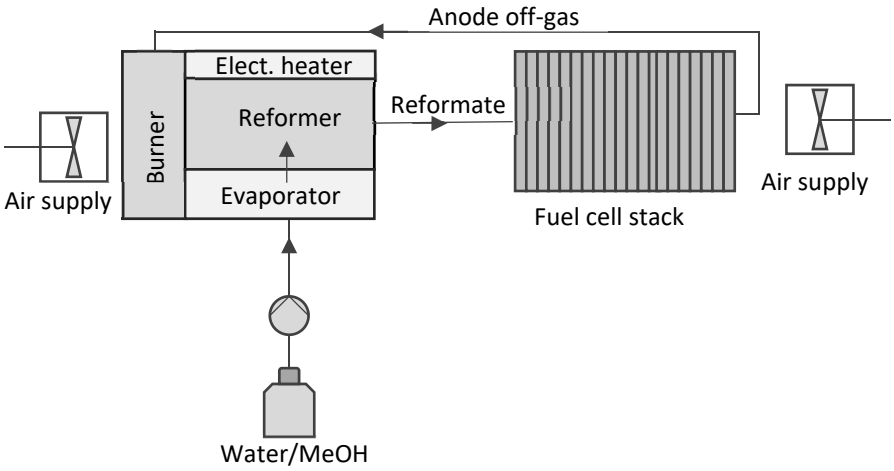


**Fig. 1.9** Standard setup for external reforming in a power supply.

Different designs for combustors and reformers can also be adopted. For example, by changing reformer and combustor from parallel channel design to serpentine, the flow velocity increases, diminishing the thickness of the stagnant film adjacent to the wall, leading to an increase of the heat transfer coefficient [150]. In small devices the heat management is critical because of the high surface-to-volume ratio. A cylindrical design organized in a "thermal cascade" can be adopted to minimize heat losses, having cool layers covering hotter ones, thus the combustor is inserted in the center followed by the vaporizer and the reformer [151].

### 1.6.2. Internal reforming

Fuel cells are exothermic devices, while methanol steam reformers are endothermic; internal reforming targets to take advantage of efficient heat and mass transfer between the two devices. Internal reforming is considered when MSR catalyst is inserted in the anode compartment, where both reforming and electrochemical reactions occur simultaneously (Fig. 1.10). If a physical barrier is used between the two reactions, the configuration is classified as indirect internal reforming [148]. Due to the mismatch of operating temperatures between the reforming and electrochemical reactions, internal reforming was only attempted by few authors [156-158]. In general, internal reforming (direct/indirect) show high voltage losses and low current densities, due to insufficient

fuel supply from the reformer and electro catalyst poisoning by the presence of methanol [156-157]. The advantages of the internal reforming are the compactness and the heat integration efficiency. Moreover, the reforming conversion could also benefit from the continuous hydrogen removal from the medium, which increases the methanol conversion.

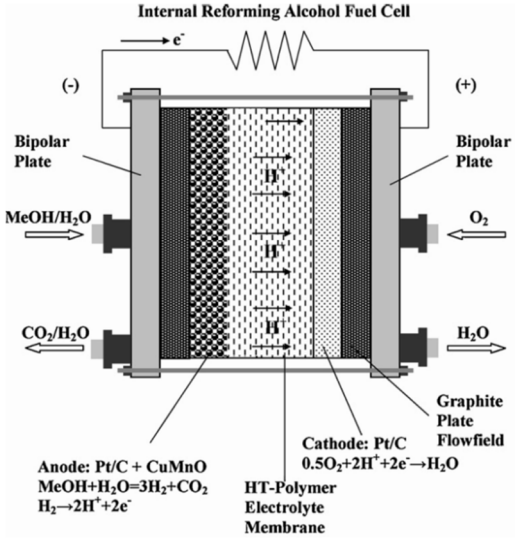


**Fig. 1.10** Direct Internal MSR (adapted from [157]).

### 1.6.3.Heat management

The heat produced in the fuel cell stack cannot be wasted, since it represents more than 50 % of the input chemical energy. Air or a thermal fluid can be used to transfer heat between different components of the power supply [62].

*Air cooled*

Air cooled power supplies such as UC25 [145] and H3-350 [146], are simpler and use cooling channels designed in the stack or very high air stoichiometry in the cathode channels to remove the excess heat (Fig. 1.8). The stack flow fields must be designed to generate low-pressure drop in the air inlets minimizing the energy consumed by blowers or fans. The heat removed from the stack is typically channeled to be used in wa-

ter/methanol evaporation. On the other hand, the heat required for the methanol reforming process, which occurs above the operating temperature of the stack, is supplied by burning the anode vent.

*Liquid cooled*

A uniform distribution of temperature among the different cells and between the inlet and the outlet of each cell is a challenging task, which becomes harder for large HT-PEMFC systems. Liquid cooling systems are often more suitable for large HT-PEMFC systems [147,152,153], since thermal fluids allow more efficient heat transfer than air and liquid pumps consume less energy than air compressors or fans. The temperature distribution on fuel cell stacks is significantly improved using thermal fluids compared to air cooling systems [152,153], however, the device becomes more complex. Several configurations for heat integration using a heat transfer fluid can be adopted. Most of them uses a serial system configuration with one fluid circuit [154,155], yet parallel configurations with two fluid circuits have also been suggested [62,155]. The serial configuration use a single pump to drive the fluid through a circuit with several temperature levels. The fluid is heated in burner, cooling as it transfers heat to the reformer and continues to cool as it flows through the fuel evaporator. The fluid before reaching the stack goes through a heat exchanger to decrease the temperature below the stack operating temperature. In the H3-5000 a 5 kW stack module from Serenergy [154], the thermal fluid circuit does not include the heat exchange with the reformer or the burner (Fig. 1.11). The H3-5000, is equipped with a radiator and a heat exchanger to reduce the fluid temperature, an expansion vessel to maintain constant the fluid pressure, an electrical heater for the start-up and a pump to drive the fluid through the circuit.

In the parallel configuration, two separate circuits, a low temperature (433–453 K) and a high temperature (around 573 K) are used. The low temperature circuit includes the stack, the evaporator and a convective cooler with a fan. The high temperature circuit includes the reformer, a heat exchanger and the catalytic burner. In start-up mode, electrical heaters assist to warm up of both liquid circuits.

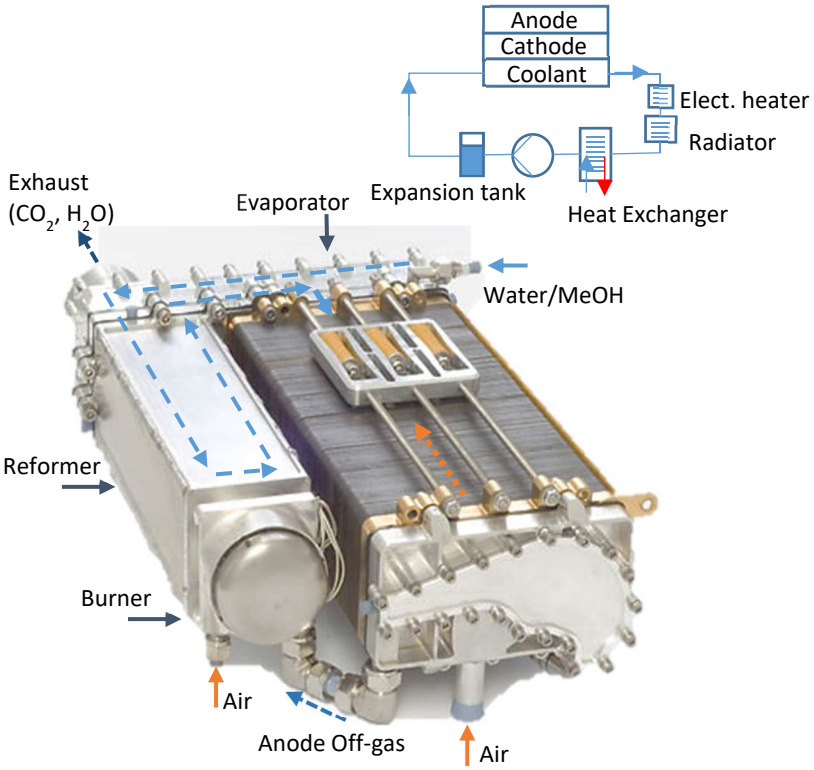


**Fig. 1.11** H3-5000, a 5 kW stack liquid cooled [154].

## 1.7. Hydrogen Purification*

The presence of contaminants in the methanol reformate stream ($CO_2$, $H_2O$, $CH_3OH$ and CO) can affect the performance of the HT-PEMFC, especially at high current densities, reducing the overall efficiency [159,160]. Several approaches can be adopted to produce a purer hydrogen stream. These includes the use of membrane reactors [161,162], adsorptive reactors [163], hybrid adsorptive membrane reactor [164] and fluidized bed adsorptive membrane reactors [165].

---

* The content of this subchapter is adapted from: A. Iulianelli, P. Ribeirinha, A. Mendes, A. Basile, Methanol steam reforming for hydrogen generation via conventional and membrane reactors: A review, Renewable and Sustainable Energy Reviews 29 (2014) 355–368 and P. Ribeirinha, M. Boaventura, J. M. Sousa, A. Mendes, Multifunctional hybrid sorption-enhanced membrane reactor, in A. Basile, F. Dalena, J. Tong, T. Veziroğlu, eds., Hydrogen Production, Separation and Purification for Energy, IET (2017) 373-399.

These technologies present several benefits, namely: (i) increase of the reaction conversion by shifting the equilibrium towards the reaction products and increase of the reactants residence time due to selective removal of one or more reaction products; (ii) reduction of the downstream purification requirements by, for example, *in-situ* separation of the desired product; iii) reduction of the operating temperature. The hydrogen production using membrane reactors are mostly settled on Pd and Pd alloys (Ag, Cu, Au) membranes [161,162]. The Pd based membranes present high selectivity towards hydrogen and high permeation at temperatures above 523 K [162]. Other metals such as vanadium, tantalum or niobium also show high permeability to hydrogen, however they present high surface resistance to hydrogen transport due to their high reactivity with gases [166]. The hydrogen transport in palladium membranes occurs through a solution/diffusion mechanism [167]. The mechanism follows six steps: a) adsorption of the molecular hydrogen on membrane surface; b) dissociation of molecular hydrogen; c) dissolution of atomic hydrogen into the palladium matrix; d) diffusion of atomic hydrogen through the membrane; e) re-combination of atomic hydrogen to form hydrogen molecules; f) desorption of the hydrogen molecules. The hydrogen flux through thick Pd and Pd-alloy membranes (>10 μm) is limited by the hydrogen diffusion through the membrane [168] and can be expressed by Sievert's equation, as follows:

$$J_{H_2,\text{Sieverts-Fick}} = \frac{P_{e,H_2}}{\delta} \cdot \left( p_{H_2,\text{retentate}}^{0.5} - p_{H_2,\text{permeate}}^{0.5} \right) \tag{1.54}$$

where $J_{H2}$ is the hydrogen flux through the membrane, $P_e$ is the membrane permeability to hydrogen, $\delta$ is the membrane thickness, $p_{H2,retentate}$ and $p_{H2,permeate}$ are the partial pressures in the retentate and permeate sides, respectively.

Pd based membrane reactors applied to MSR can produce a pure hydrogen stream, enhance the conversion and allow the reaction to be carried out at lower temperature. The conversion enhancement is attributed to the partial suppression of the MSR backward reaction and the increase of the residence time due to the partial removal of hydrogen from the reaction bulk. Performing the reaction at low temperature also suppresses the side reactions (MD and RWGS) [169]. The main disadvantages of using a membrane reactor based on Pd membranes are the costs and irreversible damages caused by impurities. The presence of hydrogen sulfide, sulfur dioxide, mercury vapour, thiophene, arsenic, unsaturated hydrocarbons, or chlorine carbon from organic materials may contaminate dense Pd-based membranes [170]. The presence of CO, especially

at lower temperatures (<423 K) or at higher concentrations blocks the hydrogen permeation, by adsorbing on the hydrogen adsorption sites [171]. Several other challenges such as membrane fouling, thermal and mechanical stability, hydrogen embrittlement and the energy for driving the hydrogen permeation (either using steam or high vacuum at the permeate side) limit the implementation of membrane reactors at the industrial scale.

Microporous membranes, such as silica and alumina-based membranes or molecular sieve carbon-based membranes have also been considered in steam reforming application for hydrogen removal from the reaction bulk; they are cheaper than Pd membranes, but difficult to prepare without defects, specially silica and alumina-based membranes, and present low selectivity towards hydrogen [169,172,173]. Porous membranes filled with ionic liquids have also been suggested for hydrogen production via low temperature methanol steam reforming [169,138]. These membranes have the particularity of being selective to $CO_2$, allowing air to be used as sweep gas and therefore avoiding the usage of vacuum pumps. Although ionic liquid membranes are still in an early stage for steam reforming applications, they represent a very promising technology.

## 1.8. Motivation and outline

The exploitation of HT-PEMFC systems integrating *in situ* hydrogen production by methanol steam reforming has been increasing in the past few years for mobile and vehicle applications. Operating the reformer and the fuel cell at similar temperatures is possible and expected to significantly improve the system overall energy efficiency and to simplify the system construction and operation. Accordingly, this thesis aims to study and optimize the main aspects related to the integration of a methanol steam reformer and HT-PEMFC. Which includes, preparation and characterization of a highly active MSR catalyst, kinetic modelling, design of reformers and bipolar plates, experimental and simulated integration of MSR with HT-PEMFCs and strategies for hydrogen purification.

The present work is divided in nine chapters, starting with a brief introduction (Chapter 1) about the importance of fuel cells, along with an overview of hydrogen production and purification. Chapter 2, “A novel catalyst for low temperature MSR reaction” presents the development and physicochemical and kinetic characterization of a novel $CuO/ZnO/Ga_2O_3$ catalyst and the comparison with two different commercial catalysts. In

Chapter 3, “Designing a methanol steam reformer” three different reformers, a tubular, a multi-channel and a radial are studied experimentally and by CFD modeling. This study allows a better understanding on the influence of pressure drop, temperature and flow distribution in the performance of a reformer, providing important background for further improving the design and operation of reformers. In Chapter 4, “Integration of a reformer with a HT-PEMFC – Part A” and Chapter 5 “Integration of a reformer with a HT-PEMFC – Part B” is studied experimentally the integration of a reformer and a fuel cell operating at the same temperature. For this purpose, specific bipolar plates were developed and different types of commercial MEAs were tested. In Chapter 6 “Integration of a reformer with a HT-PEMFC – Part C (modelling)” a 3D non-isothermal CFD model was developed to simulate and study the operation of HT-PEMFC integrated with a methanol steam reformer at different operating temperatures. In Chapter 7, “H2 production with low carbon content using PBMRs” a 3D non-isothermal PBMR CFD model was developed to evaluate the hydrogen purification of a methanol reformate stream using a PBMR equipped with supported ionic liquid membranes or with palladium membranes. In Chapter 8, “Integration of a PBMR with a HT-PMFC (modelling)” is studied by simulation the *in-situ* hydrogen production and purification using a packed bed reformer integrated with a HT-PEMFC. The MSR catalyst is considered into the anodic compartment of a HT-PEMFC, separated from the membrane electrode assembly by highly permeable and hydrogen selective palladium-alloy membrane. Finally, in Chapter 9, “Conclusions and future work” presents the main conclusions of the present thesis along with future work suggestions.

## 1.9. References

[1] [access date November 2017], United Nations Org. http://www.un.org/en/development/desa/news/population/world-urbanization-prospects-2014.html

[2] [access date November 2017], International Energy Outlook 2013 (IEO2013) projects, https://www.eia.gov/outlooks/ieo/pdf/0484(2013).pdf

[3] [access date November 2017], The Guradian, https://www.theguardian.com/environment/2013/oct/15/ european-cities-dangerous-air-pollution

[4] [access date November 2017], European Union, http://europa.eu/rapid/press-release_IP-17-238_en.htm

[5] [access date November 2017], UNFCCC Paris Agreement, https://unfccc.int/resource/docs/2015/cop21/eng/l09r01.pdf

[6] ] [access date November 2017], International Energy Agency – World Energy Outlook 2016, https://www.iea.org/ media/ publications/ weo/WEO2016Chapter1.pdf

[7] M. Wang, Z. Wanga, X. Gong, Z. Guo, The intensification technologies to water electrolysis for hydrogen production – A review, Renewable and Sustainable Energy Reviews 29 (2014) 573–588

[8] A. Basile, F. Dalena, J. Tong T. N. Veziroğlu (eds.), Hydrogen Production, Separation and Purification for Energy, IET (2017)

[9] A. M. Adris, B. B. Pruden, C.J. Lim, J. R. Grace, On the reported attempts to radically improve the performance of the steam methane reforming reactor, Canadian Journal of Chemical Engineering74 (1996) 177-182

[10] D.J. Durbin, C. Malardier-Jugroot, Review of hydrogen storage techniques for on board vehicle applications, International Journal of Hydrogen Energy, 38(34) (2013) 14595–14617

[11] I. Cumalioglu, A. Ertas, Y. Ma , T. Maxwell State of the Art: Hydrogen storage, Journal of Fuel Cell Science and Technology 5(3) (2008) 1-10

[12] [access date November 2017], Burckhardt Compression AG, Winterthur/Switzerland, https://www.burckhardtcompression.com/ media/downloads/technical-article/

[13] B. Sakintunaa, F. Lamari-Darkrimb, M. Hirscherc, Metal hydride materials for solid hydrogen storage: A review, International Journal of Hydrogen Energy 32(9) (2007) 1121–1140.

[14] K.R. Cooper, V. Ramani, J. M. Fenton Experimental methods and data analyses for polymer electrolyte fuel cells, Scriber Associates, Southern Pines (2005)

[15] J. Vermeijlen, L. Janssen, G. Visser, Mechanism of hydrogen oxidation on a platinum-loaded gas diffusion electrode, Journal of Applied Electrochemistry, 27(5) (1997) 497–506

[16] A. Damjanovic, V. Brusic, Electrode kinetics of oxygen reduction on oxide-free platinum electrodes, Electrochimica Acta 12(6) 1967 615-628

[17] K. R. Williams, Francis Thomas Bacon 21 December 1904-24 May 1992, Biographical Memoirs of Fellows of the Royal Society. 39 (1994) 2–9

[18] G. Merle, M. Wessling, K. Nijmeijer, Anion exchange membranes for alkaline fuel cells: A review, Journal of Membrane Science 377 (2011) 1–35

[19] A. Kirubakaran, S. Jain, R.K. Nema, A review on fuel cell technologies and power electronic interface, Renewable and Sustainable Energy Reviews 13 (2009) 2430–2440

[20] E. Gülzow, M. Schulze, Long-term operation of AFC electrodes with CO2 containing gases, Journal of Power Sources 127 (2004) 243–251

[21] P. Gouérec, L. Poletto, J. Denizot, E. Sanchez-Cortezon, J.H. Miners, The evolution of the performance of alkaline fuel cells with circulating electrolyte, Journal of Power Sources 129 (2004) 193–204

[22] [access date November 2017], Fuel Cell Today Bank Knowledge – PAFC System Survey, www.fuelcelltoday.com

[23] N. Rajalakshmi, K. S. Dhathathreyan, Present Trends in Fuel Cell Technology Development, Nova Publishers (2008) 57-64

[24] L. Carrette, K. A. Friederich, U. Stimming, Fuel cells-fundamentals and applications, Fuel Cells from Fundamentals to Systems 1(1) (2001) 5–39

[25] EG & GT Technical Services Inc., Fuel Cell Handbook seventh edition. US Department of Energy publication, Morgantown, West Virginia (2004)

[26] J. Larmine, Dicks A. Fuel cell systems explained. UK: John Wiley and Sons Ltd; (2000)

[27] N. Sammes, R. Bove, K. Stahl, Phosphoric acid fuel cells: Fundamentals and applications, Current Opinion in Solid State and Materials Science 8 (2004) 372–378

[28] A.L. Dicks, Molten carbonate fuel cells, Current Opinion in Solid State and Materials Science 8 (2004) 379–383

[29] L-K. Chen, J. Zuo, C-J. Lin, A novel MCFC cathode material modified by the EPD technique, Fuel Cells 3(40) (2003) 220–3

[30] D. Jung, I. Lee, H. Lim, D. Lee, On the high creep resistant morphology and its formation mechanism in Ni–10 wt.%Cr anodes for molten carbonate fuel cells. Journal of Materials Chemistry 13(7) (2003) 1717-1722

[31] K. Tanimoto, Y. Miyazaki, M. Yanagida, S. Tanase,T. Kojima, N. Ohtori, et al., Cell performance of molten-carbonate fuel cell with alkali and alkaline-earth carbonate mixtures, Journal of Power Sources 39 (1992) 285–97

[32] V. Cigolotti, S. McPhail, A. Moreno, S-P. Yoon, J-H. Han, S-W. Nam, T-H. Lim, MCFC fed with biogas: Experimental investigation of sulphur poisoning using impedance spectroscopy, International Journal of Hydrogen Energy 36 (2001) 10311–10318

[33] E. Baur, H. Z. Preis. Uber Brennstoff-Ketten mit Festleitern. Zeitschrift fur Elektrochemie 43 (1937) 727–32

[34] A. B. Stambouli, E. Traversa, Solid oxide fuel cells (SOFCs): a review of an environmentally clean and efficient source of energy, Renewable and Sustainable Energy Reviews 6 (2002) 433–455

[35] [access date November 2017], Fuel cell materials by Nextech materials, http://nexceris.com/market-solutions/power-and-energy/#sofc

[36] M. Farooque, H.C. Maru, Fuel cells — The clean and efficient power generators, IEEE Proc 89 (2001) 1819–29

[37] [access date November 2017], http://americanhistory.si.edu/fuelcells/pem/pemmain.htm

[38] C. Heitner-Wirguin, Recent advances in perfluorinated ionomer membranes: structure, properties and applications, Journal of Membrane Science 120 (1996) 1–33

[39] J.S. Wainright, J.T. Wang, D. Weng, R.F. Savinell, M. Litt, Acid-Doped Polybenzimidazoles: A New Polymer Electrolyte, Journal of the Electrochemical Society, 142 (1995) 121–123

[40] S. K. Zecevic, J. S. Wainright, M. H. Litt, S. Lj. Gojkovic, R. F. Savinell, Kinetics of O2 Reduction on a Pt Electrode Covered with a Thin Film of Solid Polymer Electrolyte, Journal of The Electrochemical Society (9) (1997) 2973-2982

[41] J.W. Gibbs, A Method of Geometrical Representation of the Thermodynamic Properties of Substances by Means of Surfaces, Transactions of the Connecticut Academy of Arts and Sciences 2 (1873) 382-404

[42] [access date November 2017], http://dieselturbo.man.eu/docs/default-source/shopwaredocuments archive/two-stroke-low-speed-diesel-engines.pdf?sfvrsn=2

[43] [access date November 2017], https://web.archive.org/web/20131113162749/http://www.mhi.co.jp/en/news/story/1105261435.html

[44] D. T. Sawyer, A. Sobkowiak, and J. L. Roberts, Electrochemistry for Chemists, John Wiley, NY, 1995

[45] R. Guidelli, R. G. Compton, J. M. Feliu, E. Gileadi, J. Lipkowski, W. Schmickler and S. Trasatti, Defining the transfer coefficient in electrochemistry: An assessment (IUPAC Technical Report), Pure and Applied Chemistry 86(2) (2014) 245–258

[46] L. Liu, W. Chen, Y. Li, An overview of the proton conductivity of nafion membranes through a statistical analysis, Journal of Membrane Science 504 (2016) 1–9

[47] J.J. Sumner, S.E. Creager, J.J. Ma, D.D. DesMarteau, Proton conductivity in Nafions 117 and in a novel bis[(perfluoroalkyl)sulfonyl]imide ionomer membrane, Journal of The Electrochemical Society 145 (1998) 107–110

[48] G.A. Giffin, M. Piga, S. Lavina, M.A. Navarra, A. D'Epifanio, B. Scrosati, V. Di Noto, Characterization of sulfated-zirconia/Nafions composite membranes for proton exchange membrane fuel cells, Journal of Power Sources 198 (2012) 66–75

[49] A. Heinzela, V.M. Barragánb, A review of the state-of-the-art of the methanol crossover in direct methanol fuel cells, Journal of Power Sources 84(1) (1999) 70–74

[50] H. A. Gasteiger, S. S. Kocha, B. Sompalli, F. T. Wagner, Activity benchmarks and requirements for Pt, Pt-alloy, and non-Pt oxygen reduction catalysts for PEMFCs, Applied Catalysis B: Environmental, 2005, 56, 9–35

[51] [access date November 2017], USDrive Fuel cell Technical Team Roadmap, https://energy.gov/sites/prod/files/2014/02/f8/fctt_roadmap_june2013.pdf

[52] M Chen, Y. Xing, Polymer-Mediated Synthesis of Highly Dispersed Pt Nanoparticles on Carbon Black, Langmuir, 21(20) (2005) 9334–9338

[53] X. Yua, S. Yeb, Recent advances in activity and durability enhancement of Pt/C catalytic cathode in PEMFC: Part II: Degradation mechanism and durability enhancement of carbon supported platinum catalyst Journal of Power Sources 172(1) (2007) 145–154

[54] P. Mani , R. Srivastava , P. Strasser, Dealloyed Pt−Cu Core−Shell Nanoparticle Electrocatalysts for Use in PEM Fuel Cell Cathodes, The Journal of Physical Chemistry C, 112(7) 2008 2770–2778

[55] ] [access date November 2017], International Organization for Standardization, ISO/TS 14687-2, Hydrogen Fuel-Product Specification—Part 2: Proton exchange membrane Fuel Cell applications for road vehicles; (2012)

[56] L-Y Sung, B. J. Hwang, K-L Hsueh, F-H Tsau Effects of anode air bleeding on the performance of CO-poisoned proton-exchange membrane fuel cells, Journal of Power Sources 195(6) (2010) 1630-1639

[57] [access date November 2017], https://energy.gov/eere/fuelcells/doe-technical-targets-polymer-electrolyte-membrane-fuel-cell-components

[58] W. Schmittinger , A. Vahidi, A review of the main parameters influencing long-term performance and durability of PEM fuel cells, Journal of Power Sources 180(1) (2008) 1–14

[59] [access date November 2017], http://www.greencarcongress.com/2014/11/20141118-mirai.html (Whec)

[60] J.T. Wang, R. F. Savinell, J. Wainright, M. Litt, H. Yu, A H2/O2 fuel cell using acid doped polybenzimidazole as polymer electrolyte, Electrochimica Acta, 41, (1996), 193–197

[61] J. Mader, L. Xiao, T.J. Schmidt, B.C. Benicewicz, Polybenzimidazole/Acid Complexes as High-Temperature Membranes. In Fuel Cells II; Scherer, G. G., Ed.; Advances in Polymer Science, 216; Springer-Verlag: Berlin, Germany, 2008; pp 63–124

[62] Q. Li, D. Aili, H.A Hjuler, J.O. Jensen, High Temperature Polymer Electrolyte Membrane Fuel Cells, Springer Switzerland (2016)

[63] A. Iulianelli, A. Basile, Sulfonated PEEK-based polymers in PEMFC and DMFC applications: a review, International Journal of Hydrogen Energy, 37 (2012) 15241-1525

[64] J. A. Asensio, E.M. Sanchez, P. Gomez-Romero, Proton-conducting membranes based on benzimidazole polymers for high-temperature PEM fuel cells. A chemical quest, Chemical Society Reviews 39 (2010) 3210–3239

[65] P. Atkins and J. De Palma, Atkin's Physical Chemistry 8th ed. W. H. Freeman and Company, New York (2006)

[66] J.R.P. Jayakody, S.H. Chung, L. Durantino, NMR studies of mass transport in high-acid-content fuel cell membranes based on phosphoric acid and polybenzimidazole, Journal of The Electrochemical Society 154 (2007) B242–B246

[67] R. Bouchet, E. Siebert, Proton conduction in acid doped polybenzimidazole. Solid State Ionics, 118 (1999) 287-299

[68] J.S. Wainright, J.T. Wang, D. Weng, Acid- doped polybenzimidazoles—a new polymer electrolyte, Journal of The Electrochemical Society 142 (1195) L121–L123

[69] A. Sannigrahi, D. Arunbabu, T. Jana, Thermore- versible gelation of polybenzimidazole in phosphoric acid, Macromol Rapid Commun, 27 (2006) 1962–1967

[70] S.C. Kumbharkar, M.N Islam, R.A. Potrekar, Variation in acid moiety of polybenzimidazoles: investigation of physicochemical properties towards their applicability as proton exchange and gas separation membrane materials, Polymer 50 (2009) 1403–1413

[71] R.H. He, Q. Li, A. Bach, Physicochemical properties of phosphoric acid doped polybenzimidazole membranes for fuel cells. Journal of Membrane Science 277 (2006) 38–45

[72] B.D. James, A.B. Spisak, W.G. Colella, Manufacturing cost analysis of stationary fuel cell systems. Strategic Analysis Inc., Arlingto (2012)

[73] B. Schwanitz, A. Rabis, M. Horisberger, Sputtered cathodes for polymer electrolyte fuel cells: insights into potentials, challenges and limitations, Chimia (Aarau) 66 (2012)110–119

[74] W. Liu, P. Rodriguez, L. Borchardt, Bimetallic aerogels: high-performance electrocatalysts for the oxygen reduction reaction, Angewandte Chemie International Edition 52 (2013) 9849–9852

[75] M. Debe, Tutorial on the fundamental characteristics and practical properties of nanostructured thin film (NSTF) catalysts, Journal of The Electrochemical Society 160 (2013) F522–F534
[76] D. F. van der Vliet, C. Wang, D. Tripkovic, D. Strmcnik, X.F. Zhang, M. K. Debe, et al. Mesostructured thin films as electrocatalysts with tunable composition and surface morphology, Nature Materials 11 (2012) 1051–1058
[77] S. J. Andreasen, J.R. Vang, S. K. Kær, High temperature PEM fuel cell performance characterisation with CO and CO2 using electrochemical impedance spectroscopy, International Journal of Hydrogen Energy 36(16) (2011) 9815-9830
[78] Q. Li, J. Jensen, R. Savinell and N. Bjerrum, High Temperature Proton Exchange Membranes Based on Polybenzimidazoles for Fuel Cells, Progress in Polymer Science, 34 (2009) 449-447
[79] C. Song, Fuel processing for low-temperature and high-temperature fuel cells: Challenges, and opportunities for sustainable development in the 21st century, Catalysis Today 77 (2002) 17-49
[80] T.J. Schmidta, J. Baurmeister, Durability and Reliability in High-Temperature Reformed Hydrogen PEFCs, ECS Transactions 3(1)(2006) 861-869
[81] S.K. Das, A. Reis, K.J. Berry, Experimental evaluation of CO poisoning on the performance of a high temperature proton exchange membrane fuel cell, Journal Power Sources, 193 (2009) 691-698
[82] Q.F. Li, H.C. Rudbeck, A. Chromik, Properties, degradation and high temperature fuel cell test of different types of PBI and PBI blend membranes, Lournal of Membrane Science 347 (2010) 260–270
[83] J.H. Liao, Q. Li, H.C. Rudbeck, Oxidative degradation of polybenzimidazole membranes as electrolytes for high temperature proton exchange membrane fuel cells, Fuel Cells 11 (2011) 745–755
[84] Q.F. Li, C. Pan C, J.O. Jensen , Cross-linked polybenzimidazole membranes for fuel cells. Chem Mater Chemistry of Materials 9 (2007) 350–352
[85] E.H Brown, C.D. Whitt, Vapor pressure of phosphoric acid, Industrial & Engineering Chemistry Research 44 (1952) 615–618
[86] S. Yu, L. Xiao, B.C. Benicewicz, Durability studies of PBI-based high temperature PEMFCs, Fuel Cells, 8 (2008) 165–174
[87] A. Honji, T. Mori, K. Tamura, Agglomeration of platinum particles supported on carbon in phosphoric acid, Journal of The Electrochemical Society, 135 (1988) 355–359
[88] P. Bindra, S.J. Clouser, E. Yeager, Platinum dissolution in concentrated phosphoric acid. Journal of The Electrochemical Society, 126 (1979) 1631–1632
[89] L.M Roen, C.H. Paik, T.D. Jarvic, Electrocatalytic corrosion of carbon support in PEMFC cathodes. Electrochemical and Solid-State Letters 7 (2004) A19–A22
[90] J. Zhang, PEM fuel cell electrocatalysts and catalyst layers: fundamentals and applications. Springer, London (2008)
[91] M. Conte, Energy | Hydrogen Economy, Encyclopedia of Electrochemical Power Sources (2009) 232-254
[92] G.A. Olah, A. Goeppert, G.K.S. Prakash, The Hydrogen Economy and its Limitations, in Beyond Oil and Gas: The Methanol Economy, Wiley-VCH Verlag GmbH & Co. KgaA. (2009) 143-178
[93] N.W. Deluca, Y.A Elabd, Polymer electrolyte membranes for the direct methanol fuel cell: a review, Journal of Polymer Science: Polymer Physics, 44 (2006) 2201-2225
[94] B.A. Peppley, J.C. Amphlett, L.M. Kearns, R.F. Mann, Applied Catalysis A: General 179 (1999) 31–49

[95] B.A. Peppley, J.C. Amphlett, L.M. Kearns, R.F. Mann, Part 1, Applied Catalysis A: General 179 (1999) 21-30

[96] D.R. Palo, R.A. Dagle, J.D. Holladay, Methanol Steam Reforming for Hydrogen Production, Chemical Reviews 107 (2007) 3992-4021

[97] T. Conant, A. Karim, V. Lebarbier, Y. Wang, F. Girgsdies, R. Schlögl, A. Datye, Stability of bimetallic Pd-Zn catalysts for the steam reforming of methanol, Journal of Catalysis 257 (2008) 64–70

[98] P.H. Matter, D.J. Braden, U.S. Ozkan, Steam reforming of methanol to H2 over non reduced Zr-containing CuO/ZnO catalysts, Journal of Catalysis 223 (2004) 340-351

[99] M.V. Twigg, M.S. Spencer, Deactivation of copper metal catalysts for methanol decomposition, methanol steam reforming and methanol synthesis, Topics in Catalysis 22 (2003) 191-203

[100] T. Valdés-Solís, G. Marbán, A.B. Fuertes Nanosized catalysts for the production of hydrogen by methanol steam reforming, Catalysis Today 116 (2006) 354–360

[101] J. C. Amphlett, M. J. Evans, R. A. Jones, R. F. Mann, R. D. Weir, Hydrogen production by the catalytic steam reforming of methanol part 1: The thermodynamics, The Canadian Journal of Chemical Engineering 59 (1981) 720–727

[102] H. Jeong, K.I. Kimb, T.H. Kimb, C.H. Ko, H.C. Park, I.K. Song, Hydrogen produc-tion by steam reforming of methanol in a micro- channel reactor coated with Cu/ZnO/ ZrO2/Al2O catalyst, Journal of Power Sources, 159 (2006) 1296–1299

[103] L. Yong-Feng, D. Xin-Fa, L. Wei-Ming, Effects of ZrO2-promoter on catalytic per-formance of CuZnAlO catalysts for production of hydrogen by steam reforming of methanol, International Journal Hydrogen Energy 29 (2004) 1617–1621

[104] L. Ma, B. Gong, T. Tran, M.S. Wainwright, Cr2O3 promoted skeletal Cu catalysts for the reactions of methanol steam reforming and water gas shift, Catalysis Today 63 (2000) 499–505

[105] P. Clancy, J. Breen, J. Ross, The preparation and properties of coprecipitated Cu-Zr-Y and Cu-Zr-La catalysts used for the steam reforming of methanol, Catalysis Today 127 (2007) 291–294.

[106] T. Shishido, Y. Yamamoto, H. Morioka, K. Takaki, K. Takehira, Active Cu/ZnO and Cu/ZnO/Al2O3 catalysts prepared by homogeneous precipitation method in steam reforming of methanol, Applied Catalysis – A 263 (2004) 249–253

[107] O. Jakdetchai, N. Takayama, T. Nakajima, Activity enhancement of CuZn-impregnated Fsm-16 by modification with 1,3-butanediol for steam reforming of methanol, Kinetics and Catalysis 46 (2005) 56–64.

[108] B. Lindström, L.J. Pettersson, P.G. Menon, Activity and Characterization of Cu/Zn, Cu/Cr and Cu/Zr on -Alumina for methanol reforming for fuel cell vehicles, Applied Catalysis – A 234 (2002) 111–125

[109] J. Papavasiliou, G. Avgouropoulos, T. Ioannides, Reforming of methanol over copper-manganese spinel oxide catalysts, Catalysis Communications 6 (2005) 497–501

[110] H. Oguchi, T. Nishiguchi, T. Matsumoto, H. Kanai, K. Utani, Y. Matsumura, S. Imamura, Steam reforming of methanol over Cu/CeO2/ZrO2 catalysts, Applied Catalysis - A, 281 (2005) 69–73

[111] Y. Liu, T. Hayakawa, T. Tsunoda, K. Suzuki, S.Hamakawa, K. Murata, R. Shiozaki, T. Ishii, M. Kumagai, Topics in Catalysis, 22 (2003) 205–213

[112] J. Agrell, H. Birgersson, M. Boutonnet, I. Melián-Cabrera, R. Navarro, J. Fierro, Production of hydrogen from methanol over Cu/ZnO catalysts promoted by ZrO2 and Al2O3, Journal of Catalysis 219 (2003) 389–403

[113] H.-M. Yang, P.-H. Liao, Preparation and Activity of Cu/ZnO–CNTs nano-catalyst on steam reforming of methanol, Applied Catalysis - A, 317 (2007) 226–233
[114] C.-Z. Yao, L.-C. Wang, Y.-M. Liu, G.-S. Wu, Y. Cao, W.-L. Dai, H.-Y. He, K.-N. Fan, Effect of preparation method on the hydrogen production from methanol steam reforming over binary Cu/ZrO2 catalysts, Applied Catalysis - A, 297 (2006) 151–158
[115] W. Tong, A. West, K. Cheung, K-M Yu, S. C. E. Tsang, Dramatic Effects of Gallium Promotion on Methanol Steam Reforming Cu−ZnO Catalyst for Hydrogen Production: Formation of 5 Å Copper Clusters from Cu−ZnGaOx, ACS Catalysis 3 (2013) 1231−1244
[116] N. Iwasa, S. Masuda, N. Takezawa, Steam reforming of methanol over Pd/ZnO: effect of the formation of PdZn alloys upon the reaction. Reaction Kinetics and Catalysis Letters 55 (1995) 349–353
[117] N. Iwasa, T. Mayanagi, S. Masuda, N. Takezawa, Steam reforming of methanol over PdZn catalysts, Reaction Kinetics and Catalysis Letters, 69 (2000) 355–360
[118] N. Iwasa, S. Kudo, H. Takahashi, S. Masuda, N. Takezawa, Highly selective supported Pd catalyst for steam reforming of methanol, Reaction Kinetics and Catalysis Letters 19 (1993) 211–216
[119] N. Iwasa, T. Mayanagi, W. Nomura, M. Arai, N. Takezawa, Effect of Zn addition to supported Pd catalyst in the steam reforming of methanol, Applied Catalysis - A 248 (2003) 153–160
[120] Y.H. Chin, Y. Wang, R.A. Dagle, X.S. Li, Methanol steam reforming over Pd/ZnO: catalyst preparation and pretreatment studies, Fuel Processing Technology 83 (2003) 193–201
[121] C. Qi, J.C. Amphlett, B.A. Peppley, Methanol steam reforming over NiAl and NiAl (Au, Rh, Ir)-layered double hydroxide derived catalysts. Reaction Kinetics and Catalysis Letters 104 (2005) 57–62
[122] A. Karim, T. Conant, A. Datye, The role of PdZn alloy formation and particle size on the selectivity for steam reforming of methanol, Journal of Catalysis 243 (2006) 420–427.
[123] G. Kolb, S. Keller, S. Pecov, H. Pennemann, R. Zapf, Development of micro-structured catalytic wall reactors for hydrogen production by methanol steam reforming over novel Pt/In2O3/Al2O3 catalysts. Chemical Engineering Transactions 24 (2011) 133-138
[124] G. Kolb, S. Keller, D. Tiemann, K-P. Schelhaas, J. Schürer, O. Wiborg, Design and operation of a compact microchannel 5kWel, net methanol steam reformer with novel Pt/In2O3 catalyst for fuel cell applications. Chemical Engineering Journal 207-208 (2012) 388-402
[125] RL. Barbosa, V. Papaefthimiou, Y.T. Law, D. Teschner, M. Hävecker, A. Knop-Gericke, et al., Methanol steam reforming over indium-promoted Pt/Al2O3 catalyst: nature of the active surface. The Journal of Physical Chemistry C 117 (2013) 6143-6150
[126] V. Pour, J. Barton, A. Benda, Kinetics of catalyzed reaction of methanol with water vapour, Collection of Czechoslovak Chemical Communications 40 (1975) 2923–2934
[127] J. Barton, V. Pour, Kinetics of catalytic conversion of methanol at higher pressures, Collection of Czechoslovak Chemical Communications45 (1980) 3402
[128] K. Takahashi, N. Takezawa, H. Kobayashi, The mechanism of steam reforming of methanol over a copper-silica catalyst, Applied Catalysis 2 (1982) 363–366
[129] C.J. Jiang, D.L. Trimm, M.S. Wainwright, N.W. Cant, Kinetic study of steam reforming of methanol over copper-based catalysts, Applied Catalysis A 93 (1993)
[130] V. Hessel, S. Hardt, H. Lowe, Chemical Micro Processing Engeneering, Wiley-VCH (2004)

[131] R. Besser, Thermal integration of a cylindrically symmetric methanol fuel processor for portable fuel cell power, International Journal of Hydrogen Energy 36 (2011) 276-283
[132] [access date November 2017], https://phys.org/news/2014-10-fuel-cell-efficiency.html
[133] S. Mahabunphachai, M. Koç, Fabrication of micro-channel arrays on thin metallic sheet using internal fluid pressure: Investigations on size effects and development of design guidelines, Journal of Power Sources 175(1) (2008) 363-371
[134] H. An, A. Angli, B. Agus, P. Sasmito, C. Jundika, A. Kurnia, V. Sachin, Jangam, S. Arun, Mujumdar, Computational fluid dynamics (CFD) analysis of micro-reactor performance: Effect of various configurations, Chemical Engineering Science, 75 (2012) 85–95
[135] J. Jang, C. Cheng, Y. Huang, C. Lee, C. Leu, Optimal design of parallel channel patterns in a micro methanol steam reformer, International Jornal of Hydrogen Energy 37 (2012) 16974-16985
[136] A. Pattekar, M. Kothare, A microreactor for hydrogen production in micro fuel cell applications, Journal of Microelectromechanical Systems 13 (2004) 7–18
[137] J. Telotte, J. Kern, S. Palanki, Miniaturized methanol reformer for fuel cell powered mobile applications, International Journal of Chemical Reactor Engineering., 6 (2008) 64
[138] J. Suh, M. Lee, R. Greif, P. Costas, Grigoropoulos, Transport phenomena in a steam-methanol reforming microreactor with internal heating, International Journal of Hydrogen Energy 34 (2009) 3
[139] T. Terazaki, M. Nomura, K. Takeyama, O. Nakamura, T. Yamamoto, Development of multi-layered micro-reactor with methanol reformer for small PEMFC, Journal of Power Sources 145 (2005) 691–696.
[140] Y. Kawamura, N. Ogura, T. Yamamoto, A. Igarashi, A miniaturized methanol reformer with Si-based microreactor for a small PEMFC, Chemical Engineering Science 61 (2006) 1092–1101.14–322
[141] A. Karim, J. Bravo, D. Gorm, T. Conant, A. Datye, Comparison of wall-coated and packed-bed reactors for steam reforming of methanol, Catalysis Today 110 (2005) 86–91
[142] J. Bravo, A. Karim, T. Conant, G. Lopez, A. Datye, Wall coating of a CuO/ZnO/Al2O3 methanol steam reforming catalyst for micro-channel reformers, Chemical Engineering Journal 101 (2004) 113–121
[143] M. Lee, R. Greif, P. Costas., Grigoropoulos, H. Park, F. Hsu, Transport in packed-bed and wall-coated steam-methanol reformers, Journal of Power Sources 166 (2007) 194–201
[144] A. Karim, J. Bravo, A. Datye, Non isothermally in packed bed reactors for steam reforming of methanol Applied Catalysis A: General 282 (2005) 101–109
[145] [access date November 2017], Ultracell, http://www.ultracell.co.uk/
[146] [access date November 2017], SerEnergy, http://serenergy.com/
[147] S. Andreasen, S. Kær, S. Sahlin, Control and experimental characterization of a methanol reformer for a 350 W high temperature polymer electrolyte membrane fuel cell system international, International Journal Hydrogen Energy 38(3) (2013) 1676–1684
[148]A. Qi, B. Peppley, K. Karan, Integrated fuel processors for fuel cell application: A review, Fuel Processing Technology 88 (2007) 3–22
[149] C. Hsueh, H. Chua, W .Yan, C. Chen, Transport phenomena and performance of a plate methanol steam micro-reformer with serpentine flow field design, Applied Energy 87 (2010) 3137–3147
[150] C. Hsueh, H. Chu, W. Yan, G. Leu, J. Tsai, Three dimensional analysis of a plate methanol steam micro reformer and a methanol catalytic combustor with different flow channel designs, International Journal Hydrogen Energy 36 (2011) 13575-13586

[151] R. Besser, Thermal integration of a cylindrically symmetric methanol fuel processor for portable fuel cell power international, International Journal Hydrogen Energy 36 (2011) 276-283
[152] J. Weiss-Ungethum, I. Burger, N. Schmidt, Experimental investigation of a liquid cooled high temperature proton exchange membrane (HT-PEM) fuel cell coupled to a sodium alanate tank. International Journal Hydrogen Energy 39 (2014) 5931–5941
[153] J. Supra, H. Janßen, W. Lehnert, Temperature distribution in a liquid-cooled HT-PEMFC stack, Int J Hydrog Energy 38 (203) 1943–1951
[154] [access date November 2017], SerEnergy presentation , http://www.h2fc-fair.com/hm13/images/ppt/10we/1530.pdf
[155] S. J. Andreasen, S. K. Kær, K. K. Justesen, S. L. Sahlin, High Temperature PEM Fuel Cell Systems, Control and Diagnostics, High Temperature Polymer Electrolyte Membrane Fuel Cells, 459-486
[156] C. Pan, R.H. He, Q.F. Li, J.O. Jensen, N.J. Bjerrum, H.A. Hjulmand, A.B. Jensen, Integration of high temperature PEM fuel cells with a methanol reformer, Journal of Power Sources, 145 (2005) 392-398.
[157] G. Avgouropoulos, T. Ioannides, J.K. Kallitsis, S. Neophytides, Development of an internal reforming alcohol fuel cell: Concept, challenges and opportunities, Chemical Engineering Journal, 176 (2011) 95-101.
[158] F. Weng, C. Chenga, K. Chen, Hydrogen production of two-stage temperature steam reformer integrated with PBI membrane fuel cells to optimize thermal management, International Journal of Hydrogen Energy 38 (2013) 6059-6064
[159] S.S. Araya, S.J. Andreasen, S.K. Kær, Experimental Characterization of the Poisoning Effects of Methanol-Based Reformate Impurities on a PBI-Based,HighTemperature PEM, Fuel Cell Energies, 5, 2012, 4251-4267
[160] G. Bandlamudi, Systematic characterization of HT PEMFCs Containing PBI/H3PO4 systems. Thermo-dynamic analysis and Experimental investigations, Logos Verlad Berlin GmbH, 2011
[161] A. Criscuoli, A. Basile, E. Drioli, O. Loiacono, An economic feasibility study for water gas shift membrane reactor, Journal of Membrane Science181 (2001) 21–27
[162] G. Saracco, V. Specchia, Catalytic Inorganic-Membrane Reactors: Present Experience and Future Opportunities, Catalysis Reviews: Science and Engineering 36 (1994) 305
[163] G.H. Xiu, J.L. Soares ,P. Li, A.E. Rodrigues, Simulation of five-step one-bed sorption-enhanced reaction process, American Institute of Chemical Engineers Journal 48(12) (2002) 2817–2832
[164] B. Park, T.T. Tsotsis, Models and Experiments with Pervaporation Membrane Reactors Integrated with an Adsorbent System, Chemical Engineering and Processing 43 (2004) 1171
[165] Y. Chen, A.S. Mahecha-Botero, C.J. Lim, J.R. Grace, J. Zhang, Y. Zhao, C. Zheng, Hydrogen Production in a Sorption-Enhanced Fluidized-Bed Membrane Reactor: Operating Parameter Investigation, Industrial & Engineering Chemistry Research 53 (2014) 6230
[166] R. E. Buxbaum, T. L. Marker, Hydrogen transport through non-porous membranes of palladium-coated niobium, tantalum and vanadium, Journal of Membrane Science 85(1) (1993) 29-38
[167] A. Doukelis, K. Panopoulos, A. Koumanakos, E. Kakaras, Palladium Membrane Technology for Hydrogen Production, Carbon Capture and Other Applications: Principles, Energy Production and Other Applications, Woodhead Publishing (2014)
[168] C.H. Kim, J.Y. Han, N.C. Kim, S.K. Ryi, D.W. Kim, Characteristics of dense palladium alloy membranes formed by nano-scale nucleation and lateral growth, Journal of Membrane Science 502 (2016) 57–64

[169] A. Iulianelli, P. Ribeirinha, A. Mendes, A. Basile, Methanol steam reforming for hydrogen generation via conventional and membrane reactors: A review, Renewable and Sustainable Energy Reviews 29 (2014) 355–368

[170] D.J. Edlund, W.A. Pledger, Thermolysis of hydrogen sulfide in a metal-membrane reactor, Journal of Membrane Science 77 (1993) 255-264

[171] H. Amandusson, L.G. Ekedahl, H. Dannetun, The effect of CO and O2 on hydrogen permeation through a palladium membrane, Applied Surface Science 153 (2000) 259-267.

[172] B.L. Bischoff, R.R. Judkins, Development of inorganic membranes for Hydrogen separation, Oak Ridge National Laboratory report (2008)

[173] R. Riedel, I.W. Chen, Ceramics Science and Technology, vol.3: Synthesis and Processing, Wiley-VCH (2011) 480-488

CHAPTER 1

# Chapter 2

# A novel catalyst for low temperature MSR reaction

## 2.1. Abstract

Highly active catalysts for the methanol steam reforming (MSR) capable of operating efficiently at the same temperature of high temperature polymer electrolyte membrane fuel cells (HTPMFCs) devices are strongly desired. A novel CuO/ZnO/$Ga_2O_3$ catalyst was synthesized by co-precipitation method and characterized by ICP-AES, $N_2$-physisorption, SEM-EDX and XRD. This catalyst showed a catalytic activity 2.2 times higher than commercial CuO/ZnO/$Al_2O_3$ catalysts at 453 K. Two kinetic models one empirical and one mechanistic were applied to describe the methanol steam reforming reaction over one of the most promising catalyst family.

---

The content of this chapter is adapted from, P.Ribeirinha, C.Mateos-Pedrero, M.Boaventura, J.Sousa, A.Mendes, CuO/ZnO/Ga2O3 catalyst for low temperature MSR reaction: Synthesis, characterization and kinetic model, Applied Catalysis B: Environmental, 221 (2018) 371-379.

## 2.2. Introduction

Methanol can be produced from renewable sources, is easy to store and has higher volume energy density than compressed or chemically bonded hydrogen storage technologies [1, 2]. Methanol, due to the absence of C-C bonds, has a low reforming temperature (513 K – 533 K) [2] making it suitable for fuel cell applications as a hydrogen source. Moreover, the hydrogen-rich gas stream produced by methanol steam reforming (MSR) can be fed directly to high temperature polymer electrolyte membrane fuel cells (HT-PEMFC), due to the high CO tolerance (up to 3 % [3]). However, the low catalytic activity of commercial reforming catalysts at the operating temperatures of HT-PEMFCs (393 K – 453 K) [4, 5] increases the complexity and reduces the efficiency of power supplies based on HT-PEMFCs integrated with reformers. Thermodynamically, the methanol conversion by MSR reaction is almost complete at 453 K [6], therefore catalysts with high activity at *ca.* 453 K, are conceivable and strongly desired.

Copper-based catalysts, such as $CuO/ZnO/Al_2O_3$, are the most commonly used catalysts for MSR due to their low cost and considerably high activity at temperatures of *ca.* 523 K, despite the pyrophoric nature and low stability [7, 8]. The changes in oxidation state, reduction of the active area by sintering, coke deposition, catalyst poisoning (*e.g.* chloride and sulphur) are the main reasons for the catalyst deactivation [9, 10]. To improve the copper-based catalyst several approaches are reported in literature, from the employment of different preparation methods [11, 12] to the addition of promoters [13-16]. The $Al_2O_3$ is typically used as support and improves the surface area [8]; adding $ZrO_2$ to Cu-based $Al_2O_3$ supported, improves the reducibility and copper dispersion [14], while adding $CeO_2$ has shown to increase the thermal stability and increases the CO conversion through WGS reaction [15, 16]. Recently, a gallium-promoted copper-based catalyst prepared by co-precipitation method demonstrated to be highly active, stable and selective at temperatures lower than 473 K [15, 17-19]. The incorporation of Ga into the Cu–Zn oxide showed to improve the catalytic activity, by originating a nonstoichiometric cubic spinel phase containing interstitial $Cu^{1+}$ ions, resulting in extremely small (< 5 Å) and highly dispersed copper clusters [17, 18].

The search for a more suitable catalyst for MSR has led to consider metals from groups VIII–X due to their high activity, stability and low CO production [20-25]. Pd-based catalysts, for instance, display an unusual behaviour since they form Pd-alloys (*e.g.* Zn

and Ga) after proper reductive pre-treatment, modifying the catalytic function of Pd [20-22]. Pt-based catalysts on the other hand demonstrated very high activity; *e.g.* $Pt/In_2O_3/Al_2O_3$ showed an activity 10 times higher than commercial Cu-based catalyst [22- 25]. This high activity of $Pt/In_2O_3/Al_2O_3$ has been assigned to the contact regions between the metallic Pt with partially reduced $In_2O_3$ [25]. The major challenges of using commercially noble metals for MSR is the prohibitive high noble metal loading (typical ranging from 5.0 to 15.0 wt.%), which limits their economic viability.

Kinetic modelling of the methanol steam reforming process is a very important tool for scaling, designing and optimizing reformers. Several power-law and Langmuir–Hinshelwood reaction rate expressions for MSR over $CuO/ZnO/Al_2O_3$ have been reported in literature, typically for operating temperatures above 473 K [26-31]. In this work two kinetic models, one empirical and one mechanistic are proposed for characterizing one of the most promising catalysts for MSR, a novel highly active gallium-promoted copper-based catalyst supported on ZnO operating at temperatures between 453 K and 493 K. The $CuO/ZnO/Ga_2O_3$ catalyst was synthesized *by the co-precipitation method* and characterized concerning the morphology, structure and composition *by ICP-AES, $N_2$-physisorption, SEM-EDX and XRD*. Additionally, the catalytic activity of the *in*-house catalyst was compared with two commercial catalysts, $CuO/ZnO/Al_2O_3$ from BASF RP60 (hereafter mentioned as RP60) and from Süd-Chemie G66MR (hereafter mentioned as G66MR). The proposed kinetic models were fitted to the experimental results using a 1D isothermal packed bed reactor simulator.

### 2.3. Kinetic models

The kinetic models proposed in this study only consider the MSR reaction (Eq. 2.1); reverse water gas shift (RWGS, Eq. 2.2) and methanol decomposition (MD, Eq. 2.3) reactions were not considered due to their very low rates at temperatures below 493 K [32].

$$CH_3OH + H_2O \rightleftarrows CO_2 + 3H_2 \quad \Delta H°_{298K} = +49.40\ kJ{\cdot}mol^{-1} \tag{2.1}$$

$$CO_2 + H_2 \rightleftarrows CO + H_2O \quad \Delta H°_{298K} = +41.14\ kJ{\cdot}mol^{-1} \tag{2.2}$$

$$CH_3OH \rightleftarrows CO + 2H_2 \quad \Delta H°_{298K} = +90.54\ kJ{\cdot}mol^{-1} \tag{2.3}$$

Two types of kinetic models were developed, one empirical (power-law model) and one based on mechanistic assumptions. Empirical models, despite their simplicity,

can fit very accurately the experimental results and are easy to implement [30, 31]. The mechanistic models, on the other hand, are based on physical assumptions and can express accurately the sequence of the reaction steps for the $H_2$ formation [26].

### 2.3.1. Empirical model

The power-law model expressed by Eq. 2.4 was adopted in this work to describe the MSR reaction on *in-house* catalyst ($CuO/ZnO/Ga_2O_3$). The temperature dependence of the reaction rate was assumed to follow an Arrhenius-type behavior (Eq. 2.5).

$$r_{MSR} = k_{MSR}(T)\, p_{CH_3OH}^{a} p_{H_2O}^{b} p_{H_2}^{c} p_{CO_2}^{d} \tag{2.4}$$

$$k_{MSR}(T) = k_0 e^{-\frac{Ea}{RT}} \tag{2.5}$$

where, $r$ is the reaction rate of the methanol steam reforming reaction, $k$ is the kinetic constant of the MSR reaction, $p$ are the partial pressures of each component and $a$, $b$, $c$ and $d$ are the apparent reaction orders of methanol, water, hydrogen and carbon dioxide, respectively. $k_0$, is the Arrhenius pre-exponential factor and $E_a$ is the activation energy. The model has a total of 6 parameters, including the activation energy and pre-exponential factor.

### 2.3.2. Mechanistic Model

The mechanistic model suggested by Peppley *et al.* [26] to describe the physical processes that occur in the MSR over the $CuO/ZnO/Al_2O_3$ catalyst was also considered in this work. The model comprises a set of Langmuir–Hinshelwood rate expressions, similar to those proposed by Jiang *et al.* [33], which can be described as follows by Eq. 2.6 – 2.14:

$$S_1 + S_{1a} + CH_3OH\,(g) \underset{k_{-\,CH_3O^{(1)}}}{\overset{k_{CH_3O^{(1)}}}{\rightleftarrows}} CH_3O^{(1)} + H^{(1a)} \tag{2.6}$$

$$S_1 + S_{1a} + H_2O\,(g) \underset{k_{-\,OH^{(1)}}}{\overset{k_{OH^{(1)}}}{\rightleftarrows}} OH^{(1)} + H^{(1a)} \tag{2.7}$$

$$2S_{1a}+H_2\ (g) \underset{k_{-\,H^{(1a)}}}{\overset{k_{H^{(1a)}}}{\rightleftarrows}} 2H^{(1a)} \tag{2.8}$$

$$CH_3O^{(1)}+S_{1a} \underset{k_{-\,CH_2O^{(1)}}}{\overset{k_{CH_2O^{(1)}}}{\rightleftarrows}} CH_2O^{(1)} + H^{(1a)} \tag{2.9}$$

$$CH_3O^{(1)}+CH_2O^{(1)} \underset{k_{-\,C_2H_5O_2^{(1)}}}{\overset{k_{C_2H_5O_2^{(1)}}}{\rightleftarrows}} CH_3OCH_2O^{(1)} + S_1 \tag{2.10}$$

$$CH_3OCH_2O^{(1)}+S_{1a} \underset{k_{-\,CH_3OCHO^{(1)}}}{\overset{k_{CH_3OCHO^{(1)}}}{\rightleftarrows}} CH_3OCHO^{(1)} + H^{(1a)} \tag{2.11}$$

$$CH_3OCHO^{(1)}+OH^{(1)} \underset{k_{-\,HCOOH^{(1)}}}{\overset{k_{HCOOH^{(1)}}}{\rightleftarrows}} HCOOH^{(1)} + CH_3O^{(1)} \tag{2.12}$$

$$HCOOH^{(1)}+S_{1a} \underset{k_{-\,HCOO^{(1)}}}{\overset{k_{HCOO^{(1)}}}{\rightleftarrows}} HCOO^{(1)} + H^{(1a)} \tag{2.13}$$

$$HCOO^{(1)}+S_{1a} \underset{k_{-\,CO_2{}^{(1)},a}}{\overset{k_{CO_2{}^{(1)},a}}{\rightleftarrows}} H^{(1a)} + CO_2{}^{(1)} \tag{2.14}$$

The final rate expression for the MSR reaction is expressed by Eq. 2.15. Details of the derivation are reported elsewhere [26].

$$r_{MSR} = \frac{\dfrac{k_{MSR}K^{*}_{CH_3O^{(1)}}p_{CH_3OH}}{p_{H_2}^{1/2}}\left(1-\dfrac{p_{H_2}^{3}p_{CO_2}}{k_{MSR}p_{H_2O}p_{CH_3OH}}\right)C_{S1}^{T}C_{S1a}^{T}S_a}{\left(1+\dfrac{K^{*}_{CH_3O^{(1)}}p_{CH_3OH}}{p_{H_2}^{1/2}}+\dfrac{K^{*}_{OH^{(1)}}p_{H_2O}}{p_{H_2}^{1/2}}+K^{*}_{HCOO^{(1)}}p_{H_2}^{1/2}p_{CO_2}\right)\left(1+\sqrt{K^{*}_{H^{(1a)}}p_{H_2}}\right)} \tag{2.15}$$

Eq. 2.15 considers the adsorption equilibrium constants ($K^{*}_{i}$) for the intermediate species (Eqs. 2.6 – 2.14), the MSR equilibrium constant ($K_{MSR}$) and the total catalyst surface concentrations of sites 1 ( $C_{S1}^{T}$) and 2 ($C_{S2}^{T}$). The temperature dependence of the kinetic constant was calculated according to the Arrhenius equation (Eq. 2.5) and the temperature dependence of the adsorption equilibrium constants was calculated according to van't Hoff equation (Eq. 2.16):

$$\ln K_i = -\frac{\Delta H}{RT} + \frac{\Delta S}{R} \tag{2.16}$$

where, $\Delta H$ and $\Delta S$ are the enthalpy and entropy of adsorption respectively. The model has a total of 10 parameters, including the activation energy and pre-exponential factor.

### 2.3.3. Parameter estimation

The parameters of the kinetic models (Eqs. 2.4 and 2.15) were obtained by non-linear regression method [34, 35]. The experimental reaction rates were determined based on the first derivative of the polynomial equation used to fit the experimental methanol conversion as a function of space-time ratio ($m_{cat}/F_{MeOH}$); the parameters were then obtained minimizing the mean residual sum of the squares (MSRR) of the experimental and model reaction rates. The power-law model has 6 parameters, including the activation energy and pre-exponential factor. According to the values reported in the literature [28-31], the apparent reactions orders were allowed to be any real number between -2 and 2 and the activation energy between 60 and 100 kJ·mol$^{-1}$. The mechanistic model has a total of 10 parameters or 20 when included the temperature dependence, by Arrhenius and by van't Hoff equations. Following the same strategy reported in literature [27, 28, 34], the number of parameters was reduced to 6 introducing an initial estimation of the heat of adsorption reported by Skrzypek *et al.* [29].

### 2.3.4. Simulator

The packed bed reactor model was written and implemented using Fortran. The model considers the steady state mass balance equations for each species, the pressure drop, the MSR reaction rates and the respective boundary conditions. The model considers the following simplifications:

- isothermal behavior;
- the gas mixtures follow the ideal gas law;
- no diffusion limitations in the catalyst were considered;
- axially dispersed plug flow with pressure drop described by the Ergun equation,
- negligible radial gradients and uniform cross-sectional void fraction.

*Partial mass balance equation:*

$$\frac{d}{dz}(up_i) - D_{ax}\frac{d}{dz}\left(P\frac{d}{dz}\left(\frac{p_i}{P}\right)\right) - \frac{m_{cat}}{\varepsilon V}RT\nu_i r_{MSR} = 0 \tag{2.17}$$

where $u$ is the interstitial velocity, $p_i$ is the partial pressure of species $i$, $D_{ax}$ is the effective axial dispersion coefficient, $P$ is to total pressure, $m_{cat}$ is catalyst mass, $\varepsilon$ is porosity of the catalyst bed, $R$ is the gas constant, $v_i$ is the stoichiometry coefficient of species $i$ and $r_{MSR}$ is the MSR reaction rate.

*Total mass balance equation:*

$$\frac{\mathrm{d}}{\mathrm{d}z}(uP) - \frac{m_{cat}}{\varepsilon V}RT\sum \nu_i r_{MSR} = 0 \tag{2.18}$$

*Pressure drop equation:*

$$-\frac{dP}{dz} = 150\frac{\mu u}{d_p^2}\frac{(1-\varepsilon)^2}{\varepsilon^2} + \frac{7}{4}\frac{\rho_{gas}u^2}{d_p}\frac{(1-\varepsilon)}{\varepsilon} \tag{2.19}$$

where, $D$p is the catalyst diameter, $\mu$ is the gas viscosity and $\rho_{gas}$ is the gas density.

*Boundary conditions*

At the reactor's inlet ($z$ = 0),

$$D_{ax}\frac{d}{dz}\left(\frac{p_i}{P}\right) = u\frac{p_i - p_i^{\text{inlet}}}{P}, \qquad u = u^{inlet} \tag{2.20}$$

At the reactor's outlet ($z$ = $l$),

$$\frac{d}{dz}\left(\frac{p_i}{P}\right) = 0, \qquad P = P^{out} \tag{2.21}$$

The variables present in Eq. 2.17 – 2.21 were converted to dimensionless variables obtaining a new set of equations, which can be found elsewhere [36].

*Numerical solution strategy*

To solve the partial differential equations and avoid the numerical instability, an additional time derivative term was added to their right-hand side, transforming the

equations into a pseudo-transient problem [36]. The equations were spatially discretized (50 elements) using the finite volumes method. High-resolution schemes (WACEB were used to calculate the partial pressures of the components [37]. The time integration was carried out using the numerical package developed at the Lawrence Livermore National Laboratory LSODA [38]. The equations were solved until a steady-state solution was reached.

## 2.4. Experimental

*Catalyst synthesis and physicochemical characterization*

The $CuO/ZnO/Ga_2O_3$ catalyst (65/25/10 wt. %) was prepared by co-precipitation from a 1.1 M aqueous mixture of metal nitrates ($Cu(NO_3)_2$, $Zn(NO_3)_2$ and $Ga(NO_3)_3$), with dropwise addition (0.27-0.64 $cm^3 \cdot min^{-1}$) of an aqueous solution of $NH_4HCO_3$ (1.3 M) under vigorous stirring at fixed conditions of pH (6.5) and temperature (333 K). After 2 h of aging, the resulting precipitate was filtered and thoroughly washed with distilled hot water. The procedure was repeated for several times until the pH value of the filtrate reached the pH of the distilled water. The precipitate was then dried at 383 K overnight and calcined under static air as follows: from 25 K to 473 K (heating rate: 2 $K \cdot min^{-1}$; dwell time: 1 h), from 473 K to 633 K (heating rate: 2 $K \cdot min^{-1}$; dwell time: 1 h), and finally kept at 633 K for 8.5 h.

The $CuO/ZnO/Ga_2O_3$ catalyst was characterized and evaluated using a variety of methods. The metal content (Cu) was determined from induced coupled plasma (ICP-AES). The morphology and qualitative composition was assessed by scanning electron microscopy equipped with an energy dispersive x-ray high vacuum detector (SEM-EDX). The catalyst surface area was determined by Multi point Brunauer-Emmett-Teller (BET) performed on a Quantachrome Autosorb AS-1 instrument at 77 K. Prior to the analysis the samples were outgassed in vacuum at 473 K for 2 h. The pore size (mesoporosity) was calculated from the $N_2$-physisorption isotherm using the Barrett-Joyner-Halenda (BJH) method. The porosity and bulk density were determined by mercury porosimetry on Quantachrome Poremaster using a maximum filling pressure of *ca.* 3500 bar. The structure of the catalyst was studied by X-ray powder diffraction (XRD). The XRD pattern of the selected samples was collected using a PANalytical X'Pert Pro operating in Bragg-

Bretano focusing geometry and using Cu *Kα* radiation at wavelengths Cu $K\alpha_1$ = 1.5406 Å and Cu $K\alpha_2$ = 1.54443 Å. The data were collected at 2θ angles (20–80°).

*Effect of the particle size on the methanol conversion*

Commercial catalyst RP60 ($CuO/ZnO/Al_2O_3$) was used to evaluate the effect of the particle size on the methanol conversion. The catalyst pellets were milled and sieved into particle sizes of 50-150 μm, 100-250 μm, 250-400 μm, 400-600 μm, 600-1000 μm and pellets of 1.5 mm of diameter. The characterization procedure was the same as described below, except that 1.5 g of catalyst was used instead of 0.5 g.

*Kinetic characterization*

A differential reactor was filled with 0.5 g of catalyst (*in-house*, RP60 and G66MR catalyst) with particle size ranging between 100-250 μm and mixed with 0.5 g of glass beads of the same diameter to achieve near isothermal conditions. The reactor length to catalyst diameter ratio was preserved higher than 50 ($l_{reactor}$ / $d_{particle} \geq 50$)) and the reactor diameter to catalyst diameter ratio was higher than 30 ($d_{reactor}$ / $d_{particle} \geq 30$) [39]. Glass wool was inserted in the top and bottom of the reactor to avoid the catalyst particles to be dragged by the stream. During the reduction process, the MSR catalysts lose mass and consequently reduce their volume; to avoid channelling the reactor was placed inside the oven in vertical orientation with the temperature being controlled inside the catalyst bed. The catalyst was reduced during 30 min with a mixture of hydrogen, 10 $cm^3 \cdot min^{-1}$, and of nitrogen, 190 $cm^3 \cdot min^{-1}$, with a temperature ramp of *ca.* 5 $K \cdot min^{-1}$ from 433 K to 478 K to avoid sintering the catalyst. The methanol conversion, hydrogen and CO production were accessed between 453 K and 523 K, $m_{cat}/F_{MeOH}$ between 30 $kg \cdot s \cdot mol^{-1}$ and 550 $kg \cdot s \cdot mol^{-1}$, operating pressure between 1-3 bar and steam-to-carbon ratio (S/C) of 1:1, 1:1.5, 1:2. The condensable components were removed from the reformate stream using a cold trap, while the non-condensable species concentrations, namely hydrogen and carbon dioxide, were determined using a mass spectrometer (Pfeiffer OmniStartm). The CO concentration was determined using a specific analyser (Signal Inst. 7000FM GFC). The performance of the three catalysts was accessed after the activation process (reduction) and after 80 h time-on-stream at 80 % methanol conversion.

## 2.5. Results and Discussion

### 2.5.1. Physicochemical characterization of the in-house catalyst

The physicochemical properties of the in-house catalyst ($CuO/ZnO/Ga_2O_3$) were characterised using the following techniques: ICP-AES (catalyst composition), $N_2$-physisorption (BET surface area), mercury porosimetry (porosity), SEM-EDX (structure) and XRD (crystallinity). The metal content (Cu) of the *in-house* catalyst obtained by ICP is shown in Table 2.1; the Cu content (51.4 wt. %) is close to the nominal content (52 wt. %), indicating that the preparation method was adequate. The highest catalytic activity reported in literature for this family of catalysts was achieved for a Cu atomic content of 43 % [17, 18]. Increasing the Cu content by reducing the Ga content originates a negligible loss in catalytic activity [17], but represents an important reduction in the catalyst cost. Commercial $CuO/ZnO/Al_2O_3$ catalysts normally present a Cu atomic content of *ca*. 65 wt. % [40]. The BET surface area of the $CuO/ZnO/Ga_2O_3$ catalyst was 55 $m^2 \cdot g^{-1}$, which is in line to the surface area obtained by Tong *et al.* [17] for its most active catalysts, but it is lower than the surface area of the of commercial catalyst G66MR, *ca.* 60 $m^2 \cdot g^{-1}$ [40]. The $CuO/ZnO/Ga_2O_3$ porosity and bulk density obtained by mercury porosimetry were 0.54 and 0.44 $kg \cdot dm^{-3}$, respectively. The bulk density of the in-house is quite low; commercial catalysts are typically pelletized at high pressures in the presence of binders, which increase significantly the density. This is the case of commercial catalyst G66MR, which shows a density of 1.1 $kg \cdot dm^{-3}$ according to the manufacture.

**Table 2.1** Cu content assessed by ICP-AES, BET surface area (sBET) and average pore size ($d_p$) calculated from $N_2$ physisorption.

| Sample | Cu content (wt.%) | sBET ($m^2 \cdot g^{-1}$) | $d_p$ (nm) | Total Porosity | Bulk Density ($kg \cdot dm^{-3}$) |
|---|---|---|---|---|---|
| In-house | 51.4 | 55 | 19.3 | 0.54 | 0.44 |
| G66MR | 65 [40] | 60 [40] | - | - | 1.1 |

The structure of the $CuO/ZnO/Ga_2O_3$ catalyst, after calcination and reductive treatment with $H_2$ was studied by XRD; the results are shown in Fig. 2.1. The XRD patterns of the calcined $CuO/ZnO/Ga_2O_3$ sample exhibit the main lines of CuO (JCPDS file no. 48-1548) at 35.5° (11-1) and 38.7° (111) with some minor and broad reflections at

31.7° and 36.8° corresponding to (100) and (101) planes of ZnO (JCPDS file no. 36-1451). The XRD pattern (Fig. 2.1) of the reduced catalyst shows peaks at 43.5˚ Cu(111), 50.3˚ Cu(200) and 74.3˚ Cu(220) ascribed to $Cu^0$ (JCPDS file no. 04-0836). As for the calcined sample, the peaks of ZnO are also observed. It is clear in the figure that after reduction the peaks became sharper and narrower, characteristic of a high crystallinity. XRD patterns of the calcined and reduced CuZnGa catalysts in this study did not show any peak characteristic of crystalline Ga phases, suggesting that Ga particles are very small and highly dispersed. This was reported for CuZnGa catalysts with similar composition [41] and for Ga doped CuZn samples where the formation of a $ZnGa_2O_4$ phase appears to depend on the calcination temperature and sample composition [42]. The absence of Ga peaks suggests that Ga particles are very small and highly dispersed. SEM-EDS results (Fig. 2.2) show Cu, Zn and elements homogeneously distributed on the catalysts surface.

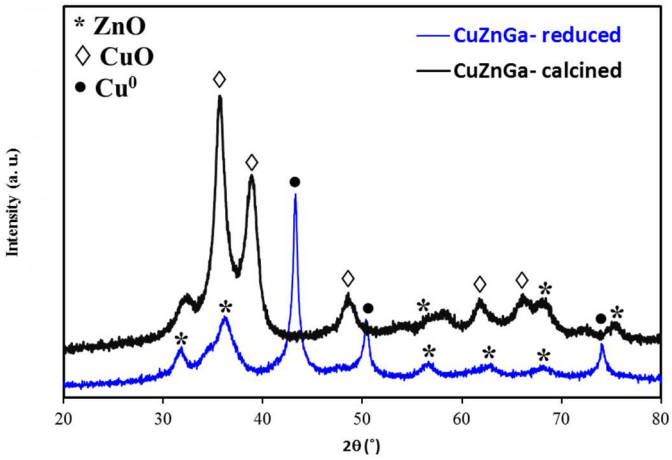


**Fig. 2.1** XRD patterns of the $CuO/ZnO/Ga_2O_3$ sample after calcination in air at 633 K for 8.5 h ($CuO/ZnO/Ga_2O_3$-calcined) and reduced in $H_2$ at 478 K for 30 min ($CuO/ZnO/Ga_2O_3$-reduced).

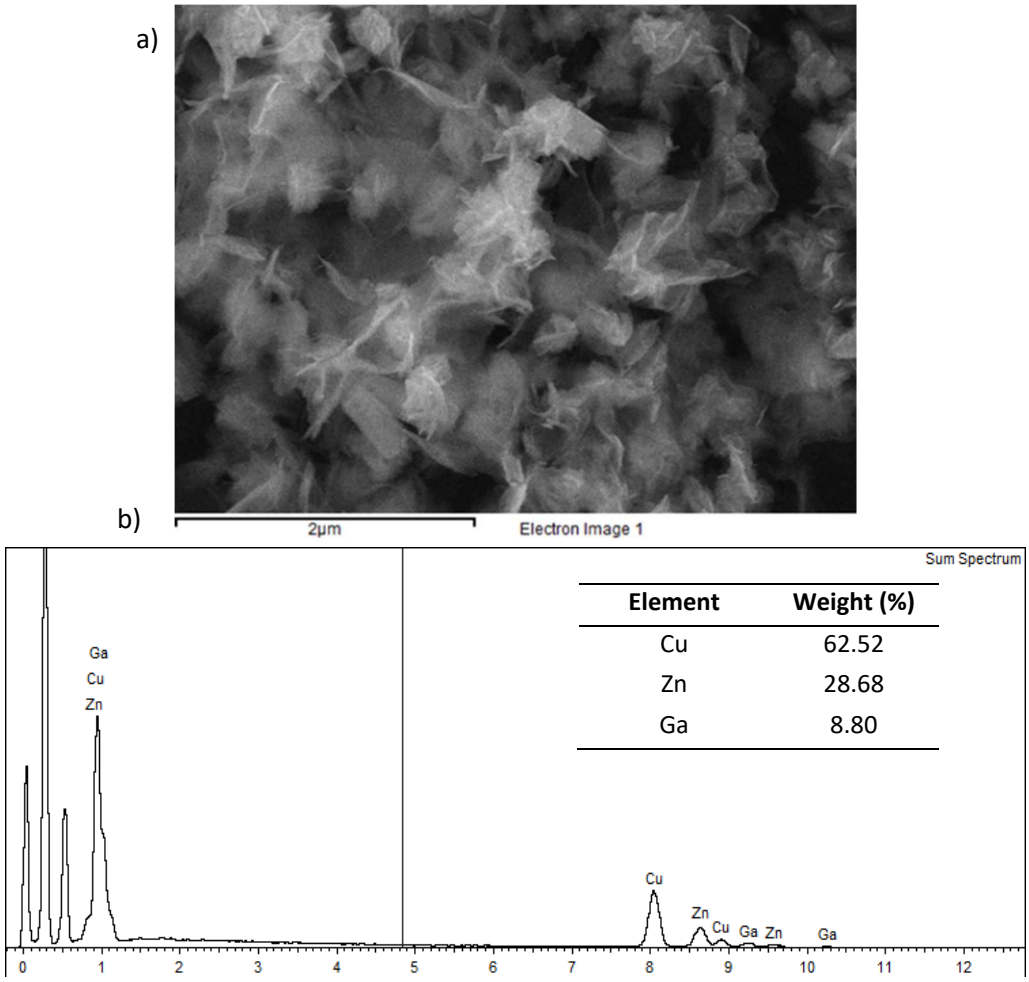


**Fig. 2.2** SEM image (a) and EDS results (b) of the CuO/ZnO/$Ga_2O_3$ catalyst.

### 2.5.2. Catalyst particle size effect, diffusion limitations

It is well known that the mass transport of reagents from the bulk to the catalyst active sites may play an important effect on the rate of the reaction [43]. To compare catalysts and obtain the correct kinetic rate parameters, the size of the catalyst particles was reduced to a size were the diffusion control limitations were virtually eliminated. Small amounts of the *in-house* catalyst were produced in each batch, therefore to perform this experiments the commercial RP60 catalyst was used, since a large quantity of

catalyst was required. Fig. 2.3 shows the methanol conversion as a function of space-time ratio for different catalyst particle sizes at 453, 473 and 493 K using a RP60 catalyst.

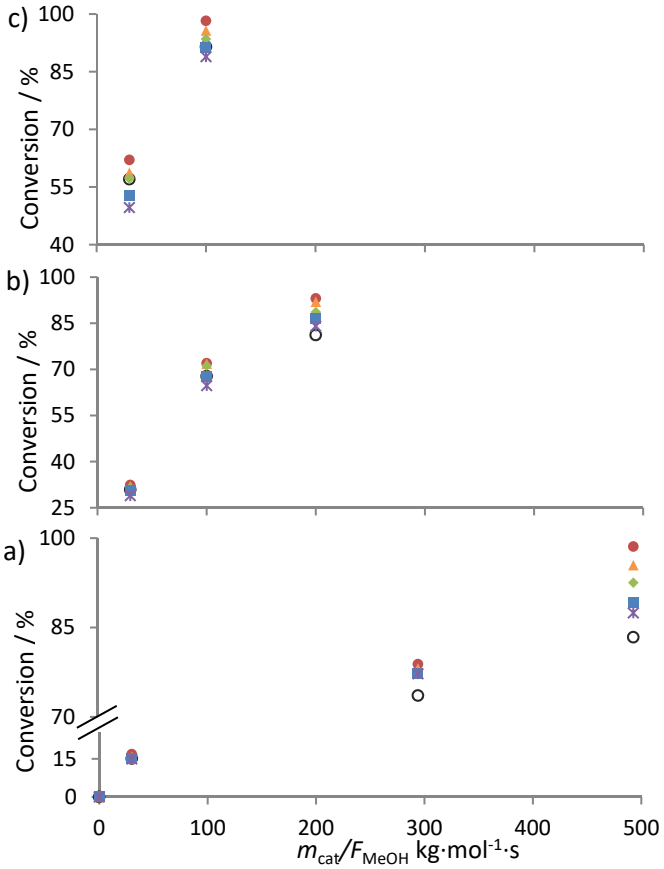


**Fig. 2.3** Catalyst (RP60) particle size effect on the methanol conversion at 453 K (a), 473 K (b) and 493 K (c), *P* = 1 bar, and S/C = 1.5. 0-100 µm (○); 100-250 µm (●); 250-400 µm (▲); 400-600 µm (♦); 600-1000 µm (■); pellets (x).

At temperature of 453 K, the effect of the particle size on the methanol conversion is negligible, gaining only importance for space-time ratios higher than 300 kg·s·mol$^{-1}$, when small particle sizes show high methanol conversions. For sizes smaller than 100 µm, it is observed an inversion of this trend; very small particle sizes (powders) originate flow channelling that decreases the methanol conversion. Particle sizes between 100 µm and 250 µm show high methanol conversions for all tested space-time ratios and temperatures. The kinetics of the reaction at low space-time ratios and low temperature

is rate limited, moving for diffusional control as the temperature and/or space-time ratio increases [43]; in the case of small particle sizes, the diffusional control occurs at higher temperatures and higher space-time ratios when compared to larger catalyst particles. Lee *et al.* [28] observed no intraparticle diffusion limitations at temperatures below 473 K for particle size ranging between 300 µm - 400 µm using a commercial catalyst, and Agrell *et al.* [44] concluded that only at temperatures above 493 K diffusion limitations are observed for a particle size between 120 µm and 250 µm. The smaller catalyst particles originate higher methanol conversions, however for large reformers the use of small particles is not recommended due the high pressure drop in the catalyst bed, but for small reactor this issue is not a limitation.

### 2.5.3. Performance of the In-house and commercial catalysts

The reduction of the catalysts (activation process) is an exothermic process that influences the catalyst ability to perform the methanol steam reforming reaction. The catalyst reduction with hydrogen at high temperatures such as 513 K is a very fast process that may sinter the catalyst due to the heat released in the process. Small particles of catalyst are more prone of sintering than pellets; therefore, the reduction process was performed using hydrogen diluted with nitrogen (1:19 v/v) at low temperatures (< 478 K). Fig. 2.4 shows the methanol conversion as a function of the space-time ratio immediately after activation for the *in-house* catalyst ($CuO/ZnO/Ga_2O_3$) and commercial catalysts G66MR and RP-60 ($CuO/ZnO/Al_2O_3$). The two commercial catalysts present similar performances at 453 K, while the in-house catalyst shows clearly a higher performance. The methodology reported in the literature to compare catalyst activities is not consensual [17, 23]; in this study, the activity was compared based on the space-time ratio required to achieve 50 % of methanol conversion. The in-house catalyst presents between 2.2 and 2.3 times higher activity than G66MR and RP-60, since it achieves 50 % of methanol conversion at a $m_{cat}/F_{MeoH}$ of *ca.* 60 $kg \cdot s \cdot mol^{-1}$, while the commercial catalysts achieve the same methanol conversion at 130-140 $kg \cdot s \cdot mol^{-1}$.

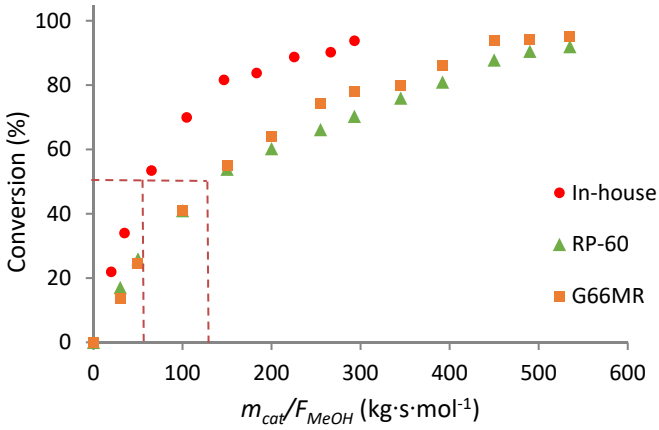


**Fig. 2.4** Methanol conversion as function of the space-time ratio, for the in-house, G66MR and RP-60 catalysts, at 453 K, *P* = 1 bar, *S/C* = 1.5 and particle size of 100-250 μm.

The $CuO/ZnO/Ga_2O_3$ exhibited a catalytic activity similar to the one reported in literature for this catalyst family [17-19]. Using a $CuO/ZnO/Ga_x$ with an atomic content of 48.7 % of Cu, 31.3% of Zn and 20 % of Ga, Tong *et al.* [17] reported a methanol conversion of 33 % at 468 K and $m_{cat}/F_{MeoH}$ of 18 kg·s·mol$^{-1}$m, while in this work the conversion for the same operating conditions was 37 %. Lotric *et al.* [19] using a $CuZnGaO_x$ catalyst with the molar ratio of 5:3:2 (Cu:Zn:Ga) reported 80 % of methanol conversion at 453 K and $m_{cat}/F_{MeoH}$ of 150 kg·s·mol$^{-1}$; similar conversion is depicted in Fig. 2.4 for the same space-time ratio.

Fig. 2.5 shows the methanol conversion as a function of the temperature for the three catalysts. The in-house catalyst shows a higher performance than the commercial ones at low temperature; at 443 K, the in-house catalyst has a methanol conversion of *ca*. 22 %, while the commercial catalyst has less than 9 %. Above 493 K, all the catalysts show similar methanol conversions. This similar performance may be attributed to the reduction of the active area due to sintering of the small Cu nanoparticles leading to an irreversible performance loss.

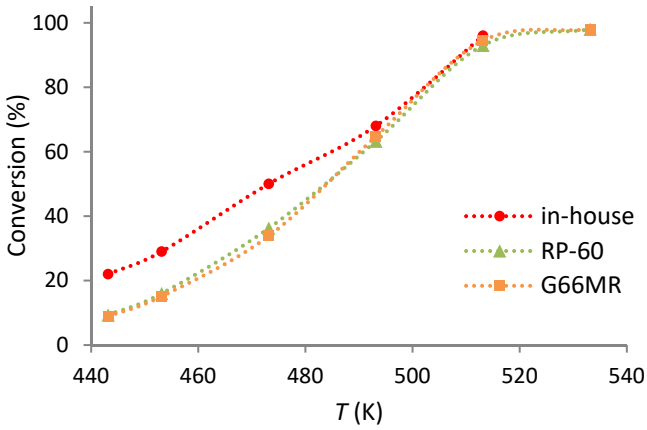


**Fig. 2.5** Methanol conversion as function of temperature for the in-house, G66MR and RP-60 catalysts, at $m_{cat}/F_{MeOH}$ =30 kg·s·mol$^{-1}$, $P$ = 1 bar, $S/C$ = 1.5 and particle size of 100-250 µm.

The CO content at 453 K is low for all the tested catalysts reaching a maximum of *ca.* 2000 ppm, when all methanol is converted (Fig. 2.6). At this operating temperature, the carbon monoxide production comes almost exclusively from the RWGS. Therefore, the CO concentration increases with the hydrogen and carbon dioxide partial pressures that increase with the space-time ratio ($m_{cat}/F_{MeOH}$). It is also clear from Fig. 2.6, that the in-house catalyst does not promote the CO production; e.g. at 80 % of methanol conversion the CO content in the reformate stream is *ca*. 600 ppm, while the commercial catalysts have a CO content of *ca.* 1700 ppm. For HT-PEMFC applications, which is the goal of this work, the CO tolerance is up 30 000 ppm [3], therefore the methanol conversion at low temperatures is more critical than the CO production. On the other hand, for automotive application using low-temperature PEMFC the CO content in hydrogen stream should be less than 0.2 ppm, according to ISO/TS 14687-2 [45], which requires, independently of the catalyst performance, a hydrogen purification step.

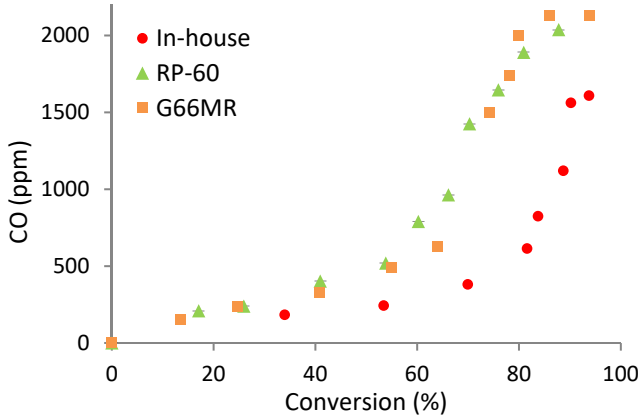


**Fig. 2.6** CO production as function of methanol conversion for the in-house, G66MR and RP-60 catalysts, at 453 K, *P* = 1 bar, *S/C* = 1.5 and particle size of 100-250 μm.

The effect of the total operating pressure on the methanol conversion was addressed, as depicted in Fig. 2.7. The decrease of the methanol conversion with the total pressure increase is noticeable for all studied temperatures and space-time ratios. In fact, the principle of Le Chatelier states that with a total pressure increase, the side of the equilibrium with smaller number of moles is more favourable. The kinetic model developed by Peppley *et al.* [26] for the methanol steam reforming (MSR) using a $CuO/ZnO/Al_2O_3$ catalyst (BASF K3-110) also predicts that increasing pressure would favour the reverse reaction, leading to a decrease of the overall reaction rate. No significant benefit is disclosed of operating at high pressure, except when reformate is directly fed to a high temperature polymer electrolyte membrane fuel cell (HT-PEMFC). Waller *et al.* [46] concluded that the performance losses in the fuel cell due to the anode feed dilution could be overcome through increasing the operating pressure and/or temperature within reasonable limits.

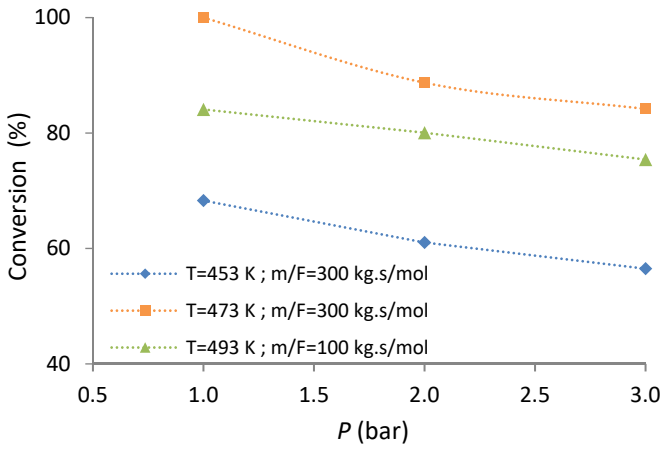


**Fig. 2.7** Methanol conversion as a function of pressure using RP60 catalyst, at 453 K, $m_{cat}/F_{MeOH}$ = 300 kg·s·mol$^{-1}$, *S/C* = 1.5 and particle size of 100-250 µm.

The steam-to-carbon ratio can influence the methanol conversion, but also represents an energy cost due to water vaporization. Fig. 2.8 shows the methanol conversion as a function of the steam-to-carbon ratio, at 453 K. An increase of the methanol conversion is observed when the steam-to-carbon ratio varies from 1 to 2 while a further increase has no significant effect. Considering the energy costs of water vaporization in a HT-PEMFC integrated with a reformer, steam-to-carbon ratios above 2 are questionable.

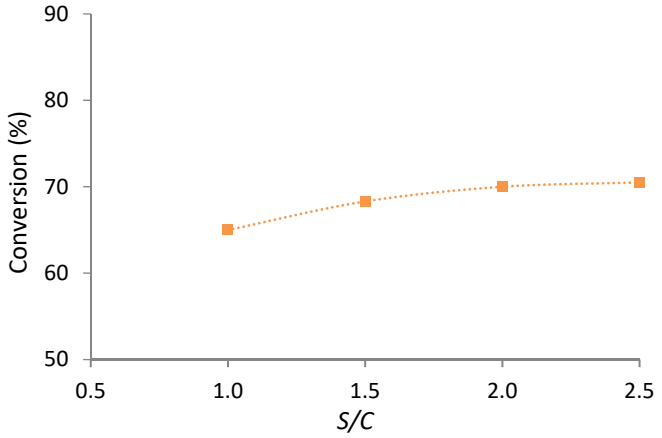


**Fig. 2.8** Methanol conversion as a function of steam-to-carbon ratio using RP60 catalyst at 453 K, $m_{cat}/F_{MeOH}$ =300 kg·s·mol$^{-1}$, *P* = 1 bar and particle size of 100-250 µm.

The catalytic activity decreases after a few hours of operation levelling out afterwards; it is therefore important to access the catalysts deactivation and the catalysts performance at the steady state. Starting with the same methanol conversion for the tested catalysts, *ca.* 80% (space-time ratio of 300 kg·s·mol$^{-1}$ for commercial catalysts and 150 kg·s·mol$^{-1}$ for the *in*-house catalyst) the reaction was left running during *ca.* 80 h (time-on-stream) at 453 K (Fig. 2.9).

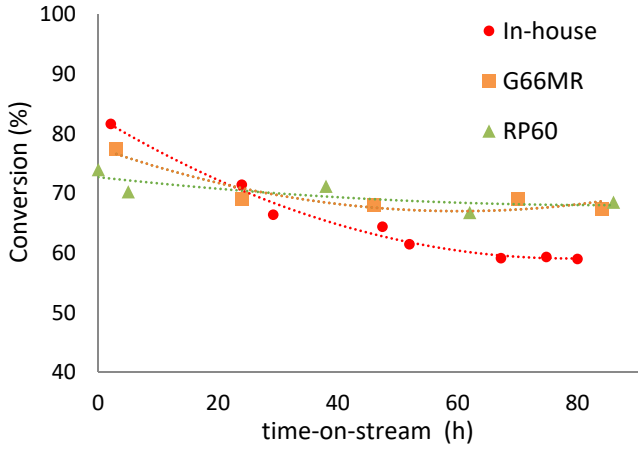


**Fig. 2.9** Conversion as a function of the time for *in-house* ($m_{cat}/F_{MeOH}$ =150 kg·s·mol$^{-1}$), G66MR and RP-60 catalysts, at 453 K, *P* = 1 bar, *S/C* = 1.5 and particle size of 100-250 µm. $m_{cat}/F_{MeOH}$ =150 kg·s·mol$^{-1}$ for commercial catalysts and $m_{cat}/F_{MeOH}$=150 kg·s·mol$^{-1}$ for the *in*-house catalyst.

The commercial catalyst RP60 shows to be the most stable catalyst with a conversion loss of six percentage points, while the in-house catalyst shows *ca.* twenty percentage points of conversion loss. Again, this higher conversion loss of the in-house catalyst should be assigned to the agglomeration of the very small copper clusters (sintering), which reduces the active surface area, and due to partial oxidation of the cooper particles [47]. In addition, the noticeable fragmentation of the fragile catalyst particles inside the reactor may cause flow channelling and then loss of conversion. Fig. 2.10 shows the methanol conversion as a function of the space-time ratio at 453 K for the different catalysts after 80 h of operation. Despite a considerable loss in performance, the in-house catalyst still shows higher performance than the commercial catalysts. The $CuO/ZnO/Ga_2O_3$ achieves 50 % of methanol conversion at a space-time ratio of *ca.* 95 kg·s·mol$^{-1}$, while the commercial catalysts reach this methanol conversion value at *ca.*

160 kg·s·mol$^{-1}$. These results indicate an in-house catalyst activity 1.7 times higher than the commercial catalysts. After 80 h of operation, both commercial catalysts present equal performance in all the tested range of temperatures and space-time ratios.

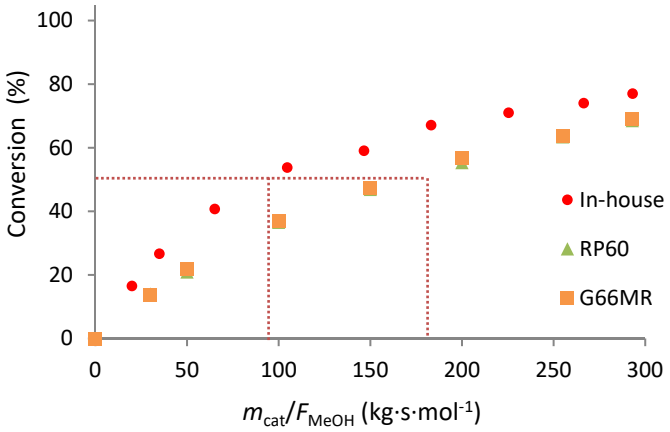


**Fig. 2.10** Methanol conversion as function of the space-time ratio, for *in-house*, G66MR and RP-60 catalysts, at 453 K, $P$ = 1 bar, $S/C$ = 1.5 and particle size of 100-250 µm.

### 2.5.4. Kinetic models, in-house catalyst

For the commercial catalysts such as RP60 or G66MR several mechanistic and empirical kinetic models can be found in literature [27, 34]. However, only Lotric *et al.* [19] presented a power-law empirical relation to describe the reaction kinetics of the MSR reaction over the catalyst CuO/ZnO/$Ga_2O_3$. Moreover, that model [19] was developed considering the initial activity of the catalyst, neglecting the deactivation observed for this type of catalyst. The estimated parameters for the power-law and mechanistic models were obtained after stabilization of the catalytic activity of the in-house catalyst and are reported in Table 2.2.

The goodness of the fitting was assessed using parity plots and the models predictions were compared with the experimental data. As previously mentioned, the variables present in Eq. 2.17 – 2.21 were converted to dimensionless variables, where the effective axial dispersion coefficient ($D_{ax}$) was replaced by the dimensionless Peclet number. According to the literature, for the operating conditions considered in this work, the

Peclet number should assume a large value (>100), since the axial dispersion in the reactor channel is negligible and the flow in the channel is close to plug flow [34,35].The parameter and operating conditions used for the simulations are presented in Table 2.3.

**Table 2.2** Estimated parameters for the power-law and mechanistic model.

| Parameter | Power-law model | Mechanistic model |
|---|---|---|
| $k_0$ | $8.51 \times 10^8$ mol·kg$^{-1}$·s·bar$^{-1.72}$ | $7.1 \times 10^{10}$ mol·kg$^{-1}$·s$^{-1}$ |
| $E_a$ | 90.8 kJ·mol$^{-1}$ | 103.2 kJ·mol$^{-1}$ |
| $a$ | 0.37 | - |
| $b$ | 1.35 | - |
| $c$ | 0 | - |
| $d$ | 0 | - |
| $\Delta H^0_{298}$, $CH_3O^{(1)}$ | - | -18.8 kJ·mol$^{-1}$ |
| $\Delta S^0_{298}$, $CH_3O^{(1)}$ | - | -55.4 J·mol$^{-1}$·K$^{-1}$ |
| $\Delta H^0_{298}$, $OH^{(1)}$ | - | -17.3 kJ·mol$^{-1}$ |
| $\Delta S^0_{298}$, $OH^{(1)}$ | - | -43.8 J·mol$^{-1}$·K$^{-1}$ |
| $\Delta H^0_{298}$, $H^{(1a)}$ | - | -57.4 kJ·mol$^{-1}$ |
| $\Delta S^0_{298}$, $H^{(1a)}$ | - | -154.2 J·mol$^{-1}$·K$^{-1}$ |
| $\Delta H^0_{298}$, $HCOO^{(1)}$ | - | 128.3 kJ·mol$^{-1}$ |
| $\Delta S^0_{298}$, $HCOO^{(1)}$ | - | 84.6 J·mol$^{-1}$·K$^{-1}$ |

**Table 2.3** Parameter used in the simulation.

| Property | Value |
|---|---|
| Bulk density (kg·m$^{-3}$) | 0.44 |
| Porosity | 0.54 |
| Particle size (μm) | 100 – 250 |
| Temperature (K) | 453 – 493 |
| *S/C* | 1.5 |
| Pressure (bar) | 1 |

The calculated and experimental reaction rates using the power-law model present a good fitting, as shown in the parity plot (Fig. 2.11a), with a MRSS = $2.8 \times 10^{-6}$. The simulation results using the power-law model, despite its simplicity, shows a good agreement with the experimental data for the studied conditions, as depicted in Fig. 2.11b; the maximum relative difference between experimental and simulated results is less than 8 % (at 493 K) and the coefficient of determination ($R^2$) is > 0.97. The obtained power-law model assumes a zero order apparent reaction for hydrogen and carbon dioxide (Table 2.2). Several authors also reported in the literature apparent reaction of

zero order for hydrogen and carbon dioxide using power-law models to predict the methanol conversion of different *in*-house and commercial catalysts [19, 34, 40]. However, it is well-known that the partial pressures of hydrogen and carbon dioxide affect the MSR reaction rate [26-28]. This inability to describe correctly the reaction rates highlights the limitations of power-law models and emphasizes the need of mechanistic models.

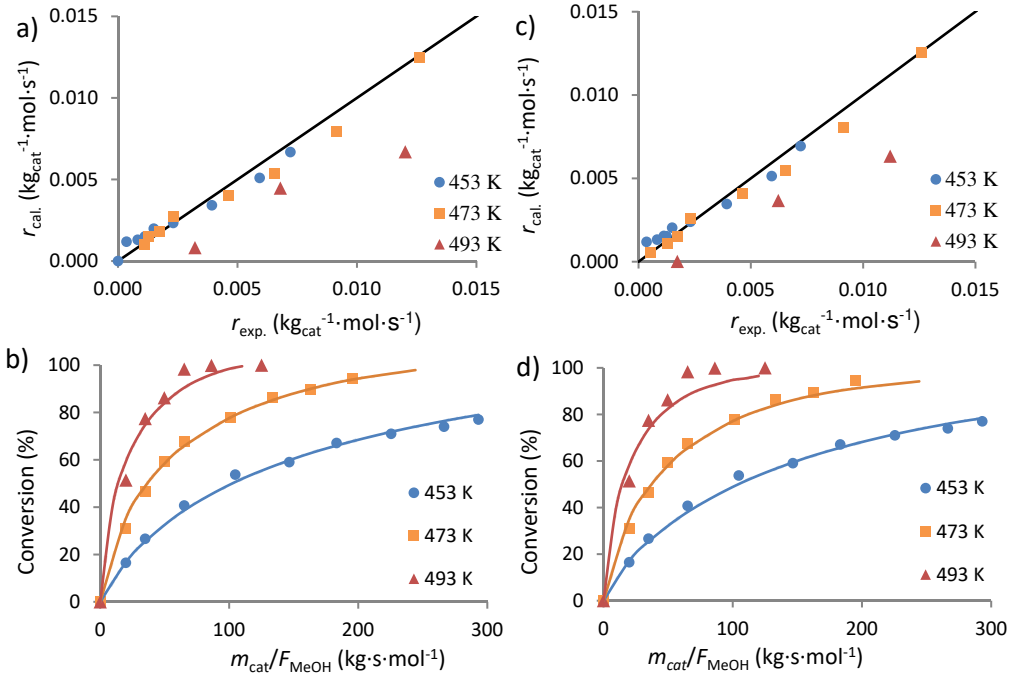


**Fig. 2.11** Parity plot of the experimental and calculated methanol consumption rate using the power-law model (a) and the mechanistic model (c). Experimental (symbols) and simulated (lines) results of methanol conversion as a function of space-time ratio and for different temperatures, using the power-law model (b) and mechanistic model (d).

The mechanistic model also displays a good fitting between the calculated and experimental reaction rates (Fig. 2.11c) with a MRSS = $3.2 \times 10^{-6}$. In general, the obtained parameters are similar to those reported in literature for the same mechanistic model [26, 34]. The main difference is related to the MSR reaction rate ($k_{MSR}$); Peppley *et al.* [26] reported for the commercial catalyst BASF K3-110 almost the same value for the activation energy, *ca.*103 kJ·$mol^{-1}$ vs 103.2 kJ·$mol^{-1}$ in this work, but a lower $k_0$, *ca.* $8 \times 10^9$ mol·$kg^{-1}$·$s^{-1}$ vs $7.1 \times 10^{10}$ mol·$kg^{-1}$·$s^{-1}$ in this work. Silva *et al.* [40] reported for the

commercial catalyst G66MR a MSR reaction rate of 0.025 $mol \cdot kg^{-1} \cdot s^{-1}$ at 453 K, while in this work and for the same temperature the MSR reaction rate obtained was 0.090 $mol \cdot kg^{-1} \cdot s^{-1}$. Fig. 2.11d shows the simulator predictions using the mechanistic model and experimental results for the methanol conversion. A good agreement to the experimental data for the studied conditions is observed; the maximum relative difference between experimental and simulated results is less than 10 % and the coefficient of determination ($R^2$) is > 0.97. Both models show high accuracy and can be used for scaling, design and optimize reformers for the HT-PEMFC applications.

## 2.6. Conclusions

A highly active $CuO/ZnO/Ga_2O_3$ was synthesized by co-precipitation method. The developed catalyst was characterized concerning morphology, structure and composition. The physicochemical study conducted over the *in*-house $CuO/ZnO/Ga_2O_3$ indicates that the preparation method was adequate for providing very small and highly dispersed copper particles. The performance of the developed catalyst was compared to two commercial $CuO/ZnO/Al_2O_3$ catalysts, BASF RP60 and Süd-Chemie G66MR, using a tubular MSR reactor. Catalyst particles size ranging between 100 and 250 μm were found to maximize the methanol conversion. Increasing the operating pressure above 1 bar was found to be detrimental for the methanol conversion and no significant gain is observed for values of steam-to-carbon ratio above 2. In-house $CuO/ZnO/Ga_2O_3$ catalyst immediately after the activation shows a methanol conversion *of ca.* 2.2 times higher than BASF RP60 and Süd-Chemie G66MR, levelling out to *ca.* 1.7 times after 80 h of time-on-stream. The two kinetic models, a power-law and mechanistic, were used to describe the methanol steam reforming reaction over a novel *in-house* catalyst. After proper parameter estimation, the two models were validated using a packed bed reactor simulator, showing for both cases a good agreement between the predicted and experimental methanol conversions.

## 2.7. References

[1] M. Conte, Energy | Hydrogen Economy, Encyclopedia of Electrochemical Power Sources (2009) 232-254.
[2] S. Sá, H. Silva, L. Brandão, J. M. Sousa, A. Mendes Catalysts for methanol steam reforming—A review, Applied Catalysis B: Environmental, 99 (2010) 43-57.
[3] S.K. Das, A. Reis, K.J. Berry, Experimental evaluation of CO poisoning on the performance of a high temperature proton exchange membrane fuel cell, Journal Power Sources, 193 (2009) 691-698.
[4] G. Schuller, F. Vázquez, W. Waiblinger, S Auvinen, P. Ribeirinha, Heat and fuel coupled operation of a high temperature polymer electrolyte fuel cell with a heat exchanger methanol steam reformer, Journal of Power Sources, 347 (2017) 47–56.
[5] S.L. Sahlin, S.J. Andreasen, S. K. Kær, System model development for a methanol reformed 5 kW high temperature PEM fuel cell system, International journal of hydrogen energy, 40 (2015) 13080-13089
[6] J. C. Amphlett, M. J. Evans, R. A. Jones, R. F. Mann, R. D. Weir, Hydrogen production by the catalytic steam reforming of methanol part 1: The thermodynamics, The Canadian Journal of Chemical Engineering 59 (1981) 720–727.
[7] D.R. Palo, R.A. Dagle, J.D. Holladay, Methanol Steam Reforming for Hydrogen Production, Chemical Reviews 107 (2007) 3992-4021
[8] M. B. Fichtl, D. Schlereth, N. Jacobsen, I. Kasatkin, J. Schumannd, M. Behrensd, et al, Kinetics of deactivation on Cu/ZnO/Al2O3 methanol synthesis catalysts, Applied Catalysis A: General, 502 (2015) 262-270.
[9] H.H. Kung, Deactivation of methanol synthesis catalysts - a review, Catalysis Today, 11 (4) (1992) 443-453
[10] M.V. Twigg, M.S. Spencer, Deactivation of copper metal catalysts for methanol decomposition, methanol steam reforming and methanol synthesis, Topics in Catalysis 22 (2003) 191-203
[11] J-P Shen, C. Song, Influence of preparation method on performance of Cu/Zn-based catalysts for low-temperature steam reforming and oxidative steam reforming of methanol for H2 production for fuel cells Catalysis Today 77 (2002) 89–98.
[12] C-Z Yao, L-C Wang, Y-M Liu, Gi-S Wu, Y. Cao, W-L Dai, et al, Effect of preparation method on the hydrogen production from methanol steam reforming over binary Cu/ZrO2 catalysts Applied Catalysis A: General, 297 (2006) 151-158.
[13] R. O. Idem, N. N. Bakhshi Production of Hydrogen from Methanol over Promoted Coprecipitated Cu-Al Catalysts: The Effects of Various Promoters and Catalyst Activation Methods, Industrial Engineering Chemistry Research 34 (1995) 1548–1557.
[14] L. Yong-Feng, D. Xin-Fa, L. Wei-Ming Effects of ZrO2-promoter on catalytic performance of CuZnAlO catalysts for production of hydrogen by steam reforming of methanol, international Journal Hydrogen Energy, 29 (2004), 1617-1621
[15] A. Pohar, S. Hoˇcevar, B. Likozar, J. Levec, Synthesis and characterization of gallium-promoted copper–ceriacatalyst and its application for methanol steam reforming in a packed bed reactor, Catalysis Today 256 (2015) 358–364.
[16] X. Zhang, P. Shi Production of hydrogen by steam reforming of methanol on CeO2 promoted Cu/Al2O3 catalysts J Mol Catal A Chem, 194 (2003) 99-105

[17] W. Tong, A. West, K. Cheung, K-M Yu, S. C. E. Tsang, Dramatic Effects of Gallium Promotion on Methanol Steam Reforming Cu−ZnO Catalyst for Hydrogen Production: Formation of 5 Å Copper Clusters from Cu−ZnGaOx, ACS Catalysis 3 (2013) 1231−1244.

[18] K. M. K. Yu, W. Tong, A. West, K. Cheung, T. Li, G. Smith, *et al.*, Non-syngas direct steam reforming of methanol to hydrogen and carbon dioxide at low temperature Nature Communications 3 (2012) 1230

[19] A. Lotric, M. Sekavcnik, A. Pohar, B. Likozar, S. Hocevar, Conceptual design of an integrated thermally self-sustained methanol steam reformer e High-temperature PEM fuel cell stack manportable power generator, International Journal of Hydrogen Energy 42 (2017) 16700-16713

[20] C.S.R. Azenha, C. Mateos-Pedrero, S. Queirós, P. Concepción, A. Mendes, Innovative ZrO2-supported CuPd catalysts for the selective production of hydrogen from methanol steam reforming, Applied Catalysis B: Environmental 203l (2017) 400–407.

[21] K. M. Eblagon, P. H. Concepción, H. Silva, A. Mendes, Ultraselective low temperature steam reforming of methanol over PdZn/ZnO catalysts—Influence of induced support defects on catalytic performance, Applied Catalysis B: Environmental, 154–155 (2014) 316-328.

[22] N. Iwasa, N. Takezawa, New supported Pd and Pt alloy catalysts for steam reforming and dehydrogenation of methanol, Topics in Catalysis. 22 (2003) 215–224.

[23] G. Kolb, S. Keller, S. Pecov, H. Pennemann, R. Zapf, Development of micro-structured catalytic wall reactors for hydrogen production by methanol steam reforming over novel Pt/In2O3/Al2O3 catalysts. Chemical Engineering Transactions 24 (2011) 133-138.

[24] G. Kolb, S. Keller, D. Tiemann, K-P. Schelhaas, J. Schürer, O. Wiborg, Design and operation of a compact microchannel 5kWel, net methanol steam reformer with novel Pt/In2O3 catalyst for fuel cell applications. Chemical Engineering Journal 207-208 (2012) 388-402.

[25] RL. Barbosa, V. Papaefthimiou, Y.T. Law, D. Teschner, M. Hävecker, A. Knop-Gericke, *et al.*, Methanol steam reforming over indium-promoted Pt/Al2O3 catalyst: nature of the active surface. The Journal of Physical Chemistry C 117 (2013) 6143-6150.

[26] BA. Peppley, JC. Amphlett, LM. Kearns, RF. Mann. Methanol steam reforming on Cu/ZnO/Al2O3 catalysts. Part 2: a comprehensive kinetic model, Applied Catalysis A, 179 (1999) 31-49.

[27] P. Ribeirinha, M. Abdollahzadeh, M. Boaventura, A. Mendes H2 production with low carbon content via MSR in packed bed membrane reactors for high-temperature polymeric electrolyte membrane fuel cell, Applied Energy 188 (2017) 409–419.

[28] J.K. Lee, J.B. Ko, D.H. Kim, Methanol steam reforming over Cu/ZnO/Al2O3 catalyst: kinetics and effectiveness factor. Applied Catalysis A: General 278 (2004) 25-35.

[29] Skrzypek, J. Sloczynski, S. Ledakowicz, Methanol Synthesis, ISBN 83-01-11490-8, Polish Scientific Publishers, Warsaw, 1994

[30] P. Ribeirinha, M. Boaventura, José Carlos B. Lopes, José M. Sousa, A. Mendes, Study of different designs of methanol steam reformers: Experiment and modelling, International Journal of Hydrogen Energy 39 (2014) 19970–19981.

[31] K. Kobl, S. Thomas, Y. Zimmermann, K. Parkhomenko, A-C Roger, Power-law kinetics of methanol synthesis from carbon dioxide and hydrogen on copper–zinc oxide catalysts with alumina or zirconia supports, Catalysis Today 270 (2016) 31-42.

[32] H Purnama, T Ressler, R.E Jentoft, H Soerijanto, R Schlögl, R Schomäcker, CO formation/selectivity for steam reforming of methanol with a commercial CuO/ZnO/Al2O3 catalyst Applied Catalysis A: General 259 (2004) 83–94.

[33] C.J. Jiang, D.L. Trimm, M.S. Wainwright, N.W. Cant, Kinetic mechanism for the reaction between methanol and water over a Cu-ZnO-Al2O3 catalyst, Applied Catalysis A: General, 97 (1993) 145-158.

[34] S. Sá, J.M. Sousa, A. Mendes, Steam reforming of methanol over a CuO/ZnO/Al2O3 catalyst, part I: Kinetic modelling, Chemical Engineering Science 66 (2011) 4913-492.1

[35] C. Cao, G. Xia, J. Holladay, E. Jones, Y. Wang, Kinetic studies of methanol steam reforming over Pd/ZnO catalyst using a microchannel reactor, Applied Catalysis A: General 262(1) (2004) 19-29

[36] S. Sá, H. Silva, J. M. Sousa, A. Mendes, Hydrogen production by methanol steam reforming in a membrane reactor: Palladium vs carbon molecular sieve membranes, Journal of Membrane Science 339 (2009) 160–170

[37] B. Song, G.R. Liu, K.Y. Lam, R.S. Amano, On a higher-order bounded discretization scheme, International Journal for Numerical Methods in Fluids 32 (2000) 881–897.

[38] L. Petzold Automatic selection of methods for solving stiff and nonstiff systems of ordinary differential equations SIAM Journal on Scientific and Statistical Computing 4 (1983) 136-148

[39] G. F. Froment and K. B. Bischoff, Chemical reactor analysis and design (1990) Wiley, New York

[40] H. Silva, C. Mateos-Pedrero, P. Ribeirinha, M. Boaventura, A. Mendes, Low-temperature methanol steam reforming kinetics over a novel CuZrDyAl catalyst, Reaction Kinetics, Mechanisms and Catalysis 115 (2015) 321–339

[41] X. Liu, J. Toyir, P. R. de la Piscina, N.Homs, Hydrogen production from methanol steam reforming over $Al_2O_3$- and $ZrO_2$-modified $CuOZnOGa_2O_3$ catalysts, International Journal of Hydrogen Energy 42(19) (2017) 13704-13711

[42] M. M-J Li, J. Zheng, J. Qu, F. Liao, E. Raine, W. C. H. Kuo, *et al.*, The remarkable activity and stability of a highly dispersive beta-brass Cu-Zn catalyst for the production of ethylene glycol, Nature:Scientific Reports 6 20527 (2016)

[43] H. Scott Fogler, Elements of Chemical Reaction Engineering (4th Edition), Upper Saddle River, NJ: Prentice Hall PTR, 2006

[44] Agrell, H. Birgersson, M. Boutonnet, Steam reforming of methanol over a Cu/ZnO/Al2O3 catalyst: a kinetic analysis and strategies for suppression of CO formation, Journal of Power Sources 106 (2002) 249–257

[45] International Organisation for Standardisation, ISO/TS 14687-2, Hydrogen Fuel-Product Specification—Part 2: Proton exchange membrane Fuel Cell applications for road vehicles; 2012.

[46] M.G. Waller, M R. Walluk, T A. Trabold, Performance of high temperature PEM fuel cell materials. Part 1: Effects of temperature, pressure and anode dilution, International Journal of Hydrogen Energy 41(4) (2016) 2944–2954.

[47] P. Kurra, I. Kasatkin, F. Girgsdies, A. Trunschke, R. Schlögl T. Ressler, Microstructural characterization of Cu/ZnO/Al2O3 catalysts for methanol steam reforming - A comparative study, Applied Catalysis A: General 348 (2008) 153–164

# Chapter 3

# Designing a methanol steam reformer

## 3.1. Abstract

Three reformers with different designs (multi-channel, radial and tubular) were developed for thermal integration with a high temperature polymeric electrolyte membrane fuel cell (HT-PEMFC). They were characterized experimentally at temperatures between 443 K and 473 K, using the commercial catalyst G66 MR from Süd-Chemie ($CuO/ZnO/Al_2O_3$). The reactors were modelled and simulated using a computational fluid dynamics (CFD) analysis. The models were validated using experimental data. The results showed that the multi-channel design is the best solution for thermal integration with a HT-PEMFC, presenting high methanol conversion and low pressure drop. Regarding the heat transfer ability, the multi-channel showed also the best performance, presenting the lowest temperature sink among the studied reformers. The low flow velocities and the absence of metallic surfaces in the radial reformer had detrimental effect on the heat transfer. Concerning the flow distribution, a coefficient of variation of 0.6 % was observed in the multi-channel reformer. A quasi plug flow behavior was found in the tubular and a multi-channel (channels region only) reformer, while in the radial a not fully developed laminar flow was found. At temperatures lower than 473 K was found that the reformate stream did not require further purification to be fed to a HT-PEMFC due to the low CO concentration (<1600 ppm). The advantages and limitations of each design is discussed based on experimental data and CFD modeling.

---

The content of this chapter is adapted from, P. Ribeirinha, M. Boaventura, J. C. Lopes, J. Sousa, A. Mendes, Study of Different Designs of Methanol Steam Reformers: Experiment and Modelling, International Journal of Hydrogen Energy 39(35) (2014) 19970–19981.

## 3.2. Introduction

Polymer electrolyte membrane fuel cells (PEMFC) are compact electrochemical devices that convert chemical into electrical energy in an efficient way. They require high purity hydrogen as a feeding fuel, especially with very low carbon monoxide content. Hydrogen, however, has a very low volume energy density and shows limitations regarding storage and transportation. To overcome these challenges, *in-situ* hydrogen production from fuels such as methane, methanol or ethanol is being considered. Methanol under standard conditions has a much higher volume energy density ($1.8x10^4$ $kJ \cdot dm^{-3}$ [1]) than hydrogen (13 $kJ \cdot dm^{-3}$ [1]) and it is easier to handle, store and particularly due to absence of C-C bonds has a low reforming temperature (513 K – 533 K).

The integration of *in-situ* hydrogen production by methanol steam reforming (MSR) with HT-PEMFC is already used in power supplies manufactured by few companies such as Ultracell [2], AixCellSys [3] and Serenergy [4]. In most cases, as the power supplies developed by the previous companies, the MSR reactor operates as a standalone device (external reforming) [5]. It presents the advantage of not being restricted to the fuel cell stack configuration, allowing different arrangements reformer/fuel cell and higher operation temperature. As a drawback, external reforming does not take the advantage of the heat released in the electrochemical reaction for the reforming reaction.

*Advantages of internal reforming*

A fuel cell is an exothermic device that wastes ca. 50 % of the input chemical energy while MSR reaction is endothermic. The integration of a cellular methanol steam-reforming reactor (MSR-C) intercalated with a PEMFC in a stack arrangement, in order to take advantage of this synergetic effect, should be a very advantageous approach. However, fuel cells operate typically at around 363 K (LT-PEMFC) or 433 K (HT-PEMFC), and a MSR operates at 523 K. Due to this operating temperature mismatching, many authors have chosen to study the two systems in a separated way. But, if the operation temperature of the FC (HT-PEMFC) is increased and the operating temperature of the MSR [6, 7] is decreased, internal integration would be possible. The two systems should operate at temperatures ca. 453 K, but for this arrangement a more active catalyst is required. At 453 K, the conversion of the commercial catalyst $CuO/ZnO/Al_2O_3$ for a

$m_{cat}/F_{MeOH}$ of 30 kg·s·mol$^{-1}$ is around 13 % [8]. To obtain an acceptable methanol conversion (>95 %) at this temperature, larger amounts of catalyst are required.

The thermal integration of MSR/HT-PEMFC considering internal reforming was first investigated by Pan *et al.* [6], who studied the performance of a two-cell stack (HT-PEMFC) coupled with a reformer operating at temperatures between 453 K and 473 K. However, the heat required to carry out the MSR reaction was not coming exclusively from the electrochemical reaction, but also from electrical heaters. Avgouropoulos *et al.* [7, 9] proposed a direct internal reforming setup, coupling the electrochemical reactions and the MSR reaction at the FC anode chamber. The reaction was carried out between 473 K and 483 K using a PEM from ADVENT TPS, and a $CuMnO_x$ reforming catalyst. This application allowed a continuous electrochemical hydrogen removal from the reforming reaction, enhancing the methanol conversion. However, the membranes showed to be intolerant to the high methanol concentrations, resulting in low power output [9]. The thermal integration of a MSR-C with a FC in a stack arrangement relies on the catalyst activity at low temperatures; nevertheless, a new generation of catalysts for low temperature methanol steam reforming (LT-MSR) is expected to overcome this issue [10].

### *Design of the Reformers*

To achieve an efficient integration of MSR/HT-PEMFC, the reformer must be optimized to maximize the heat transfer with a uniform flow distribution and low pressure drop. Typically, the MSR reaction is carried out in a tubular packed bed reactor, due to its simplicity and low cost. However, well-structured flat micro or mini reactors are more suitable and present advantages, such as higher surface-to-volume ratio, better heat and mass transfer properties and flow patterns that fit with the reaction needs [11]. Most studies describing well-structured flat reactors for MSR reaction have flow fields based on single channel design or based on a series of parallel channels, as discussed below.

Different reformer designs, such as coil-shaped or serpentine-shaped, can be obtained from a single channel design. The performance of single channel reactors lays between plug flow and laminar reactors [12]. This type of design improves significantly the mixing, reaction and heat-transfer rates [13-15].

Compared to other designs, single channel designs show even flow distributions and higher flow velocities, which reduces the stagnant film adjacent to the channel walls and improves the heat-transfer rates [13-16]. High reaction rates are also observed in

this designs which lead higher conversions. Despite the advantages, single channel designs impose a significant pressure drop penalty that may be a limitation for compact applications [14].

Reformers with parallel channels have been intensively reported in literature [17, 18, 19]. Based on parallel channels, several other designs can be obtained, such as wavy, pinhole and oblique-fin [14]. They are relatively easy to manufacture, show high conversions and low-pressure drop. However, parallel channels designs are more prone to uneven flow distributions. By adjusting the channels width [18] or by imposing a considerable pressure drop at the entrance of the channels the flow distribution can be optimized. In fixed bed reactors, depending on the specific design of the reactor, the pressure drop generated on the catalyst bed can be sufficient to obtain even flow distributions. Rebrov *et al.* [19] defined the guidelines to improve the heat distribution on parallel multi-channel reactors that includes adjusting the thickness of the channel walls and using a non-uniform coolant flow.

The radial design is not very common for MSR applications despite presenting interesting features, such as large mean cross-sectional area and short flow travel distance compared to single channel reactors, resulting in low pressure drop. In a single channel reformer, the flow velocity increases due to the pressure difference between the inlet and the outlet and also due to an increase on the molar flow rate, according to the MSR reaction stoichiometry. In the radial design, however, the flow velocity decreases as it moves towards the outlet, when the reactor is fed from the center to the periphery, due to an increase of the cross-sectional area. For a diffusion-limited reaction, a large variation of surface velocity is detrimental for the conversion of the reactor [20, 21]. In the present work, three cellular reformers with different designs (multi-channel, radial and tubular packed bed reactors) were manufactured and analyzed, either experimentally or by CFD in what concerns their performance for the MSR.

## 3.3. Experimental

The cellular reformers were designed to be sandwiched with HT-PEMFC in a stack arrangement. Heat and mass transport, pressure drop, flow-pattern and reactor volume were aspects taken into account since they affect the reformer performance [11]. The

previous aspects are all important, but the reformer size is critical due to practical reasons, which depends directly on the catalyst activity.

Three stainless steel packed bed reformers were manufactured with different designs, namely multi-channel, radial and tubular. They were based on the best available literature information; though new features were introduced in order to improve their performance (Fig. 3.1). Although stainless steel 316 is not as good as aluminum in terms of thermal conductivity, it presents better chemical stability towards methanol.

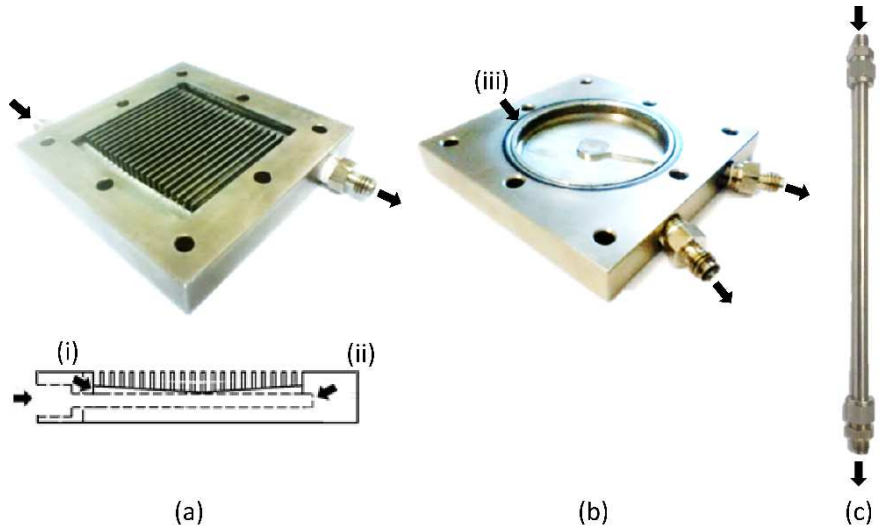


**Fig. 3.1** Manufactured reactors: a) Multi-channel reformer, top and section view; b) Radial reformer; c) Tubular reformer. i) slit; ii) distributor; iii) metal sintered ring for feed distribution;

The multi-channel reformer (Fig 3.1a) was designed to match a 25 $cm^2$ HT-PEMFC area, with outer dimensions of 95 mm x 95 mm x 10 mm. The reformer has 21 channels with 51 mm of length and 2 mm of width. The channels depths gradually increase towards the central part of the cell, from 4 mm to 6 mm. The inlet and outlet holes were drilled under the catalyst bed and act as distributors. They connect with the catalyst bed through a slit on the top. A stainless steel mesh (ca. 200 mesh) was used to cover the slits in order to avoid dragging the catalyst out from the bed. Two holes with different depths were made under the catalyst bed to insert thermocouples at different axial positions. The radial reformer (Fig. 3.1b) was also designed to match a 25 $cm^2$ HT-PEMFC and the outer dimensions are 95 mm x 95 mm x 8 mm. To hold the catalyst in place, a sintered ring was used, with inner diameter of 59 mm, thickness of 2 mm and height of

5 mm. The sintered ring creates also a small pressure drop which benefits the flow distribution. Next to the sintered ring a small channel collects the reformate stream and directs it to the outlet. The tubular reformer (Fig. 3.1c) was used as reference and it has 325 mm of length, 7 mm of internal diameter and 10 mm of external diameter.

The reactors performance was assessed using commercial catalyst G66 MR from Süd-Chemie ($CuO/ZnO/Al_2O_3$). The reformers were filled with 15.5 g of commercial catalyst, closed and placed inside an oven with controlled temperature. The catalyst was reduced *in situ* during 3 hours with 50 $cm^3 \cdot min^{-1}$ of hydrogen, at 443 K. The reduction reaction was performed at low temperature to avoid the catalyst sintering. The reforming reaction was carried out between 453 K and 513 K and at space time values ($m_{cat}/F_{MeOH}$) between 50 $kg \cdot s \cdot mol^{-1}$ and 1500 $kg \cdot s \cdot mol^{-1}$. The water/methanol mixture was pumped using an HPLC pump (LaPrep P130). The value of the molar steam to carbon ratio (S/C) was 1.5, since it is considered a good compromise to maximize the methanol conversion without wasting much energy in water evaporation [6].

The water/methanol mixture was evaporated using a serpentine placed inside the oven with forced air circulation. The phase transition of the water/methanol mixture creates strong flow fluctuations. In order to minimize that effect, the operating pressure was adjusted to 1.5 bar using a relief valve placed after the reformer.

The reformate stream was passed through a cold trap to remove the condensable components; the flow of the non-condensable species was measured using a mass flow meter (Bronkhorst); hydrogen and carbon dioxide concentration was determined by mass spectrometry (Pfeiffer OmniStar$^{tm}$) and CO using a specific analyzer (Signal Inst. 7000FM GFC). To determine the pressure drop in the reformers, the pressure was measured at the inlet using a nitrogen flow of 100 $cm^3 \cdot min^{-1}$ at 453 K. The effect of the pressure drop on the methanol conversion was also assessed at different operating pressures (1 bar to 3 bar).

### 3.4. CFD Modeling

The experimental evaluation of reactors concerning heat profiles and flow distribution is a very difficult and time consuming process. CFD techniques are non-intrusive tools that provide a good agreement between numeric and experimental results. Therefore, a CFD analysis was carried out using commercial software Fluent, from Ansys™. The

reformers (Fig. 3.1) were modelled using a three-dimension approach and validated with the data collected from the experimental runs.

### 3.4.1. Mathematical model

The model proposed in this study was based on assumptions as described next. The model was considered in steady-state. In the temperatures range considered, all the reaction species were in gas phase, behaving as ideal gases. In the operating conditions, the fluid flow was assumed laminar and Newtonian. The catalyst bed porosity was considered homogeneous, with uniform particles size and isotropic. No diffusion limitations in the catalyst were considered. Regarding the heat transfer in the reformer, both conduction and convection mechanisms were considered. Due to the good thermal conductivity of the SS316, no temperature gradients were assumed in the metal envelop of the reformers. The methanol steam reforming reaction was assumed as taking place only in the catalyst bed. The catalyst properties used in the simulations are given in Table 3.1.

**Table 3.1** Physical characteristics of Süd-Chemie G66MR catalyst [22].

| Property | Value |
|---|---|
| Density ($\rho_{catalyst}$ / kg·m$^{-3}$) | 1.1 |
| Porosity ($\varepsilon$) | 0.38 |
| Particle size ($D_p$, μm) | 100 – 250 |
| Thermal conductivity ($\lambda$, W·m$^{-1}$·K$^{-1}$) | 0.30 |

*Boundary conditions*

The boundary conditions considered for the reformer model are as follows:

- At the inlet, the flow velocity, gas composition and temperature were considered constant and equal to a specified value ;
- At the outlet, the pressure was considered to be 1.5 bar, gradients of temperature and species mass fraction are equal to zero;
- At the wall, the temperature was considered constant and the flow obeys to the no slip condition.

In order to analyse the effect of the mesh on the numerical results, several runs were performed. The mesh considered in the simulations gives a methanol conversion

with a maximum difference of 0.05 % relatively to the value obtained using a mesh with the double of nodes. The meshes considered for the multi-channel, radial and tubular models have a number of nodes of $5.9 \times 10^5$, $2.9 \times 10^5$ and $2.1 \times 10^5$, respectively.

The mass, energy and momentum equations for the reaction species are described in the following:

*Continuity Equation*

$$\nabla \rho \vec{u} = 0 \tag{3.1}$$

Eq. 3.1 is the mass conservation equation, where $\rho$ is the fluid density (kg·m$^{-3}$), $\vec{u}$ is the fluid velocity vector (m·s$^{-1}$) and $\nabla$ is the gradient.

*Momentum Balance*

$$\rho \vec{u} \nabla \vec{u} = -\nabla P + \nabla \tau + S, \qquad \text{where} \quad \tau = \mu \left( \nabla \vec{u} + \nabla \vec{u}^{T} - \frac{2}{3} \nabla \vec{u} \mathrm{I} \right),$$
$$S = -\left( \frac{\mu}{\alpha} \vec{u} + \frac{1}{2} C_2 \left| \vec{u} \right| \vec{u} \right), \qquad \alpha = \frac{D_p^2}{150} \frac{\varepsilon^3}{(1-\varepsilon)^2}, \qquad C_2 = \frac{3.5}{D_p} \frac{(1-\varepsilon)}{\varepsilon^3} \tag{3.2}$$

Eq. 3.2 is the conservation momentum equation and is known as the Navier-Stokes equation, in an inertial reference frame. The left member is the convective acceleration and represents the fluid particles acceleration with space. $\nabla P$ is the pressure (Pa) gradient and is the isotropic part of Cauchy stress tensor; $\nabla \tau$ is the anisotropic part of the stress tensor and describes the viscous forces, where $\mu$ represents the viscosity (kg·m$^{-1}$·s$^{-1}$) and $I$ is the unit tensor or identity matrix; $S$ is the source term and represents the external body forces. In this model, the source term is the pressure gradient (drop) in a porous media and is composed by viscous losses (first term) and inertia losses (second term), where $D_p$ is particle diameter (m) and $\varepsilon$ is the media porosity.

*Mass Balance*

$$\nabla \rho \vec{u} \omega_i = \nabla J_i + M_i \nu_i r_{MSR}, \qquad J_i = \rho D_i \nabla \omega_i + D_{T,i} \frac{\nabla T}{T} \tag{3.3}$$

To calculate the local mass fraction of the species $i$, $\omega_i$, it was used a convection-diffusion equation (Eq. 3.3). $J_i$ is the mass diffusion flux of the species $i$ (kg·m$^{-2}$· s$^{-1}$) and is composed

by a mass diffusion term described by the Fick's law (being $D_i$ the mass diffusion coefficient) and a thermal diffusion term, known as Soret effect (being $D_{T,i}$ the thermal diffusion coefficient). The second term on the right side is the mass flux of species *i* due to the chemical reaction, where $M_i$ is the molar mass of species *I* (kg·kmol$^{-1}$), $\nu_i$ is the stoichiometric coefficient of species *i* in MSR reaction and $r_{MSR}$ is the reaction rate (kmol·m$^{-3}$·s$^{-1}$).

*Energy Balance*

$$\nabla\vec{u}\rho H_0 = \nabla\left(K_{eff}\nabla T - \sum_i H_i J_{i,j} + \tau_{eff}\vec{u}\right) - \nabla\vec{u}P + S_H,$$
$$S_H = \sum_{i=1}^{N}\left(\Delta H_{k,298} + \sum_i \nu_i \int_{298}^{T} Cp_i dT\right)(r_i),\ H_i = \int_{T_{ref}}^{T} Cp_i dT,\ H_0 = \sum_i^{N_c} y_i H_i \quad (3.4)$$

Eq. 3.4 represents the conservation of energy. The left member is the total energy flux, where $H_0$ is the total enthalpy. In the right side, the first three terms are the energy flux by conduction, diffusive flux and by viscous forces, respectively. $K_{eff}$ is the effective thermal conductivity, which takes into account the thermal conductivity in the solid phases and gas phase (W·m$^{-1}$·K$^{-1}$) and *T* is the temperature (K). The fourth member is the pressure work. $S_H$ is the source term and represents the heat flux due to the chemical reaction, where $C_p$ is the specific heat capacity (J·kg$^{-1}$·K$^{-1}$)

### 3.4.2.Kinetic model

In this work, a power law kinetic model was used, as presented in Eq. 3.5. These kinetic models are mechanistic derived, but they are simple and have been successfully used to fit experimental data in the literature [23-24].

The kinetic model used in this study only considers the MSR reaction; WGS and MD reactions were not considered due to their very low reaction rates at temperatures below 473 K [24]. This assumption is also supported by the very low CO concentrations measured in the reformate stream (Fig. 3.4), which showed to be never higher than 0.15 %. The negative exponents on $H_2$ and $CO_2$ concentrations in Eq. 3.5 are related to the reversibility of the MSR reaction:

$$-r = k_0 e^{-\frac{E_a}{RT}} C_{CH_3OH}^{0.56} C_{H_2O}^{0.28} C_{H_2}^{-0.07} C_{CO_2}^{-0.09} \quad (3.5)$$

where, $-r$ is the reaction rate of the methanol steam reforming reaction ($kg.m^{-3}.s^{-1}$), $k_0$, is the Arrhenius pre-exponential factor ($6.3x10^7$ $kmol^{0.32}\cdot m^{-0.96}\cdot s^{-1}$) and $E_a$ is the activation energy ($80x10^6$ $J\cdot kmol^{-1}$). The kinetic parameters were estimated based on the experimental results obtained with the tubular reactor. The parameters estimation was carried using the differential method by fitting a non-linear regression to the conversion vs. $m_{cat}/F_{MeOH}$ experimental data and minimizing the sum of residual squares.

## 3.5. Results and discussion

### 3.5.1. Model validation

Fig. 3.2 shows the experimental and simulated methanol conversion and hydrogen production over different space-time values at 453 K, 463 K and 473 for the three reformers. The simulation results using the kinetic model (Eq. 3.5) present a good agreement with the experimental data for the studied conditions, as shown in the parity plot (Fig. 3.3). The reformers performance presents some differences concerning the attained methanol conversion, depending on the temperature and space time ratio values. Nevertheless, and excepting the radial reactor for the lowest temperature (Fig. 3.2), full conversion may be reached for contact times above a threshold value (defined on section 4.2), which lowers with temperature increase, as expected due to higher catalyst activity. The radial reformer is clearly less efficient than the other two, except for the high contact time region (high space time ratio) and for the temperatures of 463 K and 473 K. The tubular and multi-channel reactors perform quite similar, with a small difference in the intermediate contact time region for the lowest temperature (453 K), which progressively moves for low contact time values as the temperature increases. The reasons for this behavior are discussed below (section 4.4). The low reaction rate of the catalyst at 453 K demands more catalyst to achieve the full conversion, which is problematic in compact systems.

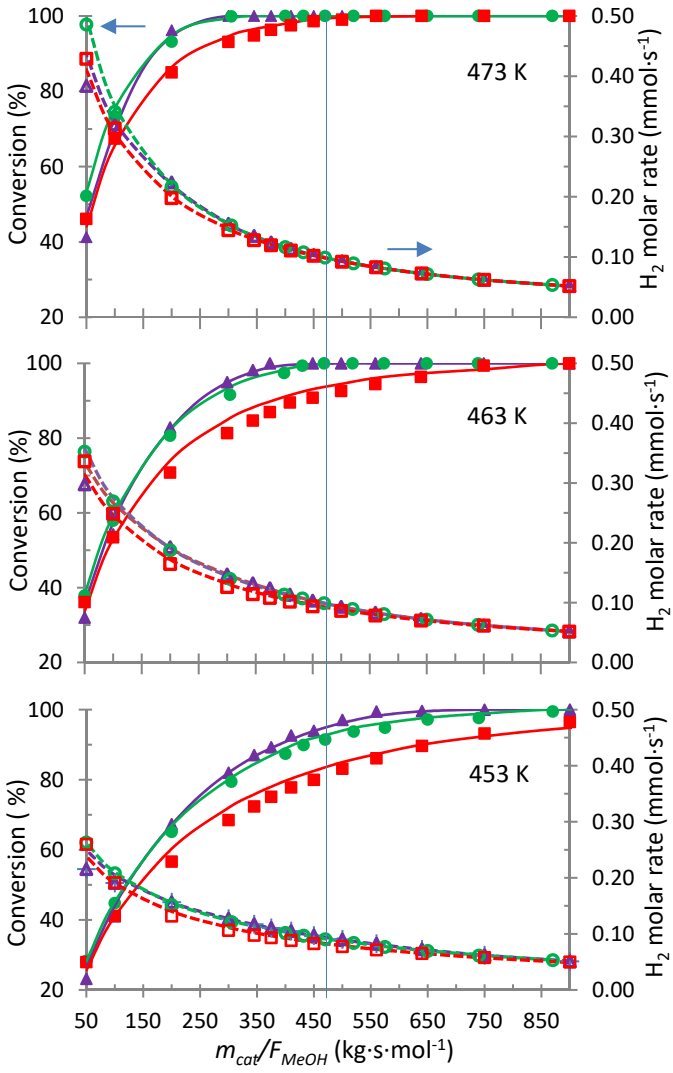


**Fig. 3.2** Experimental (symbols) and simulated (lines) results for the methanol conversion (left axis) and produced hydrogen molar flow rate (right axis) versus the space time ratio at different temperatures; Tubular reactor (purple); Multi-channel reactor (green); Radial reactor(red).

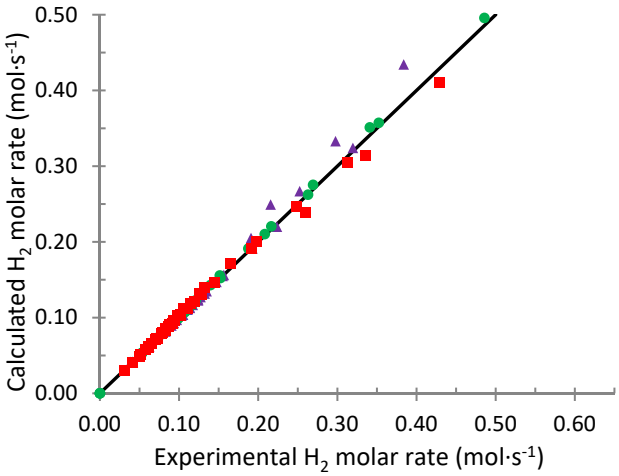


**Fig. 3.3** Parity plots of the experimental and calculated hydrogen molar rate. Tubular reactor (purple); Multi-channel reactor (green); Radial reactor (red).

### 3.5.2. Performance analysis

As previously mentioned, the goal of this work is the thermal integration of a MSR-C with a fuel cell in a stack arrangement. HT-PEMFCs with PBI membranes operate at a maximum temperature of 473 K, since higher temperatures compromise the stability of the membrane [25]. However, other membranes based on pyridine aromatic polyethers promise to be more stable at higher temperatures [26].

A 25 $cm^2$ HT-PEMFC, operating at 0.6 $A \cdot cm^{-2}$, requires ca. $9.34 \times 10^{-5}$ $mol \cdot s^{-1}$ of hydrogen (assuming that ca. 20 % of hydrogen is vented). Though the experimental assessment of the HT-PEMFC tolerance to methanol bleeding was not performed, it has been assumed a minimum methanol conversion of 95 %, thus requiring a minimum methanol flow rate of $3.3 \times 10^{-5}$ $mol \cdot s^{-1}$. Taking into account the catalyst mass placed in the reactors (15.5 g), the maximum $m_{cat}/F_{MeOH}$ is 473 $kg \cdot s \cdot mol^{-1}$. At the same operating condition using a reformer of 320 $cm^3$ filled with 149 g of catalyst pellets of $CuO/ZnO/Al_2O_3$, Pan *et al.* [6] reported nearly 100 % of methanol conversion for $m_{cat}/F_{MeOH} > 1200$ $kg \cdot s \cdot mol^{-1}$. Better results were achieved in this work, even though none of the previous reformers produce the required hydrogen flow rate ($9.34 \times 10^{-5}$ $mol \cdot s^{-1}$) at 453 K. The multi-channel reformer reached 95 % of methanol conversion at $m_{cat}/F_{MeOH}$ of 600 $kg \cdot s \cdot mol^{-1}$ and 453 K, while the radial reformer reached the same value only at space-time values higher than 1000 $kg \cdot s \cdot mol^{-1}$.

To produce the required hydrogen flow rate ($9.34x10^{-5}$ mol·s$^{-1}$) with 95 % of methanol conversion, it is necessary to operate at temperatures higher than 453 K. At 463 K, the multi-channel and the tubular reformers satisfied the previous conditions. The radial reformer at that temperature still was under performing. All these reformers were characterized using fresh catalyst; typically catalysts deactivate *ca*. 20 % after few hours of time on stream [8]. Despite this fact, the tubular and multi-channel reformers still were capable to produce enough hydrogen to feed a 25 cm$^2$ HT-PEMFC, operating at 0.6 A·cm$^{-2}$

Large reformers, such as the one used by Pan *et al.* [6], exhibit heat transfer limitations. Additionally, large catalyst particles, in the range of in the range of few millimeters, were used to minimize the pressure drop. As a consequence, the overall reaction rate becomes limited by the mass transfer of reactants between the bulk fluid and catalytic surface. Thus, it is important to achieve a balance between particle size and pressure drop. The pressure drop in the reformers was assessed using a nitrogen flow of 100 cm$^3$·min$^{-1}$ at 453 K. The highest pressure-drop value was obtained for the tubular reformer, *ca*. 170 mbar, while the multi-channel and radial reformers showed less than 10 mbar of pressure drop. The pressure drop and operating pressure showed a small influence on the methanol conversion, decreasing less than 5 % in all reformers when the pressure changes from 1 to 3 bar at 453 K

According to the literature, carbon monoxide concentration lower than 20 000 ppm – 30 000 ppm [6] does not affect significantly the HT-PEMFCs performance. The experimental carbon monoxide concentration in the reformate stream as a function of the space-time, at 453 K and 473 K and for the three reactors is presented in Fig. 3.4. The results show a maximum CO concentration of *ca.* 900 ppm at 453 K and 1600 ppm at 473 K. This way, the reformate stream does not require further purification to feed a HT-PEMFC. At temperatures lower than 573 K the methanol decomposition reaction has very low conversion being the CO almost exclusively produced from the reverse water gas shift reaction [9]. As a result, the CO concentration increases with the partial pressure of the MSR reaction products ($H_2$ and $CO_2$). As shown in Fig. 3.4, the multi-channel reactor produces similar concentrations of CO as the tubular and higher than the radial reformer, mainly due to heat profiles as it will be discussed later.

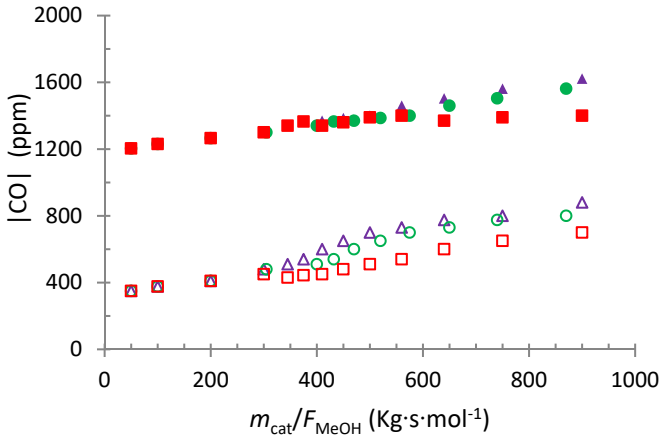


**Fig. 3.4** CO concentration versus the space time ratio, at 453 K (empty symbols) and 473 K (filled symbols) and at 1.5 bar; - ▲ - Tubular reactor; - ● - Multi-channel reactor; -■ - Radial reactor.

### 3.5.3. Flow distribution

To show an optimised performance, the reformer design must provide a good flow distribution, assuring that all the available catalyst is fully used. However, the catalyst full exploitation also depends on the size and shape of the respective particles, for a given set of operating conditions. Catalyst powders are composed of very small irregular particles, which benefit the mass diffusion into the catalyst particle surface, but have a detrimental effect on pressure drop and flow distribution [27]. To minimize these negative aspects, sieves with mesh size of 100 – 250 µm were used, in order to obtain a narrow catalyst powder size distribution. In the following, the flow distribution in the different reactors will be analyzed in more detail.

*Flow velocity profiles in the multi-channel reactor*

Multi-channel designs characteristically exhibit small-pressure drop and the flow distribution through the channels depends on the Reynolds number [14]. To optimize the flow distribution in the multi-channel reformer, an inlet and outlet distributor was used in the present study located underneath the catalyst bed as described previously. The porous media (catalyst bed) imposes a momentum resistance (sink) due to viscous and inertia losses (Eq. 3.2), which contributes for a homogenization in the flow distribution.

Fig. 3.5 shows the simulated average flow velocity on the channels, at the middle axial position, for the multi-channel reformer. The coefficient of variation of the flow velocity in the channels was calculated to assess the goodness of the flow distribution. The coefficient of variation was in the range 0.6 % to 0.8 % for a space-time ratio from 900 kg·mol·s$^{-1}$ to 50 kg·mol·s$^{-1}$, respectively. The results obtained for the flow velocity distribution are similar with those obtained by Jang *et al.* [18] for a multi-channel reformer. These authors improved the flow velocity distribution in a multi-channel reformer optimising the width of the channels. Although the CV values are very small, slightly higher flow velocities were observed in the outer channels relatively to the inner channels. In the development of the multi-channel reactor, a larger quantity of catalyst was considered in the middle of the bed, where the temperature of the stack (MSR/HT-PEMFC) is higher. Therefore, the channels depth was increased from the outer to the inner channels leading to this difference in the flow velocity among the channels. This small difference in flow velocity among channels should represent a minor penalty for the hydrogen production.

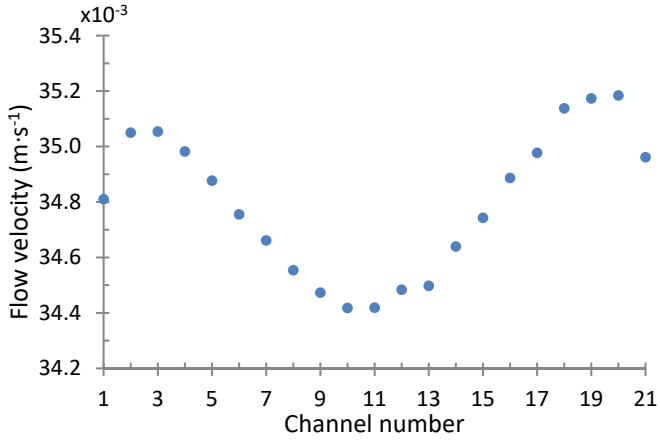


**Fig. 3.5** Flow velocity determined in the middle of the channels for multi-channel reformer with $m_{cat}/F_{MeOH}$ = 300 kg·mol·s$^{-1}$, wall temperature 453 K, $P_{out}$ = 1 bar and $S/C$ = 1.5.

Fig. 3.6 shows the simulated flow distribution of the multi-channel reformer. In the channels region is observed a quasi plug flow behaviour that benefits the performance. However, dead zones are observed in the distributors near the entrance and exit

walls, due to the central position of inlet and outlet distributor slit. As a result, the catalyst in these regions is poorly used, which has a negative effect in the hydrogen production. This negative effect, explains the difference in the methanol conversion observed in Fig. 3.2 between tubular and multi-channel reformers at temperature of 453 K. These dead zones however were expected, as long as they do not affect significantly the flow distribution in the channels and in order to use all the available volume of the reformer, they were considered acceptable.

To improve this reactor performance, the inner and outlet distributor should be thinner and the slits should be located not in the middle of the distributors but by the reactor walls. This would improve the flow distribution and consequently the methanol conversion.

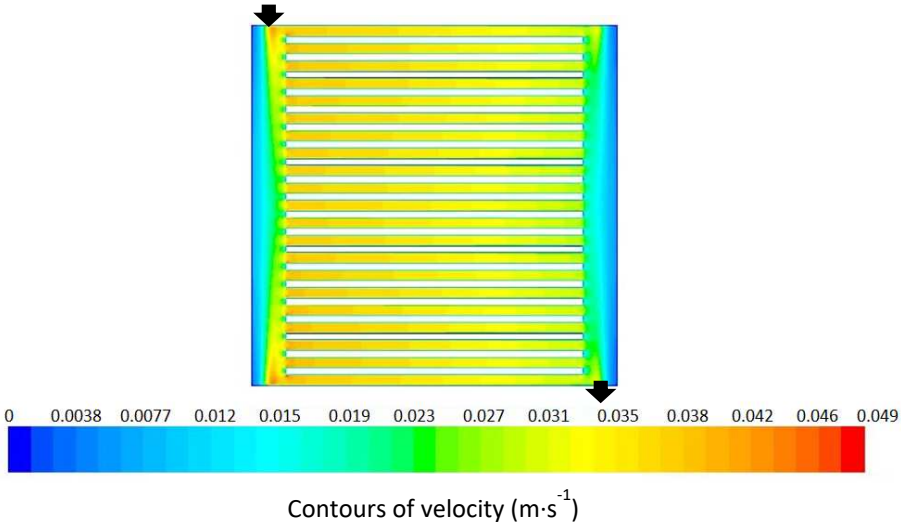


**Fig. 3.6** Flow velocity contours of multi-channel reformer with $m_{cat}/F_{MeOH}$ = 300 kg·mol·s$^{-1}$, wall temperature 453 K, $P_{out}$ = 1 bar and $S/C$ = 1.5.

The tubular reformer behaved as a plug flow reactor with no dead zones, as expected (not shown). The plug flow behaviour and the absence of dead zones on the tubular reformer explain the higher methanol conversion at 453 K when compared to the multi-channel and radial reformer.

*Flow velocity profiles in the radial reactor*

The velocity profile obtained for the radial reformer (Fig. 3.7b) agrees with the results reported by Pattekar *et al.* [21] where low and steady flow velocities are observed. However, the high performances presented by Pattekar *et al.* for this design were not observed in the present work. The low performance of the radial reformer can be justified by the flow velocity profile; this reformer presents a laminar flow with a very interesting behaviour, with large regions near the upper and lower walls with very low flow velocity, as shown in Fig. 3.7b. This behaviour differs from the multi-channel reformer, where the reactor design creates stagnant regions and channels with different flow velocities.

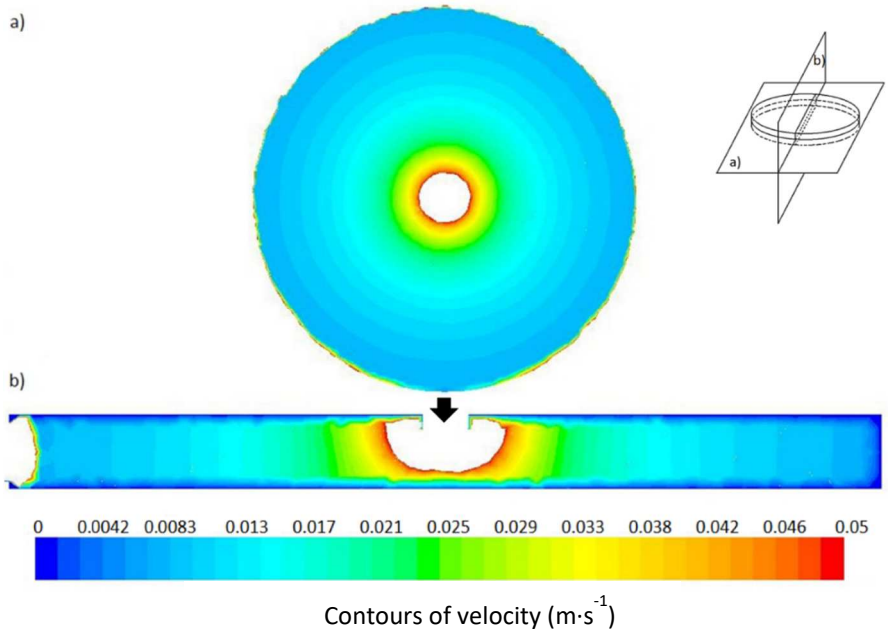


**Fig. 3.7** Flow velocity contours of radial reformer with $m_{cat}/F_{MeOH}$ = 300 kg·mol·s$^{-1}$, wall temperature 453 K, $P_{out}$ = 1 bar and *S/C* = 1.5: a) radial section view (half-height); b) front section view. Velocities higher than 0.05 m·s$^{-1}$ have been removed for a better illustration of the stagnate regions.

Typically, in laminar flows the fluid profile becomes fully developed at a short distance from the leading edge. A fluid profile is considered fully developed, when the boundary layer thickness (i.e. the layer in which the velocity grows from zero at the wall

- no slip condition - to 99% of the maximum velocity in the middle of the channel) reaches a constant value. However, when the radial reformer is fed through the centre, the flow velocity decreases and depends on the balance between the increase of the cross-section area (velocity decrease), the pressure drop (velocity increase) and the total moles number due to the reaction stoichiometry (velocity increase). As a result, the flow never becomes fully developed, since the boundary layer increases as the fluid velocity decreases. The thickness of the boundary layer is related to the inefficiency on the catalyst usage in this reactor.

For a diffusion-limited or close to diffusion-limited reaction, the low flow velocity can benefit the reaction conversion. However, if very small catalyst particles are used, the reaction is rate limited, so the velocity effect on the methanol conversion should be minor. On the other hand, very low flow velocities create stagnated regions near to the wall and as a result, the catalyst is poorly used, as previously mentioned. Despite the low performance observed towards the methanol conversion, the radial reformer, due to the short flow travel distance of the fluid, presents the lowest pressure drop among the three reformers. This design can be an interesting option when the pumping power is a limitation. Even though, by reducing the height of the catalyst bed, higher flow velocities are achieved reducing the boundary layer and enhancing the hydrogen production.

### 3.5.4.Heat transfer

The slow reaction kinetics at 453 K demands high space-time values to achieve >95 % of methanol conversion. On the other hand, the low flow velocity increases the thickness of the stagnated gas film on the reactor walls leading to a high heat transfer resistance [28]. The thermal conductivity is also affected by the void fraction, larger near the wall than in the bulk, limiting the number of contact points between the catalyst particles and the reactor wall. In the following, the temperature profiles for the different reactors are presented and discussed.

#### *Temperature profiles in the tubular reactor*

The temperature contours for the tubular reformer in the MSR reaction, at a wall temperature of 453 K and a space-time of 300 $kg \cdot s \cdot mol^{-1}$, is shown in Fig. 3.8. As it can

be observed, there is a temperature sink of 7 K at the entrance of the reactor. This temperature drop indicates the existence of heat transfer limitations in this region of the reformer. The reasons for that are related with the endothermic nature of the reaction, the low thermal conductivity of the catalyst and the maximum reaction rate value in the inlet region.

Any drop in the temperature leads to a decrease of the conversion. Thus, it is of high importance to minimize as possible any temperature decrease. The heat demand in the reformer is not uniform, being higher close to the entrance where the reforming reaction is faster. However, it only reports to the initial stage of the reaction. To evaluate the limitations on the heat transfer the average temperature of the reformer was considered, since it provides an overall evaluation of the reactor. For temperature of 453 K and a space-time of 300 kg·s·mol$^{-1}$, the average temperature of the reformer was 451.5 K, which does not significantly influence the methanol conversion, shown in Fig. 3.9. As the reaction rate increases with the operating temperature, the heat transfer limitations become more important (*e.g.,* at 473 K and for full methanol conversion, the temperature sink is 12.5 K and the average temperature is 470 K, data not shown). Therefore, to minimize the heat transfer limitations at higher operating temperatures the tube diameters must be reduced.

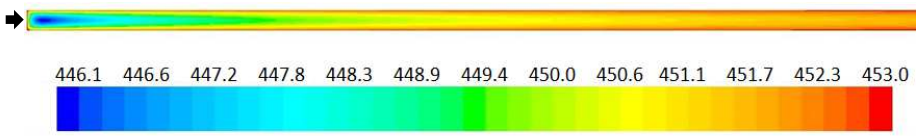


**Fig. 3.8** Temperature contours for tubular reformer in the MSR reaction, with $m_{cat}/F_{MeOH}$= 300 kg·mol·s$^{-1}$, wall temperature 453 K, $P_{out}$ = 1 bar and *S/C* = 1.5.

For the same reaction volume, smaller diameters correspond to longer lengths, which minimize the temperature sink, enhance the methanol conversion but originate higher pressure drops. Karim *et al.* [23] estimated that the smallest diameter required for a packed bed to achieve near isothermal operation was 300 μm at 503 K. The benefit of operating at isothermal conditions must be evaluated. In order to analyse this benefit, different simulations were performed to compare the non-isothermal with the isothermal conditions (isothermal conditions were attained by increasing the catalyst thermal

conductivity), which results are presented in Fig. 3.9. At 453 K the benefit of having isothermal conditions showed to be small; for a space-time of 300 kg·s·mol$^{-1}$ the methanol conversion is 84.1 % while at non-isothermal is 82.0 %. However, higher operating temperatures revealed the heat transfer limitations of this reformer, and at 473 K and for a space-time of 150 kg·s·mol$^{-1}$ the methanol conversion is 90.0 % while for non-isothermal conditions is 85.9 %. From these results, one can concluded that the diameter of the tubular reformer is acceptable to operate at 453 K, but for higher temperatures, smaller diameters are required.

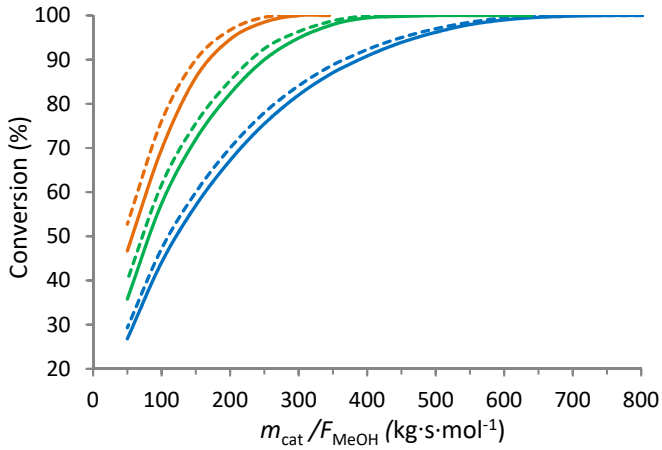


**Fig. 3.9** Methanol conversion for plug-flow reactor at isothermal conditions (dash line) and tubular reformer at non-isothermal conditions (full line), with wall temperature of 453 K (blue), 563 K (green) and 473 K (brown), $P_{out}$ = 1 bar and $S/C$ = 1.5.

*Temperature profiles in the multi-channel reactor*

The temperature contours for the multi-channel reformer in the MSR reaction, at wall temperature of 453 K and space-time of 300 kg·s·mol$^{-1}$, are plotted in Fig. 3.10. The temperature sink is 4 K, lower than the obtained for the tubular reformer. Moreover, the reformer operates almost at isothermal conditions in the region of the channels. As a result, the reformer average temperature was 452.5 K, indicating minor heat transfer limitations. Even at 473 K, the average temperature is 472.1 K with a maximum temperature sink of 7.4 K (not shown). Operating the multi-channel reformer at 473 K with isothermal condition and space time of 150 kg·s·mol$^{-1}$ (CDF results) shows *ca.* 1 percentage point difference on the methanol conversion compared to non-isothermal conditions.

This shows that the major limitation of the multi-channel reformer is not related to heat transfer limitations but with the flow distribution.

As the reaction rate increases with the temperature, it emphasizes the heat transfer limitations in the reformers and it gains significant influence on the methanol conversion. The inversion on the performance between multi-channel and tubular reformer (Fig. 3.2) as the temperature increases, especially at low space-time values, is related to the higher efficiency on the heat transfer of the multi-channel reformer at higher temperatures.

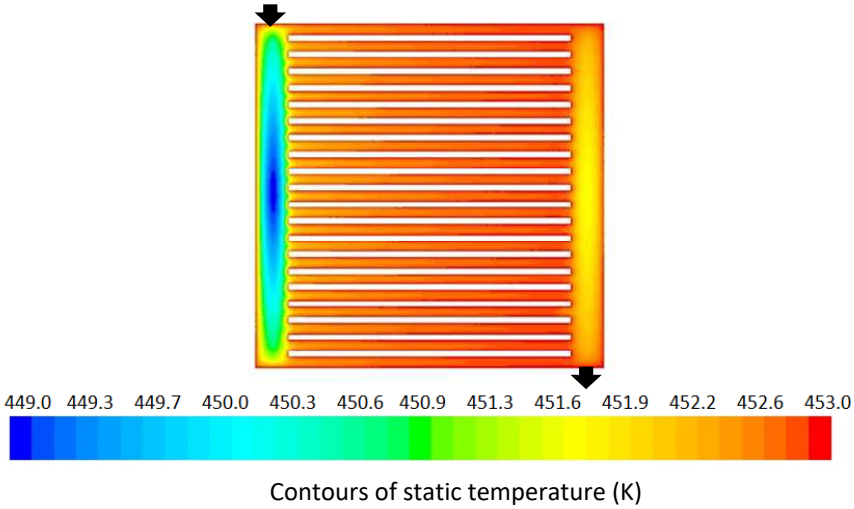


**Fig. 3.10** Temperature contours for multi-channel reformer in the MSR reaction, with $m_{cat}/F_{MeOH}$ = 300 kg·mol·s$^{-1}$, wall temperature 453 K, $P_{out}$ = 1 bar and $S/C$ = 1.5.

*Radial - temperature profiles*

The radial reformer presents important limitations regarding heat transfer as shown in Fig. 3.11. As previously mentioned low flow velocities have detrimental effect on heat transfer by convection and the small metallic surface area in the radial reformer reduces the heat transfer wall/catalyst particle by conduction. Although the temperature sink is 5 K lower than in the tubular at 453 K with $m_{cat}/F_{MeOH}$ of 300 kg·s·mol$^{-1}$, the radial reformer presents an average temperature of 451.3 K. The highest flow velocity was observed in the middle of the reformer, where the temperature was lower than 450.0 K (Fig. 3.11), pointing toward the low conversions observed in this reformer. This design presents limitations regarding the heat transfer, which could be minimized by

reducing the height of the catalyst bed. The insertion of metallic fins in an axial position would also increase the heat transport to the catalyst bed, but it would reduce the catalyst load.

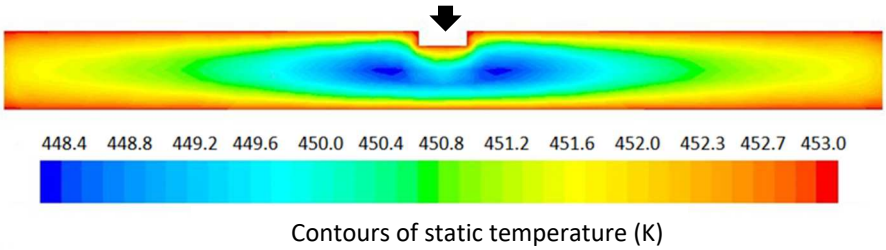


**Fig. 3.11** Temperature contours for radial reformer during MSR reaction, with $m_{cat}/F_{MeOH}$ = 300 kg·mol·s$^{-1}$, wall temperature 453 K, $P_{out}$ = 1 bar and $S/C$ = 1.5.

## 3.6. Conclusions

Three different methanol reformer designs for thermal integration with a HT-PEMFC were thoroughly studied experimentally and by CFD simulation. The results showed that the multi-channel design is the best solution for the thermal integration, with high methanol conversion and low pressure drop. The narrow channels and the high metallic surface area in the multi-channel provided the lowest temperature sink among the studied reformers due to an efficient heat transfer from the wall to the bulk. The multi-channel showed a good flow distribution with a coefficient of variation in flow velocity between channels in the range of 0.6 % to 0.8 %.

Severe heat transfer limitations were observed in the radial reformer due to low flow velocities and small metallic surface area. The low flow velocity in the bed of the radial reformer had a negative effect on the catalyst usage reducing the methanol conversion. To obtain isothermal condition the tubular reformer diameter or the multi-channel width must be reduced, but at low temperatures, *ca.* 453 K, it presents small benefit, due to the low reaction rate. The low activity of the MSR catalysts, at 453 K is still an issue to be solved. Nevertheless, the multi-channel reformer, at *ca.* 463 K, can produce enough hydrogen to feed directly a HT-PEMFC with low CO content.

## 3.7. References

[1]P. Atkins and J. De Palma, Atkin's Physical Chemistry 8th ed. W. H. Freeman and Company, New York (2006).

[2] [access date December 2013], http://www.ultracellpower.com/sp.php?rmfc

[3] T. Huck, P. Engelhardt, K. Lucka, Highly integrated micro fuel cell system based on a methanol steam reformer and a HT PEM fuel cell. 15th Europeam Fuel Cell Forum. Lucern, Switzerland (2011).

[4] S. Andreasen, S. Kær, S. Sahlin, Control and experimental characterization of a methanol reformer for a 350W high temperature polymer electrolyte membrane fuel cell system, International Journal of Hydrogen Energy 38 (2013) 1676–84.

[5] A. Qi, B. Peppley, K. Karan, Integrated fuel processors for fuel cell application: A review, Fuel Processing Technology 88 (2007) 3–22.

[6] C. Pan, R. He, Q. Li, J. Jensen, N. Bjerrum, H. Hjulmand, Integration of high temperature PEM fuel cells with a methanol reformer, J. Power Sources, 145 (2005) 392-398.

[7] G. Avgouropoulos, T. Ioannides, J. Kallitsis, S. Neophytides, Development of an internal reforming alcohol fuel cell: Concept, challenges and opportunities, Chem. Eng. J., 176 (2011) 95–101.

[8] A. Iulianelli, P. Ribeirinha, A. Mendes, A. Basile, Methanol steam reforming for hydrogen generation via conventional and membrane reactors: A review, Renewable and Sustainable Energy Reviews 29 (2014) 355–368.

[9] G. Avgouropoulos, S. Neophytides, Performance of internal reforming methanol fuel cell under various methanol/water concentrations, Journal Applied Electrochemistry, 42 (2012) 719–726.

[10] K. Yu, W. Tong, A. West, K. Cheung, T. Li, George Smith, Y. Guo, S. Tsang, Non-syngas direct steam reforming of methanol do hydrogen and carbon dioxide at low temperature, Nature Communications, 2 (2012), 1230-1236.

[11] V. Hessel, S. Hardt, H. Lowe, Chemical Micro Processing Engeneering, Wiley-VCH (2004).

[12] S. Agrawal, K. Nigam, Modelling of a coiled tubular chemical reactor, Chemical Engineering Journal, 84 (2001) 437–444.

[13] A. P. Sasmito, J. C. Kurnia, A. S. Mujumdar, Numerical Evaluation of Transport Phenomena in a T-junction Microreactor with Coils of Different Configurations, Industrial & Engineering Chemistry Research, 51 (2012)1970–1980.

[14] H. An, A. Angli, B. Agus, P. Sasmito, C. Jundika, A. Kurnia, V. Sachin, Jangam, S. Arun, Mujumdar, Computational fluid dynamics (CFD) analysis of micro-reactor performance: Effect of various configurations, Chemical Engineering Science, 75 (2012) 85–95.

[15] C. Hsueh, H. Chu, W. Yan, G. Leu, J. Tsai, Three dimensional analysis of a plate methanol steam micro reformer and a methanol catalytic combustor with different flow channel designs, International Journal of Hydrogen Energy, 36 (2011) 13575-13586.

[16] F. Mehri, M. Taghizadeh, Performance assessment of a spiral methanol to hydrogen fuel processor for fuel cell applications, Journal of Natural Gas, 21 (2012) 526-533.

[17] Sohn, Y. Byun, J. Cho, J. Choe, K. Song, Development of the integrated methanol fuel processor using micro-channel patterned devices and its performance for steam reforming of methanol, International Journal of Hydrogen Energy 32, (2007) 5103 – 5108.

[18] J. Jang, C. Cheng, Y. Huang, C. Lee, C. Leu, Optimal design of parallel channel patterns in a micro methanol steam reformer, International Journal of Hydrogen Energy, 37 (2012) 16974-16985.
[19] E.V. Rebrov, J.C. Schouten, M.H.J.M deCroon, Single-phase fluid flow distribution and heat transfer in microstructured reactors, Chemical Engineering Science, 66 (2011) 1374–1393.
[20 ] J. Telotte, J. Kern, S. Palanki, Miniaturized methanol reformer for fuel cell powered mobile applications, International Journal of Chemical Reactor Engineering, 6 (2008) 64-72.
[21] A. Pattekar, M. Kothare, A radial microfluidic fuel processor, Journal of Power Sources, 147 (2005) 116-127.
[22] S. Sá, A. Mendes, J. Sousa, Ph.D Thesis: Methanol Steam Reforming for Fuel Cell Applications, FEUP-PDEQB, (2011).
[23] A. Karim, J. Bravo, A. Datye, Non isothermally in packed bed reactors for steam reforming of methanol, Applied Catalysis A: General, 282 (2005) 101–109.
[24] S. Samms, R. Savinell, Kinetics of methanol-steam reforming in a internal reforming fuel cell, Jornal of Power Sources 112 (2002) 13-29.
[25] Q. Li, J. Jensen, R. Savinell and N. Bjerrum, High Temperature Proton Exchange Membranes Based on Polybenzimidazoles for Fuel Cells, Progress in Polymer Science, 34 (2009) 449-447
[26] M. Geormezia, C. Chochosb, N. Gourdoupib, S.G. Neophytidesb, J. Kallitsisa, High performance polymer electrolytes based on main and side chain pyridine aromatic polyethers for high and medium temperature proton exchange membrane fuel cells, Journal of Power Sources, 196 (2011) 9382–9390
[27] M. Losey, M. Shmidt, K. Jensen, Micro-fabricated multiphase packed bed reactors: characterization of mass transfer and reaction, Industrial & Engineering Chemistry Research, 40 (2001) 2555–2562.
[28] D. Mears, Diagnostic Criteria for heat transport limitations in fixed bed reactors, Journal of Catalysis 20 (1971) 127–131.

# Chapter 4

# Integration of a reformer with a HT-PEMFC – Part A

## 4.1. Abstract

A fuel cell is an exothermic device that wastes ca. 50 % of the input chemical energy while methanol steam-reforming (MSR) reaction is endothermic. The integration of a low temperature methanol steam-reforming cell (MSR-C) with a high temperature polymer electrolyte membrane fuel cell (HT-PEMFC) in a combined stack arrangement allows the thermal integration of both reactors. A novel bipolar plate of poly(p-phenylene sulfide) (PPS) featuring the fuel cell flow field in one side and the reformer flow field in the other was designed, built and assessed. For the first time are reported high current densities (>0.5 $A \cdot cm^{-2}$) with the integrated system running at 453 K. The system was also ran for more than 100 h at 453 K, at 0.3 $A \cdot cm^{-2}$, with a methanol conversion of > 90 %. It was observed some degradation of the membrane electrode assembly (MEA) due to the continuous presence of methanol in the reformate stream. Electrochemical impedance spectroscopy (EIS) analyses revealed an overall increase of the resistances. The self-thermal sustainability of the combined device was only reached for > 0.75 $A \cdot cm^{-2}$ due to the poor thermal insulation of the combined reactor.

---

The content of this chapter is adapted from, P. Ribeirinha, I. Alves, F Vidal Vázquez, G. Schuller, M. Boaventura, A. Mendes, Heat integration of methanol steam reformer with a high-temperature polymeric electrolyte membrane fuel cell, Energy 120 (2017) 468–477.

## 4.2. Introduction

High temperature polymer electrolyte membrane fuel cells (HT-PEMFCs) are electrochemical devices that operate usually between 393 K and 453 K [1-5]. The most promising electrolyte for HT-PEMFC is polybenzimidazole (PBI) impregnated with phosphoric acid that was initially developed by Savinell *et al.* in 1995 [2, 3]. *m*-PBI, (poly[2,2'-(m-phenylene)-5,5'-bibenzimidazole]) commonly referred as PBI is an aromatic heterocyclic polymer with high mechanical strength, good chemical resistance and glass transition temperature of 703 K. Due to a low proton conductivity (*ca*. 3.82 $mS \cdot cm^{-1}$ at 473 K [6]), PBI must be doped with an acid such as phosphoric acid to increase the proton conductivity above 0.05 $S \cdot cm^{-1}$ for fuel cell applications [4]. Other examples of polymer electrolyte membranes for HT-PEMFC are sulfonated poly-ether-ether-ketone (S-PEEK) blended with poly-benzimidazole (PBI) or S-PEEK derivative membranes such as sulfonated poly-ether-ether-ketone with cardo group (S-PEEK-WC) [7] and pyridine based aromatic polyether doped with phosphoric acid electrolyte (Advent®). HT-PEMFC presents several advantages when compared to typical PEMFC based on perfluorinated membranes (<363 K) namely higher electrochemical kinetics, simplified water management and heat recovery and higher carbon monoxide tolerance. However, HT-PEMFC has yet to show similar long-term stability of PEMFC based on perfluorinated membranes [8].

Hydrogen is the most preeminent fuel for fuel cell applications but has low volume energy density, is difficult to store and to transport and requires an entirely new distribution infrastructure. Hydrogen, however, can be efficiently produced *in-situ* through catalytic reforming of hydrocarbonates such as methane, methanol or ethanol [9, 10]. High temperature fuel cells, such as solid oxide fuel cell (SOFC) or molten carbonate fuel cells (MCFC) can perform internal reforming of hydrocarbonates or exploit efficiently solid fuels such as bituminous coal, lignite, biomass or bio-waste converted to hydrogen by a gasification process [11-13]. SOFCs or MCFCs are especially attractive for combined heat and power (CHP) generation applications or integrated within high efficiency hybrid cycles [11, 14]. Methanol, on the other hand, is the most attractive fuel for *in-situ* hydrogen production for portable or small stationary applications due to its high hydrogen/carbon ratio, absence of carbon-to-carbon bonds that allows low reforming temperature (513 K - 533 K) and considerably high energy density [15,16]. In PEMFCs, methanol can bed feed directly, but it considerable decreases the performance due to poor oxidation kinetics and methanol crossover from the anode to the cathode [17]. High

temperature DMFCs were first studied in the 1990's using phosphoric acid doped PBI as electrolytes [18-20]; an assembled prototype HT-DMFC reached a maximum of 0.1 $W \cdot cm^{-2}$, at 473 K [19].

Hydrogen generation *in-situ* by methanol steam reforming (MSR) to supply HT-PEMFC is being used in commercial power supplies namely by Ultracell [15] and by Serenergy [16]. In this power supply, a combustor burns a small fraction of fuel that provides heat for the following steps, namely fuel vaporization and MSR reaction. Fuel cells are exothermic devices that waste *ca.* 50 % of the input chemical energy as heat, representing more energy than the required for fuel vaporization and MSR reaction combined. Due to the mismatch of typical operating temperature between reformer and HT-PEMFC (533 K vs 433 K) the heat released by the fuel cell is normally wasted. Nevertheless, synergetic heat integration could be achieved if the operating temperatures are the same. Pan *et al.* reported the first attempt to integrate a HT-PEMFC with a MSR both devices operating between 453 K and 473 K [21]. The results showed insufficient fuel supply from the reformer, even at 473 K, resulting in high voltage losses, 160-200 mV at low current densities, compared to a mixture feed with volume fractions of 75% $H_2$ and 25 % $CO_2$. Avgouropoulos *et al.* [22-24] took a different approach by incorporating the methanol reforming catalyst in the HT-PEMFC anodic compartment. The results reported show a very low performance of the fuel cell due to contamination of the electrocatalyst by methanol [22]. These authors were able to improve the fuel cell performance by inserting a plate between the gas diffusion layer and the membrane electrode assembly (MEA), reporting a cell voltage of 642 mV at 0.2 $A \cdot cm^{-2}$, at 483 K [24].

Feeding directly a HT-PEMFC anode with reformate involves several concerns, namely methanol slip, CO poisoning and dilution of hydrogen. Concerning the effect of methanol slip from the MSR on the performance of HT-PEMFC only few studies have been reported [24-26]. Methanol oxidizes the anode catalyst competing with hydrogen for the active sites, despite the complex mechanism and lower reaction rate than hydrogen oxidation [25]. Methanol also permeates via diffusion from the anode to the cathode reducing the $O_2$ availability and depolarizing the cathode [20]. The high operating temperatures of phosphoric acid doped PBI based fuel cells allows considerable high tolerance towards CO, yet CO adsorbs on the platinum surface, used as electrocatalyst, creating a monolayer and blocking active site for the adsorption/desorption of $H_2$. A tolerance of Pt/C catalyst was observed for CO concentration until 5 % at 453 K, at moderate

values of voltage [27]. The presence of $CO_2$ in the reformate dilutes the fuel and limits the maximum current density of the fuel cell [28] and can have a negative effect due to formation of CO via the reverse water–gas shift reaction on platinum sites [29,30].

The materials and design used to produce the bipolar plates are one of the important key components to achieve the integration of a MSR-C with a HT-PEMFC. Traditionally, graphite is the most commonly material used to machine bipolar plates, due to excellent corrosion resistance, low bulk density and high electrical conductivity. Yet, the brittleness of graphite makes it difficult to machine [31]. Metallic bipolar plates are cheaper, easy to machine and can be produce with very low thicknesses, but they show low corrosion resistance. The corrosion process leads to an undesirable increase of electrical resistance due to the formation of a less conductive oxide film on the surface of the metallic material [32]. Polymer-graphite composites are being considered to produce bipolar plates, showing to be little affected by corrosion in PEM fuel cells. Polyphenylene sulfide (PPS) is a thermoplastic polymer with high chemical and thermal stabilities and very interesting mechanical properties [31]. PPS characteristics made this polymer suitable to produce composite bipolar plates with improved mechanical and electrical properties [33, 34].

To achieve an efficient heat integration of MSR-C/HT-PEMFC, the reformer must maximize the heat transfer with a uniform flow distribution and low-pressure drop. In the literature, most of studies describing well-structured flat reactors for MSR reaction have flow fields based on single channel design or based on a series of parallel channels [9]. Parallel channels or based on parallel channels designs have been pointed as the best option to carry out the MSR reaction due to high conversions, good heat transfer and low-pressure drop [35]. This configuration however, is more prone to uneven flow distributions, especially if it is not imposed a considerable pressure drop between the manifold and the channels, which increases considerable the complexity of the reactor. Multiple serpentine designs, in the other hand, are simple to manufacture and provide good flow distributions minimizing the pressure drop.

In the present work, the heat integration of a methanol steam reformer with a HT-PEMFC working both devices at the same temperature was attempted. A new bipolar plate was designed, featuring the fuel cell anode flow field in one side and the reformer flow field in the other. The integrated unit will be assembled using membranes based on pyridine based aromatic polyether doped with phosphoric acid; despite being already

commercialized, only a few studies have been reported considering the performance and stability of these membranes at high temperatures (>453 K) [22-24]. The fuel cell and the reformer performances were assessed individually and as an integrated unit working at different temperatures. The fuel cell was characterized by polarization curves and electrochemical impedance spectroscopy considering different fuels, including reformate produced by the MSR without pre-treatment.

## 4.3. Experimental

*Bipolar plate design*

A bipolar plate made in PPS with outer dimensions of 9.5 cm x 9.5 cm x 1.7 cm was designed to have a fuel cell flow field in one side and the reformer flow field in the other (Fig. 4.1). The fuel cell flow field has a pin-hole design with outer 5.0 cm x 5.0 cm, while the reformer has a triple serpentine design with total volume of 13.7 $cm^3$.

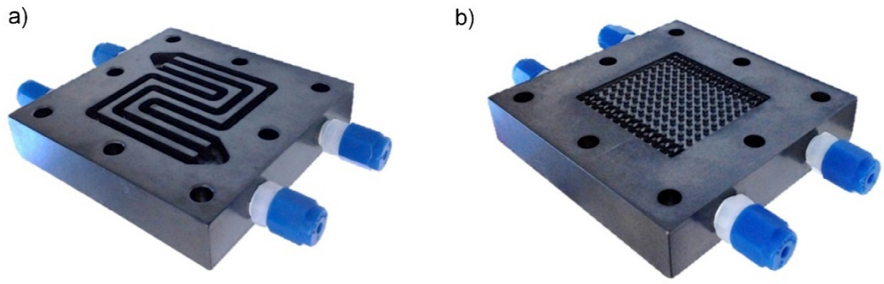


**Fig. 4.1** Bipolar plate made of PPS; a) reformer side; b) Fuel cell side.

*Assembling the HT-PEMFC and MSR-C integrated unit (MSR-C/HT-PEMFC)*

The MEAs were from Advent TPS®, with an active area of 25 $cm^2$. The membrane is based on pyridine type structures incorporated around a stable polymer backbone and has a thickness of 60-65 µm. The catalyst loading on both the anode and the cathode is 1 mg Pt/$cm^2$. The MEAs were placed in a single cell composed by one bipolar plate with pin-hole geometry (cathode) and the new bipolar plate developed in this work (anode). PTFE gaskets supplied by Advent TPS® with thickness of 310 µm were used to assure the fuel cell sealing; they provided a MEA compression of *ca.* 18 %.

The reformer channels were filled with *ca.* 18 g of BASF (RP-60) catalyst with particle size between 200-400 µm and sealed with a silicon gasket of 1.5 mm of thickness. The MSR-C/HT-PEMFC was covered by two metal endplates and all parts were tighten by eight bolts with a torque of 3.5 N·m.

*Fuel cell and reformer test bench*

The schematic diagram of the test bench is shown in Fig. 4.2. The temperature was kept using two silicon heaters glued to the MSR-C/HT-PEMFC and controlled by a Eurotherm 3016 PID controller. The MSR-C/HT-PEMFC was covered with glass wool and aluminium foil for a good thermal insulation.

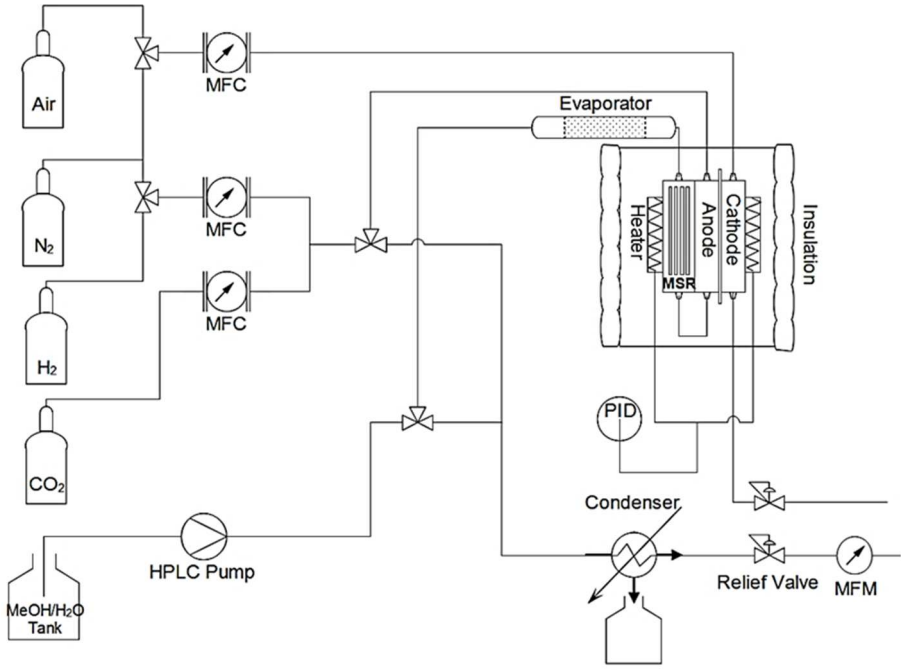


**Fig. 4.2** Scheme of the experimental unit used for the MSR-C/HT-PEMFC characterization.

Mass flow controllers from Bronkhorst were used to control the gases flow rate, while the operating pressure was adjusted using relief valves. The water/methanol mixture with a molar steam to carbon ratio (S/C) of 1.5 was pumped using an HPLC pump (Knaur Smartline 1050). The evaporation was carried in a tubular device filled with glass beads to homogenize the temperature and controlled by a Eurotherm 3016 PID controller. At the outlet of the anode, the stream passed through a condenser (based in Peltier

element) to remove the condensable components; the flow of the non-condensable species was measured using a mass flow meter from Bronkhorst.

The system was controlled using an application developed in LabView [36] (National Instruments) and the electrochemical tests were performed using a Zahner IM6e electrochemical workstation coupled with a potentiostat PP-241.

*MSR-C/HT-PEMFC characterization*

The fuel cell was placed in an oven at RT and the temperature set to 453 K. The MEAs were activated accordingly to the specifications of the supplier, at open circuit voltage until the cell reached 393 K and at constant 0.20 $A \cdot cm^{-2}$ until 453 K, with air stoichiometry ($\lambda_{Air}$) of 2 and hydrogen stoichiometry ($\lambda_{H2}$) of 1.2. The cell was kept under these conditions during *ca.* 14 h. While activating the MEA, the reformer catalyst was also activated using excess hydrogen from the anode outlet.

The MEAs were characterized using an air stoichiometry ($\lambda_{Air}$) of 2 and hydrogen stoichiometry ($\lambda_{H2}$) of 1.2. When reformate was used as fuel, the water/methanol flow rates were adjusted according to the fuel cell current density and they were established based on the hydrogen production observed for fresh reforming catalyst, as depicted in Table 4.1. For current densities above 0.2 $A \cdot cm^{-2}$ the $\lambda_{H2}$ was not possible to maintain at 1.2, without introducing high amounts of non-reacted methanol in the FC.

**Table 4.1** Water/methanol flow rates used to feed the reformer at different current densities.

| HT-PEMFC current density ($A \cdot cm^{-2}$) | Water/methanol flowrate ($cm^3 \cdot min^{-1}$) |
|---|---|
| < 0.2 | 0.05 |
| 0.3 | 0.06 |
| 0.4 | 0.08 |
| 0.5 | 0.10 |

The experiments were performed at 453 K and 463 K using three MEAs, labelled from one to three. In the first experiment, using MEA1, the HT-PEMFC was fed with pure hydrogen, gas mixture with volume fractions of 75% $H_2$ and 25 % $CO_2$ and reformate supplied from the MSR. The reformate was feed in cycles of 7 h at constant 0.3 $A \cdot cm^{-2}$ and 453 K; between cycles (overnight) the fuel cell was fed with pure hydrogen and kept at

constant 0.2 A·cm$^{-2}$. In the second experiment, using MEA2, the fuel cell was continuously fed with reformate during 100 h, at constant 0.3 A·cm$^{-2}$ and 453 K. In the third experiment, using MEA3, the temperature of the MSR-C/HT-PEMFC was increased to 463 K and the same procedure of the second experiment was followed. The Advent TPS® MEAs were characterized by polarization curves and electrochemical impedance spectroscopy (EIS). Polarization curves were obtained galvanostatically between 0.05 A·cm$^{-2}$ and 0.6 A·cm$^{-2}$. EIS were obtained between 100 kHz and 100 mHz with a perturbation amplitude of 5 mV. The impedance data was fitted to an equivalent circuit (EC) model (Fig. 4.3) [36, 37]. The two first parallel RC circuits connected in series represent the rate determining processes at the anode ($R_{ct,a}$, $CPE_a$) and cathode ($R_{ct,c}$, $CPE_c$); $R_{ct,a}$ and $R_{ct,c}$ corresponds the charge transfer resistance between electrode and electrolyte at the anode and at the cathode sides, respectively, whereas $CPE_a$ and $CPE_c$ are constant phase elements. The two RC circuits are connected by an ohmic resistance, $R_{ohmic}$, representing the ohmic losses at the electrolyte. The third parallel RC circuit ($R_N$, $C_N$) represents the limitations in the mass transport processes (finite diffusion limitations), where $R_N$ is a resistance and $C_N$ is a capacitor. One coil or inductive element ($L$) was added to describe the inductance of the EIS equipment cables.

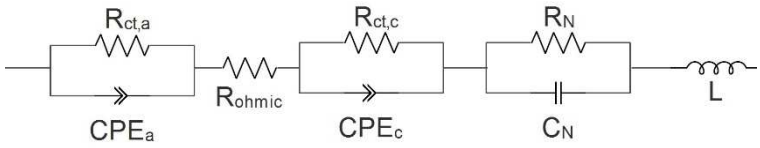


**Fig. 4.3** Fuel cell equivalent circuit model used in the analysis of the impedance data.

Besides the electrochemical characterization, titrations were performed to determine the phosphoric acid content in different sections of the MEA. The samples were cut with a mallet handle die, delaminated and placed in a glass beaker containing a 2-propanone solution. The solution was stirred using magnetic stirrer for at least 30 min and then titrated with sodium hydroxide solution.

The performance of the reformer was assessed at two instants, immediately after the catalyst activation (hereafter referred as fresh catalyst) and after having concluded the MEA characterization (hereafter referred as aged catalyst); the methanol conversion was determined measuring the mass flow of the reformate stream without the condensable components.

## 4.4. Results and Discussion

### 4.4.1. Cellular reformer performance

The bipolar plate side containing the MSR was designed taking into account several aspects such heat and mass transport, pressure drop, flow-pattern and reactor volume as an effort to approach to an ideal plug flow reactor operated at isothermal conditions. The performance of the reformer was assessed for fresh catalyst and after the electrochemical characterization tests, here addressed as aged catalyst, as depicted in Fig. 4.4.

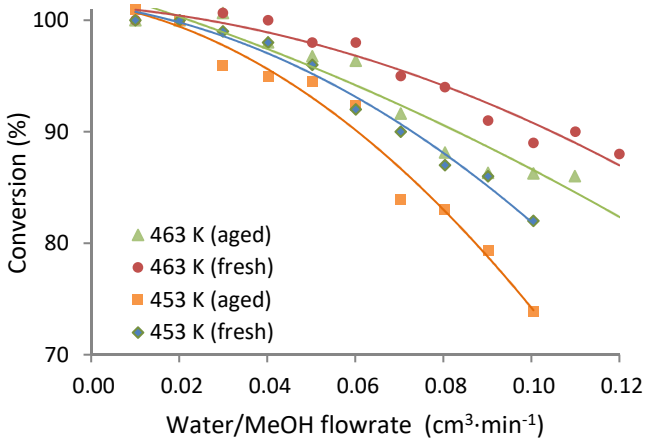


**Fig. 4.4** Methanol conversion as function of feed flow rate at different temperatures, for fresh catalyst and for aged catalyst; solid lines were added for readability.

For the water/methanol flow rate of 0.06 $cm^3 \cdot min^{-1}$ ($m_{cat}/F_{MeOH}$ =1170 $kg \cdot mol^{-1} \cdot s$) used in the stability tests for MEA2 and MEA3, the methanol conversion in the beginning of the experiments was 92 % and 98 % at 453 K and 463 K, respectively. Typically, full methanol conversion is achieved at 453 K at steady state for space-time ratios of *ca.* 1000 $kg \cdot mol^{-1} \cdot s$ [35] using a differential reactor loaded with the commercial catalyst. Therefore, higher conversions would be expected for the studied reformer. A non-uniform flow distribution among the channels could be pointed out as the reason for the low performance of the reformer in general. Noteworthy, the reformer, after the experiments was opened and examined; the catalyst bed was perfectly filled and no drag or preferential flow paths were observed. The decrease in the performance after several

hours of operation, at both operating temperatures (453 K and 463 K) was associated to the typical catalyst deactivation. Copper based commercial catalysts normally present an initial loss in activity of *ca.* 20 %, before reaching steady state, which occurs after a few hours of time-on-stream [9]. In this work, the CO content was not determined, since CO production at the operation temperatures considered is lower than 2000 ppm [35] and should not affect the HT-PEMFC performance [21].

High current densities require high hydrogen-feed flow rates leading to low methanol conversions. Fig. 4.5 relates the current density and the methanol conversion with the hydrogen flow rate (hydrogen produced and the required to feed the 25 $cm^2$ HT-PEMFC with a $\lambda_{H2}$ of 1). As shown in Fig. 4.5, for current densities above 0.3 $A \cdot cm^{-2}$ and operating temperature of 453 K the reformer is not able to produce a reformate stream with a methanol conversion above 90 %. Considering that the polarization curves were obtained galvanostatically between 0.05 $A \cdot cm^{-2}$ and 0.6 $A \cdot cm^{-2}$, significant amounts of non-reacted methanol was present in the reformate stream and fed to the fuel cell. The low conversions and consequently the low hydrogen flow rates observed for "aged" catalyst influences the PEMFC performance as it will be discussed later.

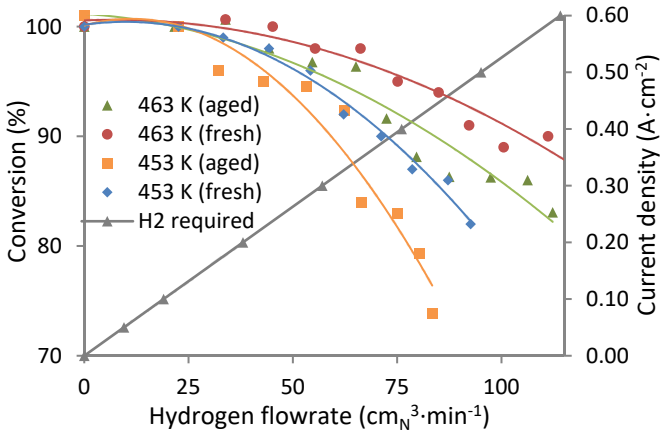


**Fig. 4.5** Methanol conversion (left axis) and current density (right axis) versus hydrogen flow rate at different temperatures; solid lines were added for readability.

### 4.4.2. Fuel cell performance

*I-V Curves*

The integrated MSR-C/HT-PEMFC device was examined immediately after the catalyst and MEA activations. Fig. 4.6 shows the polarization curve of MEA1 at 453 K with pure hydrogen (used as reference), $H_2/CO_2$ mixture and reformate as fuels. After the 10$^{th}$ cycle with reformate, at constant 0.3 A cm$^{-2}$, MEA1 was characterized with reformate (final reformate) and it was left stabilizing overnight at 0.2 A.cm$^{-2}$ with pure hydrogen. MEA1 was characterized in the day after with pure hydrogen ($H_2$ after 10$^{th}$ cycle) to assess the fuel cell performance degradation. MEA1 showed lower initial performance when compared with other commercial MEAs based on phosphoric acid doped PBI membrane, with pure hydrogen as fuel [26]. Despite the low performance at temperature 453 K, MEAs from Advent TPS® promise to be more stable at higher temperatures (453 to 473 K) [38]. Switching the anode feed from pure hydrogen to the $H_2/CO_2$ mixture decreased the fuel cell performance, mainly due to hydrogen dilution; this effect is more noticeable at high current densities, *e.g.* the electric potential difference ($\Delta V$) at 0.5 A·cm$^{-2}$ decreased 9 % (30 mV). Switching from $H_2/CO_2$ mixture to reformate produced by the MSR showed a further decrease in the fuel cell performance, once again more expressive for higher current densities. This behaviour was assigned to the higher hydrogen dilution due to presence of water vapour, unreacted methanol and $CO_2$ and, due to the presence of CO. Despite the lower performance with reformate as fuel, the integrated MSR-C/HT-PEMFC was capable to produce a current density of 0.5 A·cm$^{-2}$ for a potential difference of 0.323 V. Pan *et al.* reported a current density of 0.1 A·cm$^{-2}$ for a potential difference of *ca.* 0.25 V using integrated MSR/HT-PEMFC at 453 K [21]. Avgouropoulos *et al.,* on the other hand, reached a maximum current density of 0.25 A·cm$^{-2}$ for a potential difference of *ca.* 0.45 V at 483 K, by incorporating the methanol reforming catalyst in the HT-PEMFC anodic compartment (internal reforming) [24].

From the intermediate measurements using pure hydrogen as a feed, the performance degradation with the increasing number of reformate cycles can be observed (Fig. 4.6). The potential difference of the FC fed with pure hydrogen after 10 cycles dropped of 9 % (44 mV) and 21 % (75 mV) at 0.3 A·cm$^{-2}$ and 0.5 A·cm$^{-2}$, respectively, when compared to the values obtained after activation; while the potential difference of the FC fed with reformate after 10 cycles dropped 17 % (83 mV) and 41 % (149 mV) at

0.3 A·cm$^{-2}$ and 0.5 A·cm$^{-2}$, respectively. The low performance of the fuel cell with the reformate is explained by the low quality of the reformate stream at the end of the experiments, providing a low hydrogen stoichiometry and having high concentrations of unreacted methanol, additionally to the permanent degradation of the MEA components (Fig. 4.5).

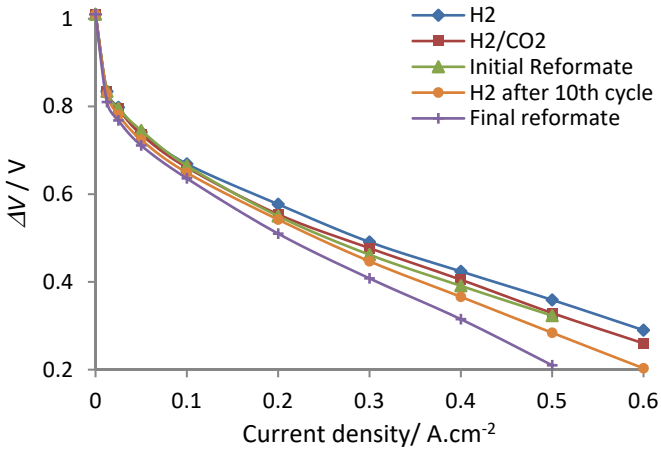


**Fig. 4.6** Polarization curves of MEA1 at 453 K with hydrogen, $H_2/CO_2$ mixture and the methanol reformate as fuel; solid lines were added for readability.

MEA2 was initially examined by polarization measurements at 453 K using pure hydrogen, $H_2/CO_2$ mixture and methanol reformate as fuels. After 100 h with continuous feed of reformate at a current density of 0.3 A·cm$^{-2}$, MEA2 was characterized with reformate (final reformate) and it was left stabilizing overnight at 0.2 A·cm$^{-2}$ with pure hydrogen. In the day after, MEA2 was characterized with pure hydrogen (final $H_2$) to assess the fuel cell performance degradation. When fresh, MEA2 showed $\Delta V$ = 607 mV with hydrogen at 0.2 A·cm$^{-2}$, while MEA1 has shown a $\Delta V$ of 577 mV. This difference in $\Delta V$ indicates that MEAs have not been activated at the same extent, despite the similar activation time. This aspect has already been reported in literature for commercial MEAs based on phosphoric acid doped PBI membranes [39, 40].

The initial effect of replacing pure hydrogen by the $H_2/CO_2$ mixture or by reformate is similar to the one observed previously for MEA1. The operation of the HT-PEMFC during 100 h with reformate as fuel, led to a decrease in the performance (Fig. 4.7). The $\Delta V$, when pure hydrogen is used as fuel, decreased 13 % (66 mV) and 31% (110 mV) at

0.3 A·cm$^{-2}$ and 0.5 A·cm$^{-2}$, respectively, while the $\Delta V$ with reformate decreased 17 % (66 mV) and 60 % (213 mV) at 0.3 A·cm$^{-2}$ and 0.5 A·cm$^{-2}$. The low performance of the HT-PEMFC with hydrogen as fuel (final $H_2$) indicates a permanent degradation of the MEA, caused by the low methanol conversion observed in the reformer, at the end of the experiments.

MEA2 shows a higher drop in the performance, after 100 h of operation with reformate as fuel, than MEA1, after 10 cycles with reformate. These 10 cycles correspond actually to *ca.* 70 h of operation with reformate for a total of *ca.* 250 h; the lower performance degradation of MEA1 was then assigned to the shorter contact time with the reformate, since the performance of a HT-PEMFC is negatively affected by the time of operation in the presence of methanol and by the concentration of methanol [26, 40].

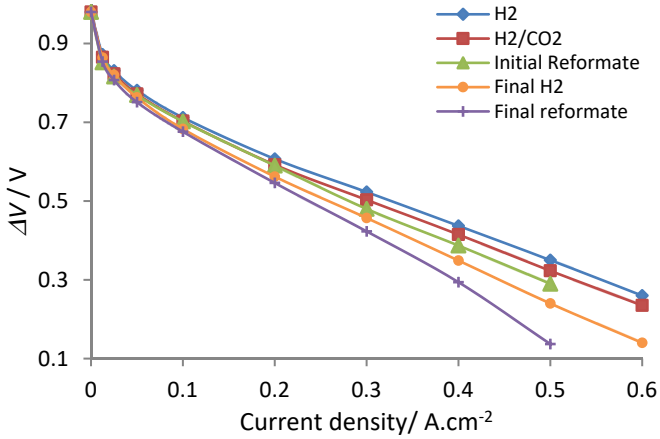


**Fig. 4.7** Polarization curve of MEA2 at 453 K with pure hydrogen, $H_2/CO_2$ mixture and the methanol reformate as fuel; solid lines were added for readability.

No significant differences in the performance of MSR catalyst before and after the electrochemical characterization of MEA1 and MEA2, was observed. MEA1 was also left overnight with pure hydrogen at 0.2 A·cm$^{-2}$ which allowed the MEA to recover and to stabilise, as reported by Boaventura *et al.* [40].

MEA3 was tested at 463 K in similar conditions of MEA2. Fig. 4.8 shows the polarization curve of MEA3 at 463 K with pure hydrogen, the $H_2/CO_2$ mixture and the methanol reformate as fuels. The initial performance of MEA3 with pure hydrogen was better

than MEA1 and MEA2 (Fig. 4.8), as expected, due to improvement of electrochemical kinetics with temperature.

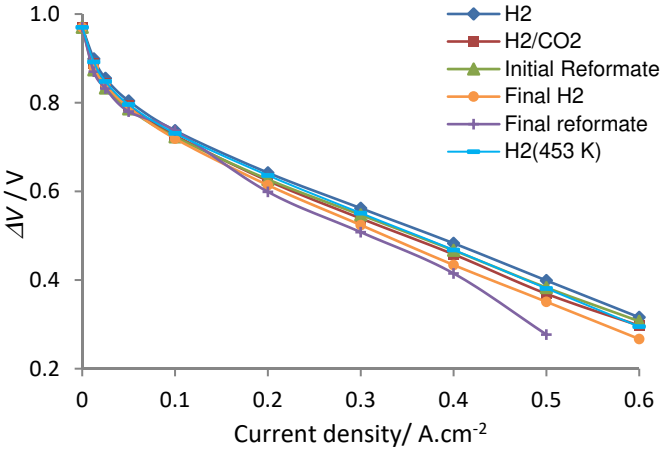


**Fig. 4.8** Polarization curve of MEA3 at 463 K with pure hydrogen, $H_2/CO_2$ mixture and the methanol reformate as fuel; solid lines were added for better readability.

The polarization curves with the $H_2/CO_2$ mixture show 8 % (30 mV) less energy efficiency at 0.5 A·cm$^{-2}$ when compared to hydrogen, similar to the previous MEAs. The initial polarization curve with reformate as fuel shows a slightly better performance than the obtained with the $H_2/CO_2$ mixture, presenting an energy efficiency decrease of only 4 % (15 mV) at 0.5 A·cm$^{-2}$, compared with hydrogen. High operating temperature favours both the methanol reforming conversion and electrochemical kinetics. At 463 K the methanol conversion for fresh catalyst was always higher than 90 % for the range flow rates used, thus low methanol content was present in the reformate. The small improvement obtained with reformate compared to the $H_2/CO_2$ mixture could be related to an increase in the protonic conductivity due to water presence, since it can represent a volume fraction of *ca.* 10 %. In the case of the previous MEAs, when fed with reformate, their performance was lower than with the $H_2/CO_2$ mixture; at 453 K the reformate has a higher concentration of methanol (Fig. 4.8). The performance of MEA3 with reformate, after 100 h of aging, shows a small loss of efficiency than the other MEAs (e.g. $\Delta V$ loss of 7 % (28 mV) and 12 % (48 mV) respectively at 0.3 A·cm$^{-2}$ and 0.5 A·cm$^{-2}$ with hydrogen as fuel). However, for current densities above 0.3 A·cm$^{-2}$, it is clear the inability of the reformer to provide the required hydrogen flow rate.

*Stability analysis*

Fig. 4.9 shows the electric potential difference history for MEA1 when supplied with reformate as fuel and for a current density of 0.3 A·cm$^{-2}$. The experiment was carried during 250 h, but only 70 h on-stream with reformate resulting in $\Delta V$ variation rate of 0.77 mV·h$^{-1}$ at 0.3 A·cm$^{-2}$ for the time with reformate as fuel. Between cycles the fuel cell was left overnight at 0.2 A·cm$^{-2}$ with pure hydrogen allowing the fuel cell to recover flushing out the water and methanol partially recovering the potential difference. Despite this fact, the performance degradation was higher than the reported by Avgouropoulos *et al.* [23]; using the same type of MEAs, they found a degradation rate of 0.15 mV·h$^{-1}$ at 0.2 A·cm$^{-2}$ and 473 K under H2/air feed and after 170 h of steady operation. Water vapour and methanol interact strongly with $H_3PO_4$, permeating from the anode to the cathode side [23, 41]; the presence of methanol in the electrolyte makes the proton conductivity to decrease. The major pathway for the performance degradation of the MEA, however relates to the adsorption of methanol on the anode and cathode catalyst [26, 40].

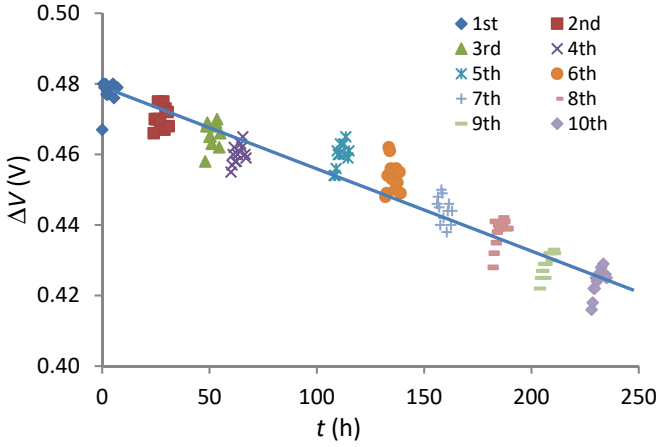


**Fig. 4.9** Electric potential difference history for MEA1 at 0.3 A·cm-2 with reformate as fuel.

The $\Delta V$ variation rate history at 0.3 A·cm$^{-2}$, for MEA2 and MEA3, with reformate as fuel is depicted in Fig. 4.10. MEA3 shows the lowest degradation among the MEAs tested, with a $\Delta V$ variation rate of 0.39 mV·h$^{-1}$ at 0.3 A·cm$^{-2}$, while MEA2, in the other hand, has a $\Delta V$ variation rate of 0.57 mV·h$^{-1}$, at the same current density. The lowest

degradation of MEA3, should be assigned to low methanol content in the reformate stream, due to the highest operating temperature.

The presented results for the Advent MEAs are far from the reported in literature for long-term stability tests of PBI based MEAs, with a $\Delta V$ variation rate of 5 $\mu V \cdot h^{-1}$, at 0.2 $A \cdot cm^{-2}$ with hydrogen at 423 K– 433 K [8]. Considering a synthetic reformate stream with a water volume fraction of 2.5 % and a methanol content of 2.5 %, Araya *et al.* [26] reported a degradation rate of 0.9 $mV \cdot h^{-1}$. MEA2 was tested during 100 h at 453 K with a reformate stream with 90 % of methanol converted, which corresponds to a water volume content of 14.0 % and a methanol content of 2.3 %; this reformate has a methanol content similar to the synthetic reformate reported by Araya and co-authors.

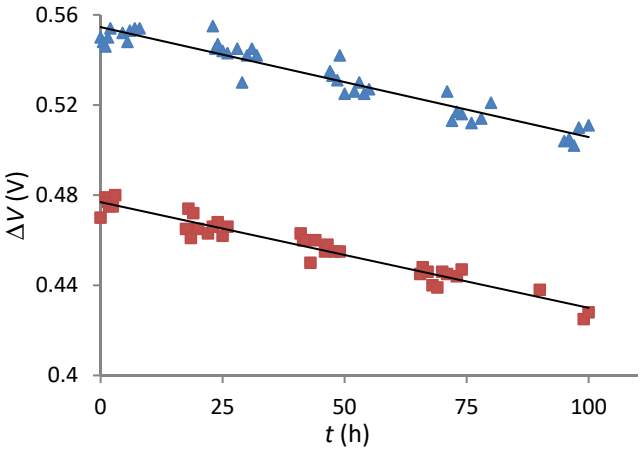


**Fig. 4.10** Electric potential difference variation with time for MEA2 (■) and MEA3 (▲) at 0.3 $A \cdot cm^{-2}$ with reformate as fuel.

*EIS analysis*

To understand the origin of voltage loss and the irreversible degradation, EIS analysis was performed. Fig. 4.11a shows the Nyquist plot for MEA1 at 453 K and 0.3 $A \cdot cm^{-2}$, fed with hydrogen, $H_2/CO_2$ mixture and reformate, obtained after activation and after the 10 cycles with reformate. Alongside, Fig. 4.11b shows the resistances history of the fuel cell equivalent circuit model (Fig. 4.3) when fed with hydrogen and reformate. A small effect is observed when the fuel is changed from hydrogen to the $H_2/CO_2$ mixture (Fig. 4.11a) in whole frequency range, with a slight increase in the ohmic resistance (interception of the Nyquist plot with the real axis). With reformate as fuel a decrease in

the ohmic resistance is observed. This fact was assigned to the presence of water vapour, which enhances the proton conduction in PBI-based polymer electrolytes [41]. The ohmic resistance, ($R_{ohmic}$) is 0.39 $\Omega \cdot cm^2$ in the presence of hydrogen, while in the presence of the reformate stream is equal to 0.36 $\Omega \cdot cm^2$. After the 10 cycles with reformate the $R_{ohmic}$ increases and once again is smaller with reformate than with hydrogen as fuel. The $R_{ohmic}$ along the cycles is also observed in the Fig. 4.11b; suggesting a permanent loss of the proton conductivity. In fact, methanol as a polar molecule can create stronger hydrogen bonds with the $H_3PO_4$/polymer matrix reducing the phosphoric acid available for proton conduction.

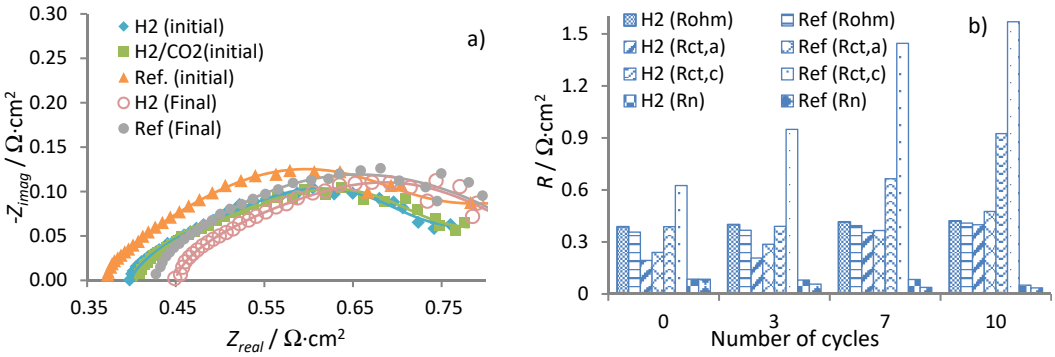


**Fig. 4.11** Impedance analysis of MEA1 at 0.3 A·cm-2; a) Nyquist spectra before and after 10 cycles with reformate (the lines represent de modelling results); b) evolution of the resistances along the reformate cycle.

The high frequency resistance, normally attributed to the electrochemical reaction resistance at the anode ($R_{ct,a}$) increases along the cycles, showing a slight decrease when the feed was changed from reformate to pure hydrogen. This activity decrease was assigned to the methanol adsorption on the catalyst and consequent formation of CO [42, 43], that leads to an increase of the anode overpotencial and then to a drop on the fuel cell efficiency. Besides, the reformate stream has lower hydrogen partial pressure, which also contributes for a higher $R_{ct,a}$. The intermediate frequency resistance, normally attributed to the electrochemical reaction resistance at the cathode ($R_{ct,c}$) had a high increased along the cycles and showed to be intrinsically related to the MEA degradation; a significant increase in the $R_{ct,c}$ was always observed when the fed was changed from

pure hydrogen to reformate. Methanol crossover was observed for this type of membrane [23]; since the methanol oxidation in the presence of oxygen is catalysed by platinum nanoparticles, the methanol oxidation will compete with electrochemical reaction for the catalyst active sites. Therefore, the increase of $R_{ct,c}$ immediately after the activation of MEA1, when the feed was changed from hydrogen to the reformate stream, should be assigned to the decrease of the catalyst active area due to methanol crossover. The low frequency resistance, $R_N$, normally attributed to the mass transport resistance, shows a slight decrease along the cycles with lower resistance value when the reformate stream was used as fuel. Although due to strong instability of the spectra in this region, no further analysis can be made.

Fig. 4.12a-b show the Nyquist plots for the operation of MSR-C/HT-PEMFC device at 453 K (MEA2) and 463 K (MEA3), both at 0.3 A·cm$^{-2}$, under hydrogen, the $H_2/CO_2$ mixture and the reformate feed. Fig. 4.12c-f show the resistances history of the fuel cell equivalent circuit during the 100 h of operation with reformate as fuel. The resistances were also determined for hydrogen as fuel before and after the 100 h of continuous operation. The ohmic resistance of MEA2 is higher than MEA3, independently of the anode fuel (Fig. 4.12a-c). In fact, $R_{ohm}$ decreases with temperature due to the higher mobility of protons [44] and increases along the reformate aging time. Like in the case of MEA1, after the aging period $R_{ohmic}$ decreases when hydrogen feed is switched to reformate. The anode resistance increases when hydrogen feed is switched to reformate (Fig. 4.12d), due to reduction of the catalyst active area and to lower hydrogen partial pressure, as mentioned before. The low $R_{ct,a}$ of MEA3 was assigned to the higher temperature, which increases the electrochemical reaction rate and reformer performance, producing a reformate stream with higher concentration of hydrogen and lower concentration of methanol. Oxygen reduction (cathode) is the limiting electrode reaction; as a result the methanol crossover from the anode to the cathode is likely to have a significant effect on $R_{ct,c}$, as it is observed for MEA2 immediately after the first hours of operation with reformate (Fig. 4.12d,e). No significant increase of $R_{ct,c}$ is observed in MEA3 along the 100 h of aging period, as a consequence of the high methanol conversion obtained with the reformer operating at 463 K; after the aging period, $R_{ct,c}$ values obtained with the reformate and hydrogen are very close. The high operating temperature of MEA3 increase the electrochemical reaction rate and reformer conversion, resulting in

the lowest $R_{ct,c}$ observed among the three MEAs. $R_N$ of both MEAs have almost the same value fresh and after the 100 h aging period with the reformate.

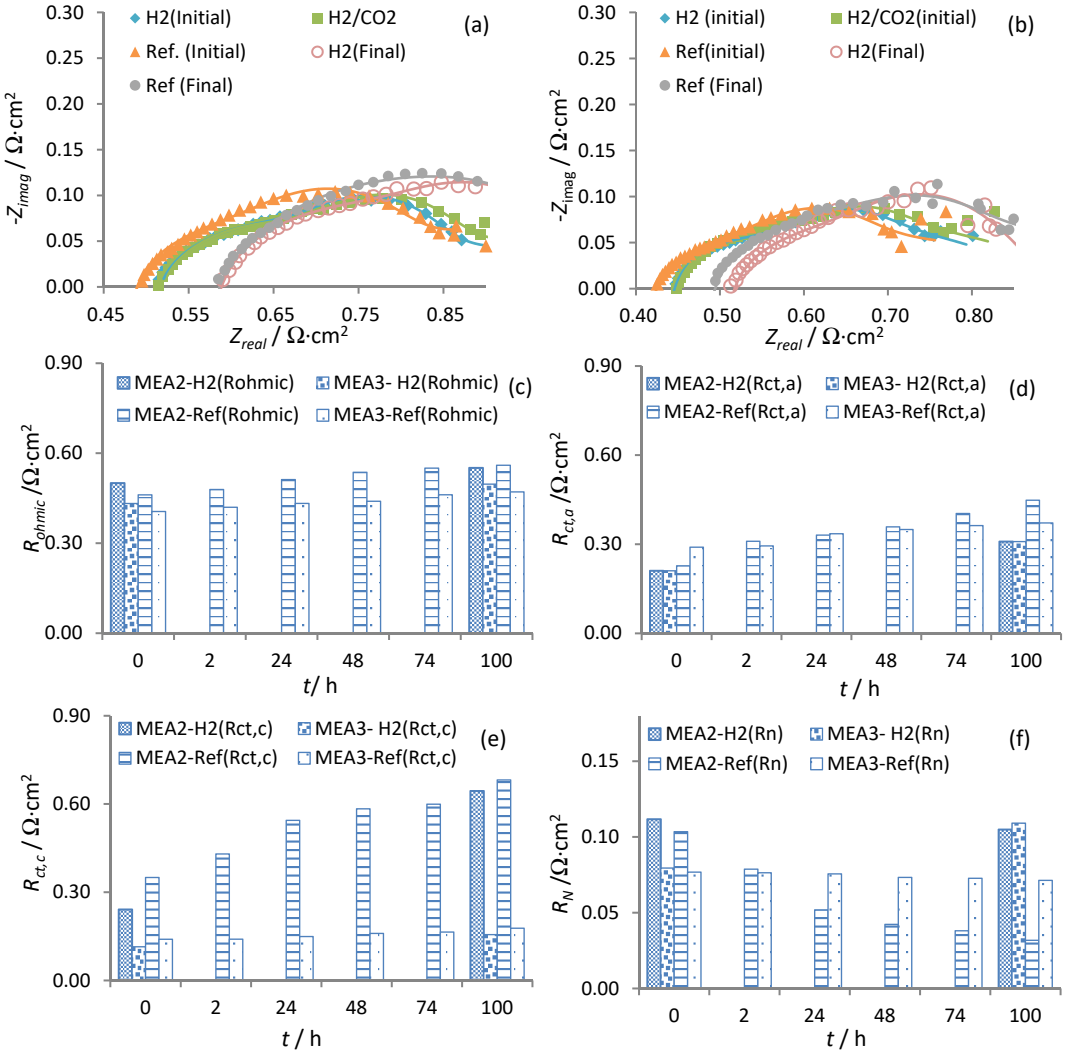


**Fig. 4.12** Nyquist spectra of MEA2 (a) and MEA3 (b) before and after the aging period with reformate (the lines represent the model); history of ohmic (c), anode (d), cathode (e) and mass transport (f) resistances with reformate as fuel.

### 4.4.3. Titrations

The phosphoric acid (PA) content at different zones in the studied MEAs was obtained – Fig.4.13. The reference value was obtained as the average over all position of a fresh MEA. Anode and cathode feeds were supplied in counter-current – Fig.4.1. The PA content in the MEAs decreased after the aging period, *ca.* 25 % at the cathode inlet and anode outlet zones. Comparing the studied three aged MEAs, MEA1 shows the lowest PA contents that should be assigned to the longer operating time. The operating temperature, 453 K and 463 K, displays no significant role on the PA depletion. PA leaching is more likely to occur during the start/stop events, when condensed liquid water is formed. However, the MEAs in this work were not submitted to temperature cycles and then PA leaching should not be considered.

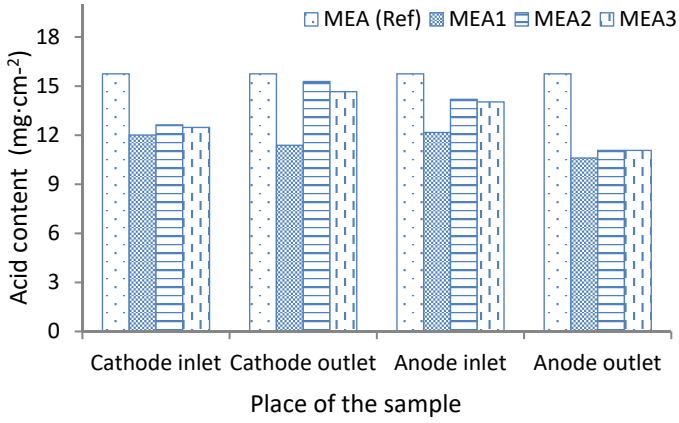


**Fig. 4.13** Phosphoric acid content at different zones of the reference and aged MEAs.

### 4.4.4. Thermal sustainability

The heat integration between a MSR and HT-PEMFC and the operation of both devices at the same temperature can increase the overall energy efficiency by more than ten percentage points [45]. Moreover, operating at the same temperature increases the simplicity of PEMFC systems. Fig. 4.14 shows the heating power supplied to the MSR-C/HT-PEMFC integrated device required to maintain the temperature constant. The integrated device was covered with a 0.5 cm thick sheet of glass wool; however, a loss of

*ca*. 56 W was observed when the MSR-C/HT-PEMFC was operated at 453 K. As the fuel cell loading increases, it generates more wasted heat, but even at the highest current density allowed by the reformer (0.5 A·cm$^{-2}$), the fuel cell was not able to cover the loss of heat through the thermal insulation. A better insulation was required to achieve the thermal equilibrium, made namely of materials such as silicon rubber or armaflex® capable to fit to the shape of the MSR-C/HT-PEMFC device. In a stack of fuel cells and cellular reformers, and with a better thermal insulation, it would expected that the fuel cell covers the heat needs for current densities of *ca.* 0.15 A·cm$^{-2}$. Despite, the thermal integration of a MSR and HT-PEMFC could represent a significant improvement in the overall efficiency of the device; commercial MSR catalysts require higher catalytic activity, without limiting the fuel cell operation to low current densities.

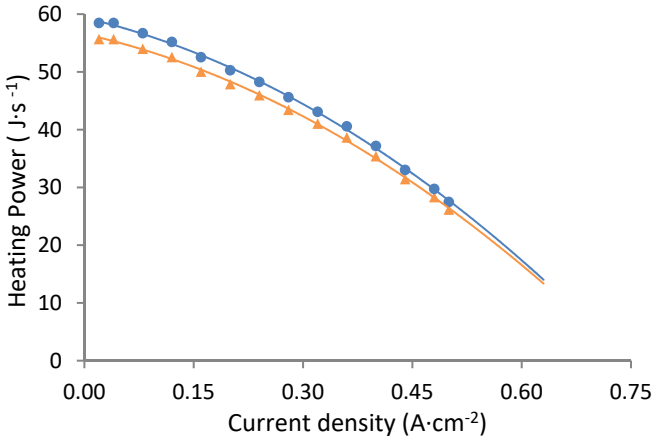


**Fig. 4.14** Heating power as function of the FC current density at 453 K (▲) and 463 K (●).

## 4.5. Conclusions

A new combined MSC-C/HT-PEMFC, featuring the fuel cell anode flow field in one side and the reformer flow field in the other, was built and assessed within a temperature range of 453 K and 463 K. High current densities (>0.5 A·cm$^{-2}$), with the combined reactor running at 453 K, are reported for the first time. The initial maximum power density delivered by the MSC/HT-PEMFC system at 453 K was only slightly lower (30 mV) than when hydrogen is fed directly to the HT-PEMFC. These results demonstrate that a

MSR and HT-PEMFC can operate at the same temperatures producing high current densities.

After several hours of operation, the degradation of the MEA was noticeable, both at 453 K than at 463 K, because of the low methanol conversion (<99 %). Electrochemical impedance spectroscopy (EIS) analysis showed a decrease in the ohmic resistance when the anode fuel was switched from hydrogen to reformate. It is known that the presence of water vapour can enhanced the proton conduction in PBI-based polymer electrolytes [41]. The anode resistance increased with reformate as fuel, due to the catalyst active decrease and lower hydrogen partial pressure. The cathode resistance increased with reformate as fuel, due to the methanol crossover from the anode to the cathode, especially at lower temperatures where the methanol conversion was also lower.

The self-thermal sustainability of the combined device was only reached for > 0.75 $A \cdot cm^{-2}$ due to the poor thermal insulation of the combined reactor. The heat integration of MSC/HT-PEMFC in a stack arrangement is currently under investigation.

## 4.6. References

[1] M. Díaz, A. Iranzo, F. Rosa, F. Isorna, E. López, J. Bolivar, Effect of carbon dioxide on the contamination of low temperature and high temperature PEM (polymer electrolyte membrane) fuel cells. Influence of temperature, relative humidity and analysis of regeneration processes, Energy 90 (2015) 299–309

[2] J.T. Wang, R. F. Savinell, J. Wainright, M. Litt, H. Yu, A H2/O2 fuel cell using acid doped polybenzimidazole as polymer electrolyte, Electrochimica Acta, 41, (1996), 193–197.

[3] J.S. Wainright, J.T. Wang, D. Weng, R.F. Savinell, M. Litt, Acid-Doped Polybenzimidazoles: A New Polymer Electrolyte, Journal of the Electrochemical Society, 142 (1995) 121–123.

[4] J. Mader, L. Xiao, T.J. Schmidt, B.C. Benicewicz, Polybenzimidazole/Acid Complexes as High-Temperature Membranes. In Fuel Cells II; Scherer, G. G., Ed.; Advances in Polymer Science, 216; Springer-Verlag: Berlin, Germany, 2008; pp 63–124.

[5] G. Elden, M. Çelik, G. Genç, H. Yapıcı, The effects of temperature on transport phenomena in phosphoric acid doped polybenzimidazole polymer electrolyte membrane fuel cell Energy, 103, 2016, 772-783

[6] P. Genova-Dimitrova, B. Baradie, D. Foscallo, .Poinsignon, J.Y. Sanchez, Ionomeric membranes for proton exchange membrane fuel cell (PEMFC): sulfonated polysulfone associated with phosphatoantimonic acid Journal of Membrane Science 185 (2001) 59

[7] A. Iulianelli, A. Basile, Sulfonated PEEK-based polymers in PEMFC and DMFC applications: a review, International Journal of Hydrogen Energy, 37 (2012) 15241-1525.

[8] Q. Li, R. He, J. Jensen, Bjerrum, PBI-based polymer membranes for high temperature fuel cells – preparation, characterization and fuel cell demonstration, Fuel Cells 4(3) (2004) 147-159.

[9] A. Iulianelli, P. Ribeirinha, A. Mendes, A. Basile, Methanol steam reforming for hydrogen generation via conventional and membrane reactors: A review Renewable and Sustainable Energy Reviews, 29 (2014) 355–368.

[10] S. Authayanun, D.Saebea, Y. Patcharavorachot, A. Arpornwichanop, Effect of different fuel options on performance of high-temperature PEMFC (proton exchange membrane fuel cell) systems, Energy 68 (2014) 989–997.

[11] S. Cordiner, M. Feola, V. Mulone, F. Romanelli, Analysis of a SOFC energy generation system fuelled with biomass reformate, Applied Thermal Engineering, 27 (4), 2007, 738-747

[12] M. Yari, A. S. Mehr, S. M. S. Mahmoudi, M. Santarelli, A comparative study of two SOFC based cogeneration systems fed by municipal solid waste by means of either the gasifier or digester, Energy, 114, 2016, 586-602

[13] S. Eom, S. Ahn, Y. Rhie, K.Kang, Y. Sung, C. Moon, G.Choi, D.l Kim, Influence of devolatilized gases composition from raw coal fuel in the lab scale DCFC (direct carbon fuel cell) system, Energy, 74, 2014, 734-740

[14] V. Liso, A. C. Olesen, M. P. Nielsen, S.K. Kær, Performance comparison between partial oxidation and methane steam reforming processes for solid oxide fuel cell (SOFC) micro combined heat and power (CHP) system, Energy, 36(7), 2011, 4216-4226

[15] [access date August 2015], http://www.ultracell-llc.com/assets/UltraCell_BT-press-release-Feb-20-2015-FINAL.pdf

[16] S. Andreasen, S. Kær, S. Sahlin, Control and experimental characterization of a methanol reformer for a 350W high temperature polymer electrolyte membrane fuel cell system, International Journal of Hydrogen Energy 38 (2013) 1676–84.
[17] N.W. Deluca, Y.A Elabd., Polymer electrolyte membranes for the direct methanol fuel cell: a review, Journal of Polymer Science: Polymer Physics, 44 (2006) 2201-2225.
[18] W.F. Lin, J.T. Wang, R.F. Savinell, On-line FTIR spectroscopic investigations of methanol oxidation in a direct methanol fuel cell Journal of the Electrochemical Society, 144 (1997) 1917-1922.
[19] J.T. Wang, J.S. Wainright, R.F. Savinell, M. Litt, A direct methanol fuel cell using acid-doped polybenzimidazole as polymer electrolyte, Journal of Applied Electrochemistry, 26 (1996) 751-756.
[20] J.T. Wang, S. Wasmus, R.F. Savinell, Real-Time Mass Spectrometric Study of the Methanol Crossover in a Direct Methanol Fuel Cell, Journal of the Electrochemical Society, 143 (1996) 1233-1239.
[21] C. Pan, R.H. He, Q.F. Li, J.O. Jensen, N.J. Bjerrum, H.A. Hjulmand, A.B. Jensen, Integration of high temperature PEM fuel cells with a methanol reformer, Journal of Power Sources, 145 (2005) 392-398.
[22] G. Avgouropoulos, T. Ioannides, J.K. Kallitsis, S. Neophytides, Development of an internal reforming alcohol fuel cell: Concept, challenges and opportunities Chemical Engineering Journal, 176 (2011) 95-101.
[23] G. Avgouropoulos, S. Neophytides, Performance of internal reforming methanol fuel cell under various methanol/water concentrations, Journal of Applied Electrochemistry, 42 (2012) 719–726.
[24] G. Avgouropoulos, A. Paxinou, S. Neophytides, In situ hydrogen utilization in an internal reforming methanol fuel cell International Journal of Hydrogen Energy, 39 (2014) 18103-18108.
[25] T. Iwasita, Electrocatalysis of methanol oxidation, Electrochimica Acta , 47 (2002) 3663-3674.
[26] S.S. Araya, S.J. Andreasen, H.V. Nielsen, S.K. Kaer, Investigating the effects of methanol-water vapor mixture on a PBI-based high temperature PEM fuel cell, International Journal of Hydrogen Energy, 37 (2012) 18231-18242.
[27] S.K. Das, A. Reis, K.J. Berry, Experimental evaluation of CO poisoning on the performance of a high temperature proton exchange membrane fuel cell, Journal Power Sources, 193 (2009) 691-698.
[28] George Bandlamudi, Systematic characterization of HT PEMFCs Containing PBI/H3PO4 systems. Thermodynamic analysis and Experimental investigations, Logos Verlad Berlin GmbH, 2011
[29] F.A. de Bruijn, D.C. Papageorgopoulos, E.F. Sitters, G.J.M. Janssen, The influence of carbon dioxide on PEM fuel cell anodes. Journal Power Sources, 110 (2002) 117-124.
[30] M. A. Díaz, A. Iranzo, F. Rosa, F. Isorna, E. López, J. P. Bolivar, Effect of carbon dioxide on the contamination of low temperature and high temperature PEM (polymer electrolyte membrane) fuel cells. Influence of temperature, relative humidity and analysis of regeneration processes, Energy, 90, 2015, 299-309
[31] O. A. Velev, D.T. Tran, J.J. Kakwan, S. Gamburzev, F. Sinoneaux, S. Srinivasan Effect of bipolar plate materials on PEMFC performance, 19th Fall Meeting of the Electrochemical Society, San Antonio, TX, (1996), 101 (abstract)
[32] M. P. Brady, H. Wang, B. Yang, J.A. Turner, M. Bordignon, R. Molins, *et al.* Growth of Cr-nitrides on commercial Ni–Cr and Fe–Cr base alloys to protect PEMFC bipolar plates, International Journal of Hydrogen Energy, 32 (2007) 3778–3788.

[33] S. Radhakrishnan, B.T.S. Ramanujam, A. Adhikari, S. Sivaram, High-temperature, polymer-graphite hybrid composites for bipolar plates: effect of processing conditions on electrical properties, Journal of Power Sources, 163 (2007) 702–707.

[34] Li-gang Xia, Ai-ju Li, Wei-qiang Wang, Qiang Yin, Heng Lin, Yi-bo Zhao, Effects of resin content and preparing conditions on the properties of polyphenylene sulfide resin/graphite composite for bipolar plate 178(1) (2008) 363–367.

[35] P. Ribeirinha, M. Boaventura, J.C. Lopes, J.M. Sousa, A. Mendes, Study of different designs of methanol steam reformers: Experiment and modeling, International Journal of Hydrogen Energy. 39 (2014) 19970-19980.

[36] M. Boaventura, A. Mendes, Activation procedures characterization of MEA based on phosphoric acid doped PBI membranes, International Journal Hydrogen Energy, 35 (2010) 11649-11660.

[37] N. Wagner, T. Kaz, K.A. Friedrich Investigation of electrode composition of polymer fuel cells by electrochemical impedance spectroscopy Electrochimica Acta 53(25) (2008) 7475–7482.

[38] [access date december 2015], https://www.advent-energy.com/prod_ht_pem.aspx

[39] T. Tingelof, and J.K. Ihonen, A rapid break-in procedure for PBI fuel cells, International Journal of Hydrogen Energy, 34(15) 2009 6452-6456.

[40] M. Boaventura, I. Alves, P. Ribeirinha, A. Mendes, The influence of impurities in high temperature polymer electrolyte membrane fuel cells performance, International Journal of Hydrogen Energy, 41(43) 16 (2016) 19771-19780

[41] M.K. Daletou, J.K. Kallitsis, G. Voyiatzis, S.G. Neophytides, The interaction of water vapors with H3PO4 imbibed electrolyte based on PBI/polysulfone copolymer blends, Journal of Membrane Science, 326(1) (2009) 76–83.

[42] X. Zhao, M. Yin, L. Ma, L. Liang, C. Liu, J. Liao, T. Luc, W. Xing, Recent advances in catalysts for direct methanol fuel cells. Energy & Environmental Science, 4 (2011) 2736–2753.

[43] E. Christoffersen, P. Liu, A. Ruban, H.L. Skriver, J.K. Nørskov, Anode materials for low-temperature fuel cells: A density functional theory study, Journal of Catalysis, 199 (2001) 123–131.

[44] Q. Li, D. Aili, H.A Hjuler, J.O. Jensen, High Temperature Polymer Electrolyte Membrane Fuel Cells, Springer Switzerland (2016).

[45] A. Lotric, M. Sekavcnik, S. Hocevar Effectiveness of heat-integrated methanol steam reformer and polymer electrolyte membrane fuel cell stack systems for portable applications, Journal of Power Sources 270 (2014) 166-182

CHAPTER 4

# Chapter 5

# Integration of a reformer with a HT-PEMFC – Part B

## 5.1. Abstract

In this work an integrated unit, combining a methanol steam-reforming cell (MSR-C) and a high temperature polymer electrolyte membrane fuel cell (HT-PEMFC) was operated at the same temperature (453 K, 463 K and 473 K) allowing thermal integration and increasing the system efficiency of the combined system. A novel bipolar plate made of aluminium gold plated was built, featuring the fuel cell anode flow field in one side and the reformer flow field on the other. The combined unit (MSR-C/HT-PEMFC) was assembled using Celtec P2200N MEAs and commercial reforming catalyst $CuO/ZnO/Al_2O_3$ (BASF RP60). The water/methanol vaporisation originates oscillations in the vapour flowrate; reducing these oscillations increases the methanol conversion from 93 % to 96 %. The MSR-C/HT-PEMFC showed a remarkable high performance at 453 K. The integrated unit was operated during ca. 700 h at constant at 0.2 $A \cdot cm^{-2}$, fed alternately with hydrogen and reformate at 453 K and 463 K. Despite the high operating temperature, the HT-PEMFC showed a good stability, with an electric potential difference decreasing rate at 453 K of ca. 100 $\mu V \cdot h^{-1}$. Electrochemical impedance spectroscopy (EIS) analysis revealed an overall increase of the ohmic resistances and charge transfer resistances of the electrodes; this fact was assigned to phosphoric acid losses (electrodes and membrane) and growth of the catalyst particle size.

---

The content of this chapter is adapted from, P Ribeirinha, G Schuller, M Boaventura, A Mendes, Synergetic integration of a methanol steam reforming cell with a high temperature polymer electrolyte fuel cell, International Journal of Hydrogen Energy, 42(19) (2017) 13902-13912

## 5.2. Introduction

Polymer electrolyte membrane fuel cells (PEMFC) are an established technology. However, there are still a few obstacles to overcome for this technology to become competitive in the market of stationary and portable power sources. Hydrogen is the most suitable fuel for PEMFC applications but shows limitations regarding storage and transportation and has a very low volume energy density. Even pressurized at 800 bar, hydrogen has an energy density 1.8 times lower than methanol and 3.2 than octane (gasoline) [1]. Methanol can be used directly in PEMFC, but shows a low performance due to poor oxidation kinetics and methanol crossover from the anode to the cathode [2]. Methanol has a high hydrogen/carbon ratio and has no carbon-to-carbon bonds, which allows low-temperature steam reforming (513 K - 533 K), making it attractive for *in-situ* hydrogen production. Methanol steam reforming (MSR) is a more attractive reaction than auto-thermal reforming or partial oxidation due to higher hydrogen production and low CO content in the product stream.

PEMFCs based on polybenzimidazole (PBI) membranes doped with phosphoric acid operate at high temperatures, between 393 K and 453 K, displaying higher carbon monoxide tolerance (< 3000 ppm) when compared to PEMFC based on perfluorinated membranes (< 20 ppm) that operates at temperatures below 373 K. Commercial power supplies based on high temperature PEMFCs (HT-PEMFC) and fed with MSR reformate are presently available [3, 4]. The main challenge in this arrangement is the heat recovery, in order to maximize the overall efficiency. The heat released by a PEMFC is *ca.* 50 % of the input chemical energy, representing more energy than the heat required for fuel heating, vaporisation and reforming reaction, all combined. However, due to the mismatch on the operating temperature between the reformer (*ca.* 533 K) and the HT-PEMFC (*ca.* 433 K), the heat released by the HT-PEMFC is mostly wasted. The simplest and most efficient approach to achieve heat integration is having both devices operating at similar temperatures. Efforts have been made to develop low-temperature MSR catalysts allowing high methanol conversions at low temperatures (< 473 K) and low contact times [5, 6]. Additionally, new developments have been reported regarding solid acid fuel cells (SAFC) [7, 8], which operate at temperatures above 473 K. Despite the great advancements in both fields, the developed materials still not displaying the stability or

performance required. The heat integration, however, can be achieved using a commercial MSR catalyst and commercial PBI based MEAs by optimizing the reformer geometry, flow characteristics, catalysts loading, and steam-to-carbon ratio (S/C).

The heat integration in PEMFCs systems has been the focus of several studies, most of them related with the thermal coupling of the catalytic combustors and reformers [9-12]. Only few experimental studies considered the heat integration of the HT-PEMFC and the reformer operated at the same temperature (<473 K) [13-17]; the results show high voltage losses, even at low current densities, due to the insufficient fuel supply from the reformer and methanol poisoning. Nevertheless, Weng *et al.* [17] using two-stage temperature reformer integrated with a PBI fuel cell system operated at 473 K, obtained comparable results with a fuel cell system fed with pure hydrogen. The use of two-stage reformer allowed a higher methanol conversion compared to one-stage reformer and reduced the oscillations on the vapour flowrate caused by the phase change from liquid to gas. The heat integration of a reformer and a HT-PEMFC has also been the focus of several numerical studies [18, 19, 20]; Lotric *et al.* [21] concluded that operating both devices at the same temperature could increase the overall efficiency by more than ten percentage points. Moreover, operating both devices at the same temperature increases the simplicity of the system and reduces the amount of methanol burned in the catalytic combustor, which produces dangerous exhaust gases such as formaldehyde, CO and unburned methanol [22].

As previously mentioned the simplest and most efficient way to achieve heat integration is having both PEMFC and reformer operated at same temperature. Therefore, a novel MSR-C coupled with a HT-PEMFC operating at the same temperature was developed and intensively characterised at 453, 463 and 473 K. In the proposed design, MSR-C and HT-PEMFC share an aluminium gold coated bipolar plate, which allows an efficient heat transfer between the two cells. The methanol conversion was further improved by optimising the water/methanol vaporisation system. The vaporization process originates flowrate oscillations that were found to be quite detrimental for the methanol conversion as well for the fuel cell power output stability.

## 5.3. Experimental

*Bipolar plate design*

To achieve the heat integration between the MSR-C and the HT-PEMFC, the two devices were put together using a bipolar plate with high thermal conductivity. A novel bipolar plate made of gold plated aluminium with outer dimensions of 10.2 cm x 10 cm x 13 mm was designed and manufactured, having a fuel cell flow field in one side and a reformer flow field in the other (Fig. 5.1). The fuel cell flow field has a hexa-serpentine design with outer 7.2 mm x 7.2 mm, while the reformer has a triple serpentine design with total volume of *ca*. 30 $cm^3$.

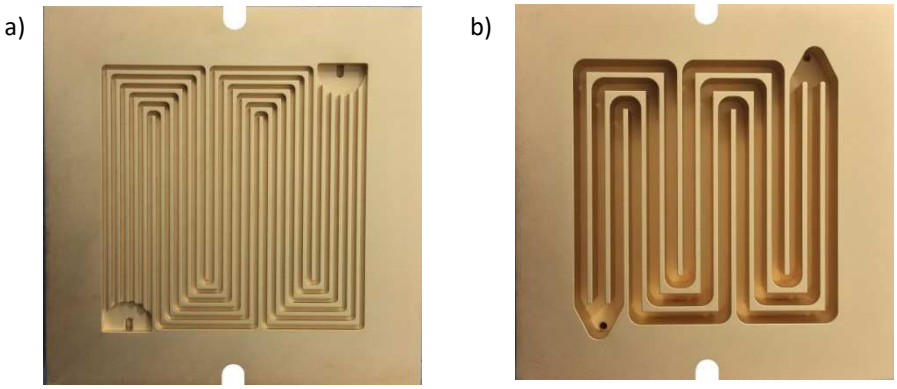


**Fig. 5.1** Bipolar plate made of aluminium gold plated; a) fuel cell side; b) reformer side.

*Assembling the integrated unit (MSR-C/HT-PEMFC)*

The membrane electrode assembly (MEAs) used were Celtec P2200N, from BASF, with an active area of 45 $cm^2$. This MEA is based on phosphoric acid doped PBI membrane, with total thickness of 852 µm. The catalyst loading was 1 $mg_{Pt} \cdot cm^{-2}$ and 0.85 $mg_{Pt} \cdot cm^{-2}$ on the anode and cathode, respectively. The MEA was placed between one bipolar plate made of graphite composite with hexa-serpentine geometry (cathode side) and the new bipolar plate developed in this work (anode side), as shown in Fig. 5.2. PTFE gaskets with thickness of 300 µm were used to assure the fuel cell sealing; they provided a MEA compression of ca. 18 %. The reformer channels (Fig. 5.1b) were filled with ca. 40 g commercial catalyst ($CuO/ZnO/Al_2O_3$) from BASF (RP-60) with particle size

between 200-400 µm and sealed with a silicon gasket of 1.5 mm of thickness. The integrate MSR/HT-PEMFC unit was covered by two metal endplates and all parts were tightened by eight bolts with a torque of 5.5 N·m.

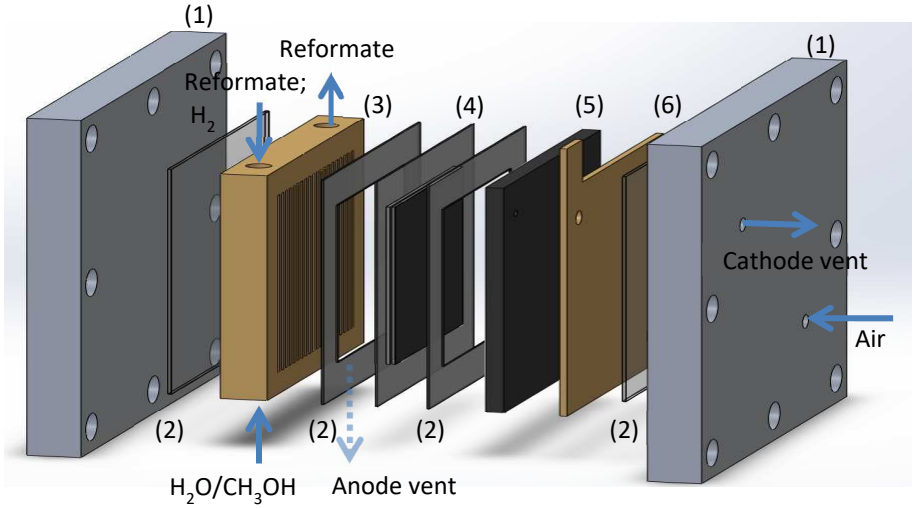


**Fig. 5.2** Assembly scheme of the integrated unit (MSR-C/HT-PEMFC); two metal end-plates frames (1), gasket (2), aluminium gold coated bipolar plate (3), MEA (4), graphite composite bipolar plate (5) and current collector (6).

*Experimental setup*

The schematic diagram of the test bench is shown in Fig. 5.3. Mass flow controllers from Bronkhorst (El-Flow®) were used to control the flow rates of the input gases, while the operating pressure was set using backpressure regulator from Swagelok (0 - 6.8 bar). The operating pressure was measured at the inlets of the fuel cell and reformer using pressure sensors from OmegaDyne Inc. (0 - 3.5 bar). The water/methanol liquid feed, with a steam to carbon molar ratio (S/C) of 1.5, was delivered to the evaporator using an HPLC pump (Knaur Smartline 1050). The evaporator was made of stainless steel tube with 7.5 mm of inner diameter of 250 mm of length and was filled with glass beads of 350 µm. Several options were considered to the base configuration (Fig. 5.3a), aiming to obtaining a constant flowrate of the vaporised fuel, namely the introduction of a carrier gas (Fig. 5.3b) and an expansion vessel of *ca.* 2 $dm^3$ (Fig. 5.3c). The evaporator and MSR-C/HT-PEMFC unit were placed inside an oven and the temperature was controlled using a Eurotherm 3016 PID controller. The reformate stream passed through a cold trap

(based in a thermoelectric element) to remove the condensable components; the flow of the non-condensable components was measured using a mass flow meter (Bronkhorst El-Flow®) hydrogen and carbon dioxide concentration was determined using a mass spectrometry (Pfeiffer OmniStartm). The system was controlled using an application developed in LabView (National Instruments) and the electrochemical tests were performed using a Zahner IM6e electrochemical workstation coupled with a potentiostat PP-241.

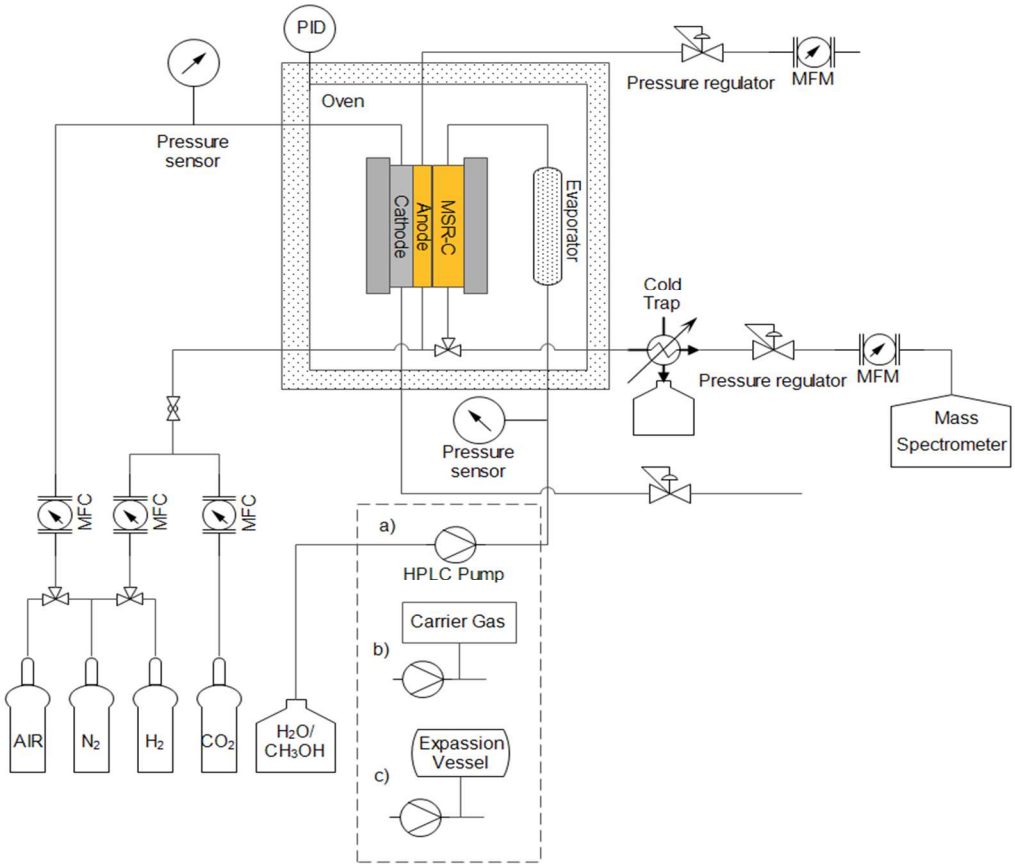


**Fig. 5.3** Scheme of the experimental unit used for the MSR-C/HT-PEMFC characterization.

*Activation of the MEA and the methanol steam reforming catalyst*

The MEA was activated at constant load of 0.20 A·cm$^{-2}$ and at 433 K for at least 50 h, with stoichiometry of 2 for air ($\lambda_{Air}$) and 1.2 for hydrogen ($\lambda_{H2}$), as recommended

by the supplier. During the activation of the MEA, the reformer catalyst was also activated using vented hydrogen from the anode outlet [23].

*Electrochemical characterization of the MSR-C/HT-PEMFC combined system*

The performance of the reformer was assessed immediately after the catalyst activation using a water/methanol mixture with a molar steam to carbon ratio (S/C) of 1.5. The methanol conversion was determined at different space-time-ratios ($m_{cat}/F_{MeOH}$) and operating temperatures (between 453 K and 473 K). The HT-PEMFC characterization was performed with $\lambda_{Air}$ of 2 and $\lambda_{H2}$ of 1.2, between 433 K and 473 K; the anode was fed with different fuels: pure hydrogen, gas mixture with volume fractions of 75% $H_2$ and 25 % $CO_2$ and reformate supplied directly from the MSR. The HT-PEMFC and the integrated unit MSR-C/HT-PEMFC were characterized by electrochemical impedance spectroscopy (EIS) and polarization curves. Nyquist spectra were obtained at 0.2 A·cm$^{-2}$, between 100 kHz and 100 mHz with a perturbation amplitude of 5 mV. Polarization curves were obtained galvanostatically between 0.05 A·cm$^{-2}$ and 0.6 A·cm$^{-2}$. The water/methanol flow rates were adjusted according to the fuel cell current density and they were established based on the hydrogen production observed for the fresh reforming catalyst, as depicted in Table 5.1.

**Table 5.1** Water/methanol flow rates used to feed the reformer at different current densities.

| HT-PEMFC current density (A·cm$^{-2}$) | Water/methanol flow rate (cm$^3$·min$^{-1}$) |
|---|---|
| 0.05 | 0.03 |
| 0.1 | 0.04 |
| 0.2 | 0.08 |
| 0.3 | 0.11 |
| 0.4 | 0.15 |
| 0.5 | 0.20 |
| 0.6 | 0.23 |

A stability test of the integrated device was performed; the electrical potential difference history at 0.2 A·cm$^{-2}$ was followed during ca. 700 h and polarization curves were performed every 20 h. The HT-PEMFC operated 250 h with hydrogen at 453 K, 200 h with reformate at 453 K, 150 h with hydrogen fuel at 463 K and 100 h with reformate fuel at 463 K.

For interpreting the Nyquist spectra, an equivalent electric model was used as presented in Fig. 5.4 [24, 25]. The two first parallel RC circuits connected in series represent the rate determining processes at the anode ($R_{ct,a}$, $CPE_a$) and cathode ($R_{ct,c}$, $CPE_c$); $R_{ct,a}$ and $R_{ct,c}$ corresponds the charge transfer resistance between electrode and electrolyte due to electrochemical reaction at the anode and at the cathode sides, respectively, whereas $CPE_a$ and $CPE_c$ are constant phase elements due to the creation of an electric double layer between the electrode and the electrolyte. The two RC circuits are connected by an ohmic resistance, $R_{ohmic}$, representing the ohmic losses mainly in the electrolyte membrane. The third parallel RC circuit ($R_N$, $C_N$) represents the limitations in mass transport processes (finite diffusion limitations), where $R_N$ is a resistance and $C_N$ is a capacitor. One coil or inductive element ($L$) was added to describe the inductance of the EIS equipment cables. The SIM module from Thales software (Zahner-Elektrik GmbH) was used to fit the model to the experimental data.

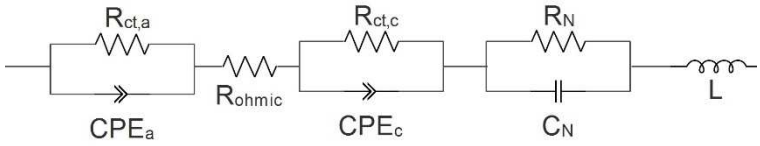


**Fig. 5.4** Fuel cell equivalent circuit model used in the analysis of the impedance data.

## 5.4. Results and Discussion

### 5.4.1. Vaporisation of the water/methanol fuel stream

The water/methanol vaporisation generates flowrate oscillations in the vaporised fuel stream that affects significantly the methanol conversion. Several authors reported reformate flowrate oscillations, but they disregarded this issue [17, 26]. Fig. 5.5 shows the reformate flow rate history for different vaporisation systems.

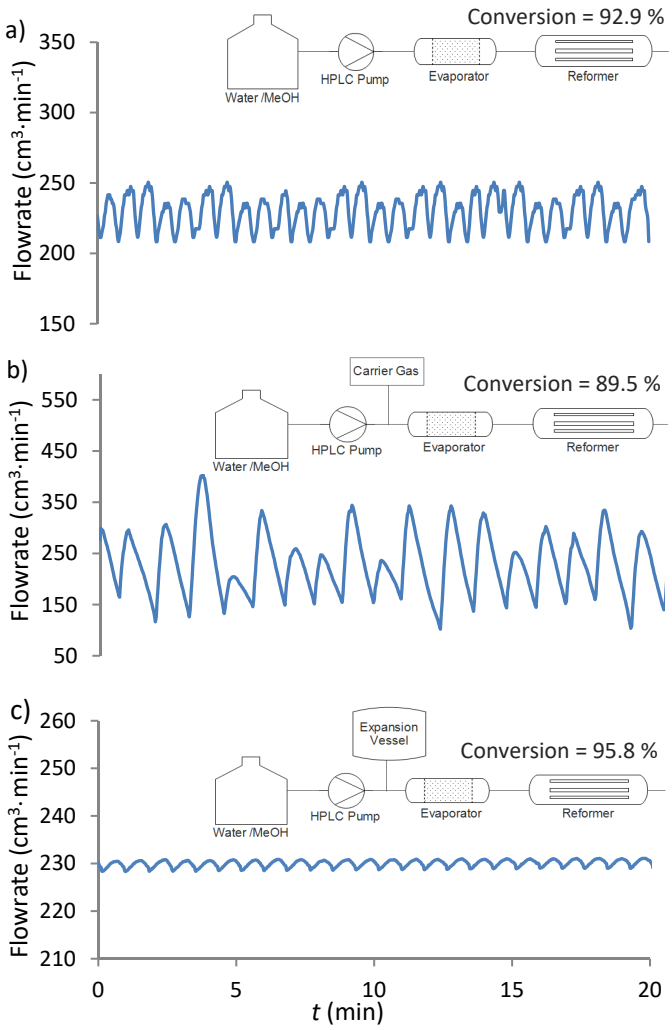


**Fig. 5.5** The reformate flow rate as a function of time for different setup configurations, with a liquid water/methanol flow rate of 0.16 $cm^3 \cdot min^{-1}$ at 453 K

The base configuration, as depicted in Fig. 5.5a, produces flow rate oscillations of *ca.* 50 $cm^3 \cdot min^{-1}$ for a nominal vapour flowrate of *ca*. 230 $cm^3 \cdot min^{-1}$. This system comprises a heated column filled with glass beads fed using a HPLC pump. The introduction of a carrier gas (30 $cm^3 \cdot min^{-1}$ of nitrogen), as suggested by some authors [5, 6], originated even larger flowrate oscillations (Fig. 5.5b). The carrier gas mixed with liquid/mixture generates a saturated vapour flow, which diminishes the vapour flowrate oscillations;

but, high flowrates of the carrier gas reduces the hydrogen concentration in the reformate stream, affecting the FC performance. Introducing an expansion vessel (Fig. 5.5c), on the other hand, reduced significantly flow rate oscillations (*ca.* 3 $cm^3 \cdot min^{-1}$) for the same nominal vapour flowrate of 230 $cm^3 \cdot min^{-1}$. The water/methanol phase transition originates pressure variations that are felt upstream and downstream of the evaporator; the presence of an expansion vessel before the evaporator allows the liquid to go back dissipating this pressure energy. The highest methanol conversion, 96 %, was achieved with the last configuration at 453 K and space-time ratios of 975 $kg \cdot mol^{-1} \cdot s^{-1}$; the base configuration produced a methanol conversion of 93 %, while the configuration using a carrier gas ($N_2$ at 30 $cm^3 \cdot min^{-1}$) originated a methanol conversion of 90 % for the same operating conditions. The vaporisation system configuration with an expansion vessel was the selected one.

### 5.4.2. Characterization of the cellular refomer

The MSR-C was characterized at high space-time ratios ($m_{cat}/F_{MeOH}$ >650 $kg \cdot mol^{-1} \cdot s$) and temperatures between 443 K and 473 K (Fig. 5.6). To minimize the pressure drop in the catalyst bed, the MSR-C was designed with a triple serpentine geometry (Fig. 5.1b) instead of o single serpentine, the maximum pressure drop observed at the highest water/methanol flow rate (0.23 $cm^3 \cdot min^{-1}$) was less than 0.2 bar.

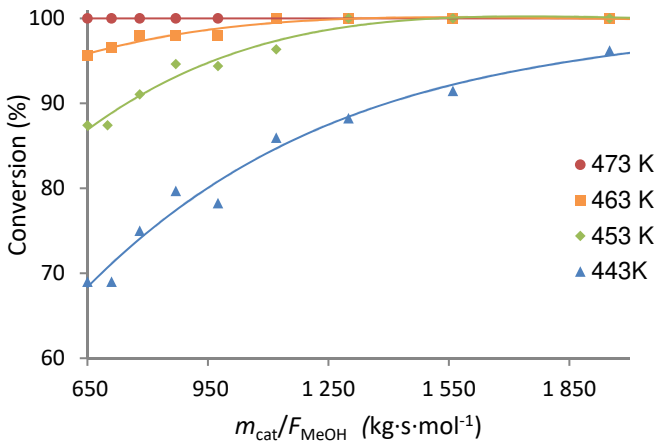


**Fig. 5.6** Methanol conversion as a function of space-time ratio for different reforming temperatures; lines represent the trend and were added for readability.

The MSR-C showed a high performance, similar to the one obtained with a tubular reactor loaded with the commercial catalyst [27]. At 453 K and 463 K full conversion was obtained at space-time ratios above *ca.* 1200 kg·mol$^{-1}$·s and 1000 kg·mol$^{-1}$·s, respectively, while at 473 K, full methanol conversion was observed for >650 kg·mol$^{-1}$·s. Below 443 K, full methanol conversion is attained only for space-time ratios >>2000 kg·mol$^{-1}$·s. In this work, the CO content was not determined since CO concentrations lower than 3000 ppm [27] do not to affect the significantly HT-PEMFC performance [13].

The FC anode feed at the different current densities was determined based on the hydrogen produced by the MSR-C using the fresh reforming catalyst, assuming 100 % of coulombic efficiency and $\lambda_{H2}$ = 1.2. Fig. 5.7 and 5.8 shows the methanol conversion and reformate composition as function of the FC current density, respectively. Higher operating temperatures allows higher hydrogen production and consequently the fuel cell can operate at higher current densities, with lower concentration of methanol in reformate stream; small amounts of methanol should be found at 463 K, <1%, even when the fuel cell operates at current density of 0.6 A·cm$^{-2}$. The MSR-C/HT-PEMFC unit, at 453 K, can operate up to a current density of 0.5 A·cm$^{-2}$, with more than 90 % of methanol conversion. Lower operational temperature, <453 K, will decrease significantly the maximum operating current density.

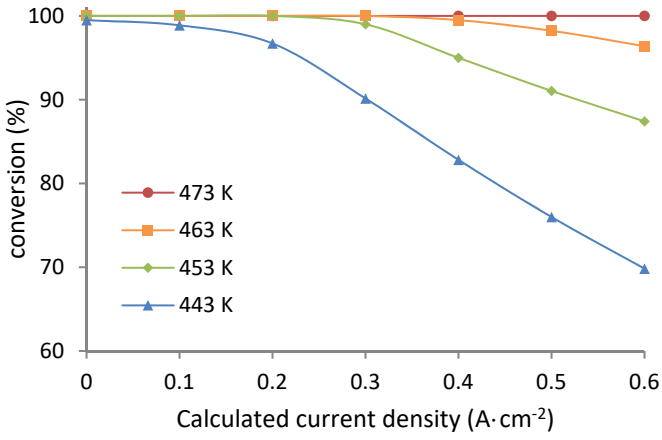


**Fig. 5.7** Methanol conversion as a function of the current density for different operating temperatures; lines were added for readability.

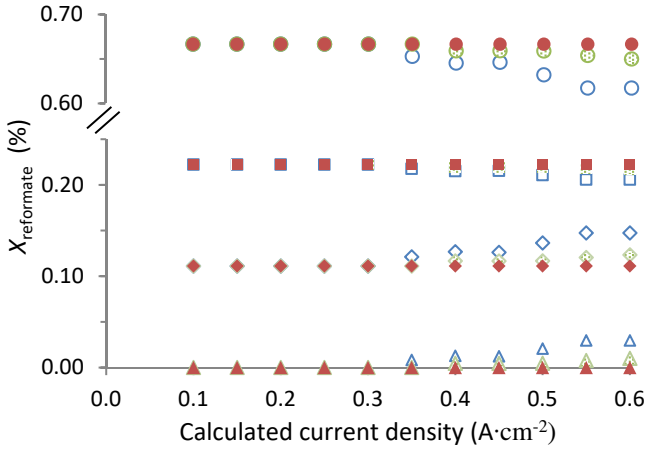


**Fig. 5.8** Methanol (triangle), water (diamond), carbon dioxide (square) and hydrogen (circle) composition as a function of the current density at 453 K(empty symbols), 463 K(pattern symbols) and 473 K (filled symbols);

### 5.4.3.Characterization of the combined MSR-C/HT-PEMFC unit

The HT-PEMFC after the activation was characterized with pure hydrogen at different temperatures (Fig. 5.9). The HT-PEMFC showed high performance as expected for this type of MEA [4, 28].

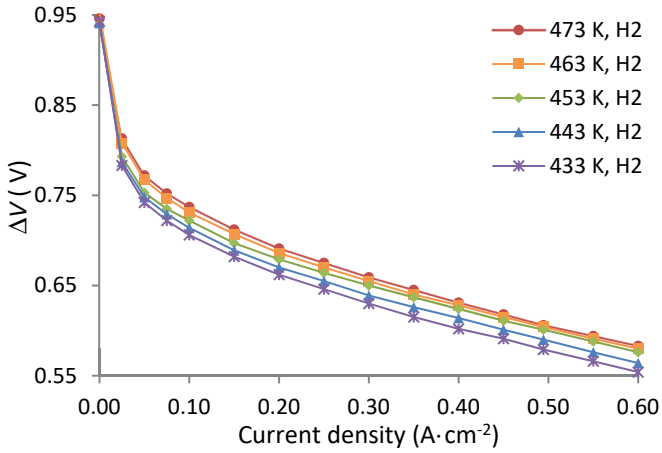


**Fig. 5.9** Electric potential difference as function of the current density for temperatures between 433 K and 473 K – fuel cell fed with hydrogen; lines were added for readability.

Increasing the operating temperature of the HT-PEMFC, the polarization curve shifts to higher potentials for the same current density, due to the improvement of electrochemical reaction kinetics and slightly higher proton conductivity [28]. Above 453 K and especially at high current densities, increasing the temperature shows less influence in the potential difference values. After the electrochemical characterization with pure hydrogen, the HT-PEMFC was also characterized with a $H_2/CO_2$ mixture and with reformate directly from the MSR-C, at several temperatures. Fig. 5.10 shows the polarization curves at different temperatures with pure hydrogen, reformate and $H_2/CO_2$ mixture.

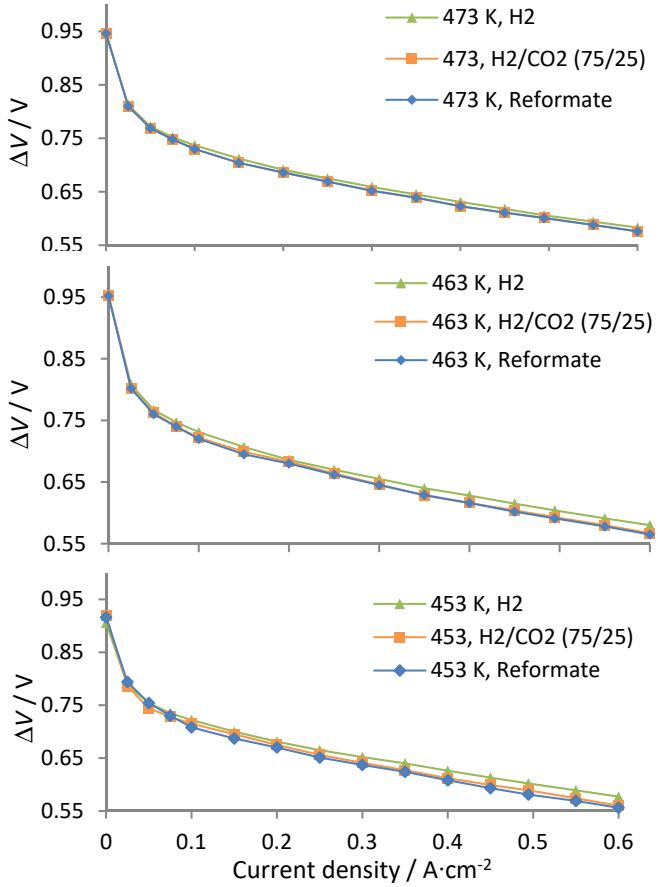


**Fig. 5.10** Electric potential as function of the current density for a) 453 K, b) 463 K and c) 473 K, using three fuel streams: pure hydrogen, $H_2/CO_2$ mixture and methanol reformate.

At 453 K, the potential difference values are slightly higher for hydrogen when compared to the $H_2/CO_2$ mixture. The values obtained with reformate are slightly lower than the ones obtained for hydrogen, but very close to the ones obtained for the $H_2/CO_2$ mixture, Fig. 5.10(a); this indicates a quite high methanol conversion at the MSR. The small decrease in the performance with reformate fuel compared to hydrogen can be attributed to the hydrogen dilution. It is clear from Fig. 5.10 (b) and (c) a positive effect of the temperature increase in the HT-PEMFC performance for $H_2/CO_2$ mixture and reformate. It was showed by Waller *et al.* [30] that increasing the temperature or the feed pressure could significantly mitigate the dilution effect of hydrogen in the feed stream. Additionally, higher methanol conversions are achieved at higher temperatures, which decreases the methanol content in the reformate stream.

To understand the influence of the temperature on the fuel cell performance, an EIS analysis was performed. The Nyquist plot obtained at 0.2 $A \cdot cm^{-2}$ with hydrogen (Fig. 5.11) shows a reduction in the size of the semi-circles associated with anodic processes (high frequencies) and cathodic processes (intermediate frequencies) as temperature increases, indicating an improvement in the electrochemical reaction kinetics. Slight differences are observed in the Nyquist plots obtained at 463 K and 473 K, in accordance to what is observed in the polarization curves (Fig. 5.9). The ohmic resistance (interception of the Nyquist plot with the real axis) is not significantly affected by the temperature in the studied temperature range; the same behaviour is observed at higher current densities (data not shown).

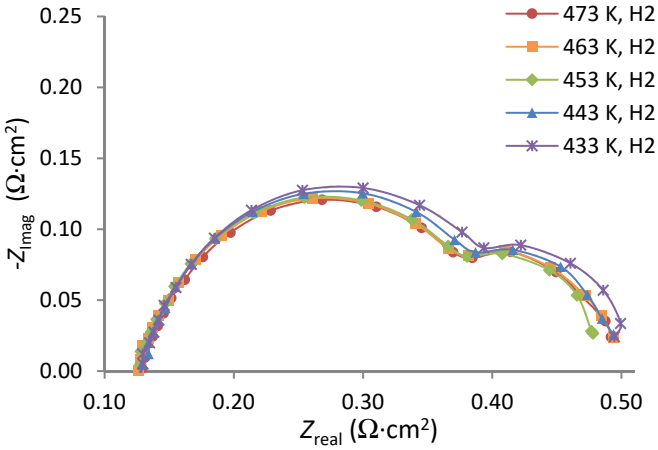


**Fig. 5.11** Nyquist plot at 0.2 $A \cdot cm^{-2}$ immediately after the activation with hydrogen and for different operating temperatures.

Increasing the temperature from 453 K to 463 K, the Nyquist plot with reformate approaches to the Nyquist plot with hydrogen – Fig. 5.12; as the reforming temperature increases the methanol conversion increases towards complete conversion, mitigating the effect of hydrogen dilution and the proton conductivity decrease due to methanol solubility into the phosphoric acid. Further increase to 473 K does not significant affect the comparative electrochemical performance of the fuel cell fed with reformate *vs* with hydrogen, Fig. 5.12. Moreover, assuming full methanol conversion, the reformate contains a volume fraction of *ca.* 11 % of unreacted water, but no significant change is observed in the $R_{ohmic,}$ when compared with hydrogen, Fig. 5.12; similar result was obtained by Boaventura *et al.* [28] using the same type of commercial MEA.

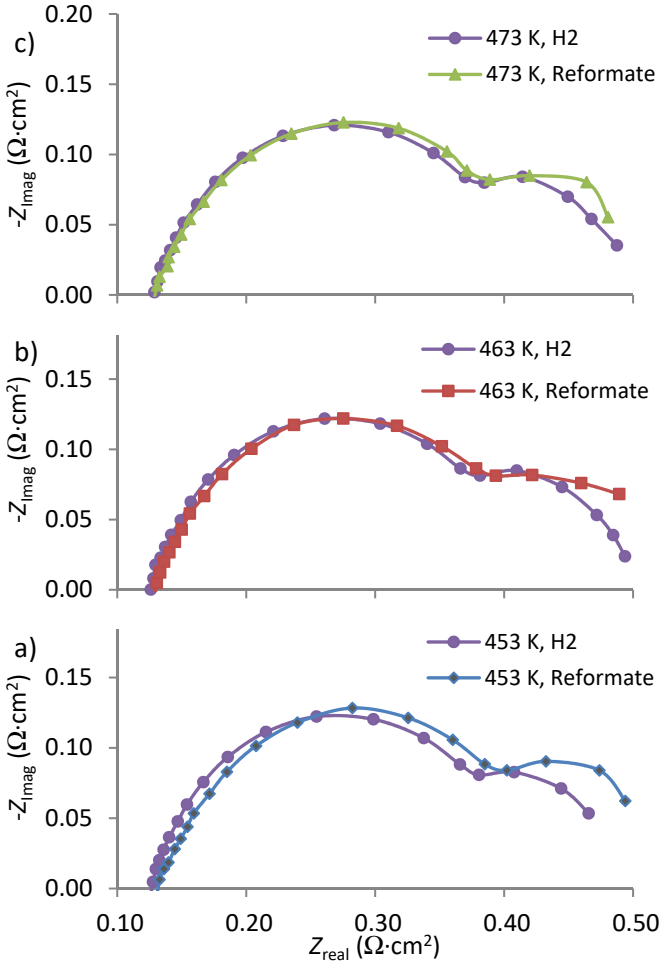


**Fig. 5.12** Nyquist plots at 0.2 A·cm$^{-2}$ with reformate and hydrogen at a) 453 K, b) 463 K and c) 473 K.

### 5.4.4. Stability test of the combined unit

The MSR-C/HT-PEMFC device was operated during *ca.* 700 h at constant at 0.2 A·cm$^{-2}$, alternating the feed between hydrogen and reformate and the temperature, between 453 K and 463 K; Fig. 5.13 illustrates these operating conditions and $\Delta V$ histories. The initial $\Delta V$ increase in the Period I (at 453 K and using hydrogen fuel) is related to the MEA stabilization. After this stabilization period the $\Delta V$ variation rate decreased at 100 μV·h$^{-1}$ for Period I – hydrogen feed and operation at 453 K. In long term stability tests of HT-PEMFC equipped with Celtec®-P 1000 MEA at 433 K and constant current density of 0.2 A·cm$^{-2}$, the typically potential difference loss is *ca.* 5 μV·h$^{-1}$ [31, 32, 33]. However, shorter stability tests <1000 h at the same operating conditions show higher $\Delta V$ losses of *ca.* 25 μV·h$^{-1}$ [34, 35]. The higher $\Delta V$ losses during the first 1000 h are normally attributed to the catalyst particle size growth [34, 35]; should be noted that in this study, not only were the test performed at higher temperature than the literature studies (>453 K), but the MEA was not fresh due to the initially characterization at different temperature (453 K to 473 K) with different fuels. Oono *et al.* [36] studied the effect of temperature on HT-PEMFC degradation and concluded that increasing the operating temperature results in a higher cell $\Delta V$, but decrease cell lifetime due to a faster growth of the catalyst particle size and a higher evaporation rate of the phosphoric acid. In this study, the operation of the MSR-C/HT-PEMFC at lower temperatures (<453 K) would reduce the MEA degradation rate [36], but it would limit the maximum current densities to lower values while high operating temperatures (>463 K) are beneficial for the methanol conversion and consequently the maximum current densities.

When the feed was switched from hydrogen to reformate, instant $t$ = 250 h (Period II, Fig. 5.13), the $\Delta V$ loss rate increased but only slightly, to 138 μV·h$^{-1}$; this should be related to the very low methanol content of the reformate stream. Araya *et al.* [37] reported a degradation rate, also for Celtec MEAs, of 900 μV·h$^{-1}$ using a synthetic reformate stream with an overall water and methanol volume fraction of 2.5 %. Increasing the temperature from 453 K to 463 K and changing from reformate to hydrogen, instant $t$ =420 h (Period III), increased slightly the electric potential difference and the $\Delta V$ loss rate decreased slightly to 97 μV·h$^{-1}$. However, the increase in operating temperate from 453 K to 463 K did not affect the stability of the MEA during the studied period, is expected higher $\Delta V$ drop at higher temperatures for long-term tests (>1000 h) [36]. After

switching the feed from hydrogen to reformate (Period IV), instant *t* =600 h, a sudden shut down occurred, recovering afterwards; the observed potential loss rate for this period was 80 $\mu V \cdot h^{-1}$, close but lower than for the previous period when the feed was hydrogen. At 463 K, full methanol conversion is expected (Fig. 5.7 and 5.8), where any trace of methanol that may be present 453 K is converted, contributing for the stability of the MEA.

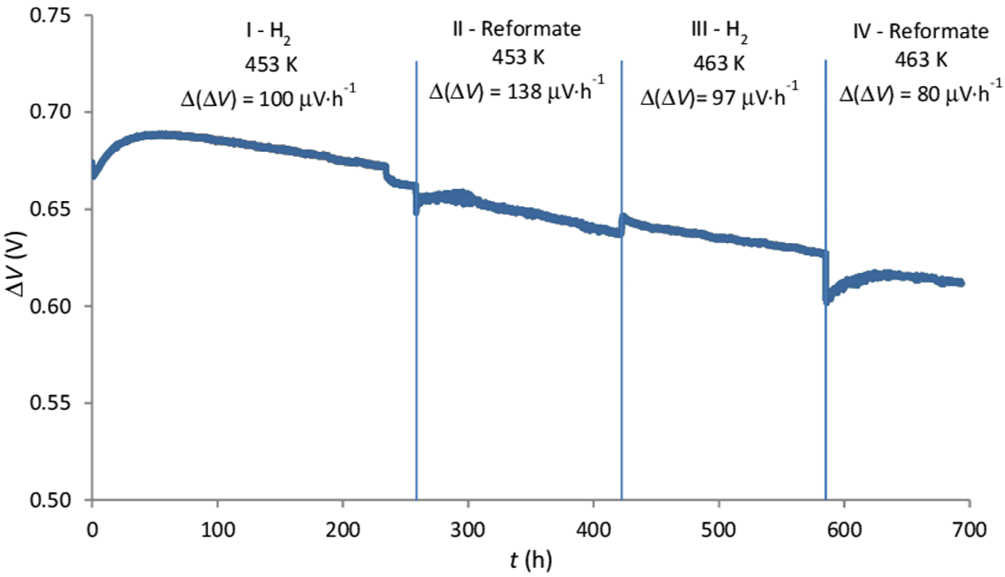


**Fig. 5.13** Aging experiment of the MEA (Celtec®-P 2200N) – $\Delta V$ and potential difference loss rate ($\Delta(\Delta V)$) as function of time at 0.2 $A \cdot cm^{-2}$. The HT-PEMFC operated first at 453 K and then at 463 K. The feed was changed from hydrogen to reformate for the two operating temperatures.

In attempt to clarify the origin of voltage loss during the durability test, an EIS analysis was performed. The Nyquist plots of the HT-PEMFC are given in Fig. 5.14, obtained at 0.2 $A \cdot cm^{-2}$ at 453 K and 463 K and for hydrogen and reformate feeds. The resistances (ohmic, charge transfer at anode and cathode and mass transport) presented in the Fig. 5.15 were obtained fitting the electric equivalent circuit (Fig. 5.4) to the experimental data (Fig. 5.14)

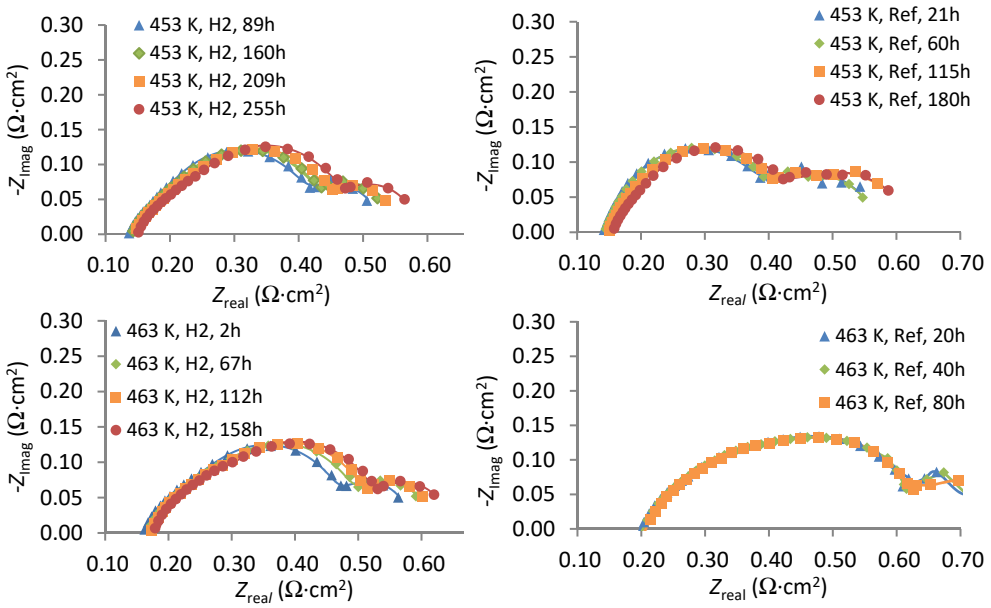


**Fig. 5.14** Nyquist plots of the as a function of time for 0.2 A·cm$^{-2}$. The HT-PEMFC operated first at 453 K and then at 463 K. The feed was changed from hydrogen to reformate for the two operating temperatures.

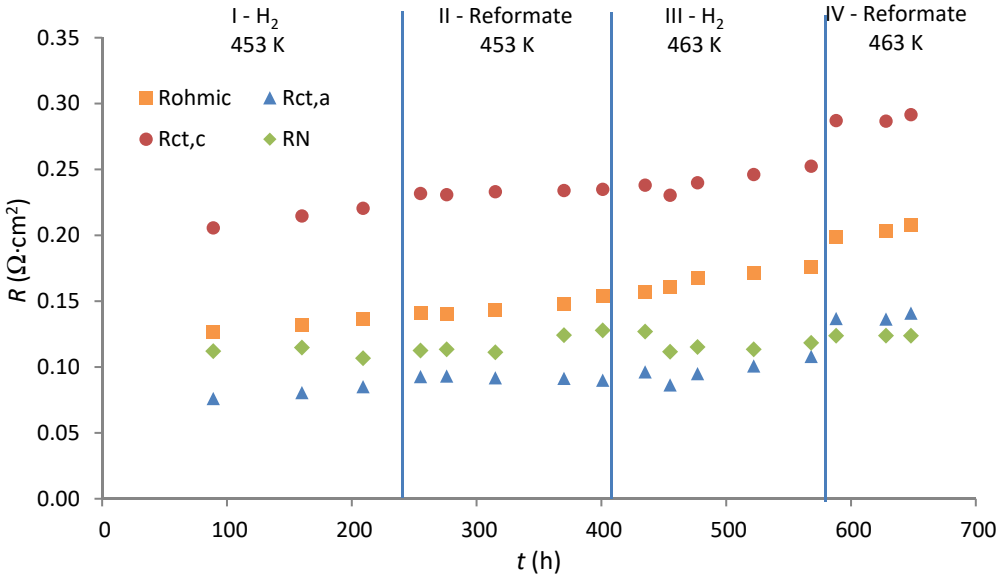


**Fig. 5.15** Ohmic, charge transfer at the anode and cathode and mass transport resistances as a function of time for 0.2 A·cm$^{-2}$. The HT-PEMFC operated first at 453 K and then at 463 K. The feed was changed from hydrogen to reformate for the two operating temperatures.

During Period I, $R_{ohmic}$ increased slightly (Fig. 5.15), with an increasing rate of $0.9x10^{-4}$ $\Omega \cdot cm^2 \cdot h^{-1}$. When hydrogen was replaced by reformate, Period II, the same increase rate was observed. The presence of water in the reformate can increase the proton conduction in the membrane and at the catalyst layer, but can also have a detrimental effect due to phosphoric acid leaching [38]. Moreover, the presence of methanol in the fuel, even in small amounts, during long operation periods has been reported to influence the $R_{ohmic}$ leading to membrane thickness reduction and mechanical degradation of the membrane [28]. The similar $R_{ohmic}$ increasing rate (*ca*. $0.9x10^{-4}$ $\Omega \cdot cm^2 \cdot h^{-1}$), shows a negligible effect of the water presence or by the presence of any trace of methanol in the feed stream. Increasing the temperature to 463 K leads to higher $R_{ohmic}$ values and to slightly faster increase rate of $R_{ohmic,}$ $1.1x10^{-4}$ $\Omega \cdot cm^2 \cdot h^{-1}$ and $1.4x10^{-4}$ $\Omega \cdot cm^2 \cdot h^{-1}$, respectively for hydrogen and reformate fuels. This increase should be related to the fast evaporation of the phosphoric acid from the membrane and catalyst layer; the phosphoric acid vapour pressure increases more than 50 % when temperature increases from 453 K to 463 K [36,39]. When hydrogen was replaced by reformate an initially jump on the $R_{ohmic,}$ was observed, caused by the shutdown during the change of fuels.

In the equivalent electric model (Fig. 5.4), two parallel RC circuits in series were used, representing the electrochemical process in the anode and cathode. Therefore, the first semicircle in the Nyquist plot (Fig. 5.14) is composed by two overlapped semicircles. However, decoupling these semicircles in HT-PEMFCs is hard to achieve, leading several authors [36, 40] to use just a single RC circuit representing the electrochemical processes for both electrodes. In the other hand, using two parallel RC the effects of the reformate contaminants ($CO_2$, CO, water, methanol) in the anode and cathode catalyst could be evaluated separately.

The charge transfer resistance at the anode ($R_{ct,a}$) shows a slight increase during Period I (Fig. 5.15); typically this increase is attributed to the catalyst agglomeration, carbon corrosion and acid loss from the electrode [34, 35]. When hydrogen was replaced by reformate feed, Period II, a slower increase of the $R_{ct,\,a}$ was observed, which was assigned to the decrease of catalyst agglomeration with the operating time [36, 40, 41]. It can be also concluded that $CO_2$, CO, water and traces of methanol present in the reformate stream had a negligible effect on the $R_{ct,a}$. Increasing the temperature to 463 K and changing the fuel to hydrogen, Period III, resulted in an immediate decrease of the $R_{ct,a}$. The electrical charge transfer resistance is typically assumed to be related to the catalyst

activity of the cathode and anode; therefore, increasing the operating temperature should increase the catalyst activity promoting the electrochemical reactions resulting in an increase of the cell voltage. Several authors reported similar reduction of the charge transfer resistance with temperature increase in HT-PEMFCs [42, 43]. However, during this period, the increasing rate of $R_{ct,a}$ was higher than during Period I – 453 K. Although higher operating temperatures could enhance the reaction rates, the degradation of the catalyst activity (agglomeration) and loss of catalytic particles due to carbon corrosion make $R_{ct,a}$ to increase [40]. When hydrogen was changed to reformate feed at 463 K, Period IV, an unexpected shutdown of the HT-PEMFC happened, which resulted in immediately jump on the $R_{ct,a}$ to high values. During Period IV $R_{ct,a}$ continued to increase but with a slower rate than the observed previously with hydrogen fuel. The charge transfer resistance at the cathode $R_{ct,c}$ shows the same trend of the $R_{ct,a}$ for the different fuels and operating temperatures. Any reduction in the active catalyst surface area due to agglomeration should take place on both anode and cathode electrodes with approximately the same extension. The $R_{ct,c}$ value is higher than $R_{ct,a}$ due to the lower reaction rate of oxygen reduction at the cathode when compared to the hydrogen oxidation at the anode. Finally, the mass transport resistance ($R_N$) in Period I showed no significant variation during the first 250 h. With reformate as fuel, Period II, an increase in the $R_N$ was observed. The mass transport resistance is related to the diffusion rate of the reactant gases (hydrogen and oxygen) through the pores of the electrode and the solubility and diffusivity in the absorbed phase of the reactant gases through the phosphoric acid, which impregnates the catalyst layer [40,42]. Therefore, in the anode side the simple dilution of the hydrogen can affect $R_N$, since the presence of $CO_2$, CO, water and methanol make the hydrogen diffusion in the absorbed phase slower (competitive absorption in the phosphoric acid). Moreover, that species ($CO_2$, CO, water and methanol) can also adsorb in the catalyst metal surface limiting the access of hydrogen to the active sites and then increasing the $R_N$ [15]. In Period III, a sudden decrease of $R_N$ was observed, showing that the negative effect caused by the reformate presence in $R_N$ was reversible. Increasing the operating temperature increases the gas diffusion rates, but also reduces the gas solubility. The dominating effect on $R_N$ depends on the current density; according Zhang *et al.* [42] at high current densities the gas solubility dominates and at lower current densities, the gas diffusivity dominates. The Nyquist plots, in this work, were obtained at 0.2 $A \cdot cm^{-2}$; therefore, the gas diffusion should play the main role. Since

the gas diffusion increases with the temperature, $R_N$ should decrease. During the following 150 h of operation with hydrogen at 463 K, Period III, a slight increase of $R_N$ was observed. However, the operation at higher temperature should enhance the oxidation of carbon to CO and CO2 and change the porosity of the backing/catalyst layer, which can explain the increase of $R_N$ as a function of the time [40]. When hydrogen was replaced by reformate, Period IV, a shutdown of the HT-PEMFC occurred, as previously mentioned, which may had affected the carbon support and resulted in small jump on $R_N$ to higher values. During the following 100 h of operation with reformate no significant variation of $R_N$ was observed.

### 5.5. Conclusions

In this work, an integrated unit combining a MSR-C and HT-PEMFC was built and operated at the same temperature (453 K, 463 K and 473 K). For that purpose, a novel bipolar plate made of aluminium gold plated featuring the fuel cell anode flow field in one side and the reformer flow field on the other was developed.

The water/methanol vaporisation generates flowrate oscillations in the vaporised fuel stream; these flowrate oscillations were found to be quite detrimental for the methanol conversion and for the power output of a fuel cell. The introduction of an expansion vessel between the HPLC pump and the evaporator, allowed a remarkable reduction of the flow rate oscillations and increase of the methanol conversion from 93 % to 96 %.

The combined MSR-C/HT-PEMFC system displayed a remarkable performance at 453 K and the highest reported in the literature for similar devices. When the fuel cell was fed directly with reformate from the MSR-C, the performance was only slightly lower than the obtained with hydrogen. An improvement of the electrochemical reaction rate with temperature was observed for both fuels; the ohmic resistance of the MEA was not significantly affected by the temperature neither by the fuel used (hydrogen/reformate).

The MSR/HT-PEMFC combined device was operated during *ca.* 700 h at 0.2 $A \cdot cm^{-2}$, first at 453 K and then at 463 K, fed alternately with hydrogen and reformate. The device demonstrated quite good stability considering the high operating temperature (453 K and 463 K); the $\Delta V$ decreasing rate at 453 K with hydrogen was 100 $\mu V \cdot h^{-1}$, slightly lower than that for the reformate, 138 $\mu V \cdot h^{-1}$. Increasing the temperature to 463 K did not affect significantly the $\Delta V$ variation rate for both fuels. The EIS analysis also demonstrated

that using reformate as fuel had no significant influence in MEA degradation compared to hydrogen during the studied period.

## 5.6. References

[1] U. Bossel, B. Eliason Energy and the Hydrogen Economy, Conference EV World, December 28 (2002).

[2] N.W. Deluca, Y.A Elabd, Polymer electrolyte membranes for the direct methanol fuel cell: a review, Journal of Polymer Science: Polymer Physics, 44 (2006) 2201-2225

[3] [access date January 2017], http://www.ultracell-llc.com/assets/UltraCell_BT-press-release-Feb-20-2015-FINAL.pdf

[4] S. Andreasen, S. Kær, S. Sahlin, Control and experimental characterization of a methanol reformer for a 350W high temperature polymer electrolyte membrane fuel cell system, International Journal of Hydrogen Energy 38 (2013) 1676–84

[5] O.Ilinich, Y. Liu, C. Castellano, G. Koermer, A. Moini, R. Farrauto, A New Palladium-Based Catalyst for Methanol Steam Reforming in a Miniature Fuel Cell Power Source. Platinum Metals Review 52 (2008) 134–143.

[6] B. Lindström, L. J. Pettersson, Hydrogen generation by steam reforming of methanol over copper-based catalysts for fuel cell applications International Journal of Hydrogen Energy 26(9) (2001) 923–933.

[7] Q. Geletu, K. Ryuji, T. Atsushi, S. Takashi, S.T. Oyama, CsH2PO4/Polyvinylidene Fluoride Composite Electrolytes for Intermediate Temperature Fuel Cells, Journal Electrochemical Society, 161 (2014) F451-F457

[8] A. Jensen, L. Qingfeng, E. Christensen, N. Bjerrum, Intermediate Temperature Fuel Cell Using CsH2PO4/ZrO2-Based Composite Electrolytes Journal Electrochemical Society, 161 (2014) F72-F76

[9] J.Y. Won, H.K. Jun, M.K. Jeon, S.I. Woo, Performance of a microchannel reactor combined with a combustor for methanol steam reforming, Catalysis Today 111 (2006) 158-163

[10] R.S. Besser, Thermal integration of a cylindrically symmetric methanol fuel processor for portable fuel cell power, International Journal of hydrogen energy 36 (2011) 276 -283

[11] T. Kim, Micro Methanol Reformer Combined with a Catalytic Combustor for a PEM Fuel Cell, International Journal of Hydrogen Energy, 34 (2009) 6790-6798

[12] J.D. Morse, R.S. Upadhye, R.T. Graff, C. Spadaccini, H.G. Park, E.K. Hart, A MEMS-based reformed methanol fuel cell for portable power, Journal of Micromechanics and Microengineering 17 (2007) S237-S242

[13] C. Pan, R.H. He, Q.F. Li, J.O. Jensen, N.J. Bjerrum, H.A. Hjulmand, A.B. Jensen, Integration of high temperature PEM fuel cells with a methanol reformer, Journal of Power Sources, 145 (2005) 392-398.

[14] G. Avgouropoulos, T. Ioannides, J.K. Kallitsis, S. Neophytides, Development of an internal reforming alcohol fuel cell: Concept, challenges and opportunities Chemical Engineering Journal, 176 (2011) 95-101.

[15] G. Avgouropoulos, S. Neophytides, Performance of internal reforming methanol fuel cell under various methanol/water concentrations, Journal of Applied Electrochemistry, 42 (2012) 719–726.

[16] G. Avgouropoulos, A. Paxinou, S. Neophytides, In situ hydrogen utilization in an internal reforming methanol fuel cell International Journal of Hydrogen Energy, 39 (2014) 18103-18108.

[17] F. Weng, C. Chenga, K. Chen, Hydrogen production of two-stage temperature steam reformer integrated with PBI membrane fuel cells to optimize thermal management, International Journal of Hydrogen Energy 38 (2013) 6059-6064

[18] E.R. Pascual, J. Soler, Modeling of an HT-based micro-combined heat and power fuel system with methanol, International Journal of Hydrogen Energy 39 (2014) 4053-4059.

[19] W. Wu, C. Pai, Control of a heat-integrated proton exchange membrane fuel cell system with methanol reforming, Journal of Power Sources 194 (2009) 920-930.

[20] H. Chang, H.C. Chiang, Y.H. Chen, Y.Y. Chang, S.H. Cheng, Simulation Study of an Integrated Methanol Microfuel Processor and Fuel Cell System, Chemical Engineering Science 74 (2012) 27-37

[21] A. Lotric, M. Sekavcnik, S. Hocevar Effectiveness of heat-integrated methanol steam reformer and polymer electrolyte membrane fuel cell stack systems for portable applications, Journal of Power Sources 270 (2014) 166-182

[22] A. Bell, Thesis of Science in Mechanical Engineering "Design of a Catalytic Combustor for Pure Methanol and HTPEM Fuel Cell Anode Waste Gas", Department of Mechanical and Industrial Engineering University of Toronto

[23] P. Ribeirinha, I. Alves, F. Vidal Vázquez, G. Schuller, M. Boaventura, A. Mendes, Heat integration of methanol steam reformer with a high-temperature polymeric electrolyte membrane fuel cell, Energy 120 (2017) 468-477

[24] M. Boaventura, A. Mendes, Activation procedures characterization of MEA based on phosphoric acid doped PBI membranes, International Journal Hydrogen Energy, 35 (2010) 11649-11660.

[25] N. Wagner, T. Kaz, K.A. Friedrich, Investigation of electrode composition of polymer fuel cells by electrochemical impedance spectroscopy, Electrochimica Acta 53(25) (2008) 7475–7482.

[26] Y. Choi, H.G. Stenger, Fuel cell grade hydrogen from methanol on a commercial Cu/ZnO/Al2O3 catalyst, Applied Catalysis B: Environmental 38 (2002) 259–269

[27] P. Ribeirinha, M. Boaventura, J.C. Lopes, J.M. Sousa, A. Mendes, Study of different designs of methanol steam reformers: Experiment and modeling, International Journal of Hydrogen Energy, 39 (2014) 19970-1998.

[28] M. Boaventura, I. Alves, P. Ribeirinha, A. Mendes, The influence of impurities in high temperaturepolymer electrolyte membrane fuel cells performance (2016), doi:10.1016/j.ijhydene.2010.08.128

[29] Q. Li, D. Aili, H.A Hjuler, J.O. Jensen, High Temperature Polymer Electrolyte Membrane Fuel Cells, Springer Switzerland (2016).

[30] Waller

[31] T.J. Schmidt, Durability and Degradation in High-Temperature Polymer Electrolyte Fuel Cell, ECS Transactions 1 (8) (2006) 19-36.

[32] T.J. Schmidt, J. Baurmeister, Properties of high-temperature PEFC Celtec®-P 1000 MEAs in start/stop operation mode, Journal of Power Sources 176 (2008) 428-434

[33] Q. Li, J.O. Jensen, R.F. Savinell, N.J. Bjerrum, High temperature proton exchange membranes based on polybenzimidazoles for fuel cells, Progress in Polymer Science, 34(5) (2009) 449–477

[34] D. Modestov, , M.R. Tarasevich1, V. Filimonov, N.M. Zagudaeva, Degradation of high temperature MEA with PBI-H3PO4 membrane in a life test, Electrochimica Acta 54(27) (2009) 7121-7127

[35] C. Wannek, B. Kohnen, H.-F. Oetjen, H. Lippert, J. Mergel, Durability of ABPBI-Based MEAs for High Temperature PEMFCs at Different Operating Conditions, Fuel Cells, 8 (2008) 87-95

[36] Y. Oono, T. Fukuda, A. Sounai, M. Hori, Influence of operating temperature on cell performance and endurance of high temperature proton exchange membrane fuel cells, J. Power Sources. 195 (2010) 1007–1014.

[37] S.S. Araya, S.J. Andreasen, H.V. Nielsen, S.K. Kaer, Investigating the effects of methanol-water vapor mixture on a PBI-based high temperature PEM fuel cell, International Journal of Hydrogen Energy, 37 (2012) 18231-18242.

[38] Galbiati, S., *et al.*, Experimental study of water transport in a polybenzimidazole-based high temperature PEMFC, International Journal of Hydrogen Energy, 37(3) (2012) 2462-2469.

[39] E.H. Brown, C.D. Whitti, Vapor Pressure of Phosphoric Acids, Industrial & Engineering Chemistry 44(3) (1952) 615–618

[40] S. Galbiati, A. Baricci, A. Casalegno, R. Marchesi, Degradation in phosphoric acid doped polymer fuel cells: A 6000 h parametric investigation, International Journal of Hydrogen Energy 38(15) (2013) 6469–6480

[41] Y. Zhai, H. Zhang, D. Xing, Z.G. Shao, The stability of Pt/C catalyst in H3PO4/PBI PEMFC during high temperature life test, Journal of Power Sources, 164 (2007), 126–133

[42] J. Zhang, Y. Tang, C. Song, J. Zhang, Polybenzimidazole-membrane-based PEM fuel cell in the temperature range of 120–200 °C, Journal of Power Sources, 172 (2007), 163–171

[43] N.H. Jalani, M. Ramani, K. Ohlsson, S. Buelte, G. Pacifico, R. Pollard, R. Staudt, R. Datta, Performance analysis and impedance spectral signatures of high temperature PBI–phosphoric acid gel membrane fuel cells, Journal of Power Sources, 160 (2006), 1096–1103

CHAPTER 5

# Chapter 6

# Integration of a reformer with a HT-PEMFC – Part C (modelling)

## 6.1. Abstract

A 3-dimensional non-isothermal simulator comprising a high temperature polymer electrolyte membrane fuel cell (HT-PEMFC) and a methanol steam-reforming cell (MSR-C) was developed in Fluent (Ansys™). The simulator takes into account most of the significant physical processes, including the electrochemical reactions and carbon monoxide poisoning effect on the electro-catalytic activity of the FC; it also considers the methanol steam reforming (MSR), water gas shift (WGS) and methanol decomposition (MD) reactions in the MSR-C. The developed model for the integrated MSR-C/HT-PEMFC unit was simulated between 443 K and 473 K and validated with experimental results reported in the literature, showing always a very good agreement. The thermal sustainability of the integrated unit was assessed, and the role of the thermal insulation and air intake (cathode) stoichiometry in the thermal equilibrium of the device were analysed. A novel MSR-C/HT-PEM stack with ten cells was proposed and simulated, showing a performance above the reported in the literature for similar devices. The results indicated that the proposed stack operates at currents between 4.5 A (0.1 A·cm$^{-2}$) and 54 A (1.2 A·cm$^{-2}$) without any external heat source. To minimize the degradation of the components the stack should adapt the operating temperature to the current density.

---

The content of this chapter is adapted from, P. Ribeirinha, M. Abdollahzadeh, J. Sousa, M. Boaventura, A. Mendes, Modelling of a high-temperature polymer electrolyte membrane fuel cell integrated with a methanol steam reformer cell, Applied Energy 202 (2017) 6-19

## 6.2. Introduction

High temperature polymer electrolyte membrane fuel cells (HT-PEMFCs) operate at temperatures between 393 K and 453 K and can be directly fed with methanol reformate stream without $H_2$ purification, due to its high tolerance to carbon monoxide (< 3000 ppm) [1-3]. The great challenge of the HT-PEMFC devices is the recovery of the heat using a simple approach, avoiding heat exchangers, evaporators and chemical reactors [4]. A HT-PEMFCs wastes ca. 50 % of the input chemical energy in the form of heat, more energy than the heat required for fuel vaporization and MSR reaction combined; to increase the energy efficiency, the thermal integration is mandatory. Several studies have been reported concerning the heat integration of HT-PEMFCs with in-situ hydrogen production systems, mostly focusing their attention to the thermal coupling with catalytic combustors and reformers [5-12]; the heat losses to the environment are considered a critical factor to the overall efficiency of the system, mainly in the small scale applications [11,12]. The heat integration of a HT-PEMFC and a reformer operated at the same temperature (<473 K) was only considered by a few authors, [13-17]. Pan *et al.* integrated a two-cell HT-PEMFC stack with a MSR, operating both devices at the same temperature, between 453 K and 473 K [13]. The results showed high voltage losses (160-200 mV) even at 473 K and low current densities, due to insufficient fuel supply from the reformer and the presence of residual methanol in the reformate stream. Avgouropoulos *et al.* incorporated the methanol reforming catalyst in the HT-PEMFC anodic compartment, naming this approach internal reforming methanol fuel cell (IRMFC) [14-15]. The results showed very low fuel cell performance due to insufficient fuel supply and catalyst poisoning by methanol. Nevertheless, Weng *et al.* using a two-stage temperature reformer integrated with a HT-PEMFC at 473 K obtained comparable results to a HT-PEMFC feed with pure hydrogen [17]. The first stage of the reformer was operated at 473 K using the heat release by the HT-PEMFC, while the second stage was operated at 513 K using a burner run with the wasted hydrogen from the fuel cell. Compared to one-stage reformer, the two-stage reformer allowed higher methanol conversion and lower fluctuations in the reformate flow rate caused by the water/methanol evaporation. The authors reported recently a combined methanol steam reformer cell (MSR-C) and a HT-PEMFC, run at the same temperature, 453 K, displaying rather high current densities (> 0.5 $A \cdot cm^{-2}$) [18, 19]. To assemble the combined unit (MSR-C/HT-PEMFC) two

novel bipolar plates were used, featuring the fuel cell flow field in one side and the reformer flow field in the other. In the first study, a membrane electrode assembly (MEAs) based on pyridine type structure membrane from Advent TPS® [18] was used, while in the second study, a MEA based on PBI phosphoric acid doped membrane from BASF [19] was used. The combined unit assembled with a MEA from BASF showed higher performance and long-term stability than the combined unit with a MEA from Advent TPS®. Moreover, the performance of the combined unit assembled with the MEA from BASF was similar to the FC fed with pure hydrogen.

Several numerical studies simulating combined fuel cell/reformer units/combustors have been reported [four, 20-22]. Sahlin *et al.* [4] investigated numerically and experimentally a 5 kW fuel cell system using a thermal fluid. The device used two separate circuits, where the heat was transferred between the reformer and the burner operating at high temperature and between the fuel cell and evaporator operating at low temperature. The authors obtained an efficiency of the system of 28-30 %. Lotric *et al.* [23] used Aspen Plus® to study the thermal integration of all endothermic and exothermic processes present in a power supply based on PEMFC stack and a methanol reformer. The authors considered a low-temperature PEMFC (working at 343 K), a conventional high-temperature PEMFC (working at 453 K); in the latter case, the authors considered the presence of a novel nanocomposite polymer membrane with a water-insoluble solid proton conducting electrolyte operating at 528 K, matching the operating temperature of the reformer. The results indicate that operating both systems at the same temperature increases more than ten percentage points the overall efficiency. Moreover, operating at the same temperature increases the simplicity of the system and eliminates the need to burn methanol to heat up the system, which can produce dangerous exhaust gases such as formaldehyde and CO [24]. Avgouropoulos *et al.* [25] assessed experimentally and by simulation the concept of a 70W IRMFC stack. The IRMFC stack was operated at 473 K; the maximum current density was rather low and stability of the combined unit was not assessed. Most of these numerical studies of combined HT-PEMFC / fuel processor units are one-dimension [20-23, 25], modelling micro-combined heat and power (CHP) plants [4, 20-23]. However, sophisticated numerical models of HT-PEMFCs based on PBI membrane doped with phosphoric acid are also available in the literature [26-36] and were summarized by Q. Li et al [26]. These models for HT-PEMFC focus on the effect of the cell design and operating conditions [27-28], the effect of temperature [29,30],

the CO poisoning effect [31,32,33], the gas crossover through the membranes [34], the gas humidification [35], mechanical and thermal stress-deformation [36] on the polarization curves of the HT-PEMFC. However, these sophisticated numerical models have never been applied to study the heat integration of HT-PEMFC and MSR.

In the present work, the heat integration of a HT-PEMFC with a methanol steam reformer cell (MSR-C) was studied by simulation and validated with experimental data published by the authors [19]. The physical model considers an integrated unit (MSR-C/HT-PEMFC) using a novel bipolar plate designed to feature a fuel cell anode flow field in one side and the reformer flow field in the other. The mathematical model considers the electrochemical reactions at the anode and cathode catalyst layers, the temperature, the CO content in the anode fuel, the phosphoric acid doping level and the influence of the water content on the membrane proton conductivity. The CO poisoning model was based on the work developed by Springer *et al.* [37] and adapted to HT-PEMFC [31, 32, 33]. This model accounts for the electrochemical oxidation of CO, as well as the adsorption/desorption processes of CO and hydrogen on Pt catalyst surface. In the reformer, it was considered the kinetic model developed by Peppley *et al.* [38] and adapted by the authors for the commercial catalyst BASF RP60 [40]. The kinetic model is based on a Langmuir–Hinshelwood model with an overall reaction network comprising methanol steam reforming (MSR) reaction, reverse water-gas-shift (RWGS) and methanol decomposition (MD). The simulation results were analysed and validated based on the performance of the HT-PEMFC and MSR separated and combined. The effect of the reformate contaminants (CO, $CO_2$, $CH_3OH$ and $H_2O$) and operating temperature on the performance of the MSR-C/HT-PEMFC combined unit was assessed. The thermal sustainability of the combined unit was also analysed, focusing on the level of thermal insulation and temperature control required for real applications. A MSR-C intercalated with a HT-PEMFC in a combined stack arrangement operating at similar temperature would simplify the heat integration and maximize the overall energy efficiency. Therefore, a novel integrated MSR-C/HT-PEM stack with ten cells is pro-posed; the simulations show that this stack can achieve high current densities (1.2 $A \cdot cm^{-2}$), above the re-ported in the literature for similar devices [13, 17, 25], without external heating. The stack operating conditions such as temperature, water/methanol flow rate, hydrogen and air flow rate, current density, potential or heat produce/consumed are studied.

## 6.3. MSR-C/HT-PEMFC model

### 6.3.1. Problem description

The model of the MSR/HT-PEMFC combined unit considers a bipolar plate with a fuel cell flow field in one side (Fig. 6.1a) and a reformer flow field in the other (Fig. 6.1b). The detailed information and experimental characterization of the combined unit can be found elsewhere [19].

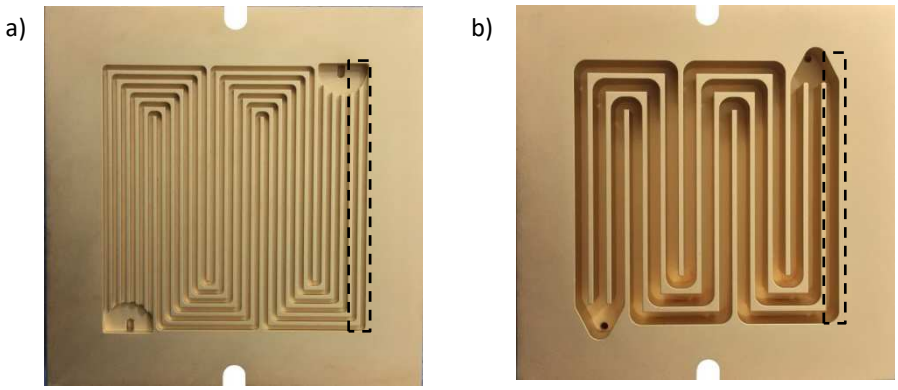


**Fig. 6.1** Bipolar plate made of gold plated aluminium. a) Fuel cell side; b) reformer side.

One third of the combined unit was modelled: one straight channel of the reformer and two straight and parallel channels of the anode and cathode, matching the real channel length of the physical device, as shown in the mesh configuration in Fig. 6.2; the other two thirds were assumed symmetric. Anode and cathode gas diffusion layers (GDL), anode and cathode catalyst layers (CL) and membrane are modelled. The dimensions of the anode and cathode GDL, anode and cathode CL and membrane were estimated based on the scanning electron microscope image of the BASF Celtec P2200N MEA, as depicted in Fig. 6.3; the relevant physical parameters are summarized in Table 6.1. The dimensions of the MEA change due to the compression during the assembly of the fuel cell. Most of the compression occurs in the GDL, where the porosity and thickness are modified. However, in HT-PEMFCs the reagent/products transport to and from the CL is slightly affected by this compression. Therefore, the actual dimensions of a new MEA were used in the model. The anode and cathode gas streams are fed in co-current and the water/methanol mixture is fed in counter current. The anode can be fed with

pure or diluted hydrogen, or with reformate. The heat is supplied to the combined system only through the end plates (vertical sidewalls - Fig. 6.2).

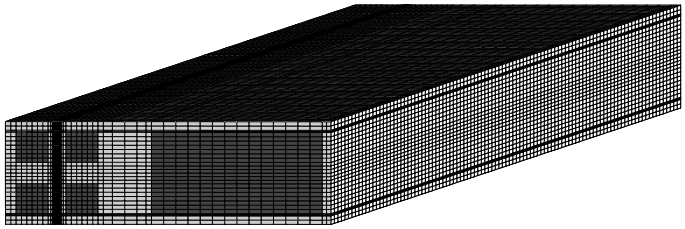

**Fig. 6.2** Computational domain and mesh configuration of the MSR-C/HT-PEMFC.

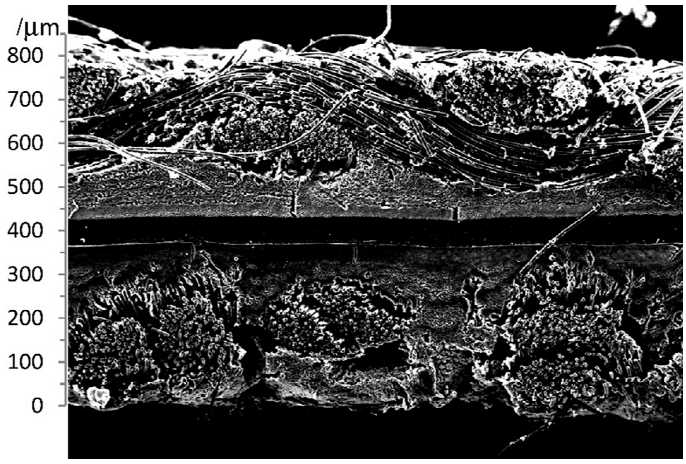


**Fig. 6.3** SEM image of the cross section of the BASF Celtec MEA P2200N.

**Table 6.1** MSR/HT-PEMFC physical properties.

| Parameter | Value |
|---|---|
| Thickness ($\delta$, μm)<br>$CL_a$, $CL_c$, $GDL_{a,c}$, membrane | 40, 30, 350, 65 |
| Reformer channel (mm) – length, width, depth | 312.5, 4, 8 |
| Ano/Cat channel (mm) – length, width, depth, rib width | 312.5, 1.5, 1.4, 1 |
| Porosity ($\varepsilon$) – GDL, CL, $MSR_{cat}$ | 0.6, 0.1, 0.32 |
| Electrolyte volume fraction ($l_m$) | 0.754 |
| Phosphoric acid doping level ($DL$) | 16.76 |
| Permeabilities ($Pe$, $m^2$) – GDL, CL, $Cat_{MSR}$ [29] | $1x10^{-13}$, $1x10^{-12}$, $1x10^{-11}$ |
| Volumetric mass density ($\rho$, $kg \cdot m^{-3}$) – $CL_{a,c}$, $GDL_{a,c}$, membrane, $MSR_{cat}$ [30,40] | 1000, 1000, 1000, 1300 |
| Specific heat capacity ($C_p$, $J.kg^{-1}.K^{-1}$) – $CL_{a,c}$, $GDL_{a,c,}$ membrane, $MSR_{cat}$[30,40] | 3300, 586, 1650, 1580, 800 |

| | |
|---|---|
| Thermal conductivity ($K$, $W \cdot m^{-1} \cdot K^{-1}$) - $CL_{a,c}$, $GDL_{a,c,}$ membrane, $MSR_{cat}$[30,40] | 1.7, 1.7, 0.95, 237.0, 0.3 |
| Electric conductivity ($\sigma_s$, $S \cdot m^{-1}$) – $CL_{a,c}$, $GDL_{a,c}$, BPP[29] | 1250, 1250, 14000 |
| Stoichiometry ($\lambda$) anode ($H_2$), cathode ($O_2$) | 1.2, 2 |
| Steam to carbon ratio (s/c) | 1.5 |
| Operating pressure ($P$, bar) | 1 |
| Operating temperature ($T$, K) | 433-473 |
| Relative humidity of gases | 0 |
| $MSR_{cat}$ mass ($m_{cat}$, kg) | 0.013 |

### 6.3.2.Mathematical model

The present work considers a three-dimensional non-isothermal model for HT-PEMFC integrated with a reformer that considers most of the significant physical processes, including CO poisoning. The model follows a single domain approach, including a full description of the transport of charge, mass and thermal energy in a single-phase system, the kinetic model for CO poisoning solved in steady and transient state, and the kinetic model for methanol steam reforming reaction.

*Main assumptions*

The following simplifications were considered in the model:

- the gas mixtures were considered ideal,
- the flow was assumed to be laminar and the effect of gravity was neglected,
- the membrane, CL, GDL, BPP and MSR catalyst were assumed isotropic and homogenous,
- the membrane was considered impermeable to all gases,
- only protons were accounted for the transport through membrane.

The model governing equations consist of conservation of mass, momentum, energy, species and charges, as described in the following subsections:

*Continuity equation:*

$$\frac{\partial(\varepsilon\rho)}{\partial t} + \nabla \cdot (\rho\vec{u}) = S_m \tag{6.1}$$

Eq. 6.1 is the mass conservation equation, where $\rho$ is the fluid volumetric mass density calculated using ideal gas equation, $\vec{u}$ is the fluid velocity vector, *t* is the time step, $\varepsilon$ is the media porosity and ∇ is the operator gradient. $S_m$ is a source term, which considers the mass production and consumption due to the electrochemical reactions, and the methanol steam reforming reactions, as follows:

$$S_m(CL_c) = \frac{M_{O_2} J_c}{4F} - \frac{M_{H_2O} J_c}{2F}$$

(6.2)

$$S_m(CL_a) = -\frac{M_{H_2} J_{a(H_2)}}{2F} - \frac{M_{H_2O} J_{a(co)}}{2F} - \frac{M_{CO} J_{a(co)}}{2F} + \frac{M_{CO_2} J_{a(co)}}{2F} \quad (6.3)$$

$$S_m(ref) = \sum_{i,j(products)} v_i M_i r_j - \sum_{i,j(reagents)} v_i M_i r_j \quad (6.4)$$

where, $M_i$ is the molar mass of the components, $J_c$, $J_{a(H2)}$ and $J_{a(CO)}$ are the volumetric current densities at the cathode and at the anode considering the electro oxidation of hydrogen and carbon monoxide, respectively. *F* is the faraday constant, $v_i$ are the stoichiometry coefficients of the reaction species at the reformer and $r_j$ is the reaction rate of reactions MSR, MD and RWGS.

*Conservation of momentum of the gas mixture:*

$$\frac{\partial}{\partial t}\left(\frac{\rho\vec{u}}{\varepsilon}\right) + \nabla\cdot\left(\frac{\rho\vec{u}\vec{u}}{\varepsilon^2}\right) = -\nabla p + \nabla.\tau + S_u \quad (6.5)$$

Eq. 6.5 is the conservation momentum equation (Navier-Stokes equation), where ∇*p* is the pressure gradient and ∇τ is the anisotropic part of the stress tensor and describes the viscous forces. The source term ($S_u$) is the pressure gradient (drop) in a porous media calculated using the Darcy's law (Eq. 6.6), which considers the intrinsic permeability, $P_e$, and the viscosity of the gases, $\mu$ calculated based on the kinetic theory [39].

$$S_u = -\frac{\mu}{P_e}\vec{u} \quad (6.6)$$

*Species conservation equation:*

$$\frac{\partial(\varepsilon\rho\omega_i)}{\partial t} + \nabla\cdot(\rho\vec{u}\omega_i) = \nabla j_i + S_i \quad (6.7)$$

Eq. 6.7 is the convection-diffusion equation, used to calculate the local mass fraction of the specie *i*, $\omega_i$. $j_i$ is the mass diffusion flux of the specie *i* and it is calculated by the Fick's law (Eq. 6.8), while $D_i^{\text{eff}}$ is the effective diffusion coefficient calculated using the Bruggman relation in a porous media (Eq. 6.9), as follows:

$$j_i = \rho D_i^{eff} \nabla \omega_i \tag{6.8}$$

$$D_i^{eff} = \varepsilon^{1.5} D_i \tag{6.9}$$

The diffusion of each species *i* ($D_i$), along with the physical properties of the gases, are presented in Table 6.2. $S_i$ are source terms due to the electrochemical reactions and the methanol steam reforming reactions, which is given as:

$$S_i(CL_c) = -\frac{M_i J_c}{n_e F} \tag{6.10}$$

$$S_i(CI_{a_{H2},a_{CO}}) = -\frac{M_i J_{a_{H2},a_{CO}}}{n_e F} \tag{6.11}$$

$$S_i = \sum_j M_i v_{i,j} r_j \tag{6.12}$$

The reaction rates ($r_j$) in the reformer were calculated using the kinetic model suggested by Peppley *et al.* [38], which considers the MSR reaction (Eq. 6.13), WGS (Eq. 6.14) and MD (Eq. 6.15):

*MSR reaction rate equation:*

$$r_{MSR} = \frac{\dfrac{k_{MSR} K^*_{CH_3O^{(1)}} p_{CH_3OH}}{p_{H_2}^{1/2}} \left(1 - \dfrac{p_{H_2}^3 p_{CO_2}}{k_{MSR} p_{H_2O} p_{CH_3OH}}\right) C_{S1}^T C_{S1a}^T S_a}{\left(1 + \dfrac{K^*_{CH_3O^{(1)}} p_{CH_3OH}}{p_{H_2}^{1/2}} + \dfrac{K^*_{OH^{(1)}} p_{H_2O}}{p_{H_2}^{1/2}} + K^*_{HCOO^{(1)}} p_{H_2}^{1/2} p_{CO_2}\right)\left(1 + \sqrt{K^*_{H^{(1a)}} p_{H_2}}\right)} \tag{6.13}$$

*Water-gas-shift reaction rate equation:*

$$r_{WGS} = \frac{k_{WGS} K^*_{OH^{(1)}} \left(\dfrac{p_{CO} p_{H_2O}}{p_{H_2}^{1/2}}\right)\left(1 - \dfrac{p_{H_2} p_{CO_2}}{k_{WGS} p_{CO} p_{H_2O}}\right) C_{S1}^{T\,2} S_a}{\left(1 + \dfrac{K^*_{CH_3O^{(1)}} p_{CH_3OH}}{p_{H_2}^{1/2}} + K^*_{HCOO^{(1)}} p_{H_2}^{1/2} p_{CO_2} + \dfrac{K^*_{OH^{(1)}} p_{H_2O}}{p_{H_2}^{1/2}} + \right)^2} \tag{6.14}$$

*Methanol decomposition reaction rate equation:*

$$r_{MD} = \frac{\dfrac{k_{MD} K^{*}_{CH_3O^{(2)}} p_{CH_3OH}}{p^{1/2}_{H_2}} \left(1 - \dfrac{p^{3}_{H_2} p_{CO_2}}{k_{MD} p_{CH_3OH}}\right) C^{T}_{S2} C^{T}_{S1a} S_a}{\left(1 + \dfrac{K^{*}_{CH_3O^{(2)}} p_{CH_3OH}}{p^{1/2}_{H_2}} + \dfrac{K^{*}_{OH^{(2)}} p_{H_2O}}{p^{1/2}_{H_2}}\right)\left(1 + \sqrt{K^{*}_{H^{(2a)}} p_{H_2}}\right)} \tag{6.15}$$

where, $k_j$ is the reaction rate constant for reaction $j$; $K_i$ is the adsorption equilibrium coefficient for species $i$; $C^{T}_{S1}$ ,$C^{T}_{S2}$, $C^{T}_{S1a}$ and $C^{T}_{S2a}$are the total catalyst surface concentrations of sites 1, 2, 1a and 2a, respectively and $S_a$ is the active surface area. The kinetic parameters were obtained from the literature [40]. The reaction rates were calculated according to the Arrhenius equation:

$$k = k_0 e^{-\frac{E_a}{RT}} \tag{6.16}$$

where, $k_0$ is the Arrhenius pre-exponential factor and $E_a$ is the activation energy. The adsorption coefficients were modified according to van't Hoff equation (Eq. 6.17) using the enthalpy ($\Delta H$) and entropy ($\Delta S$) of adsorption of the species:

$$\ln(K_i) = \frac{\Delta H}{RT} + \frac{\Delta S}{R} \tag{6.17}$$

**Table 6.2** Physical and transport properties [29-33]

| Property | Value |
|---|---|
| | $D^{T}_{i} = D^{ref}_{i} \left(\dfrac{T}{333.15}\right)^{1.5} \left(\dfrac{101325.0}{P}\right)$ (6.18) |
| Diffusivity of the gas species ( $m^2 \cdot s^{-1}$) | $D^{ref}_{H_2} = 1.055\times10^{-4}$<br>$D^{ref}_{O_2} = 2.652\times10^{-5}$<br>$D^{ref}_{CO_2} = 3.2348\times10^{-5}$<br>$D^{ref}_{CO} = 3.2348\times10^{-5}$<br>$D^{ref}_{H_2O(anode,MSR)} = 1.055\times10^{-4}$<br>$D^{ref,}_{H_2O(cathode)} = 2.982\times10^{-5}$<br>$D^{ref}_{CH_3OH} = 3.2348\times10^{-5}$ |
| Viscosity of the gas species ($kg \cdot m^{-1} \cdot s^{-1}$) | $\mu^{T}_{H_2} = 3.205\times10^{-3} \left(\dfrac{T}{293.85}\right)^{1.5} \left(\dfrac{1}{T+72}\right)$ (6.19) |

$$\mu_{H_2O}^{T} = 7.512\times10^{-3}\left(\frac{T}{291.15}\right)^{1.5}\left(\frac{1}{T+120}\right) \quad (6.20)$$

$$\mu_{O_2}^{T} = 8.46\times10^{-3}\left(\frac{T}{292.85}\right)^{1.5}\left(\frac{1}{T+127}\right) \quad (6.21)$$

$$\mu_{Others}^{T} = 8.46\times10^{-3}\left(\frac{T}{292.85}\right)^{1.5}\left(\frac{1}{T+127}\right) \quad (6.22)$$

Water saturation pressure (bar)

$$p_{sat} = 0.68737T^3 - 732.39T^2 + 263390T - -31919000 \quad (6.23)$$

Relative humidity

$$RH = \begin{cases} \dfrac{x_{H_2O}p}{p_{sat}} \text{ (in CL)} \\ \dfrac{Rh_{CL(ano)} + Rh_{CL(cat)}}{2} \text{ (in membrane)} \end{cases} \quad (6.24)$$

Specific heat capacities ($J\cdot kg^{-1}\cdot K^{-1}$)

$$Cp_{H_2} = 14283;\ Cp_{O_2} = 919.31;\ Cp_{H_2O} = 2014$$
$$Cp_{N_2} = 1042;\ Cp_{CO_2} = 919.31;\ Cp_{CO} = 919.31;\ Cp_{CH_3OH} = 919.31$$

Thermal conductivities ($W\cdot m^{-1}\cdot K^{-1}$)

$$\lambda_{H_2} = 0.1672; \qquad \lambda_{O_2} = 0.0246; \qquad \lambda_{H_2O} = 0.0261$$

Change in Entropy ($J\cdot mol^{-1}\cdot s^{-1}$)

$$\Delta S = -44.500;$$

*Energy equation*

$$\frac{\partial}{\partial t}\left(\varepsilon\rho H_{0,g} + (1-\varepsilon)\rho H_{0,s}\right) + \nabla.\left(\rho\vec{u}\left(\sum_{i}^{N_c} y_i \int_{T_{ref}}^{T} Cp_i dT\right)\right) = \nabla\left(\lambda_{eff}\nabla T\right) - \nabla\vec{u}P + S_T \quad (6.25)$$

where, $Cp_i$ is the specific heat capacity of species *i*, $\lambda_{eff}$ is the effective thermal conductivity, which takes into account the thermal conductivity in the solid and gas phase and $T$ is the absolute temperature. Heat conduction and pressure work were assumed to drive the energy flux, represented by the first two terms in the right part of Eq. 6.25. $S_T$ is the source term which includes the heat flux due to the electrochemical reaction, ohmic resistance, activation losses and MSR chemical reaction, as follows.

$$S_T(\text{membrane}) = \|\nabla\varphi_m\|^2 \sigma_m^{eff} \quad (6.26)$$

$$IS_T(\text{GDL,BPP}) = \|\nabla\varphi_s\|^2 \sigma_s^{eff} \quad (6.27)$$

$$S_T(\text{CL}_c) = \left|\frac{j_{cat}}{2F}\right|(T\Delta S) + |\eta\, j_{cat}| + \|\nabla\varphi_s\|^2 \sigma_s^{eff} + \|\nabla\varphi_m\|^2 \sigma_m^{eff} \quad (6.28)$$

$$S_T(\text{CL}_a) = |\eta\, j_{ano}| + \|\nabla\varphi_s\|^2 \sigma_s^{eff} + \|\nabla\varphi_m\|^2 \sigma_m^{eff} \quad (6.29)$$

$$S_T(\mathrm{MSR}) = \sum_{i=1}^{N}\left(\Delta H_{k,298} + \sum_i \nu_i \int_{298}^{T} Cp_i dT\right)(r_k) \tag{6.30}$$

The combined MSR-C/HT-PEMFC device was experimentally heated by electric resistances placed at the endplates and controlled by a proportional integral derivative controller (PID controller). The PID controller calculates the error, which is the difference between the set point and the measured variable. The control variable, in this case the heating power, is calculated over time to minimize the error value. The PID control equation can be written, as follows:

$$\begin{aligned} &P_{heat}(t) = KP\,e(t) + KI\int_0^t e(t)\,dt + KD\frac{de(t)}{dt}, \\ &0\ W \le P_{heat}(t) \le 120\ W \end{aligned} \tag{6.31}$$

where, $P_{heat}(t)$ is the heating power as function of time, $e(t)$ represents the error value (the difference between the set point and the measured temperature), in this case measured at the geometric centre of MSR-C/HT-PEMFC device. The heating power is the sum of the proportional gain (*KP*) multiplied by the magnitude of the error plus the integral gain (*KI*) multiplied by the integral of the error plus the derivative gain (*KD*) times the derivative of the error. The heating power was converted to heat flux and implemented in Fluent® as a boundary condition.

*Current conservation equations*

The electrochemical equations consider the hydrogen oxidation reaction at the anode and the oxygen reduction reaction at the cathode; the current is originated by the potential difference between the anode and cathode. In the catalyst layer, there is a protonic current and an electronic current. Since the electrodes are electroneutral, the charge conservation in the catalyst layer can be expressed by Eq. 6.32:

$$\nabla.\left(\vec{i}_s\right) + \nabla.\left(\vec{i}_m\right) = 0.0 \tag{6.32}$$

The current density in the CL, GDL and BPP (Eq. 6.33) and in the membrane and CL (Eq. 6.34) and can be obtained by the Ohm's law:

$$-\sigma_s^{eff}\nabla\varphi^s = \vec{i}_s \tag{6.33}$$

$$-\sigma_m^{eff}\nabla\varphi^m = \vec{i}_m \tag{6.34}$$

The conservation equations in the CL, GDL and BPP (Eq. 6.35) and in the membrane and CL (Eq. 6.36) are given by the gradient of the Eq. 6.33 and 34, respectively:

$$\nabla.\left(-\sigma_s^{eff}\nabla\varphi_s\right) = S_{\varphi_s} \tag{6.35}$$

$$\nabla.\left(-\sigma_m^{eff}\nabla\varphi_m\right) = S_{\varphi_m} \tag{6.36}$$

where, $\varphi_S$ and $\varphi_m$ are the electric and protonic overpotential respectively; $S_{\varphi_S}$and $S_{\varphi_m}$ are the source terms; the $\sigma_S^{eff}$ and $\sigma_m^{eff}$ are the effective electron and proton conductivities and are calculated by Bruggeman equation for porous medium (Eq. 6.37):

$$\sigma_m^{eff} = l_m^{1.5}\sigma_m, \qquad \sigma_s^{eff} = (1-\varepsilon-l_m)^{1.5}\sigma_s \tag{6.37}$$

where, $\sigma_m$ is the electrolyte protonic conductivity and $l_m$ is the polymer electrolyte volume fraction in the CL. Several empirical relations are reported in literature to calculate electrolyte protonic conductivity; most of them follow an Arrhenius equation law behaviour [26]. The electrolyte protonic conductivity ($\sigma_m$) depends on humidity (*RH*), temperature and membrane doping level (*DL*), and can be calculated by Eq. 6.38 [30]. The *DL* and $l_m$ were estimated using electrolyte proton conductivity determined by electrochemical impedance spectroscopy (EIS) in dry conditions at 0.05 A·cm$^2$.

$$\sigma_m = \frac{ab}{T}e^{\frac{Ea}{RT}} \tag{6.38}$$

$$a = 168DL^3 - 6324DL^2 + 65760DL + 8460 \tag{6.39}$$

$$E_a = -619.6DL + 21750 \tag{6.40}$$

$$b = \begin{cases} b = 1 + (0.01704T - 4.767)RH, & 373.15 \le T \le 413.15; \\ b = 1 + (0.1432T - 56.89)RH, & 413.15 \le T \le 453.15; \\ b = 1 + (0.7T - 309.2)RH, & 453.15 \le T \le 473.15 \end{cases} \tag{6.41}$$

The $S_{\varphi_S}$and $S_{\varphi_m}$(source terms) of the Eq. 6.35 and 36 are the volumetric exchange current densities, calculated from Butler-Volmer equation.

$$J_{a,H_2} = ai_{0,a}\theta_{H_2}\left\{\exp\left(\frac{\alpha_a}{RT}F\eta_a\right) - \exp\left(-\frac{\alpha_c}{RT}F\eta_a\right)\right\} \tag{6.42}$$

$$J_c = -ai_{0,c}\left(\frac{C_{O_2}}{C_{O_2}^{ref}}\right)\left\{\exp\left(\frac{\alpha_a}{RT}F\eta_c\right) - \exp\left(-\frac{\alpha_c}{RT}F\eta_c\right)\right\} \tag{6.43}$$

$$J_{a,CO} = ai_{0,CO}\theta_{CO}\exp\left(\frac{\alpha_{CO}}{RT}F\eta_a\right) \tag{6.44}$$

where $\eta_a$ and $\eta_c$ are the over-potential in anode and cathode, $ai_{0,a}$ and $ai_{0,c}$ are the exchange current density of the anode and cathode, $\alpha_a$ and $\alpha_c$ are the charge transfer coefficient of the anode and cathode; the parameters values are summarized in Table 6.3. The electro-oxidation of CO is also considered in the model (Eq. 6.44), despite the small effect in the overall current density; thus, $ai_{0,CO}$ and $\alpha_{CO}$ are the exchange current density and charge transfer coefficient for CO, respectively.

**Table 6.3** Electrochemical parameters

| **Parameter** | **anode** | **Cathode** |
|---|---|---|
| Over-potential, $\eta$ (V) | $\eta = \varphi^s - \varphi^m$ (6.45) | $\eta = \varphi^s - \varphi^m$ (6.46) |
| Equilibrium-potential, $U_0$ (V) | $U_0 = 1.1669\text{-}2.4\text{x}10^{-4}(T\text{-}373.15)$ (6.47) | |
| exchange current density × specific electro-active area, $ai_0$ (A·m$^{-3}$) | $ai_{0,a}^{ref}\exp\left[-1400\left(\frac{1}{T}-\frac{1}{353.15}\right)\right]$ $ai_{0,a}^{ref} = 1\times10^{8}$ (6.48) | $ai_{0,c}^{ref}\exp\left[-7900\left(\frac{1}{T}-\frac{1}{353.15}\right)\right]$ $ai_{0,c}^{ref} = 70$ (6.49) |
| Reference concentrations, $C_i^{ref}$ (mol·m$^{-3}$) | 40.88 | 40.88 |
| Transfer coefficients, $\alpha_{H2}$, | 1 | 0.97 |

The hydrogen coverage ($\theta_{H2}$) equation is a modification of the Butler-Volmer equation (Eq. 6.38), to include the CO poisoning effect. The $\theta_{H2}$ depends on the adsorption, desorption and electrochemical oxidation of the adsorbed species on the catalyst surface (Eq. 6.50 – 6.53):

$$2Pt+H_2 \underset{b_{th}}{\overset{k_{th}}{\leftrightarrow}} 2(Pt\text{-}H) \quad (6.50)$$

$$(Pt\text{-}H) \xrightarrow{k_{eh}} H^+ + e^- + Pt \quad (6.51)$$

$$Pt+CO \underset{b_{fc}}{\overset{k_{fc}}{\leftrightarrow}} (Pt\text{-}CO) \quad (6.52)$$

$$H_2O+(Pt\text{-}CO) \xrightarrow{k_{ec}} Pt+CO_2+H^+ + e^- \quad (6.53)$$

The Eq. 6.50 and 6.52 represents the chemisorption of $H_2$ and CO, and Eq. 6.51 and 53 are the electrochemical oxidation of the adsorbed species. The surface coverage of hydrogen and CO (Eq. 6.54 and 6.55, respectively) were determined based on the

model developed by Springer *et al* [37] considering the previous reactions (Eq. 6.50 – 6.53):

$$C_{Pt}^{*}\frac{\partial(\theta_H)}{\partial t} = k_{fh}p_{H_2}(1-\theta_{CO}-\theta_H)^n - b_{fh}k_{fh}\theta_H^n - i_{0,a}\theta_{H_2}\left\{\exp\left(\frac{\alpha_a}{RT}F\eta_a\right) - \exp\left(-\frac{\alpha_c}{RT}F\eta_a\right)\right\} \tag{6.54}$$

$$C_{Pt}^{*}\frac{\partial(\theta_{CO})}{\partial t} = k_{fc}p_{CO}(1-\theta_{CO}-\theta_H) - b_{fc}k_{fc}\theta_{CO} - i_{0,CO}\theta_{CO}\exp\left(\frac{\alpha_{CO}}{RT}F\eta_a\right) \tag{6.55}$$

where, $k_{fh}$ and $k_{fc}$ are the hydrogen an CO adsorption rates, respectively and $b_{fh}$ and $b_{fc}$ are the hydrogen an CO desorption rates and $C_{Pt}$ is the molar area density of catalyst active sites multiplied by the Faraday constant (assumed equal to 1 for unsteady simulations). In this work, a second-order ($n$ = 2) hydrogen adsorption reaction was considered. The adsorption and desorption rates were calculated according to the Arrhenius equation, using the kinetic parameters presented in Table 6.4. $\theta_{H2}$ and $\theta_{CO}$ were solved in steady and unsteady state. Eq. 6.56 and 6.57 show the analytical solution of $\theta_{CO}$ and $\theta_{H2}$ in steady state [31-33]. Eq. 6.58 and 6.59 shows the analytical solution of $\theta_{CO}$ and $\theta_{H2}$ in unsteady state, calculated in this work.

$$\theta_{H_2,steady} = \frac{2a_1(1-\theta_{CO})+a_3-\sqrt{\left[2a_1(1-\theta_{CO})+a_3\right]^2-4a_1(a_1-a_2)(1-\theta_{CO})^2}}{2(a_1-a_2)} \tag{6.56}$$

$$\theta_{CO,steady} = \frac{b_1(1-\theta_{H_2})}{b_1+b_2+b_3} \tag{6.57}$$

$$\theta_{H_2,unsteaty} = \frac{2a_1(1-\theta_{CO})+a_3}{2(a_1-a_2)} - \frac{\sqrt{\left[2a_1(1-\theta_{CO})+a_3\right]^2-4a_1(a_1-a_2)(1-\theta_{CO})^2+\rho\left(4a_1(1-\theta_{CO})+2a_3+4\theta_{H_2}^{t-1}(a_2-a_1)\right)+\left(C_{Pt}^{*}\right)^2}+C_{Pt}^{*}}{2(a_1-a_2)} \tag{6.58}$$

$$\theta_{CO,unsteady} = \frac{C_{Pt}^{*}\theta_{CO}^{t-1}+b_1(1-\theta_{H_2})}{C_{Pt}^{*}+b_1+b_2+b_3} \tag{6.59}$$

The transient term (time step, $\Delta t$) only appears in the coefficients (Eq. 6.60 – 6.65) when $\theta_{H2}$ and $\theta_{CO}$ are calculated in unsteady state;

$$a_1 = k_{fc}p_{CO} = k_{fc}C_{CO}RT\Delta t \tag{6.60}$$

$$a_2 = b_{fc}k_{fc}\Delta t \tag{6.61}$$

$$a_3 = i_{0,CO} \exp\left(\frac{\alpha_{CO}}{RT} F\eta_a\right)\Delta t$$

(6.62)

$$b_1 = k_{fh} p_{H_2} \Delta t = k_{fh} C_{H_2} RT \Delta t$$

(6.63)

$$b_2 = b_{fh} k_{fh} \Delta t \tag{6.64}$$

$$b_3 = a i_{0,a} \left\{ \exp\left(\frac{\alpha_a}{RT} F\eta_a\right) - \exp\left(-\frac{\alpha_c}{RT} F\eta_a\right)\right\}\Delta t \tag{6.65}$$

**Table 6.4** Kinetic parameters for the CO model [33].

| Parameter | Value |
|---|---|
| Hydrogen adsorption rate, $k^0_{fh}$ ($A \cdot m^{-2} \cdot Pa^{-1}$) | 1.597 |
| Activation energy of hydrogen adsorption, $E_{a,fh}$ ($J \cdot mol^{-1}$) | $1.04 \times 10^4$ |
| Hydrogen desorption rate, $k^0_{bh}$ (Pa) | $1.51 \times 10^{15}$ |
| Activation energy of hydrogen desorption, $E_{a,bh}$ ($J \cdot mol^{-1}$) | $8.79 \times 10^4$ |
| CO adsorption rate, $k^0_{fc}$ ($A \cdot m^{-2} \cdot Pa^{-1}$) | $1.61 \times 10^4$ |
| Activation energy of CO adsorption, $E_{a,fc}$ ($J \cdot mol^{-1}$) | $4.73 \times 10^4$ |
| CO desorption rate, $k^0_{bc}$ ($A \cdot m^{-2} \cdot Pa^{-1}$) | $2.26 \times 10^{23}$ |
| Activation enegy of CO desorption, $E_{a,bc}$ ($J \cdot mol^{-1}$) | $1.96 \times 10^5$ |
| CO exchange current density x specific electro-active area, $ai_{0,CO}$ ($A \cdot m^{-3}$) | $2.0 \times 10^3$ |
| CO transfer coefficients, $\alpha_{CO}$ | 0.5 |
| Molar area density of catalyst sites, $p$ ($mol \cdot cm^{-2}$) | 6.0 |
| Variation of free Energy of CO adsorption ($J \cdot mol^{-1}$) | 5.544 |

*Boundary and Initial condition*

The boundary conditions considered for the MSR-C/HT-PEMFC device are:

- at the inlet of anode and cathode, the mass fluxes in the channels were calculated based on the hydrogen and oxygen stoichiometry at a defined current density; the mass flux in the reformer was calculated based on the space-time-ratio ($m_{cat}/F_{MeOH}$). When reformate was used as anode fuel, the outlet composition and mass flux of the reformer channel was used as the inlet of the anode channel;
- at the outlets, the pressure was considered to be constant and equal to a specified value and gradients of temperature and species mass fraction were assumed to be equal to zero;

- at the walls, the flow obeys to the no slip condition. At the interfaces between bipolar plates, channels, GDL, CL, membrane, the boundaries were coupled for the electronic potential and temperature;
- potentiostatic boundary conditions were imposed at the surfaces of the bipolar plates (terminal surface). The electronic phase potential of the cathode and anode was assumed $\emptyset_s = 0$ and $\varphi_s = U_0 - V_{cell}$ respectively.

### 6.3.3. Numerical Procedure

The simulations were conducted using FLUENT, a platform that uses the finite-volume method to solve the differential equations. The equations, physical properties and boundary conditions of the fuel cell and reformer were implemented by developing User Defined Functions (UDF) written in C++, compiled and loaded in FLUENT. The equations of the electric potentials, PID control and CO poisoning effect were added by using User Defined Scalars (UDS). The governing equations were discretized with a second-order spatial and temporal schemes. The under relaxation was also adjusted to handle the convergence problems. The simulations were carried using potentiostatic boundary conditions starting with cell potentials close to the open-circuit voltage and progressing slowly to lower voltages for a faster stepwise convergence. In all the simulations, strict convergence criteria with residuals of $10 \times 10^{-8}$ were chosen for all variables. The computational grid used for modelling the 3D straight channel MSR-C/HTPEMFC had approximately $1.1 \times 10^5$ grid cells assuring that results output were not influenced by the grid (grid independence). The modelling domain consisted of 10 different zones, including the anode and cathode flow channels, bipolar plates, gas diffusion layers and catalyst layers, membrane and MSR catalyst bed (Fig. 6.2).

### 6.3.4. Validation of the fuel cell model

The implementation of the fuel cell and CO poisoning model was validated against the experimental data reported by Das *et al.* [41], considering the same fuel cell geometry and parameters reported by Oh *et al.* [33] (Fig. 6.4). The simulation results (Fig. 6.4) show, in general, a good agreement with the experimental results, considering both pure

hydrogen and hydrogen contaminated with CO as fuels. The CO model can input, in general, a correct drop in volumetric exchange current density (Butler-Volmer equation, Eq. 6.42).

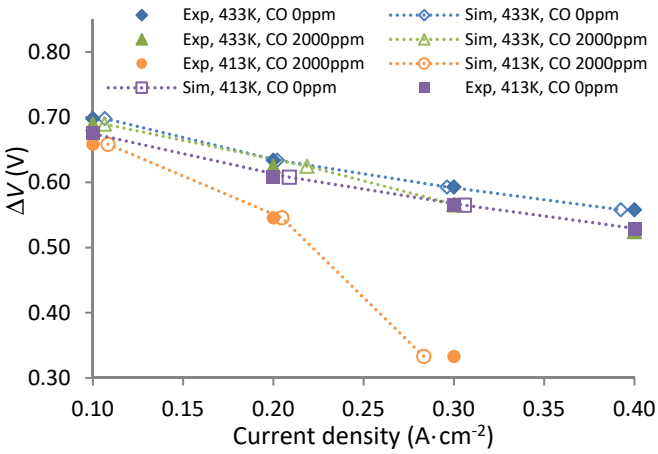


**Fig. 6.4** Electric potential difference as function current density at temperatures of 413 K and 433 K for a CO content of 0 ppm and 2000 ppm; lines represent the model results – experimental data from [41] (lines were added for readability).

## 6.4. Experimental

To achieve the heat integration between the MSR-C and the HT-PEMFC, a novel bipolar plate made of gold plated aluminium was designed, featuring a fuel cell flow field in one side and a reformer flow field in the other (Fig. 6.1). A used membrane electrode assembly (MEAS) was a Celtec P2200N from BASF with an active area of 45 $cm^2$. The reforming reaction was carried out using 40 g of commercial catalyst ($CuO/ZnO/Al_2O_3$) from BASF (RP-60). The MSR-C performance was determined at different space-time-ratios ($m_{cat}/F_{MeOH}$) and operating temperatures (between 443 K and 473 K). The HT-PEMFC characterization was performed with $\lambda_{Air}$ of 2 and $\lambda_{H2}$ of 1.2, between 433 K and 473 K; the anode was fed with different fuels: pure hydrogen, gas mixture with volume fractions of 75 % of $H_2$ and 25 % of $CO_2$ and reformate supplied directly from the MSR. A

more detailed description of the MSR-C/HT-PEMFC combined unit can be found in the literature [19].

An unused Celtec P2200N MEA was characterized by field emission scanning electron microscopy (SEM) in order to determine the thickness of the membrane, anode and cathode catalyst layer and anode and cathode gas diffusion layer.

## 6.5. Results and Discussion

### 6.5.1. Performance of the MSR-C

The MSR-C and HT-PEMFC modelling results were validated against experimental data already published by the authors [19]. Fig. 6.5 shows the simulated and experimental results for the methanol conversion using the MSR-C loaded with BASF RP-60 catalyst (Fig. 6.5) at different operating temperatures.

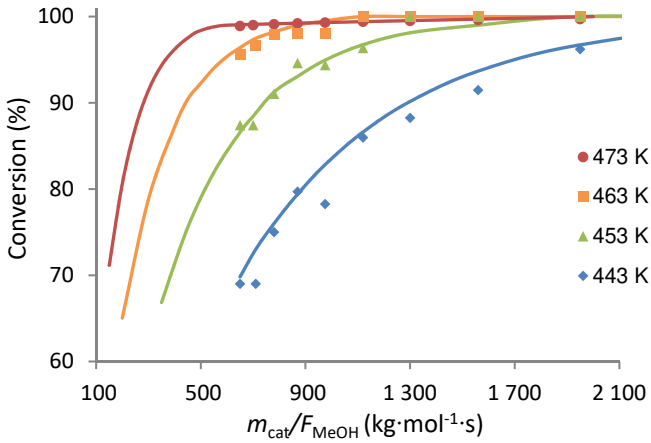


**Fig. 6.5** Experimental (dots) and simulated (lines) methanol conversion as a function of space-time ratio and for different temperatures at $P_{out}$ = 1 bar and S/C = 1.5 – experimental data [19].

The simulation results present a good agreement with the experimental data for the studied operating conditions; the maximum relative difference between experimental and simulated results is lower than 5 %. To improve the fitting between experi-

mental and simulated results the parameters in the Eq. 6.13 – 6.15, related to the reforming catalyst surface area ($S_a$), were adjusted. The value used in the simulation was $81x10^3$ $m^2 \cdot kg^{-1}$ instead of $102x10^3$ $m^2 \cdot kg^{-1}$ as reported in the literature for the BASF RP-60 catalyst [40]; the smaller active surface area was assigned to larger catalyst particle size used in this work, for producing the reforming experimental results, almost the double of the size [19].

The results show that the methanol conversion is highly dependent on the temperature and full methanol conversion, at low temperatures, can only be achieved for high space-time values, Fig. 6.5. At low temperatures (such as 443 K), the methanol conversion is very sensitive to temperature variation, becoming less sensitive at higher temperatures (such as 473 K). It should be noted that the MSR-C should operate at methanol conversions above 90 % (2.3 % of volume methanol fraction) to minimize the poisoning effect of methanol in the fuel cell [42, 43].

Fig. 6.6 shows the simulated methanol conversion as a function of hydrogen production at different temperatures. In the top horizontal axis of Fig. 6.6, it is the electrical current assuming 100 % of coulombic efficiency and $\lambda_{H2} = 1.2$. A hydrogen production of 110 $cm^3 \cdot min^{-1}$ is reached with a complete conversion of methanol at 453 K, corresponding to *ca.* 15 A, while a hydrogen production 210 $cm^3 \cdot min$ is reached with 90 % of methanol conversion production, corresponding to ca. 25 A. Higher temperatures significantly enhance the MSR reaction kinetics. At 473 K the hydrogen production was 550 $cm^3 \cdot min^{-1}$ for a methanol conversion of 90 %, corresponding to *ca.* 60 A. Pan *et al.* [13] reported similar results using an *in-house* catalyst, with a maximum hydrogen yield at full methanol conversion of 200 $dm^3 \cdot h^{-1} \cdot kg^{-1}$ at 453 K and 500 $dm^3 \cdot h^{-1} \cdot kg^{-1}$ at 473 K.

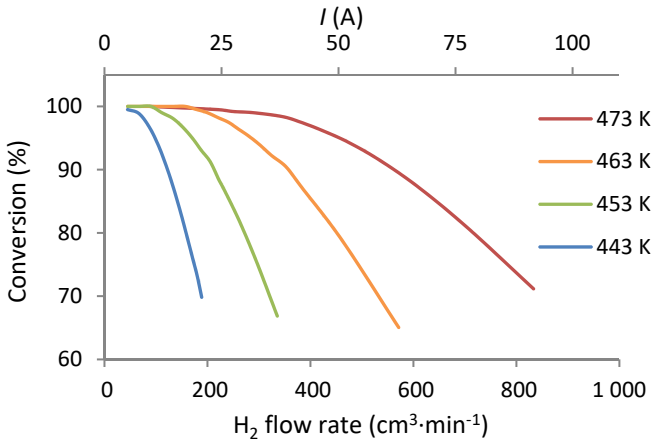


**Fig. 6.6** Simulated methanol conversion as a function of hydrogen flow rate (product) and the calculated electrical current assuming 100 % coulombic efficiency and $\lambda_{H2} = 1.2$.

Fig. 6.7 shows the simulation results of the CO production as a function of the space-time ratio at different operating temperatures. The CO production was not validated against any experimental data, since it was not available [19]. The model parameters were obtained from the literature [40] except the active surface area (Eq. 6.13 – 6.15) that has been modified, as described above. The reverse water gas shift reaction at temperatures lower than 473 K produces most of the carbon monoxide present in the reformate stream, as a result CO concentration increases with the partial pressure of hydrogen and carbon dioxide increases. The CO concentration in the reformate stream, at *ca.* 473 K and high space-time ratio, can reach considerable high values (>3 % volume fraction). The CO tolerance of HT-PEMFC also increases significantly with the temperature. At 473 K and low current densities (<0.5 $A \cdot cm^{-2}$) the HT-PEMFC can tolerate up to 5 % of CO in the fuel without significant drop in performance [44].

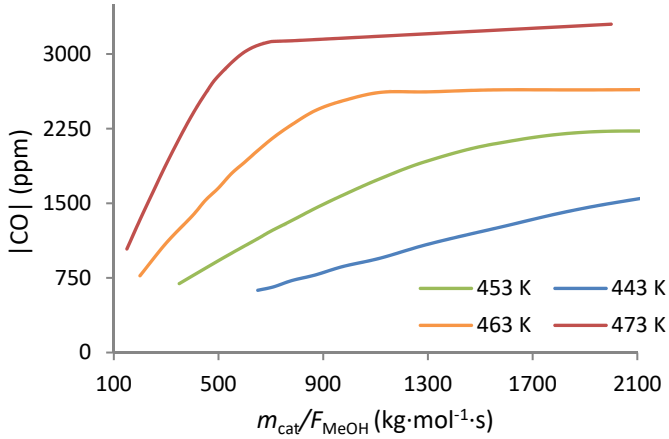


**Fig. 6.7** Simulated CO concentration as a function of space-time ratio and for different temperatures and at $P_{out}$ = 1 bar and $S/C$ = 1.5.

### 6.5.2. Performance of HT-PEMFC fed with $H_2$

Concerning the simulation of the HT-PEMFC, all parameters were obtained from the literature [29-33] except the exchange current densities and the transfer coefficients. The values of these two parameters were obtained through a fitting of the model to the experimental results shown in Fig. 6.8. The initial guess was obtained from the Tafel equation. The optimization process was based on the minimization of the sum of the squared residues between the simulated and experimental values. The fitted exchange current densities $ai^{ref}_{0,a}$ = 1x10$^8$ A·m$^{-3}$ and $ai^{ref}_{0,c}$ = 70 A·m$^{-3}$ are within the range of values reported in the literature [26]. The fitted transfer coefficients, $\alpha_a$ = 1.00 and $\alpha_c$ = 0.97, are similar to the ones reported by Ubung *et al.* [45] for the same type of commercial MEAs, $\alpha_a$ = 1.00 and $\alpha_c$ = 1.00 The transfer coefficient was kept constant for all the studied temperatures, despite it could be affected by the doping level and operating temperature [46]. The transfer coefficients play an important role on the shape of the polarization curves; higher transfer coefficients originate a faster drop in the region of the activation losses, at lower current densities, and the polarization curve becomes more flat. A change in the exchange current density, on the other hand, keeps the shape of the polarization curve, shifting the curve to lower or higher voltages (parallel curves).

Fig. 6.8 shows the experimental and simulated polarization curves obtained with the HT-PEMFC at 433 K, 453 K and 473 K, with pure hydrogen. The simulation results

present a very good agreement with the experimental data for the studied conditions; the maximum relative difference between experimental and simulated results was less than 5 %. The model was able to reproduce the improvement of electrochemical reaction rates with the temperature increase by shifting up correctly the polarization curve.

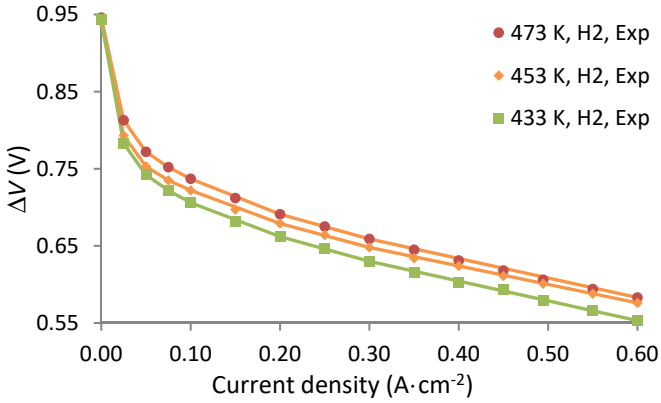


**Fig. 6.8** Modelling (lines) and experimental (dots) results of the electric potential difference as a function of the current density at temperatures of 433 and 453 K using pure hydrogen as fuel – experimental data from [19].

### 6.5.3. Performance of the combined unit

The simulation of the combined MSR-C/HT-PEMFC unit (HT-PEMFC fed directly with the produced reformate stream), was also performed and the simulated values were compared to experimental ones (Fig. 6.9).

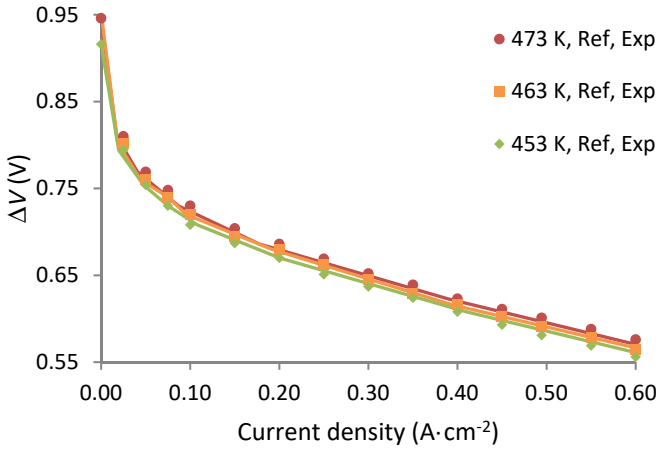


**Fig. 6.9** Modelling (lines) and experimental (dots) results of the electric potential difference as function current density at temperatures of 433 and 453 K using reformate as fuel – experimental data from [19].

The transfer coefficients and exchange current densities values obtained fitting the model to the experimental values when the HT-PEMFC was fed with pure hydrogen fuel were kept. For the model simplification, methanol was assumed as an inert in the fuel cell operation. However, methanol has been reported as poisoning agent for HT-PEMFC due to crossover to the cathode side and subsequent electrocatalytic oxidation originating mixing potentials [42, 43]. Araya *et al.* [43] fed a hydrogen stream containing a water/methanol mixture with a volume fraction of 1.5 % for each component to a HT-PEMFC working at 433 K, and concluded that the performance of the FC was not affected. In the present study, the highest methanol concentration in the reformate stream was obtained at 453 K and 0.6 $A \cdot cm^{-2}$ with a volume fraction of *ca. 2* % (methanol conversion of ca. 90 %); it is also expected that at higher temperatures the methanol tolerance increases. Considering this simplification, the model fitted quite well with the experimental data for the studied temperatures (453 K-473 K), as depicted in Fig. 6.9. The HT-PEMFC shows lower performance with reformate fuel (Fig. 6.9) when compared to pure hydrogen fuel (Fig. 6.8); this decrease was assigned to the hydrogen dilution due to presence of water vapour, $CO_2$ and the presence of unreacted methanol and CO. The improvements of electrochemical kinetics with temperature were well predicted by the

model – Fig. 6.9. The performance increase of the combined MSR-C/HT-PEMFC unit, especially for high current densities, should also be attributed to the higher hydrogen concentration.

The combined MSR-C/HTPEMFC unit displays higher energy conversion efficiency and has a simpler design when compared with the units working separately. The small decrease in the performance when reformate is used as fuel, compared to pure hydrogen, demonstrates the real possibility of operating both MSR reaction and electrochemical reaction at the same temperature. The MSR-C/HT-PEMFC performance is, however, highly dependent on the reformer capacity to convert efficiently the methanol into hydrogen. Fig. 6.10 shows the influence of the operating temperature on the maximum power density, for a methanol conversion >90 %. The simulations were not performed at 433 K due to the low methanol conversion, despite being the recommended operating temperature of BASF Celtec MEAs. The MSR-C/HT-PEMFC unit, operated at 473 K, produced a power density of *ca.* 0.5 $W \cdot cm^{-2}$ at 1.3 $A \cdot cm^{-2}$. The operation of the combined unit at this temperature is very attractive, but it is well known that high operating temperatures (>433) lead to faster degradation of the MEA, mainly due to the catalyst particle size growth and phosphoric acid losses [47, 48]. The operation of combined MSR-C/HTPEMFC unit should adapt the operating temperature to the current density, in order to minimizing the degradation of the components.

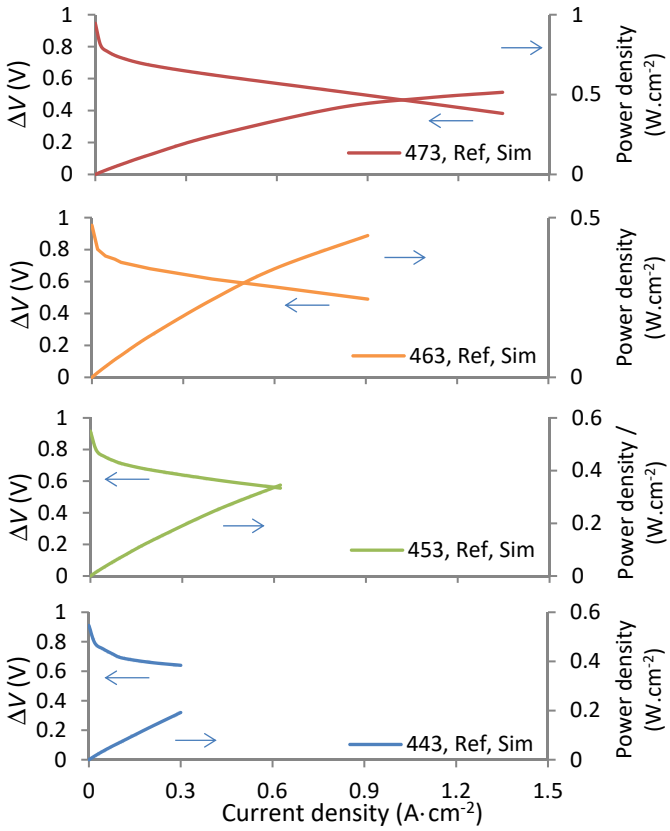


**Fig. 6.10** Simulated electric potential difference and power density as a function of the current density for different operating temperatures, considering a minimum methanol conversion of 90 %.

### 6.5.4. Thermal sustainability of the combined unit

The HT-PEMFC can produce more heat than the required to run the MSR reaction, but the heat is not distributed uniformly in the MSR-C/HT-PEMFC unit. Fig. 6.11 shows the simulated temperature distribution on the MSR-C/HT-PEMFC at 453 K (end plates) and current densities between 0.1 A·cm$^{-2}$ and 0.6 A·cm$^{-2}$. Fig. 6.12 shows the simulated average temperature inside the reformer, channel anode and channel cathode at different current densities.

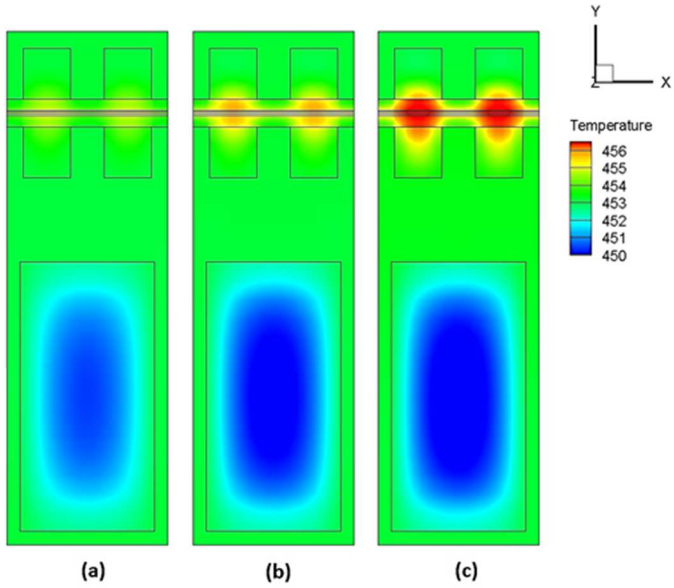


**Fig. 6.11** Temperature distribution on the MSR-C/HT-PEMFC at 453 K and operating at 0.1 A·cm$^{-2}$ (a), 0.3 A·cm$^{-2}$ (b), 0.6 A·cm$^{-2}$ (c); Temperature profiles (at right) and the temperature inside the reformer, channel anode and channel cathode (at left).

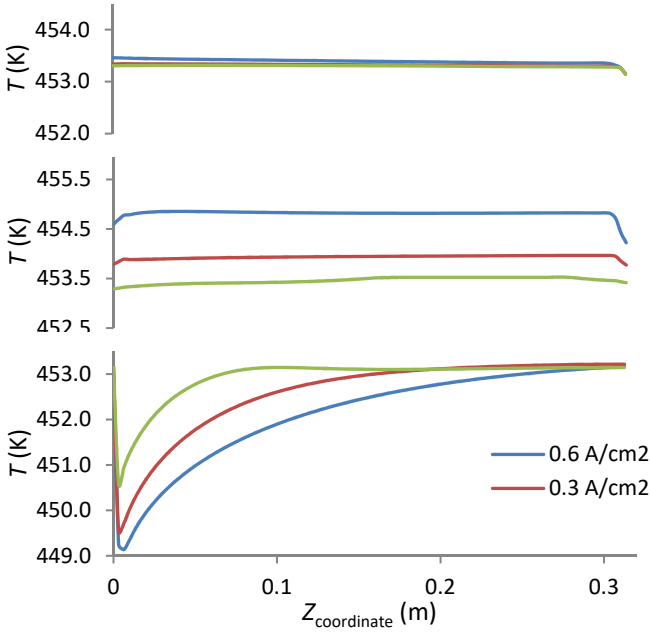


**Fig. 6.12** Average temperatures inside the cathode channel (a), anode channel (b) and reformer (c), at different current densities with an external temperature of 453 K.

As the fuel cell current density increases, it generates more heat, due to the electrochemical reaction and joule effect (ohmic losses in the electrolyte); however, the heat consumption also increases for running the reformer, evaporating and heating up the feeding water/methanol mixture (Fig. 6.11). The temperature at the cathode channels shows to be less dependent of the operating current density than the temperature at the anode channel (Fig. 6.12). This fact is assigned to the higher flow rate at cathode side, the higher heat capacity of the air and the higher stoichiometry used. Close to the inlet of the reformer channel, a temperature drop is observed, caused by the high MSR reaction rate. The temperature profile along the reformer channel is related to the MSR reaction rate.

To use efficiently the heat produced by the fuel cell a good thermal insulation is required. Fig. 6.13 shows the heat flux on the end plates required to operate the MSR-C/HT-PEMFC at 453 K as a function of thermal insulator thickness (glass wool). For thin layers of thermal insulator most of the heat produced by the fuel cell is lost to the surroundings and the thermal equilibrium is reached at very high current densities (Fig. 6.13). The heat flux required to maintain the temperature constant (453 K) increases fast when the thickness of the thermal insulator is reduced bellow 1 cm (Fig. 6.13). A suitable thermal insulation should be used to achieve the thermal equilibrium at low current densities; the glass wool thermal insulation should have a thickness between 3 cm and 4 cm, above this value, no significant gain in the heat flux is observed. Considering that the combined unit was insulated with 3 cm thick of glass wool, the heat flux required to maintain the operation at 453 K (at the end plates) could be determined as a function of current density (Fig. 6.14). The behaviour of the heat flux as function of the current density is practically linear and the interception of the curve with the x-axis represents the current density at which the thermal equilibrium can be found - where the heat produced is equal to all the heat losses. The MSR-C/HT-PEMFC unit covered with a glass wool thickness of 3 cm reaches the thermal equilibrium at less than 0.1 $A \cdot cm^{-2}$. Above the thermal equilibrium, the MSR-C/HT-PEMFC requires to be cooled to avoid temperature increase.

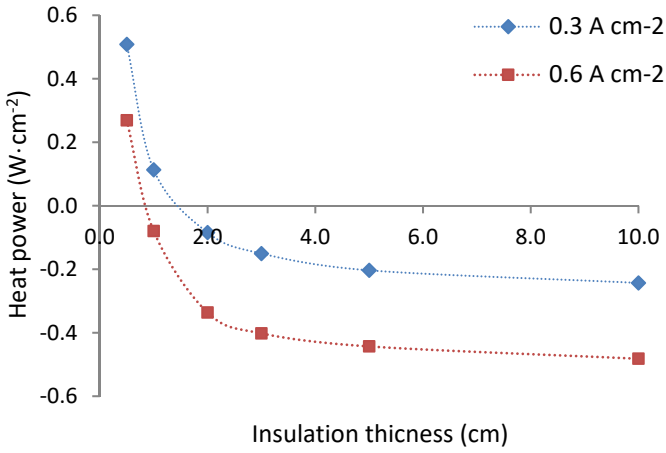


**Fig. 6.13** Heat flux as a function of the thermal insulator thickness for an operating temperature of 453 K at the end plates of MSR-C/HT-PEMFC (lines were added for readability).

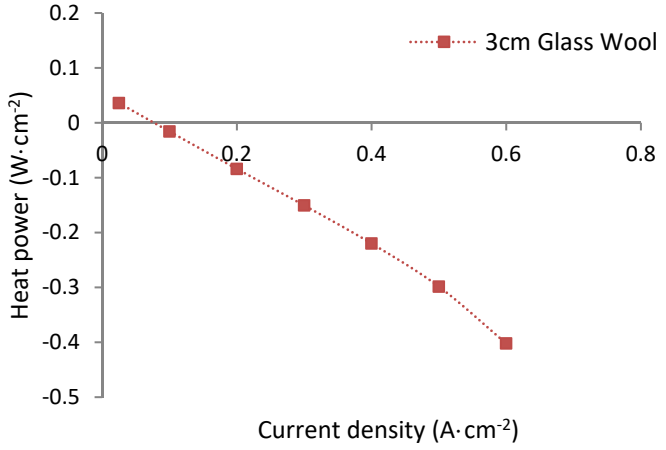


**Fig. 6.14** Heat flux as a function of the current density for an operating temperature of 453 K at the end plates of MSR-C/HT-PEMFC and considering an insulation of 3 cm thick of glass wool (lines were added for readability).

An efficient way to maintain the temperature of the MSR-C/HT-PEMFC is controlling the flow rate of the inlet gases, specifically the air at the cathode. The temperature control can be achieved introducing air at room temperature in the cathode channel and adjusting the airflow rate (stoichiometry); this approach has a fast response allowing an easy temperature control and representing as well a negligible extra energy cost.

Fig. 6.15 shows the heat flux at the end plates required by the MSR-C/HT-PEMFC to operate at 453 K as a function of the air stoichiometry, considering the air at the cathode inlet at the room temperature. The air stoichiometry shows a strong influence on the heat flux required to keep the temperature of the MSR-C/HT-PEMFC at 453 K. The thermal equilibrium at 0.3 $A \cdot cm^{-2}$ can be achieved for an air stoichiometry of *ca.* 10. Increasing the current density to 0.6 $A \cdot cm^{-2}$ requires an increase of the air stoichiometry to *ca.*14. The heat retrieved from the fuel cell can be used for the water and methanol heating and vaporization, increasing the overall energy efficiency of the device. The unreacted hydrogen and methanol at the anode outlet can also be burned providing extra-energy for the MSR-C/HT-PEMFC operation.

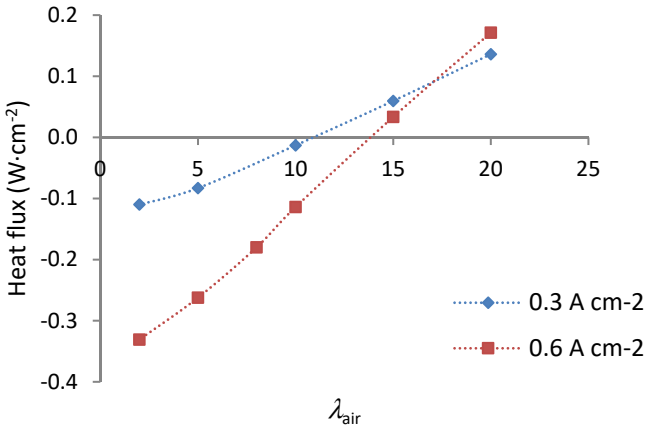


**Fig. 6.15** Heat flux as a function of the air stoichiometry for an operating temperature of 453 K at the end plates of MSR-C/HT-PEMFC and considering an insulation of 3 cm thick of glass wool (lines were added for readability).

### 6.5.5. Integrated MSR/HT-PEM stack

The conceptual design of the integrated MSR/HT-PEM stack (Fig. 6.16) considers ten cells thermally insulated with 3 cm of glass wool, a burner, a tank and a vaporizer. The heat required for the water/methanol mixture vaporization is provided by burning the unreacted hydrogen and methanol in the anode vent. The temperature control of the stack is obtained feeding air to cathode side at room temperature and adjusting the airflow rate.

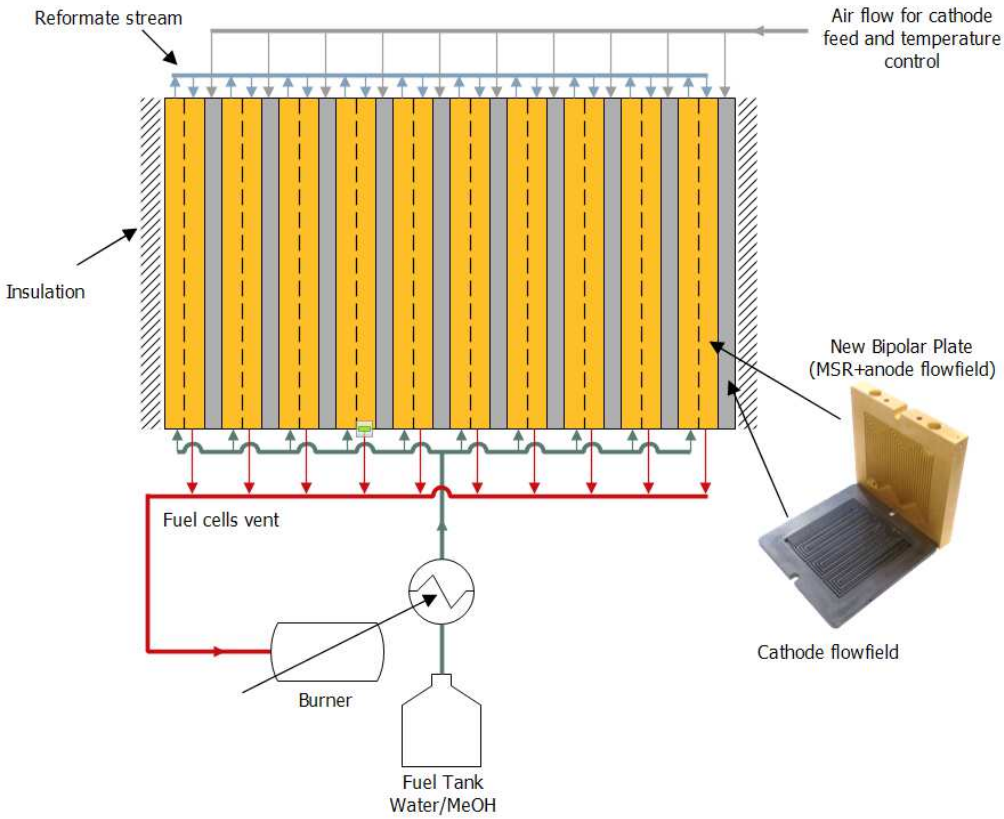


**Fig. 6.16** Conceptual design of the integrated MSR/HT-PEM stack.

The operation of the integrated MSR/HT-PEM stack was simulated assuming that the overall performance was obtained adding single combined cells. Fig. 6.17 shows the potential difference (a), temperature (b), water/methanol flow rate ($q_V$) (c), methanol conversion (d), air stoichiometry (e), heat produce by the burner and heat consumed by the vaporizer (f) as a function of the current density. The stack operation was simulated for a current between 4.5 A (0.1 A·cm$^{-2}$) and 54 A (1.2 A·cm$^{-2}$). Below 4.5 A no simulation was performed, since it was not possible to maintain the thermal equilibrium without an external heat source.

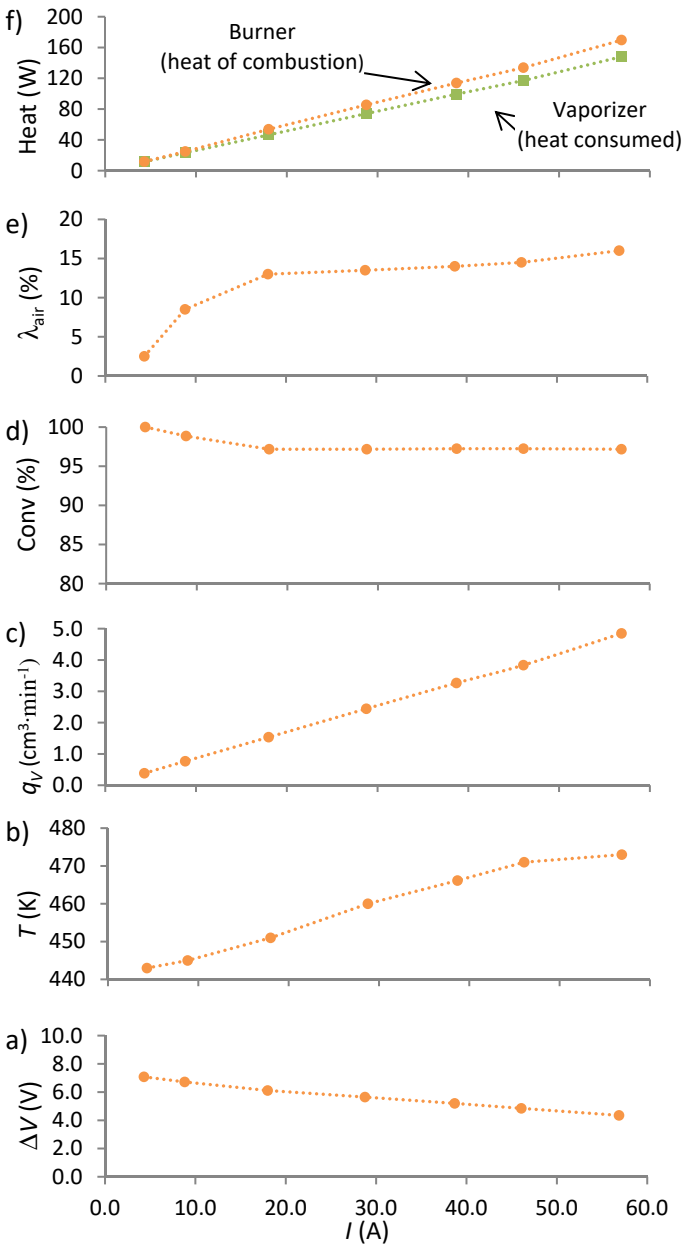


**Fig. 6.17** Operating parameters of the integrated MSR/HT-PEM stack (lines were added for readability).

The simulations were performed for an operating temperature between 443 K and 473 K, keeping the methanol conversion always above 95 % (maximum of 1 % of

methanol in the reformate stream) (Fig. 6.17d). For heating and vaporizing the water/methanol mixture, the anode vent heat of combustion was used. Fig. 6.17f shows that the burner can provide more heat than the consumed in vaporizing process of the water/methanol mixture, especially at higher current densities. Fig. 6.17e shows that the air stoichiometry has a sharp increase between 4.5 A and 18 A (0.4 $A \cdot cm^{-2}$) and a slight increase above 18 A. This fact can be assigned to the higher heat losses to the surroundings. The sensible heat of the cathode vent was wasted.

The proposed overall integrated MSR/HT-PEM stack operates without any external heat source, except during the start-up and for very low current densities (<0.1 $A \cdot cm^{-2}$). Typical HT-PEM stacks operate near-constant temperature [4,49]; however, the proposed stack requires that the operating temperature is adjusted to the current density, as seen in Fig. 6.17a,b. Operating continuously the integrated MSR/HT-PEM stack at high temperature, such as 473 K, facilitates the temperature control but have a detrimental effect on the durability of stack components.

## 6.6. Conclusions

A 3-dimensional non-isothermal model and simulator has been developed for a high temperature polymer electrolyte membrane fuel cell (HT-PEMFC) combined with a methanol steam-reforming cell (MSR-C). The model included carbon monoxide poisoning effect at the electro-catalytic activity of the MEA and the reformate production considering the MSR reaction, water gas shift (WGS) and methanol decomposition (MD). The modelling predictions for the MSR-C and HT-PEMFC units showed a very good agreement with the experimental values. The combined MSR-C/HT-PEMFC cell was operated between 443 K and 473 K. A thermal insulation with minimum 3 cm thick glass wool, or equivalent, was required to achieve the thermal equilibrium at low current densities (0.1 $A \cdot cm^{-2}$). The temperature control (cooling) of the device was achieved by feeding air to the cathode at the room temperature and by adjusting the airflow rate (stoichiometry). The proposed integrated MSR/HT-PEM stack considers ten cells and operates without any external heat source for current between 4.5 A (0.1 $A \cdot cm^{-2}$) and 54 A (1.2 $A \cdot cm^{-2}$). The stack required a continuous adjustment of the operating temperature to produce the desired current density.

## 6.7. References

[[1] J.S. Wainright, J.T. Wang, D. Weng, R.F. Savinell, M. Litt, Acid-Doped Polybenzimidazoles: A New Polymer Electrolyte, Journal of the Electrochemical Society, 142 (1995) 121–123.
[2] J. Mader, L. Xiao, T.J. Schmidt, B.C. Benicewicz, Polybenzimidazole/Acid Complexes as High-Temperature Membranes. In Fuel Cells II; Scherer, G. G., Ed.; Advances in Polymer Science, 216; Springer-Verlag: Berlin, Germany, (2008) 63–124.
[3] M. Díaz, A. Iranzo, F. Rosa, F. Isorna, E. López, J. Bolivar, Effect of carbon dioxide on the contamina-tion of low temperature and high temperature PEM (polymer electrolyte membrane) fuel cells. Influence of temperature, relative humidity and analysis of regeneration processes, Energy 90 (2015) 299–309
[4] S.L. Sahlin, S.J. Andreasen, S. K. Kær, System model development for a methanol reformed 5 kW high temperature PEM fuel cell system, International journal of hydrogen energy, 40 (2015) 13080-13089
[5] J.Y. Won, H.K. Jun, M.K. Jeon, S.I. Woo, Performance of a microchannel reactor combined with a combustor for methanol steam reforming, Catalysis Today 111 (2006) 158-163
[6] R.Y. Chein, Y.C Chen, C.M. Chang, J.N. Chung, Experimental study on the performance of hydrogen production from miniature methanol–steam reformer integrated with Swiss-roll type combustor for PEMFC, Applied Energy 105 (2013) 86-98.
[7] T. Kim, Micro Methanol Reformer Combined with a Catalytic Combustor for a PEM Fuel Cell, International Journal of Hydrogen Energy, 34 (2009) 6790-6798.
[8] V. Jaggi, S. Jayanti, A conceptual model of a high-efficiency, stand-alone power unit based on a fuel cell stack with an integrated auto-thermal ethanol reformer, Applied Energy 110 (2013) 295-303.
[9] G. Kolb, Fuel Processing for Fuel Cells, Wiley-VCH, Weinheim, (2008)
[10] G. Kolb, Review: Microstructured reactors for distributed and renewable production of fuels and electrical energy: Chemical Engineering and Processing 65 (2013) 1-44
[11] J.D. Holladay, Y. Wang, E. Jones, Review of developments in portable hydrogen production using microreactor technology, Chemical Reviews, 104 (2004) 4767-4790.
[12] I. Uriz, G. Arzamendi, P.M. Diéguez, F.J. Echave, O. Sanz, M. Montes, L.M. Gandía, a CFD analysis of the effects of the flow distribution and heat losses on the steam reforming of methanol in catalytic (Pd/ZnO) microreactors Chemical Engineering Journal 238 (2014) 37–44
[13] C. Pan, R.H. He, Q.F. Li, J.O. Jensen, N.J. Bjerrum, H.A. Hjulmand, A.B. Jensen, Integration of high temperature PEM fuel cells with a methanol reformer, Journal of Power Sources, 145 (2005) 392-398.
[14] G. Avgouropoulos, T. Ioannides, J.K. Kallitsis, S. Neophytides, Development of an internal reforming alcohol fuel cell: Concept, challenges and opportunities, Chemical Engineering Journal, 176 (2011) 95-101.
[15] G. Avgouropoulos, S. Neophytides, Performance of internal reforming methanol fuel cell under various methanol/water concentrations, Journal of Applied Electrochemistry, 42 (2012) 719–726.
[16] H.S. Wang, K.Y. Huang, Y.J. Huang, Yu-Chuan Su, F.G. Tseng, A low-temperature partial-oxidation-methanol micro reformer with high fuel conversion rate and hydrogen production yield, Applied Energy 138 (2015) 21–30.
[17] F. Weng, C. Chenga, K. Chen, Hydrogen production of two-stage temperature steam reformer integrated with PBI membrane fuel cells to optimize thermal management, International Journal of Hydrogen Energy 38 (2013) 6059-6064

[18] P. Ribeirinha, I. Alves, F. Vidal Vázquez, G. Schuller, M. Boaventura, A. Mendes, Heat integration of methanol steam reformer with a high-temperature polymeric electrolyte membrane fuel cell, Energy 120 (2017) 468–477

[19] P. Ribeirinha, G. Schuller, M. Boaventura, A. Mendes, Synergetic integration of a methanol steam reforming cell with a high temperature polymer electrolyte fuel cell, International Journal of Hydrogen Energy 42(19), 2017, 13902–13912

[20] A. H. Mamaghani, B. Najafi, A. Casalegno, F. Rinaldi, Predictive modelling and adaptive long-term performance optimization of an HT-PEM fuel cell based micro combined heat and power (CHP) plant, Applied Energy 192, 2017, 519–529

[21] A. Arsalis, S. K. Kær, M. P. Nielsen, Modeling and optimization of a heat-pump-assisted high temperature proton exchange membrane fuel cell micro-combined-heat-and-power system for residential applications, Applied Energy, 147, 2015, 569-581

[22] H. Chang, H.C. Chiang, Y.H. Chen, Y.Y. Chang, S.H. Cheng, Simulation study of an integrated methanol microfuel processor and fuel cell system, Chemical Engineering Science 74 (2012) 27-37

[23] A. Lotric, M. Sekavcnik, S. Hocevar Effectiveness of heat-integrated methanol steam reformer and polymer electrolyte membrane fuel cell stack systems for portable applications, Journal of Power Sources 270 (2014) 166-182

[24] A. Bell, Thesis of science in mechanical engineering "Design of a catalytic combustor for pure methanol and HT-PEM fuel cell anode waste gas", Department of Mechanical and Industrial Engineering University of Toronto

[25] G. Avgouropoulos, S. Schlicker, K.P. Schelhaas, J. Papavasiliou, K.D. Papadimitriou, E. Theodorakopoulou, *et al.*, Performance evaluation of a proof-of-concept 70W internal reforming methanol fuel cell system, Journal of Power Sources 307 (2016) 875-882

[26] Q. Li, D. Aili, H.A. Hjuler, J.O. Jensen, High temperature polymer electrolyte membrane fuel cells, Springer Switzerland (2016) 387-425

[27] T. Sousa T, M. Mamlouk, K. Scott, An isothermal model of a laboratory intermediate temperature fuel cell using PBI doped phosphoric acid membranes, Chemical Engineering Science 65 (2010) 2513-2530.

[28] H. Sun, C. Xie, H. Chen, S. Almheiri, A numerical study on the effects of temperature and mass transfer in high temperature PEM fuel cells with ab-PBI membrane, Applied Energy 160 (2015) 937-944

[29] P. Chippar, H. Ju, Three-dimensional non-isothermal modelling of a phosphoric acid-doped polybenzimidazole (PBI) membrane fuel cell, Solid State Ionic 225 (2012) 30-39

[30] K. Jiao, X. Li. A three-dimensional non-isothermal model of high temperature proton exchange membrane fuel cells with phosphoric acid doped polybenzimidazole membranes, Fuel Cells 10(3) (2010) 351-362

[31] K. Jiao, IE. Alaefour, X .Li, Three-dimensional non-isothermal modeling of carbon monoxide poisoning in high temperature proton exchange membrane fuel cells with phosphoric acid doped polybenzimidazole membranes, Fuel 90 (2011) 568-582

[32] K. Oh, J .Gisu, E. Cho, W. Kim, H.Ju, A CO poisoning model for high-temperature proton exchange membrane fuel cells comprising phosphoric acid-doped polybenzimidazole membranes, International Journal of Hydrogen Energy 39 (2014) 21915-21926

[33] R. K. A. Rasheed, S.H. Chan, Transient carbon monoxide poisoning kinetics during warm-up period of a high-temperature PEMFC – Physical model and parametric study, Applied Energy 140 (2015) 44–51.

[34] P. Chippar, H. Ju, Numerical modeling and investigation of gas crossover effects in high temperature proton exchange membrane (PEM) fuel cells, International Journal of Hydrogen 38(18) (2013) 7704-7714
[35] P. Chippar, K. Kang, YD. Lim, WG. Kim, H. Ju, Effects of inlet relative humidity (RH) on the perfor-mance of a high temperature-proton exchange membrane fuel cell (HTPEMFC), International Journal of Hy-drogen 39(6) (2014) 2767-2775.
[36] K. Oh, P. Chippar, H. Ju, Numerical study of thermal stresses in high-temperature proton exchange membrane fuel cell (HTPEMFC), International Journal of Hydrogen, 39(6) (2014) 2785-2794.
[37] T. E. Springer, T. Rockward, T. A. Zawodzinski, S. Gottesfeld, Model for polymer electrolyte fuel cell operation on reformate feed, effects of CO, H2 dilution, and high fuel utilization, Journal of The Electro-chemical Society, 148(1) (2001) A11-A23.
[38] BA. Peppley, JC. Amphlett, LM. Kearns, RF. Mann. Methanol steam reforming on Cu/ZnO/Al2O3 cata-lysts. Part 2: a comprehensive kinetic model, Applied Catalysis A, 179 (1999) 31-49.
[39] F.P. Incropera, D.P. Dewitt, T.L. Bergman, A.S. Lavine, Fundamentals of heat and mass transfer, sixth edition. John Wiley & Sons; 2007.
[40] P. Ribeirinha, M. Abdollahzadeh, M. Boaventura, A. Mendes H2 production with low carbon content via MSR in packed bed membrane reactors for high-temperature polymeric electrolyte membrane fuel cell, Ap-plied Energy, 188 (2017) 409–419.
[41] S. K. Das, A. Reis, K.J. Berry, Experimental evaluation of CO poisoning on the performance of a high temperature proton exchange membrane fuel cell, Journal of Power Sources 193 (2009) 691–698
[42] M. Boaventura, I. Alves, P. Ribeirinha, A. Mendes, The influence of impurities in high temperature poly-mer electrolyte membrane fuel cells performance, International Journal of Hydrogen Energy 41(43) (2016) 19771–19780
[43] S.S. Araya, S.J. Andreasen, H.V. Nielsen, S.K. Kaer, Investigating the effects of methanol-water vapor mixture on a PBI-based high temperature PEM fuel cell, International Journal of Hydrogen Energy, 37 (2012) 18231-18242.
[44] Q. Li, R. He, J.A. Gao, J. O. Jensen, N. Bjerrum, The CO poisoning effect in PEMFCs operational at temperatures up to 200 degrees C. Journal of the Electrochemical Society 150(12) (2003) A1599-A1605.
[45] E. U. Ubong, Z. Shi, and X. Wang Three-Dimensional Modeling and Experimental Study of a high tem-perature PBI-based PEM fuel cell, Journal of The Electrochemical Society, 156(10) (2009) B1276-B1282
[46] M. Mamlouk, T. Sousa, and K. Scott, A high temperature polymer electrolyte membrane fuel cell model for reformate gas, International Journal of Electrochemistry, 2011(520473) (2011) 1- 18
[47] D. Modestov, M.R. Tarasevich1, V. Filimonov, N.M. Zagudaeva, Degradation of high temperature MEA with PBI-H3PO4 membrane in a life test, Electrochimica Acta 54(27) (2009) 7121-7127
[48] Y. Oono, T. Fukuda, A. Sounai, M. Hori, Influence of operating temperature on cell performance and endurance of high temperature proton exchange membrane fuel cells, Journal of Power Sources. 195 (2010) 1007–1014.
[49] S. Andreasen, S. Kær, S. Sahlin, Control and experimental characterization of a methanol reformer for a 350W high temperature polymer electrolyte membrane fuel cell system, International Journal of Hydrogen Energy 38 (2013) 1676–84

# Chapter 7

# $H_2$ production with low carbon content using PBMRs

## 7.1. Abstract

This work compares the hydrogen purity and recovery produced by a methanol steam reforming (MSR) packed bed membrane reactor (PBMR) equipped with a membrane selective to hydrogen (Pd-Ag) and with a membrane selective to carbon dioxide (porous membrane filled with ionic liquids-ILs). A 3-dimensional non-isothermal PBMR model was developed in Fluent (Ansys™) for simulating a PBMR equipped with these two types of membranes and simulating a conventional packed bed reactor (PBR). The results indicated that selective hydrogen removal from the reaction medium originates a significant increase in the methanol conversion, while the carbon dioxide removal has a smaller effect. $CO_2$-PBMR showed to be more efficient in terms of energy consumption than $H_2$-PMBR. The simulation results showed also that ILs membranes must have a minimum permeance of ≥ $1x10^{-1}$ $mol \cdot s^{-1} \cdot m^{-2} \cdot bar^{-1}$ and $CO_2/H_2$ selectivity of ≥200 at 473 K to be attractive for this type of applications. The advantages and limitations of each reactor configuration are discussed based on experimental and simulated data.

---

The content of this chapter is adapted from: P. Ribeirinha, M. Abdollahzadeh, M. Boaventura, A. Mendes $H_2$ production with low carbon content via MSR in packed bed membrane reactors for high-temperature polymeric electrolyte membrane fuel cell, Applied Energy 188 (2017) 409–419

## 7.2. Introduction

Hydrogen is an important energy carrier. However, it has a very low volume energy density and shows limitations regarding storage and transportation. As an alternative, internal reforming or hydrogen production in-situ from fuels such methane, methanol or ethanol are being considered [1 – 3]. High temperature polymer electrolyte membrane fuel cells (HT-PEMFC) based on PBI membranes, can be directly fed with methanol steam reforming (MSR) reformate, since this device can tolerate CO concentrations up to 0.3 % [4]. The integration of hydrogen production in-situ by methanol steam reforming (MSR) with HT-PEMFC is already used in power supplies manufactured by few companies such as Ultracell [5], and Serenergy [6]. However, the presence of contaminants in the reformate stream ($CO_2$, $H_2O$, $CH_3OH$ and CO) can affect the performance of the HT-PEMFC specially at high current densities, while feeding a HT-PEMFC with a purified hydrogen stream allows higher performance and lower hydrogen stoichiometry [7,8].

Membrane reactors have been successfully applied for hydrogen production and purification to few reactions: WGS reactions and hydrocarbon steam reforming [9-13]. Membranes for hydrogen production via steam reforming are typically based on palladium or palladium alloys due to their high selectivity to hydrogen and very high permeability [9, 14-16]. One of the most remarkable procedures to produce Pd-alloy membrane was developed by SINTEF using a two-steps sputtering technique, enabling the production of a defect–free Pd-alloy film with a nominal thicknesses ranging from 2.2 to 10.0 µm [17, 18]. These defect–free Pd-alloy membranes can deliverer ≈100 % pure hydrogen at the permeate side with very high permeability ($10^{-6}$ mol·m·m$^{-2}$·s$^{-1}$·bar$^{-0.5}$ at 573 K) and applied to reactors with a configuration suitable for a specified reaction where mass transfer limitations (polarization of the concentration) in the gas phase can also be reduced [18-20]. Performing the reaction of methanol steam reforming using Pd-alloy membranes in packed bed membrane reactors (PBMR) besides the hydrogen purification, benefits the selective removal of hydrogen from the retentate side (reaction bulk), which increases the methanol conversion by hindering the backward reaction [16,21]. The methanol steam reforming reaction using Cu/ZnO/$Al_2O_3$ catalysts, however, is typically performed at temperatures between 473 K and 533 K [22], lower than the optimum temperature for Pg-Ag membranes to operate (573 K – 673K). Low temperatures lead to lower membrane permeability and the presence of CO in the reformate

steam can adsorb on the membrane surface decreasing the hydrogen permeation flux [23].

The hydrogen purification for HTPEMFC applications can also be achieved by removing the $CO_2$ and condensable components from the reformate stream. Katiyar *et al.* [24] performed a thermodynamic analysis of the MSR reaction with and without fractional removal of hydrogen and carbon dioxide using an adsorptive reactor, a membrane reactor or an adsorptive-membrane reactor. These authors concluded that carbon dioxide removal has positive effect on the performance of the reformer and is more suitable for fuel cell applications. However, adsorbents such as zeolites or activated carbons adsorb also MSR reactants; *e.g.,* zeolites are quite selective to the methanol adsorption. On the other hand, ILs membranes are very promising for producing HT-PEMFC grade hydrogen exhibiting high selectivity and permeability to carbon dioxide [25-27]. ILs membranes have been proposed as an effective process for the selective separation of different chemical species in dilute streams. Ionic liquids present very low vapour pressure, high stability at temperatures up to 573 K [28] and their solubility in the adjacent phases can be minimizing by selecting the adequate cation and anion [25]. $CO_2/CH_4$ and $CO_2/N_2$ separations have been performed successfully using ILs membranes; e.g. ionic liquids [$emim^+$][$BF_4$] and [emim+][$Tf_2N$–] showed selectivities to carbon dioxide, 27 and 21.2 respectively [28]. On the other hand, Kasahara *et al.* [29] obtained one of the highest permeabilities to carbon dioxide, 14 000 Barrer, and a very high $CO_2/N_2$ selectivity, 100, using a membrane of tetrabutylphosphonium proline-based. Also, many ILs show higher permeabilities to carbon dioxide than to hydrogen namely [$bmim^+$][$BF_4$–] that has a selectivity of $CO_2/H_2$ = 11 [30]. Other results show that permeability increases with the temperature and decreases with the increase in transmembrane pressure; furthermore, ILs membranes exhibit relatively long-term permeation stability [28].

IL membranes have not yet been considered for hydrogen production via LT-MSR in a PBMR. However, using these membranes may allow producing high-grade hydrogen via low temperature methanol steam reforming (LT-MSR) compared to traditional PBR and Pd-based PBMR [21, 24]. In the present study, is presented a CFD analysis of methanol steam reforming with hydrogen or carbon dioxide selective removal, using membrane reactors, and compared with a conventional packed bed reactor (PBR). A methanol steam reforming mechanistic kinetic model was fitted to experimental reaction rates obtained using a commercial CuO/ZnO/Al2O3 catalyst operating at low temperatures

(453K - 513K). For the first time, IL membranes have been considered for hydrogen purification in PBMR performing the methanol steam reforming. IL membranes were found to be potentially able of selectively remove the carbon dioxide from the reaction bulk producing a HT-PEMFC grade $H_2$ with minimal carbon content. The required specifications of the IL membranes for hydrogen purification in a PBMR were obtained, based on a three-dimensional non-isothermal PBMR model developed on Fluent. The temperature, pressure, flow rate of reactants and sweep gas role on the performance of the PBMR has been investigated.

## 7.3. CFD Model

### 7.3.1. Problem description

A PBMR 3-dimensional model (Fig. 7.1) was developed and implemented in commercial software Fluent, Ansys™. The model describes a tubular shell with 50 mm of length and 20 mm of outer diameter, housing a tubular selective membrane with 50 mm of length and 10 mm of inner diameter, as shown in Fig. 7.1. The membrane was assumed impermeable for simulating the PBR, permeable to hydrogen for the $H_2$-PBMR, and permeable to carbon dioxide and to hydrogen, with different selectivities, for the $CO_2$-PBMR. The model was validated with data collected from the literature.

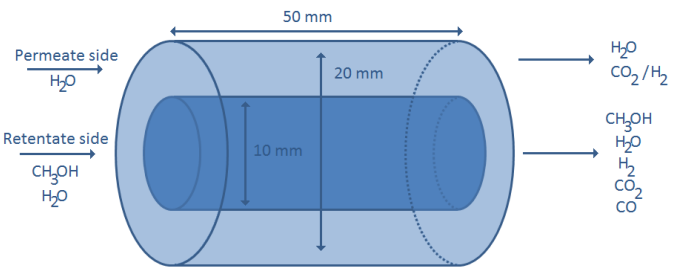


**Fig. 7.1** Model geometry of the PBR/PBMR.

### 7.3.2. Permeation model

At constant temperature, the permeation flux can be expressed as:

$$J_i = \frac{P_e}{\delta}\left(p_{i,ret}^{1/n} - p_{i,perm}^{1/n}\right) \quad (7.1)$$

where $J_i$ is the molar flux of species *i*, $P_e$ is the membrane permeability, $\delta$ is the membrane thickness and $p_{i,ret}$ and $p_{i,perm}$ are the partial pressure in the retentate and permeate sides, respectively. For Pd-Ag membranes, n was assumed equal to two, since hydrogen has a dissociative sorption on the palladium surface. Assuming *n* equal to two, Eq. 7.1 renders the Fick-Sieverts equation. For ILs membranes *n* is equal to one. $P_e$ follows the Arrhenius equation behaviour (Eq. 7.2).

$$P_e = P_{e_o} e^{-\frac{Ea}{RT}} \quad (7.2)$$

where, $P_{e0}$ is the pre-exponential factor, $E_a$ is the activation energy, *R* is the ideal gas constant and *T* is the temperature.

The Pd-Ag membrane was considered only permeable to hydrogen and the permeation parameters were obtained from Ghasemzade *et al.* [14]. The membrane tested by Ghasemzade *et al.* [14] is thicker than the ones reported by SINTEF [18, 19], although it shows one of the highest permeabilities to hydrogen reported in the literature [16]. The permeation parameters of the IL membrane were obtained from Shimoyama *et al.* [31], which considered a membrane impregnated with [bmim][Tf2N] contacting a humidified carbon dioxide stream. Table 7.1 shows the permeation values used for modelling the methanol steam reforming reactors.

**Table 7.1** Membrane properties.

| **Property** | **Pd-Ag membrane[14]** | **ILs membrane [31]** |
|---|---|---|
| $P_{e0}$ | $2.67\times10^{-5}$ mol·m·s$^{-1}$·m$^{-2}$·bar$^{-0.5}$ | $2.49\times10^{-5}$ mol·m·s$^{-1}$·m$^{-2}$·bar |
| *Ea* (J·mol) | 10 580 | 18440 |
| $\delta$ (m) | $50\times10^{-6}$ | $135\times10^{-6}$; $10\times10^{-6}$; $1\times10^{-6}$ |
| Selectivity $H_2/CO_2$ | ∞ | ∞ ; 1000; 200; 100; 50 |

### 7.3.3.Kinetic model

The kinetic model suggested by Peppley *et al.* [32] based on a steady-state analysis of the surface reaction mechanisms was used in this work for describing the MSR reaction. The kinetic parameters obtained by Peppley for catalyst BASF K3-110, did not provide a good agreement with experimental results for BASF RP60 catalyst, especially for low temperatures; BASF RP60 catalyst was considered in the present study and show to be more active than BASF K3-110. Despite the higher catalytic activity of the BASF RP60, the MSR reaction should follow the same mechanism as that presented by Peppley *et al.* [32] for BASF K3-110. The new kinetic parameters were estimated based on the experimental results obtained with a tubular packed bed reactor (Table 2). The reaction was considered rate limited, since catalyst powders with particle size between 100-250 μm were used to minimize the mass transfer of reactants between the bulk fluid and catalytic surface. The parameters estimation was carried fitting non-linear regression to the experimental conversion vs. $m_{cat}/F_{MeOH}$ and minimizing the sum of residual squares, following the same procedure reported as [32]. The enthalpies of adsorption and the active sites concentration ($C_{Si,j}^{T}$) were taken from the literature [32]. The kinetic model comprises a set of Langmuir–Hinshelwood rate expressions, which considers MSR, water-gas-shift (WGS) and methanol decomposition (MD) reactions, as described in the following:

**Table 7.2** Values of rate and equilibrium constants used in simulation.

| **Rate constants and equilibrium constants** | **$\triangle S_i$ ($J \cdot mol^{-1} \cdot K^{-1}$)** | **$k^{\infty}_i$ ($m^2 \cdot s^{-1} \cdot mol^{-1}$)** | **$\triangle H_i$ ($kJ \cdot mol^{-1}$)** | **$Ea_i$ ($kJ \cdot mol^{-1}$)** |
|---|---|---|---|---|
| $k_{MSR}$ ($m^2 \cdot s^{-1} \cdot mol^{-1}$) | - | $1.59 \times 10^{14}$ | - | $92.7 \times 10^{3}$ |
| $K^*_{CH3O(1)}$ ($bar^{-0.5}$) | -46.14 | - | -20 | - |
| $K^*_{OH(1)}$ ($bar^{-0.5}$) | -36.79 | - | -20 | - |
| $K^*_{H(1a)}$ ($bar^{-0.5}$) | -116.7 | - | -50 | - |
| $K^*_{HCOO(1)}$ ($bar^{-0.5}$) | 200.0 | - | 100 | - |
| $K^*_{CH3O2(1)}$ ($bar^{-0.5}$) | 148.3 | - | -20 | - |
| $k_{MD}$ ($m^2 \cdot s^{-1} \cdot mol^{-1}$) | - | $1.13 \times 10^{14}$ | - | $122 \times 10^{3}$ |
| $K^*_{OH(2)}$ ($bar^{-0.5}$) | 117.6 | - | -20 | - |
| $K^*_{H(2a)}$ ($bar^{-0.5}$) | -185.0 | - | -50 | - |
| $k_{WGS}$ ($m^2 \cdot s^{-1} \cdot mol^{-1}$) | - | $8.1 \times 10^{12}$ | - | $87.7 \times 10^{3}$ |

*MSR reaction rate equation:*

$$r_{MSR} = \frac{\dfrac{k_{MSR}K^{*}_{CH_3O^{(1)}}p_{CH_3OH}}{p^{1/2}_{H_2}}\left(1-\dfrac{p^{3}_{H_2}p_{CO_2}}{k_{MSR}p_{H_2O}p_{CH_3OH}}\right)C^{T}_{S1}C^{T}_{S1a}S_a}{\left(1+\dfrac{K^{*}_{CH_3O^{(1)}}p_{CH_3OH}}{p^{1/2}_{H_2}}+\dfrac{K^{*}_{OH^{(1)}}p_{H_2O}}{p^{1/2}_{H_2}}+K^{*}_{HCOO^{(1)}}p^{1/2}_{H_2}p_{CO_2}\right)\left(1+\sqrt{K^{*}_{H^{(1a)}}p_{H_2}}\right)} \tag{7.3}$$

*Water-gas-shift reaction rate equation:*

$$r_{WGS} = \frac{k_{WGS}K^{*}_{OH^{(1)}}\left(\dfrac{p_{CO}p_{H_2O}}{p^{1/2}_{H_2}}\right)\left(1-\dfrac{p_{H_2}p_{CO_2}}{k_{WGS}p_{CO}p_{H_2O}}\right)C^{T\,2}_{S1}S_a}{\left(1+\dfrac{K^{*}_{CH_3O^{(1)}}p_{CH_3OH}}{p^{1/2}_{H_2}}+K^{*}_{HCOO^{(1)}}p^{1/2}_{H_2}p_{CO_2}+\dfrac{K^{*}_{OH^{(1)}}p_{H_2O}}{p^{1/2}_{H_2}}+\right)^{2}} \tag{7.4}$$

*Methanol decomposition reaction rate equation:*

$$r_{MD} = \frac{\dfrac{k_{MD}K^{*}_{CH_3O^{(2)}}p_{CH_3OH}}{p^{1/2}_{H_2}}\left(1-\dfrac{p^{3}_{H_2}p_{CO_2}}{k_{MD}p_{CH_3OH}}\right)C^{T}_{S2}C^{T}_{S1a}S_a}{\left(1+\dfrac{K^{*}_{CH_3O^{(2)}}p_{CH_3OH}}{p^{1/2}_{H_2}}+\dfrac{K^{*}_{OH^{(2)}}p_{H_2O}}{p^{1/2}_{H_2}}\right)\left(1+\sqrt{K^{*}_{H^{(2a)}}p_{H_2}}\right)} \tag{7.5}$$

where $k_j$ is the reaction rate constant for reaction j, respectively; $K_i$ is the adsorption equilibrium coefficient for species i; $C^{T}_{S1}$ and $C^{T}_{S2}$ are the total catalyst surface concentrations of sites 1 and 2, respectively; $C^{T}_{S1a}$ and $C^{T}_{S2a}$ are the total catalyst surface concentration of sites 1a and 2a, respectively.

The kinetic constants were calculated according to the Arrhenius equation (Eq. 7.6) and the adsorption coefficients were calculated according to van't Hoff equation (Eq. 7.7).

$$k = k_0 e^{-\frac{Ea}{RT}} \tag{7.6}$$

$$\ln K_i = -\frac{\Delta H}{RT}+\frac{\Delta S}{R} \tag{7.7}$$

where $k_0$, is the Arrhenius pre-exponential factor and $E_a$ is the activation energy. The $\Delta H$ and $\Delta S$ are the enthalpy and entropy of adsorption respectively. In Table 7.3 are presented the catalyst properties used in the model.

**Table 7.3** Catalyst properties used in the model.

| Property | Value |
|---|---|
| Density ($\rho_{catalyst}$ / kg·m$^{-3)}$ | 1.1 |
| Porosity ($\varepsilon$) | 0.38 |
| Particle size ($D_p$, m) | 200x10$^{-6}$ |
| Surface area ($S_{area}$, m$^2$·kg$^{-1}$ [32]) | 102x10$^3$ |
| Thermal conductivity ($\lambda$, W·m$^{-1}$·K$^{-1}$[22]) | 0.30 |

### 7.3.4. PBMR mathematical model

The steady state PBMR model developed is based on the following main assumptions:

- non-isothermal behaviour;
- for the temperature range considered, all the species were considered in gas phase and behaving as ideal gases;
- the fluid flow was assumed to be laminar and Newtonian;
- no diffusion limitations in the catalyst were considered;
- the membrane was considered as a wall with no thickness.

*Boundary conditions*

The boundary conditions considered for the reformer are:

- At the inlet, the flow velocity, gas composition and temperature were considered constant and defined by user;
- At the outlet, the pressure was considered to be constant and equal to a specified value, gradients of temperature and species mass fraction were assumed to be equal to zero;
- At the wall, the temperature was considered constant and the flow obeying to the no slip condition.

The permeation model was implemented following two different approaches. First, the permeation was modelled considering a source/sink term (Eq. 7.8) introduced in the continuity and mass balance equations (Eq. 7.10 and 7.12) [33]. The source term allows the species to permeate (sink) in the cell thread adjacent to the membrane, at

the retentate side, and appear (source) in the cell thread adjacent to the membrane, at the permeate side:

$$S_i = \begin{cases} +\dfrac{J_i A_{cell} M_i}{V_{cell}}, \text{permeate} \\ -\dfrac{J_i A_{cell} M_i}{V_{cell}}, \text{retentate} \end{cases} \tag{7.8}$$

where $A_{Cell}$ and $V_{Cell}$ are the area and volume of the cell element respectively, and $M_i$ is the molar mass of species *i*.

The permeation was also modelled as a boundary condition – second approach, defining the mass fraction of species *i* (Eq. 7.9) on the membrane (wall), and a source term in the continuity equation (Eq. 7.10). Both approaches were implemented successfully with no significant difference in the simulation results. The source term was implemented for all permeating species using user-defined functions (UDFs) written in C++, compiled and loaded to FLUENT. The mass fraction is defined as:

$$\omega_{i,perm} = \omega_{i,ret} + \frac{J_i}{\nabla \rho D_i} \tag{7.9}$$

where, $\omega_{i,\text{perm}}$, $\omega_{i,\text{ret}}$ is the mass fraction of the species *i* in the cell element near to the membrane at the permeate and at the retentate sides, respectively.

The continuity, mass, and momentum equations for the species are described as follows:

*Continuity Equation*

$$\nabla.(\rho \vec{u}) = S_m \tag{7.10}$$

where, ρ is the fluid density (kg·m$^{-3}$), $\vec{u}$ is the fluid velocity vector (m·s$^{-1}$) and $\nabla$ is the gradient.

*Momentum Balance*

$$\nabla\left(\frac{\rho \vec{u}\vec{u}}{\varepsilon^2}\right) = -\nabla p + \nabla.\tau + S$$
$$S = -\left(\frac{\mu}{\alpha}\vec{u} + \frac{1}{2}C_2\left|\vec{u}\right|\left|\vec{u}\right|\right), \alpha = \frac{D_p^2}{150}\frac{\varepsilon^3}{(1-\varepsilon)^2}, C_2 = \frac{3.5(1-\varepsilon)}{D_P \varepsilon^3} \tag{7.11}$$

where, $\nabla$P is the pressure (Pa) gradient and is the isotropic part of Cauchy stress tensor; $\nabla\tau$ is the anisotropic part of the stress tensor and describes the viscous forces; S is the

source term and represents the external body forces. In this model, the source term is the pressure gradient in a porous media and is composed by viscous losses (first term) and inertia losses (second term), where $D_p$ is particle diameter (m) and ε is the media porosity.

*Mass Balance*

$$\nabla\left(\rho\vec{u}\omega_i\right) = \nabla\rho D_i^{eff}\nabla\omega_i + M_i\nu_i r_{MSR} \tag{7.12}$$

The local mass fraction of the species *i*, $\omega_i$, is calculated using a convection-diffusion equation (Eq. 7.12). In the right side of Eq. 7.12, the first term is the mass diffusion term described by the Fick's law, where $D_i$ is the mass diffusion coefficient, calculated in this model by the kinetic model theory. The second term on the right side is the mass flux of species i due to the chemical reaction, where $M_i$ is the molar mass of species *i* (kg·kmol$^{-1}$), $\nu_i$ is the stoichiometric coefficient of species *i* in MSR reaction and $r_{MSR}$ is the reaction rate (kmol·m$^{-3}$·s$^{-1}$).

*Energy Balance*

$$\nabla\left(\rho\vec{u}H_0\right) = \nabla\left(\lambda_{eff}\nabla T\right) - \nabla\vec{u}P + S_T$$
$$S_T(MSR) = \sum_{i=1}^{N}\left(\Delta H_{k,298} + \sum_i \nu_i \int_{T_{ref}}^{T} Cp_i dT\right)\left(r_j\right), H_i = \int_{T_{ref}}^{T} Cp_i dT,\ H_0 = \sum_i^{N_c} y_i H_i \tag{7.13}$$

where, $H_0$ is the total enthalpy (J·kg$^{-1}$), $\lambda_{eff}$ is the effective thermal conductivity, which takes into account the thermal conductivity in the solid and gas phase (W·m$^{-1}$·K$^{-1}$), *T* is the temperature (K) and $C_p$ is the specific heat capacity (J·kg$^{-1}$·K$^{-1}$). In the model is considered the energy flux by conduction and by pressure work, represented by the first two terms in the right part of the equation. $S_T$ is the source term and represents the heat flux due to the chemical reaction. The chemical reaction was implemented using the user-defined functions (UDFs) that were written in C++, compiled and hooked to FLUENT.

To analyse the effect of the mesh on the simulation results, several runs with an increasing number of elements were performed. The selected mesh for simulating the membrane reactor, gives a methanol conversion with a maximum difference of 0.05 % relative to the value obtained using a mesh with the double of elements. The mesh considered for the PBMR model is composed by 3.0x10$^4$ elements.

## 7.4. Experimental

A tubular reactor with 7.5 mm of inner diameter was filled with 1.5 g of commercial catalyst (BASF RP60) with particle size between 100-250 μm, mixed with 1.5 g of glass beads with the same diameter to minimize the temperature profiles and to operate near to isothermal conditions. The reactor was closed and placed inside an oven with controlled temperature. The temperature of the reactor was measured inside the catalyst bed. The catalyst was reduced in situ during 2 hours with 20 $cm^3 \cdot min^{-1}$ of hydrogen and 180 $cm^3 \cdot min^{-1}$ of $N_2$ at 453 K to avoid sintering the catalyst. The reforming reaction was carried out between 453 K and 513 K, at space-time values ($m_{cat}/F_{MeOH}$) between 50 $kg \cdot s \cdot mol^{-1}$ and 550 $kg \cdot s \cdot mol^{-1}$ and at operating pressures between 1 bar and 3 bar. The water/methanol mixture with molar steam to carbon ratio (S/C) of 1.5 was pumped using an HPLC pump (LaPrep P130) as shown in Fig. 7.2.

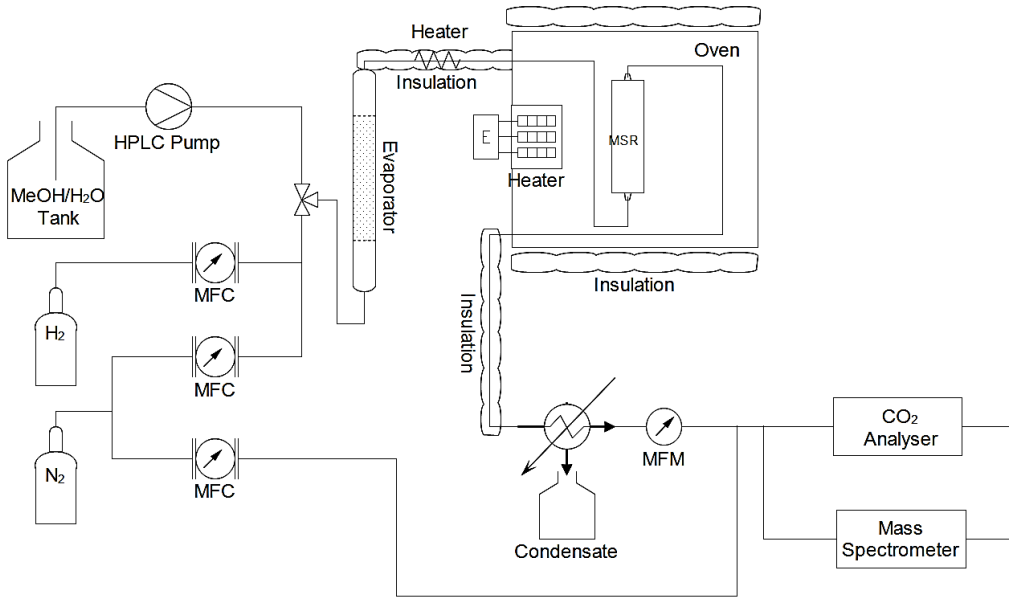


**Fig. 7.2** Scheme of the experimental unit used for catalyst characterization

The reformate stream passed through a cold trap to remove the condensable components; the flow of the non-condensable species was measured using a mass flow

meter; hydrogen and carbon dioxide concentration was determined by mass spectrometry (Pfeiffer OmniStartm) and CO concentration was determined using a specific analyser (Signal Inst. 7000FM GFC).

## 7.5. Results and Discussion

### 7.5.1. Validation of the kinetic model

To validate the MSR kinetic model, simulation results for an isothermal packed bed reactor model were compared with experimental data obtained in this work. Fig. 7.3 shows the experimental (including the experimental) and simulated methanol conversion, hydrogen and CO production as a function of the space-time and for several reaction temperatures. The simulation results present a good agreement to the experimental data for the studied conditions, as shown in the parity plot (Fig. 7.4); the maximum relative difference between experimental and simulated results is less than 5 % and the coefficient of determination ($R^2$) is >0.996 for the methanol conversion and hydrogen production and <0.957 for the CO production. As expected, the methanol conversion is highly dependent of the temperature and the hydrogen production rate decreases with the space-time. At temperatures lower than 473 K, the methanol decomposition reaction has very low conversion and the carbon monoxide is almost exclusively produced from the reverse water gas shift reaction. As a result, the carbon monoxide concentration increases with the partial pressure of hydrogen and carbon dioxide and consequently it increases for higher space-time ratios ($m_{cat}/F_{MeOH}$). Experimentally, full methanol conversion was achieved for a $m_{cat}/F_{MeOH}$ of 200 kg·mol$^{-1}$·s and for 350 kg·mol$^{-1}$·s at 493 K and 473 K, respectively. Full conversion, however, was not achieved at 453 K for the space-time range analysed. The results showed that the carbon monoxide concentration at temperatures lower than 493 K stays below 6000 ppm. According to the literature, carbon monoxide concentrations lower than 30 000 ppm [4] do not have significant impact on the HT-PEMFCs performance.

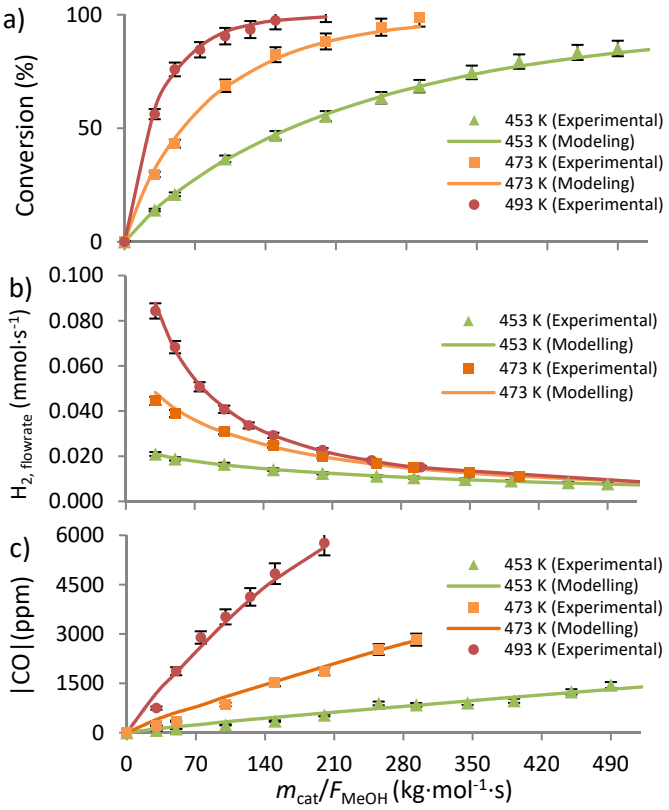


**Fig. 7.3** Experimental and simulated methanol conversion (a), $H_2$ production flowrate (b) and CO production rate (c) as a function of space-time ratio and for different temperatures, $P_{out}$ = 1 bar and *S/C* = 1.5.

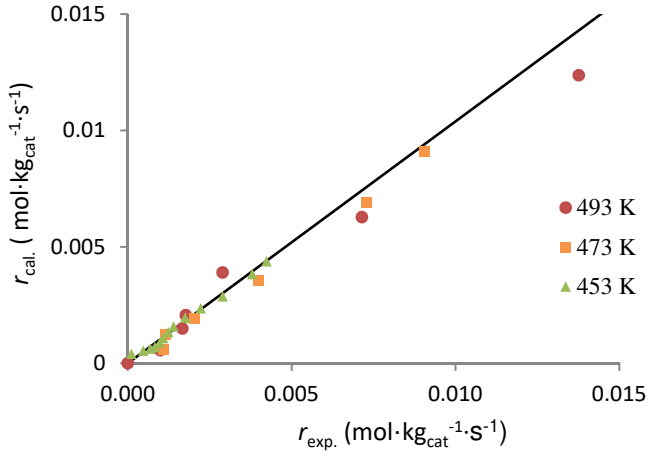


**Fig. 7.4** Parity plot of the experimental and calculated reaction of methanol consumption rate.

### 7.5.2. Validation of the permeation model

The hydrogen permeation model was validated against the experimental data reported by Ghasemzade *et al.* [14] (Fig. 7.5). Using the same MSR kinetic and the permeation parameters reported by these authors, it was obtained a good agreement between modelling and experimental data. The enhancement on the methanol conversion due to the hydrogen removal through permeation can be clearly observed in Fig. 7.5. It is also observed a decrease in the methanol conversion with the pressure increase due to the backward reaction, as reported by Peppley *et al.* [32].

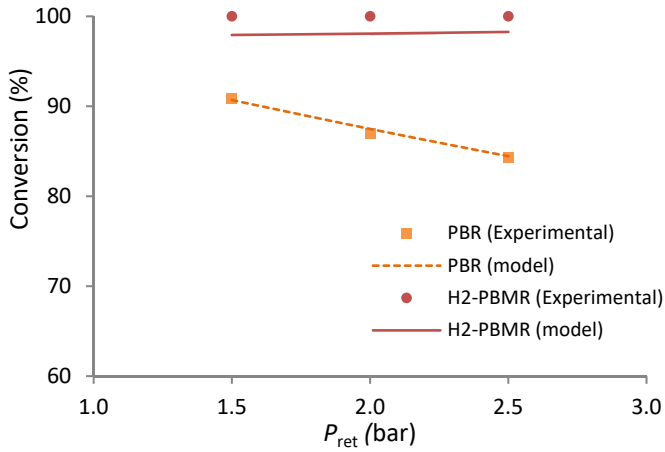


**Fig. 7.5** Methanol conversion as a function of the retentate pressure for a PBR and H2-PBMR (model and experimental) at 553 K, a steam to carbon molar ratio (*S/C*) of 1, *GHSV*=1800 $h^{-1}$ and a sweep to feed molar ratio (*SF*) of 8.9 (experimental data from [14]).

### 7.5.3. PBMR, 3-dimensional model

The 3-dimensional model provides the spatial profiles of each species and temperature in the reactor offering other means to examine the performance of the PBMR and allowing results that are more accurate compared to 1-dimensional model. Fig. 7.6 shows contours of the temperature inside the PBMR running at 473 K and for $m_{cat}/F_{MeOH}$ = 400 kg·$mol^{-1}$·s. Near to the inlet of the catalyst bed (retentate) is clearly observed a colder region with temperature sink of *ca*. 20 K. The temperature sink in that region of

the PBMR shows the existence of heat transfer limitations. This fact is related to the endothermic nature of the reaction, the high reaction rate value in the inlet region and the low thermal conductivity of the catalyst. The effective thermal conductivity of the catalyst depends on the catalyst void fraction, which reduces significantly the capacity to transport heat between the reactor wall and the centre of the catalyst bed. The temperature drop leads to a significant decrease on the methanol conversion compared to values obtained if isothermal conditions are considered.

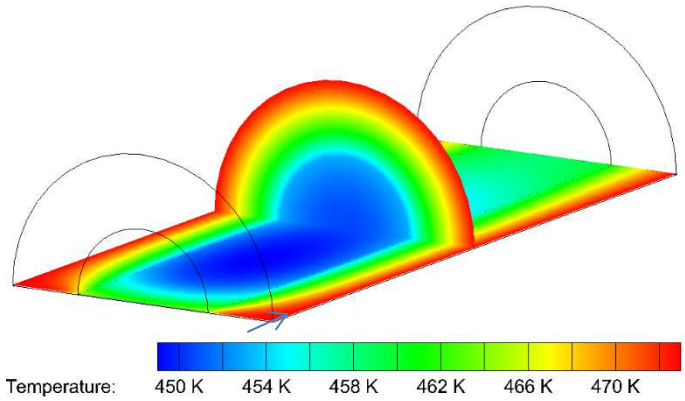


**Fig. 7.6** Temperature contours for a PBMR with a membrane at 473 K and $m_{cat}/F_{MeOH}$ = 400 kg·mol$^{-1}$·s.

Fig. 7.7 shows contours of the hydrogen and carbon dioxide mass fractions inside the $H_2$-PBMR and $CO_2$-PBMR, respectively. The highest hydrogen mass fraction is found at the middle of $H_2$-PBMR due to continuous permeation through the membrane, while in PBR the hydrogen mole fraction increases from the inlet to the outlet of the reactor. Fig. 7.7b shows a high carbon dioxide concentration near the permeate side of the membrane and a low concentration near the retentate side of the membrane. When highly permeable membranes, with a few micrometres of thickness are used, the diffusion of the permeating component through the gas phase can limit the permeation [20]. In this case the permeating component is transported more rapidly through the membrane than through the polarization gas layer (concentration polarization), reducing the concentration gradient across the membrane and consequently the membrane permeation [34].

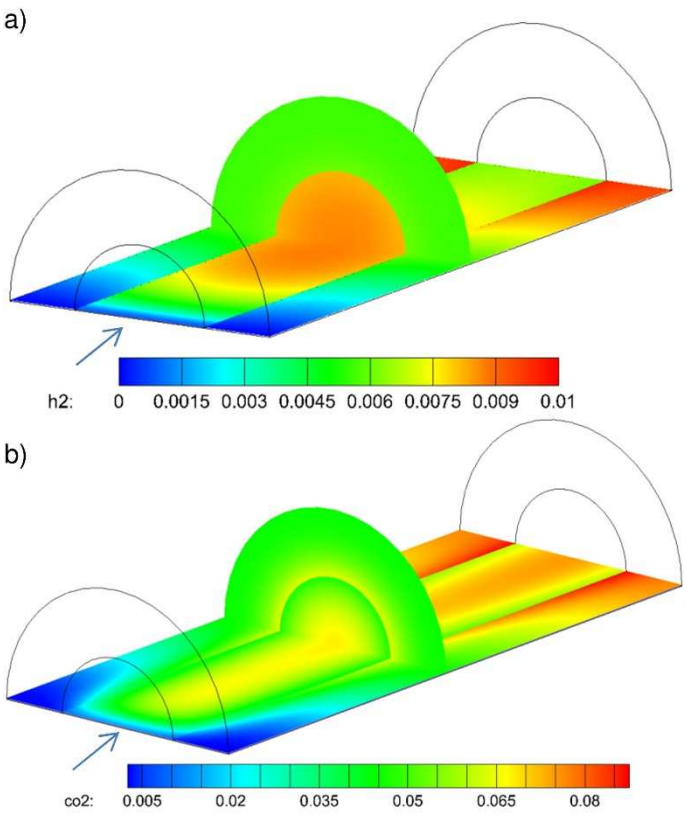


**Fig. 7.7** Hydrogen mass fraction mass fraction contours for a $H_2$-PBMR (a) and the carbon dioxide mass fraction contours for a $CO_2$-PBMR (b) at 473 K and $m_{cat}/F_{MeOH}$ = 400 kg·mol$^{-1}$·s.

### 7.5.4.Methanol conversion in PBMRs

The performance of membrane reactors is affected by temperature, pressure, space-time ratio, sweep flow rate factor (*SF*) and *S/C* ratio. Fig. 7.8 shows the methanol conversion as a function of the space-time ratio for the PBR and $H_2$-PBMR configurations at 473 K, 493 K and 513 K. Methanol conversion enhancement is observed when hydrogen is selectively removed from the reaction bulk; this enhancement is normally assigned to the partially suppression of the methanol steam reforming backward reaction [14,16]. Nevertheless, in this study a considerable increase in the residence time was observed because of the hydrogen removal from the reaction medium. For example, at 473 K, $\Delta P$ = 2 bar, *SF* = 5 and $m_{cat}/F_{MeOH}$ = 200 kg·mol$^{-1}$·s the residence time is 30.2 % greater in

the $H_2$-PBMR than in the PBR. Therefore, the most important contribution for the methanol conversion enhancement is the increase of the residence time.

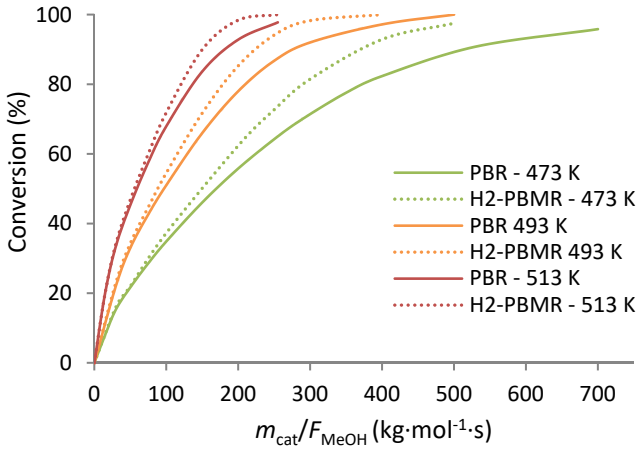


**Fig. 7.8** Simulated methanol conversion as a function of space-time for PBR and $H_2$-PBMR (selective towards $H_2$) non-isothermal at different temperatures, $P_{rent}$ = 3 bar, *SF* = 10 and *S/C* = 1.5.

Shimoyama *et al.* [31] tested an IL membrane with a thickness of ca. 135 µm; thinner membranes would display higher permeances but also may display more defects reducing the selectivity. Fig. 7.9 shows the methanol conversion as a function of the space-time ratio and temperature for both reactor configurations, PBR and $CO_2$-PBMR, at 473 K, 493 K and 513 K assuming an IL membrane 1 µm thick and displaying an infinite selectivity to carbon dioxide. Though assuming a very high performing carbon dioxide selective membrane, the selective carbon dioxide removal originates a smaller methanol conversion enhancement than when using a hydrogen selective membrane. Peppley *et al.* [32] reported already that carbon dioxide concentration have a minor effect on the methanol conversion. Actually, in the MSR reaction rate (Eq. 7.3) the order of the carbon dioxide for backward reaction is one while for hydrogen is three. Most of the methanol conversion enhancement is then related to the increase on the residence time due to the selective carbon dioxide removal from the reaction medium. For example, at 473 K, $\Delta P$ = 2 bar, SF = 5 and $m_{cat}/F_{MeOH}$ = 200 kg·mol$^{-1}$·s the residence time is 13.3 % greater in the $CO_2$-PBMR than in the PBR.

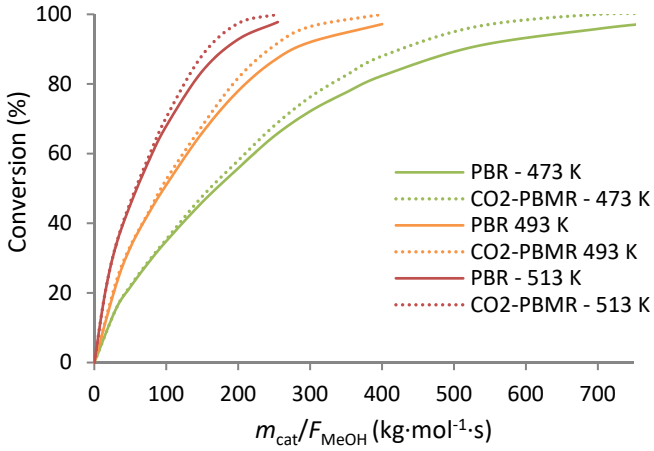


**Fig. 7.9** Simulated methanol conversion as function of space-time ratio for PBR and $CO_2$-PBMR (selective towards $CO_2$) at 473 K, $P_{ret}$ = 3 bar, *SF* = 10 and *S/C* = 1.5. The $CO_2$ selective membrane was assumed 1 µm thick with infinite ideal selectivity.

To achieve high methanol conversion at low operating temperatures low feed flow rates or high amounts of catalyst are required. Therefore, the methanol conversion enhancement obtained due to the selective removal of hydrogen or carbon dioxide becomes especially interesting for lower reaction temperatures. Since hydrogen or carbon dioxide production (MSR reaction rate) increases faster with temperature than the hydrogen or carbon dioxide permeation, the methanol conversion enhancement when using a membrane reactor is higher for lower temperatures, as shown in Fig. 7.10. This figure shows the methanol conversion for a $H_2$-PMBR and $CO_2$-PMBR with the same space-time ratio of a corresponding PBR with a methanol conversion of 85 %, as a function of the reaction temperature. At temperatures below 463 K, the effect of hydrogen selective removal in the methanol conversion reaches a plateau, with an increase of ca. 10 percentage points in the methanol conversion. In the other hand, the effect of carbon dioxide selective removal in the methanol conversion is in average 5 percentage points lower than the hydrogen selective removal. The profiles observed in Fig. 7.10 depend on the membrane and catalyst properties. Catalyst with lower activity will show this maximum of enhancement at higher temperatures, since they required higher space-time ratios to achieve high conversions.

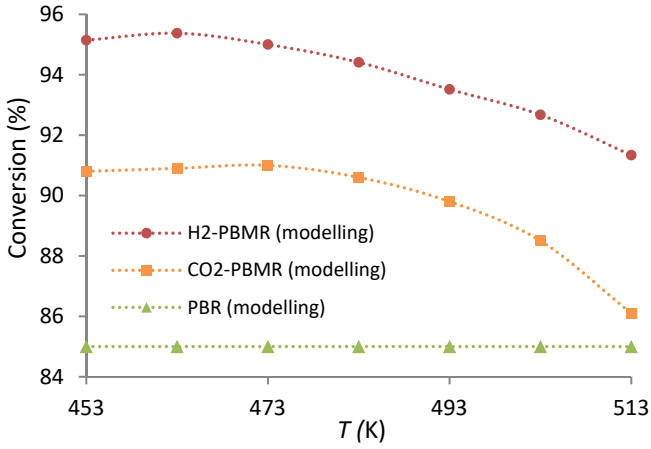


**Fig. 7.10** Methanol conversion enhancement as a function of temperature for a $H_2$-PBMR and $CO_2$-PBMR (membrane 1 µm thick) with the same space-time ratio of a corresponding PBR with a methanol conversion of 85 %, $P_{ret}$ = 3 bar, *SF* = 10 and *S/C* = 1.5. Lines were added for readability.

The enhancement in the methanol conversion depends on hydrogen/carbon dioxide permeation and is more significant when hydrogen is being selective removed than carbon dioxide. The hydrogen permeation is influenced by the SF and the partial pressure difference between permeate and retentate sides. Fig. 7.11 and 12 show the methanol conversion as a function of the total pressure and the SF, respectively. For a pressure of 2 bar in the retentate side and 10 mbar in the permeate side a methanol conversion of 92.8 % was obtained, while at 100 mbar a methanol conversion of 93.3 % was obtained. Lower pressure in the permeate side increases the hydrogen permeation, but also limits the heat transport in the permeate region decreasing the temperature on the catalyst bed. Increasing the pressure in the retentate side can also increase the hydrogen permeation and consequently the methanol conversion, *e.g.,* at 4 bar in the retentate a methanol conversion of 93.3 % was obtained. Fig. 7.11 shows that increasing the SF can increase significantly the methanol conversion, due to the increase in the permeation and heat transport. For SF= 20 the methanol conversion can be improved to 93.1%. However, assuming that the sweep gas is steam, the usage of a high SF will represent high-energy cost without a significant benefit.

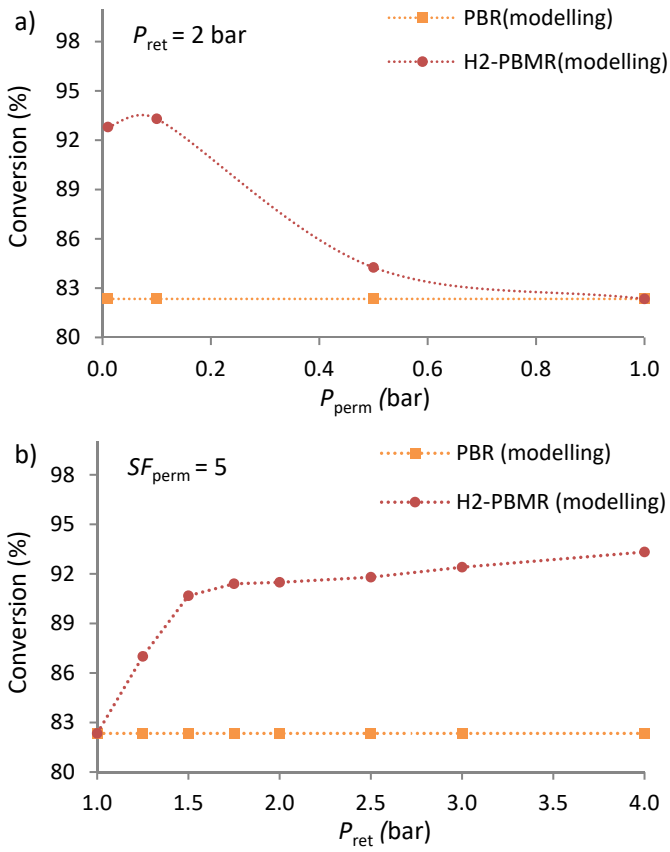


**Fig. 7.11** Methanol conversion as function of permeate (a) and retentate (b) pressure for PBR and $H_2$-PBMR, $m_{cat}/F_{MeOH}$ = 400 kg·mol$^{-1}$·s and $T$= 473 K. Lines were added for readability.

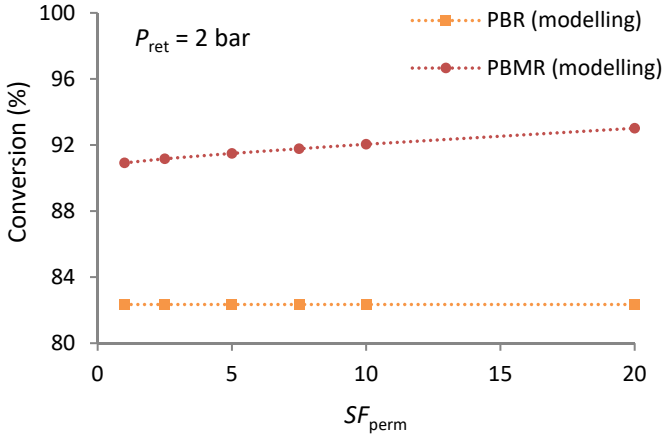


**Fig. 7.12** Methanol conversion as function of SF for PBR and $H_2$-PBMR (selective towards $H_2$), $m_{cat}/F_{MeOH}$ = 400 kg·mol$^{-1}$·s, $P_{ret}$ = 2 bar and S/$C$ = 1.5. Lines were added for readability.

### 7.5.5.Hydrogen purity in PBMRs

The benefits of using a $CO_2$-PBMR for running the MSR reaction considering the enhancement in the methanol conversion become questionable especially if it is assumed a conventional PBR followed by a membrane module for selectively remove carbon dioxide, operating at an optimised temperature. The major benefit of using a $CO_2$-PBMR is the compactness of the device, since reaction and purification processes are carried simultaneously. Feeding a HT-PEMFC with a purified hydrogen stream allows lower hydrogen stoichiometry and higher current densities [7, 8]. For example, a HT-PEMFC fed with methanol reformate (75 % $H_2$ and 25% $CO_2$) and at hydrogen stoichiometric ratio of 1.2 wastes ca. 27 % of the inlet hydrogen and the hydrogen vent concentration is 20 %. The hydrogen purity is an important issue that should be taken into account since lower hydrogen concentration originates mass transport limitation in the anode especially at high current densities [8].

The hydrogen purity of the reformate stream using a $CO_2$-PBMR depends mainly on the permeability of the of the IL membranes, while using a $H_2$-PBMR depends on the selectivity of the Pd-Ag membranes. The selectivity of Pd-Ag membranes is typically above 97%, but for membranes with thicknesses of a few micrometres, this value can decrease [9]. In this work, and according with literature [4], the Pd-Ag membrane was permeable only to hydrogen, therefore pure hydrogen is obtained in the permeate side. The IL membrane developed by Shimoyama *et al.* [31] and considered in the $CO_2$-PBMR as thickness of ca. 135 μm, however thinner membranes would display higher permeances increasing the hydrogen purity. Fig. 7.13 shows the hydrogen concentration in the retentate side after removing the condensable components for different ILs membrane thicknesses. As shown in Fig. 7.13, higher purities can be achieved decreasing the thickness of the membrane (higher permeances). The feed pressure as well the sweep gas ratio plays a more important role in the membrane permeation to carbon dioxide; for SF ≥ 10, the benefit in the $H_2$ purity is small. To perform the methanol steam reforming reaction in $CO_2$-PBMR only membranes with permeances of at least $1x10^{-1}$ mol·s $^{1}$·$m^{-2}$·$bar^{-1}$ at 473 K can be effectively used.

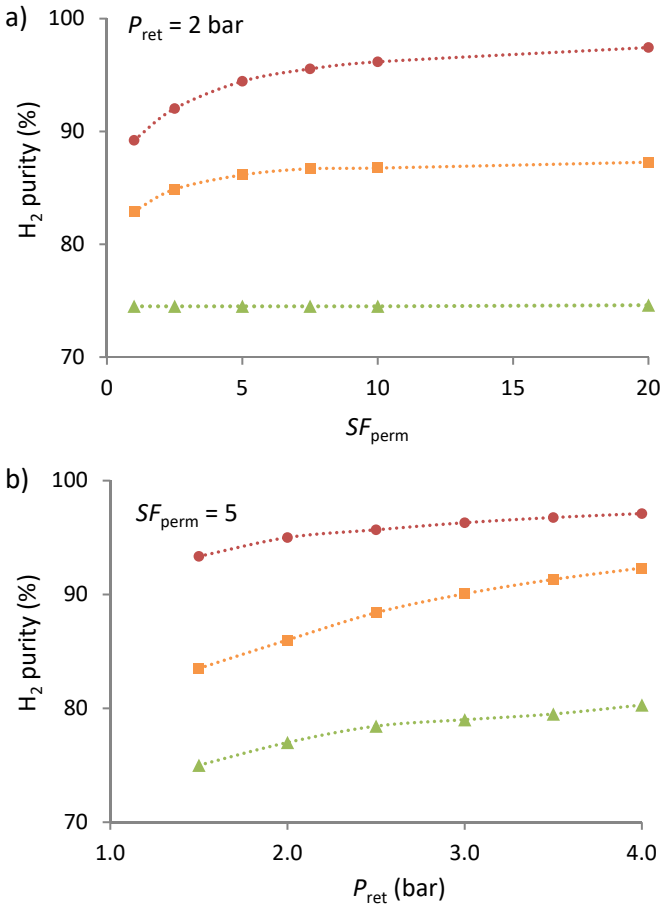


**Fig. 7.13** Simulated hydrogen purity as function of sweep factor (a) and retentate pressure (b) for a $CO_2$-PBMR at 473 K and *S/C* = 1.5 and infinite ideal selectivity. - ▲ - $\delta$=135 µm; - ■ - $\delta$ =10 µm; -● - $\delta$=1 µm. Lines were added for readability.

Fig. 7.14 shows the hydrogen purity for a 1 µm thick IL membrane with different selectivities. For membrane selectivities above 200 ($P_e(CO_2)/P_e(H_2)$ > 200) no significant increase in hydrogen purity is observed. At a SF of 10, a feed pressure of 2 bar and selectivity of 200 the hydrogen purity is ca. 95 %, which is a remarkable value. For selectivities lower than 50, the hydrogen purity is significantly affected. An IL membrane for use in a $CO_2$-PBMR should display selectivity higher than *ca*. 200.

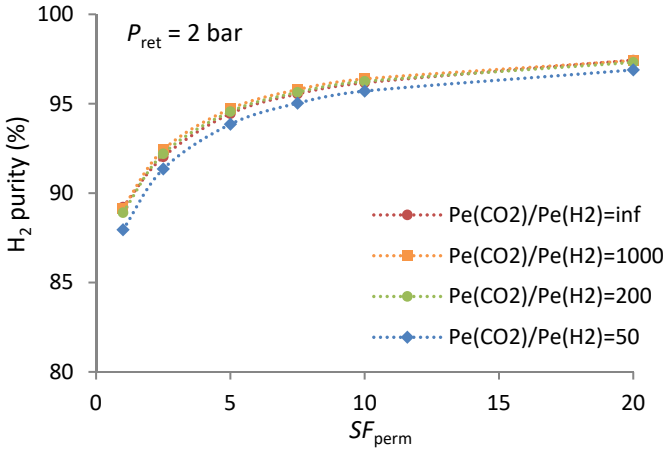


**Fig. 7.14** Simulated hydrogen purity as function of SF for a $CO_2$-PBMR with a membrane thickness of 1 µm, running at 473 K, $P_{ret}$ = 2, *S/C* = 1.5. Lines were added for readability.

### 7.5.6. Hydrogen recovery in PBMRs

For PBMRs besides the hydrogen purity, the hydrogen recovery is also important to take into account. Fig. 7.15 represents the hydrogen recovery as a function of the sweep gas factor for IL membranes with different selectivities.

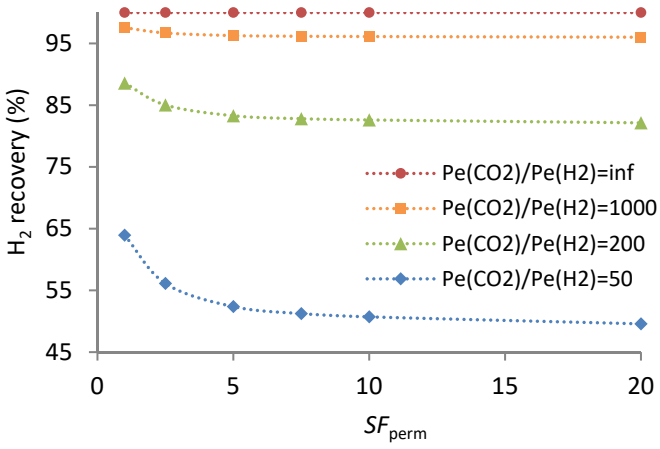


**Fig. 7.15** Hydrogen recovery as function of retentate pressure for a $CO_2$-PBMR with ILs membrane at 473 K, $P_{rent}$ = 2 bar, $m_{cat}/F_{MeOH}$ = 400 kg·mol$^{-1}$·s and *S/C* = 1.5. Lines were added for readability.

For $CO_2$-PBMR increasing the sweep gas flowrate has a low energy cost, since air can be used. For a membrane with a carbon dioxide over hydrogen ideal selectivity of 200 and a SF of 5, the recovery is 83.5 %. Sweep factors above 5 do not decrease significantly the recovery but have a positive effect on the hydrogen purity (Fig. 7.14). Since the aim of this work is to produce a hydrogen stream with low carbon content and high hydrogen recovery, the carbon dioxide to hydrogen selectivity should be above 200.

For $H_2$-PBMR, using a sweep gas to enhance the hydrogen recovery can represent high energy costs; since the hydrogen must be easily separated from the sweeping gas, water vapour is typically considered. Fig. 7.16 shows the hydrogen recovery Pd-Ag membranes at 473 K considering vacuum or a sweep gas in the permeate side.

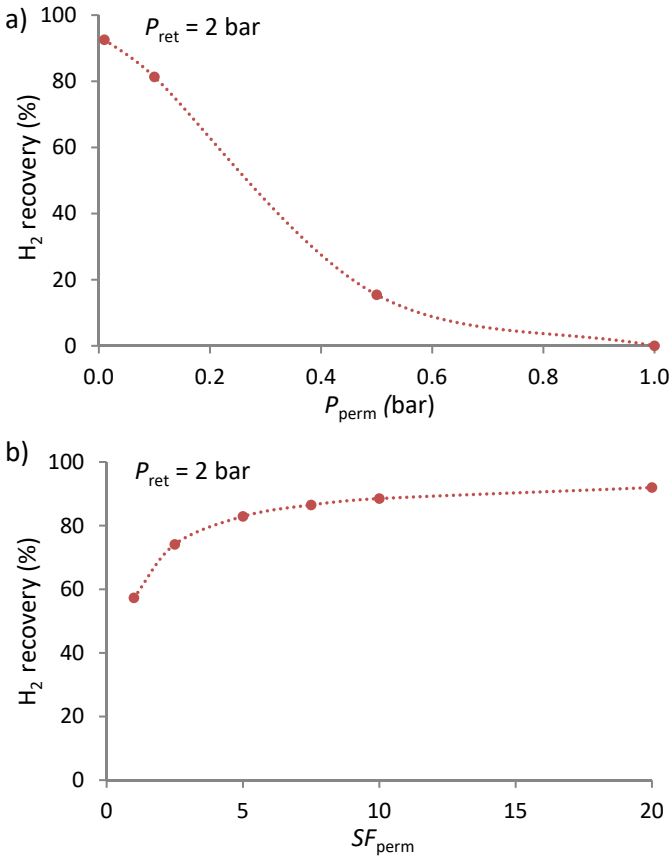


**Fig. 7.16** Hydrogen recovery as function of permeate pressure (a) and SF (b) for a $H_2$-PBMR with Pd-Ag membrane at 473 K, $m_{cat}/F_{MeOH}$ = 400 kg·mol$^{-1}$·s, $P_{rent}$ = 2 bar and $S/C$ = 1.5. Lines were added for readability.

The recovery provided by the Pd-Ag membrane depends on the operating conditions [35]. For high SF or high vacuum in the permeate side hydrogen high recoveries were obtained, ca. 90 %. However, the amount of hydrogen wasted reduces the efficiency of the system, moreover higher recoveries correspond to higher energy costs. The application of low vacuum in the permeate side (e.g. 100 mbar) is energetically more efficient than using sweep gas (due to evaporation and condensation) and allows high hydrogen recoveries (Fig. 7.16). Nevertheless, the used of vacuum pumps has other inconveniences such as higher complexity, higher equipment costs and is not applicable for small power supplies.

### 7.5.7. Energy efficiency in PBMRs

The energy needed for running the MSR in a $CO_2$-PBMR or $H_2$-PBMR should now be assessed and compared. The energy consumption per mole of methanol fed to the reformer ($E_{cons}/n_{MeOH}$) was computed considering the heating and vaporising the reactants, the energy needed to run the reformer reaction and the compressing and vacuum energy for purifying the produced hydrogen [36]. For simplicity, the compression and vacuum pumps were assumed to have an efficiency of 75 %. Concerning the IL membrane reformer, the sweep gas was assumed to be air heated at the HT-PEMFC while concerning the $H_2$-PBMR it was assumed the need of a vacuum pump at the permeate side. Since the HT-PEMFC needs to be cooled down, the energy needed for heating up the sweep air was not accounted an as energy input to the combined system.

Fig. 7.17 displays the specific energy needed for run the methanol reformer inserted in a combined LT-MSR / HT-PEMFC system as a function of the hydrogen recovery. The IL membrane was assumed to have a hydrogen ideal selectivity of 200 and 1 μm thick, while the Pd-Ag membrane was assumed permeable only to hydrogen with characteristics reported in Table 7.1. Assuming a recovery above 80 % and a hydrogen concentration higher than 95 %, the $H_2$-PBMR displays an energy consumption 5 % higher than the $CO_2$-PBMR. The advantage of the $CO_2$-PBMR grows for higher hydrogen recoveries, as depicted in Fig. 7.17.

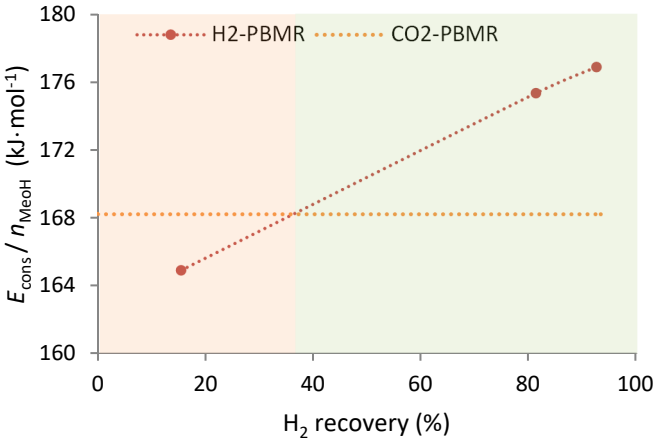


**Fig. 7.17** Energy consumption per mole of methanol fed ($E_{cons}/n_{MeOH}$) to the PBMR as a function of $H_2$ recoveries at 473 K, *S/C* = 1.5 and $m_{cat}/F_{MeOH}$ = 400 kg·mol$^{-1}$·s; the hydrogen recovery variation was achieved for IL membrane by changing the *SF*, while for Pd-Ag membrane was by changing the pressure in the permeate side.

## 7.6. Conclusions

The methanol steam reforming in packed bed membrane reactors, was discussed based on a CFD-based simulator, either considering hydrogen or carbon dioxide selective removal from the reaction bulk. The 3-dimensional isothermal PBMR model considered a Pd-Ag membrane selective to hydrogen, an ILs membrane selective to carbon dioxide, and a conventional packed bed reactor (PBR) as reference. Good agreement was obtained between modelling and experimental results. The selective hydrogen removal from the reaction bulk results in a methanol conversion enhancement assigned to the partial suppression of the backward methanol steam reforming reaction and an increase on the residence time. The MSR reaction rate increases with the temperature as well as the hydrogen permeation through the palladium-based membrane. However, the hydrogen generation increases faster with temperature than the hydrogen permeation; this makes the enhancement of methanol conversion more noticeable at lower temperatures. The $H_2$-PBMR at high hydrogen permeation driving force the hydrogen recovery is ca. 90 %. The selective carbon dioxide removal reactor originates a smaller methanol conversion enhancement than when using a hydrogen selective membrane, especially

at lower temperatures. The results indicated that only very selective and fast membranes, >1x10$^{-1}$ mol·s$^{1}$·m$^{-2}$·bar$^{-1}$ at 473 K and ideal selectivities >200, can effectively be used in a PBMR. A $CO_2$-PBMR can produce a stream with a hydrogen concentration of 95 % with a recovery of 83 % at $m_{cat}/F_{MeOH}$ = 200 kg·mol$^{-1}$, SF = 10 and running at 473 K. $CO_2$-PBMRs show to be more energy efficient than $H_2$-PBMR especially for high hydrogen recoveries.

## 7.7. References

[1] V. Eveloy, Numerical analysis of an internal methane reforming solid oxide fuel cell with fuel recycling, Applied Energy, 93 (2012) 107-115

[2] R. Chein, Y. Chen, C. Chang, J. Chung, Experimental study on the performance of hydrogen production from miniature methanol–steam reformer integrated with Swiss-roll type combustor for PEMFC, Applied Energy 105 (2013) 86–98

[3] V. Jaggi, S. Jayanti, A conceptual model of a high-efficiency, stand-alone power unit based on a fuel cell stack with an integrated auto-thermal ethanol reformer, Applied Energy 110 (2013) 295-303.

[4] C. Pan, R. He, Q. Li, J. Jensen, N. Bjerrum, H. Hjulmand, Integration of high temperature PEM fuel cells with a methanol reformer, Journal Power Sources 145 (2005) 392-398

[7] S.S. Araya, S.J. Andreasen, S.K. Kær, Experimental Characterization of the Poisoning Effects of Methanol-Based Reformate Impurities on a PBI-Based,HighTemperature PEM, Fuel Cell Energies 5 (2012) 4251-4267

[8] G. Bandlamudi, Systematic characterization of HT PEMFCs Containing PBI/H3PO4 systems. Thermodynamic analysis and Experimental investigations, Logos Verlad Berlin GmbH (2011)

[9] A. Iulianelli, P. Ribeirinha, A. Mendes, A. Basile, Methanol steam reforming for hydrogen generation via conventional and membrane reactors: A review Renewable and Sustainable Energy Reviews 29 (2014) 355–368

[10] J. Shu, B.P.A. Grandjean, A. Van Neste, Kaliaguine S., Catalytic palladium-based membrane reactors: A review, Canadian Journal of Chemical Engineering, 69(5) (1991) 1036–1060

[11] B.L. Bischoff, R.R. Judkins, Development of inorganic membranes for Hydrogen separation. Oak Ridge National Laboratory report (2008)

[12] Rahimpour M.R., Mazinani S., Vaferi B., Baktash M.S., Comparison of two different flow types on CO removal along a two-stage hydrogen permselective membrane reactor for methanol synthesis, Applied Energy, 88(1), 2011, 41-51

[13] R. Rahimpour, M.R. Dehnavi, F. Allahgholipour, D. Iranshahi, S.M Jokar, Assessment and comparison of different catalytic coupling exothermic and endothermic reactions: A review, Applied Energy 99 (2012) 496-512

[14] K. Ghasemzade, S. Liguori, P. Morrone, A. Iulianelli, V. Piemonte, A.A Babaluo, A. Basile, H2 production by low pressure methanol steam reforming in a dense Pd-Ag membrane reactor in co-current flow configuration: Experimental and modeling analysis, International Journal of Hydrogen Energy 39 (2014) 18702-18710

[15] M.P. Harold, B. Nair, G. Kolios, Hydrogen generation in a Pd membrane fuel processor: assessment of methanol-based reaction systems, Chemical Engineering Science 58 (2003) 2551-2571

[16] A. Basile, F. Gallucci, L. Paturzo, A dense Pd/Ag membrane reactor for methanol steam reforming: experimental study, Catalysis Today 104 (2005) 244-250

[17] R. Bredesen, H. Klette, Method of manufacturing thin metal membranes, US Patent, 6,086,729 (2000)

[18] H. Klette, R. Bredesen, Sputtering of very thin palladium-alloy hydrogen separation membranes, Membrane Technology 2005(5) (2005) 7–9

[19] T. Boeltken, M. Belimov, P. Pfeifer, T.A. Peters, R. Bredesen, R. Dittmeyer, Fabrication and testing of a planar microstructured concept module with integrated palladium membranes Chemical Engineering and Processing: Process Intensification 67 (2013) 136–147

[20] W. Chen, M. Hsia, Y. Chi, Y. Lin, C. Yang, Polarization phenomena of hydrogen-rich gas in high-permeance Pd and Pd–Cu membrane tubes Applied Energy 113 (2014) 41-50

[21] A. Basile, A. Iulianelli, J. Tong, Membrane reactors for the conversion of methanol and ethanol to hydrogen, Membrane Reactors for Energy Applications and Basic Chemical Production, Woodhead Publishing Series in Energy (2015) 187-208

[22] P. Ribeirinha, M. Boaventura, J.C.B. Lopes, J.M. Sousa, A. Mendes, Study of different designs of methanol steam reformers: Experiment and modeling, International, Journal of Hydrogen Energy 39 (2014) 19970-1998

[23] T.A. Peters, M. Stange, H. Klette, R. Bredesen, High pressure performance of thin Pd–23%Ag/stainless steel composite membranes in water gas shift gas mixtures; influence of dilution, mass transfer and surface effects on the hydrogen flux, Journal of Membrane Science 316 (2008) 119-127

[24] N. Katiyar, S. Kumar, S. Kumar, Comparative thermodynamic analysis of adsorption, membrane and adsorption-membrane hybrid reactor systems for methanol steam reforming, International Journal of Hydrogen Energy 38 (2013) 1363-1375

[25] L.J. Lozano, C. Godínez, A.P. de los Ríos, F.J Hernández-Fernández, S. Sánchez-Segado, F.J. Alguacil, Recent advances in supported ionic liquid membrane technology, Journal of Membrane Science 376 (2011) 1–14

[26] J. Gao, L. Cao, H. Dong, Zhang, S. Zhang, Ionic liquids tailored amine aqueous solution for pre-combustion CO2 capture: Role of imidazolium-based ionic liquids, Applied Energy 154 (2015) 771-780

[27] J. Grünauer, V. Filiz, S. Shishatskiy, C. Abetz, V. Abetz, Scalable application of thin film coating techniques for supported liquid membranes for gas separation made from ionic liquids, Journal of Membrane Science 518(15) (2016) 178-191

[28] P. Scovazzo, D. Havard, M. McShea, S. Mixon, D. Morgan, Long-term, continuous mixed-gas dry fed CO2/CH4 and CO2/N2 separation performance and selectivities for room temperature ionic liquid membranes, Journal of Membrane Science 327 (2009) 41–48

[29] S. Kasahara, E. Kamio, T. Ishigami, H. Matsuyama, Effect of water in ionic liquids on CO2 permeability in amino acid ionic liquid-based facilitated transport membranes, Journal of Membrane Science 415-416 (2012) 169–175

[30] C. Myers, H. Pennline, D. Luebke, J. Ilconich, J.K. Dixon, E.J. Maginn, J.F. Brennecke, High temperature separation of carbon dioxide/hydrogen mixtures using facilitated supported ionic liquid membranes, Journal of Membrane Science 322 (2008) 28–31

[31] Y. Shimoyama, S. Komuro, P. Jindaratsamee, Permeability of $CO_2$ through ionic liquid membranes with water vapour at feed and permeate streams, The Journal of Chemical Thermodynamics 69 (2014) 179–185

[32] B.A. Peppley, J.C. Amphlett, L.M Kearns, R.F Mann, Methanol steam reforming on Cu/ZnO/Al2O3 catalysts. Part 2: a comprehensive kinetic model, Applied Catalysis A 179 (1999) 31-49

[33] M.A. Habib, R. Ben Mansour, M.A. Nemit-allah, Modeling of oxygen permeation through a LSCF ion transport membrane, Computers & Fluids 76 (2013) 1–10

[34] M. Mulder, Basic Principles of Membrane Technology, 2nd ed. Kluwer Academic Publishers, Netherlands (1996)

[35] C. Mateos-Pedrero, H. Silva, D. Tanaka, S. Liguori, A. Iulianelli, A. Basile, A. Mendes, CuO/ZnO catalysts for methanol steam reforming: The role of the support polarity ratio and surface area, Applied Catalysis B Environmental 174 (2015) 67-73

[36] P. Atkins, J.D. Paula, Atkins Physical Chemistry, 8th ed. Oxford University Press, New York (2006)

# Chapter 8

# Integration of a PBMR with a HT-PMFC (modelling)

## 8.1. Abstract

In this work, the methanol steam reforming catalyst was considered into the anodic compartment of a high temperature polymer electrolyte fuel cell (HT-PEMFC), where reforming and electrochemical reactions occur simultaneously. To avoid the anode electro-catalyst poisoning by methanol, a Pd-Ag membrane, with a thickness of a few micrometres, was considered between the reforming catalyst and the membrane electrode assembly. A 3-dimensional non-isothermal simulator was developed in Fluent (Ansys™) considering a packed bed membrane reactor cell (PBMR-C) combined with a HT-PEMFC in a single unit. The performance of the combined unit depends on the permeability, selectivity and stability of Pd-Ag membrane at 473 K. Therefore, a self-supported Pd-Ag membrane with a thickness of 4 μm, was produced with no defects by magnetron sputtering. The membrane showed a $H_2/N_2$ molar selectivity of *ca.* 5800 and permeability of $2.94\times10^{-6}$ mol·m·s$^{-1}$·m$^{-2}$·bar$^{-0.8}$ at 473 K. The novel PBMR-C/HT-PEMFC after proper validation was analysed by simulation, showing high performance, similar to the one obtained with a HT-PEMFC fed with hydrogen and allowed efficient heat integration between electrochemical and MSR reaction. The PBMR-C/HT-PEMFC also demonstrated to be very compact. The advantages and limitations of the combined PBMR-C/HT-PEMFC unit are discussed based on the simulated results.

---

The content of this chapter is adapted from: P. Ribeirinha, M. Abdollahzadeh, A. Pereira, F. Relvas, M. Boaventura, A. Mendes, High temperature PEM fuel cell integrated with a cellular membrane methanol steam reformer: Experimental and modelling, Applied Energy 215 (2018) 659-669

## 8.2.Introduction

High temperature polymer electrolyte membrane fuel cells (HT-PEMFCs) combined with fuel processors, have been extensively reported in the literature [1-7]. Most studies focus their attention in the thermal coupling with catalytic combustors and reformers [3-7], where heat losses to the environment are a critical factor to the overall efficiency of the system [6, 7]. Several numerical studies have also been reported considering thermal fluids for heat transfer between the fuel stack and auxiliary systems [8,9], evaluating the efficiency of a HT-PEMFC stack operating at different temperatures [10,11] or considering micro-combined heat and power (CHP) plants [12,13]. The operation of a HT-PEMFC and reformer at the same temperature (<473 K) was considered by a few authors; in general, the results showed high voltage losses (160-200 mV) even at 473 K and low current densities, due to insufficient fuel supply from the reformer and the presence of residual methanol in the reformate stream [14-17]. Only recently it was reported a combined methanol steam reformer cell (MSR-C) and a HT-PEMFC able to produce high current densities (> 0.5 $A \cdot cm^{-2}$) running both devices at 453 K [18-19]. Designing a combined HT-PEMFC and fuel reformer system requires special attention due to the elevated temperatures, proper heat integration and control strategies to obtain a reliable, compact and efficient device [20]. These concerns could be mitigated by incorporating the methanol steam reforming (MSR) catalyst into the anodic compartment of the HT-PEMFC, where both reforming and electrochemical reactions occur simultaneously (internal reforming) [15, 16]. This configuration was experimentally assessed by Avgouropoulos *et al.* [15]. These authors observed high voltage losses and low current densities due to low methanol conversion, where the unconverted methanol poisons the electro-catalyst. Later, the same authors [21] incorporated a thin graphite plate as a physical barrier between the reformer and the anode electrocatalyst of the cell, to improve the gas distribution along the electrocatalytic layer, reducing the phosphoric acid back diffusion and the electro-catalyst poisoning by unreacted methanol. The fuel cell performance was improved, but still far from the reported for HT-PEMFCs fed with pure hydrogen [19]. Commercial MSR catalysts do not present yet the activity necessary to operate at low temperatures, < 473 K [14-19]. Efforts have been made to develop new low-temperature MSR catalysts; the gallium-promoted copper-based catalysts, are one

of the most promising catalysts, showing high activity and selectivity at temperatures lower than 473 K [22,23,24].

Palladium membranes show high selectivity and high permeability to hydrogen between 523 K – 873 K [25, 26]. The hydrogen purification for PEMFC applications from reformer streams is one of the most important application for Pd-based membranes [27-28]. Typically, Pd-based membranes consist of a thin layer (<20 μm) of the palladium or palladium alloy deposited onto a porous ceramic or metal substrate [28, 29]. The alloying elements, such as Ag, can improve the resistance to hydrogen embrittlement [30] and increase hydrogen permeability [31] of the membrane. The introduction of Ag decreases the hydrogen diffusivity in Pd-alloyed membranes but increases the hydrogen solubility; the maximum permeability of Pd-Ag membranes to hydrogen was found for a silver content of *ca.* 23 wt.% Ag [29]. These Pd-alloyed membranes have good mechanical stability, lower material costs and can deliverer ≈100 % pure hydrogen at the permeate side with a permeability of $10^{-6}$ mol·m·m$^{-2}$·s$^{-1}$·bar$^{-0.5}$ at temperatures above 573 K. For producing metallic thin films onto porous metallic or ceramic supports three techniques are reported: electroless plating [31, 32], chemical vapour deposition (CVD) [33, 34] and physical sputtering [35, 36]. Under controlled conditions all three methods produce good quality membranes, being the electroless plating technique a quite simple and often more effective method and the CVD method the easiest to scale up and flexible to apply a metal film on a support of different geometries. Direct current (DC) or radio frequency (RF) sputtering methods have the advantage of producing very thin Pd-Ag membranes, not supported, of good quality. One of the most remarkable procedures to prepare Pd-alloy membrane was developed by SINTEF using a two-steps sputtering technique [37, 38]. The Pd-Ag films are prepared as a foil by DC-magnetron sputtering on a silicon mono-crystalline wafer used as substrate. Noble metals do not adhere well to oxygen-rich surfaces (also named de-adhesion), since only physical bonds are created between the Pd-Ag film and substrate. Therefore, the metallic foils can be pulled off their substrate after deposition, transferred and placed onto a membrane support. This technique can produce defect–free Pd-alloy membranes with a nominal thicknesses ranging from 0.8 to 10.0 μm [37, 38], making their use possible for hydrogen purification at temperatures of *ca.* 473 K with considerable high permeances. Pd-Ag films can be easily applied to packed bed reactors with different configurations where mass transfer limitations (polarization of the concentration) in the gas phase can be reduced [39, 40]. The

use of packed bed membrane reactors (PBMR) equipped with Pd-alloy membranes to perform steam reforming of hydrocarbonates, allows the hydrogen product purification and allows increasing the conversion by hindering the backward reactions [25,28].

In this work a novel packed bed membrane reactor cell (PBMR-C) coupled with a HT-PEMFC, was suggested for the first time and studied by numerical simulation. The methanol steam reforming (MSR) catalyst was inserted in a serpentine channel of the cellular reformer, separated from the membrane electrode assembly (MEA) of the fuel cell by highly permeable and selective Pd-Ag membrane. The mathematical model used for simulating the HT-PEMFC considers the electrochemical reactions at the anode and cathode catalyst layers, the temperature, the phosphoric acid doping level and the influence of the water content on the membrane proton conductivity [10, 41, 42]. The kinetic model for the methanol steam reforming reaction was based on a Langmuir–Hinshelwood model with an overall reaction network comprising methanol steam reforming (MSR) reaction, reverse water-gas-shift (RWGS) and methanol decomposition (MD) [43]. The membrane permeability and selectivity was obtained experimentally. The combined PBMR-C/HT-PEMFC unit were discussed based on the simulated results and were compared with a HT-PEMFC fed with pure hydrogen.

## 8.3. PBMR-C/HT-PEMFC model

### 8.3.1. Physical model

The PBMR-C/HT-PEMFC physical model considers a cellular reformer separated from the MEA of the fuel cell by Pd-Ag membrane, as depicted in Fig. 8.1. The combined unit was assumed equipped with a 45 $cm^2$ Celtec P2200N MEA from BASF, with a catalyst loading of 1 mg $Pt \cdot cm^{-2}$ on the anode and 0.85 mg $Pt \cdot cm^{-2}$ on the cathode. The reformer channels were assumed filled with commercial catalyst ($CuO/ZnO/Al_2O_3$) from BASF (RP-60) with particle size between 200-400 μm. To reduce the computational costs, a simplified 3D geometry of the PBMR-C/HT-PEMFC was considered (Fig. 8.2), following the same approach reported in the literature [10, 41, 42]. Therefore, one third of the complete geometry was modelled: one straight channel of the reformer, a Pd-Ag membrane, a MEA (composed by anode and cathode gas diffusion layers – GDL, anode and cathode

catalyst layers – CL and phosphoric acid doped polybenzimidazole – PBI membrane), and two straight and parallel channels of the cathode bipolar plate, as shown in the mesh configuration in Fig. 8.2. The dimensions and relevant physical parameters are summarized in Table 8.1.

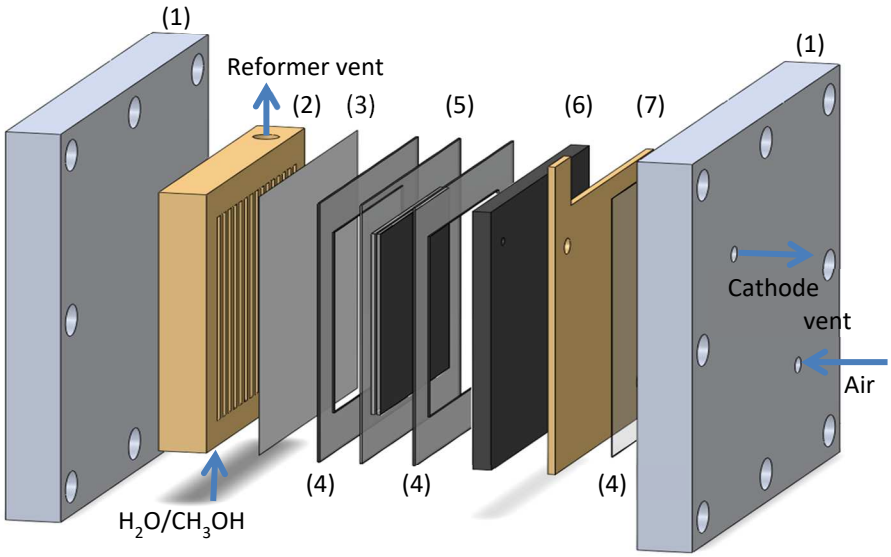


**Fig. 8.1** Assembly scheme of the integrated unit (PBMR-C/HT-PEMFC); two metal end-plates frames (1), gold coated reformer (2), Pd-Ag membrane (3), gasket (4), MEA (5), graphite composite bipolar plate (6) and current collector (7).

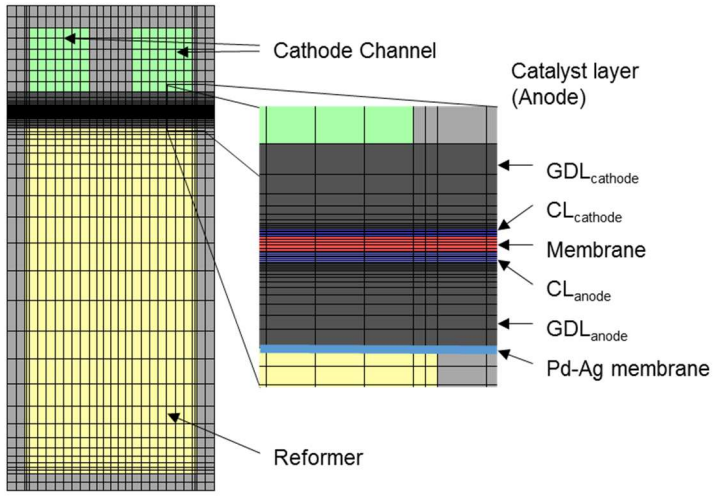


**Fig. 8.2** Computational domain and mesh configuration of the PBMR-C/HT-PEMFC.

**Table 8.1** PBMR-C/HT-PEMFC physical properties.

| Parameter | Value |
|---|---|
| Thickness ($\delta$, μm) $CL_a$, $CL_c$, $GDL_{a,c}$, PBI membrane, Pd-Ag Membrane | 40, 30, 350, 65, 4 |
| Reformer channel (mm) length, width, depth | 312.5, 4, (8, 5,2.5) |
| $BPP_{Cat}$ channel (mm) length, width, depth, rib width | 312.5, 1.5, 1.4, 1 |
| Porosity ($\varepsilon$) GDL, CL, $MSR_{cat}$ | 0.6, 0.1, 0.32 |
| Electrolyte volume fraction ($l_m$) | 0.754 |
| Phosphoric acid doping level (*DL*) | 16.76 |
| Permeabilities (*Pe*, $m^2$) [41] GDL, CL, $MSR_{cat}$ | $1x10^{-13}$, $1x10^{-12}$, $1x10^{-11}$ |
| Volumetric mass density ($\rho$, $kg \cdot m^{-3}$) $CL_{a,c}$, $GDL_{a,c,}$ membrane[41], $MSR_{cat}$[43] | 1000, 1000, 1000, 1300 |
| Specific heat capacity (Cp, $J \cdot kg^{-1} \cdot K^{-1}$) CLa,c, GDLa,c, membrane[41], MSRcat[43] | 3300, 586, 1650, 1580, 800 |
| Thermal conductivity (K, $W \cdot m^{-1} \cdot K^{-1}$) CLa,c, GDLa,c, membrane[41], MSRcat[43] | 1.7, 1.7, 0.95, 237.0, 0.3 |
| Electric conductivity ($\sigma_s$, $S \cdot m^{-1}$) [41] $CL_{a,c}$, $GDL_{a,c}$, BPP | 1250, 1250, 14000 |
| Stoichiometry ($\lambda$) hydrogen, oxygen | 1.2, 2 |
| Steam to carbon ratio (S/C) | 1.5 |
| Operating pressure (*P*, bar) | 1 |
| Operating temperature (*T*, K) | 433-473 |
| Relative humidity of gases | 0 |
| $MSR_{cat}$ mass ($m_{cat}$, kg) | 0.013, 0.008, 0.004 |

### 8.3.2.Mathematical model

The present work considers a 3-dimension non-isothermal model for HT-PEMFC combined with a PBMR-C following a single domain approach. The model presents a full description of the transport of charge, mass and thermal energy in a single-phase system, including the electrochemical model, the kinetic model for methanol steam reforming reaction and the permeation model.

#### *Main assumptions*

The following simplifications were considered in the PBMR-C/HT-PEMFC model:

- gas mixtures were considered ideal,
- flow was assumed to be laminar and the effect of gravity was neglected,

- membrane, CL, GDL, BPP and MSR catalyst were assumed isotropic and homogenous,
- fuel cell membrane was considered impermeable to all gases,
- only protons were accounted for the transport through membrane,
- the Pd-Ag membrane was considered as a wall with no thickness
- no diffusion limitations in the MSR catalyst were considered;

The model governing equations consist of conservation of mass, momentum, energy, species and charges, as described in the following subsections:

*Continuity equation:*

$$\nabla \cdot (\rho \vec{u}) = S_m \tag{8.1}$$

where, $\rho$ is the fluid volumetric mass density calculated using the ideal gas equation, $\vec{u}$ is the fluid velocity vector, and $\nabla$ is the operator gradient. $S_m$ represent the source terms, which considers the production and consumption of species due to the electrochemical reactions, the methanol steam reforming reactions and $H_2$ permeation (more detail in [41-43]), as summarized in Table 8.2.

*Conservation of momentum of the gas mixture:*

$$\nabla \cdot \left( \frac{\rho \vec{u} \vec{u}}{\varepsilon^2} \right) = -\nabla p + \nabla . \tau + S_u \tag{8.2}$$

where, $\varepsilon$ is the media porosity and $\nabla p$ is the pressure gradient and $\nabla \tau$ is the anisotropic part of the stress tensor and describes the viscous forces. The source term ($S_u$) is the pressure gradient (drop) in a porous media calculated using the Darcy's law (Eq.12, Table 8.2), which considers the intrinsic permeability ($P_e$) and the viscosity ($\mu$) of the gases.

*Species conservation equation:*

$$\nabla \cdot (\rho \vec{u} \omega_i) = \nabla j_i + S_i \tag{8.3}$$

where $\omega_i$ is the local mass fraction of the specie *i* and $j_i$ is the mass diffusion flux of the specie *i*. The mass diffusion flux is calculated by the Fick's law ( $j_i = \rho \varepsilon^{1.5} D_i \nabla \omega_i$ ) modified by the Bruggman relation for the diffusion ($D_i$) in a porous media; the physical and transport properties of the gases, are presented in Table 8.3. $S_i$ are the source terms due

to the electrochemical reactions, the methanol steam reforming reactions (MSR, WGS and MD) and the $H_2$ permeation, as summarized in Table 8.2. The kinetic parameter used in this work to obtain the reaction rates ($r_j$) MSR, MD and RWGS are summarized elsewhere [43].

*Energy equation:*

$$\nabla.\left(\rho\vec{u}\left(\sum_{i}^{N_c} y_i \int_{T_{ref}}^{T} Cp_i dT\right)\right) = \nabla\left(\lambda_{eff}\nabla T\right) - \nabla\vec{u}P + S_T \tag{8.4}$$

where, $Cp_i$ is the specific heat capacity of species *i* and $\lambda_{eff}$ is the effective thermal conductivity, which takes into account the thermal conductivity in the solid and gas phase, and *T* is the absolute temperature. $S_T$ is the source term which includes the heat flux due to the electrochemical reaction, ohmic resistance, activation losses and MSR chemical reaction,

*Charge conservation equations*

$$\nabla.\left(-\sigma_s^{eff}\nabla\varphi_s\right) = S_{\varphi_s} \tag{8.5}$$

$$\nabla.\left(-\sigma_m^{eff}\nabla\varphi_m\right) = S_{\varphi_m} \tag{8.6}$$

where, $\varphi_s$ and $\varphi_m$ are the electric and protonic overpotentials, respectively. The $S_{\varphi_s}$ and $S_{\varphi_m}$ (source terms) of the Eqs. 5 and 6 are the volumetric exchange current densities ($J_c$, $J_{a(H2)}$ and $J_{a(CO)}$) calculated using the Butler-Volmer equation, summarized in Table 8.2 (more detailed information can be found elsewhere [10, 41, 42]). The $\sigma_s^{eff}$ and $\sigma_m^{eff}$ are the effective electron and proton conductivities and are calculated by Bruggeman equation for porous medium:

$$\sigma_m^{eff} = l_m^{1.5}\sigma_m, \qquad \sigma_s^{eff} = \left(1-\varepsilon-l_m\right)^{1.5}\sigma_s \tag{8.7}$$

where, $\sigma_m$ is the electrolyte protonic conductivity and $l_m$ is the polymer electrolyte volume fraction in the CL. The effect of the relative humidity (RH), temperature and membrane doping level (*DL*), on the electrolyte protonic conductivity ($\sigma_m$) was determined following the same approach reported in [10]

**Table 8.2** Source terms of the governing equation (Eq. 8.1 – 8.6).

| **Source terms** | |
|---|---|
| $S_m(CL_c) = \frac{M_{O_2} J_c}{4F} - \frac{M_{H_2O} J_c}{2F}$ | (8.8) |
| $S_m(CL_a) = -\frac{M_{H_2} J_{a(H_2)}}{2F} - \frac{M_{H_2O} J_{a(co)}}{2F} - \frac{M_{CO} J_{a(co)}}{2F} + \frac{M_{CO_2} J_{a(co)}}{2F}$ | (8.9) |
| $S_m(GDL_a) = + \frac{j_{H_2,perm} A_{cell} M_i}{V_{cell}}$ | (8.10) |
| $S_m(ref) = \sum_{i,j(products)} v_i M_i r_j - \sum_{i,j(reagents)} v_i M_i r_j - \frac{j_{H_2,perm} A_{cell} M_i}{V_{cell}}$ | (8.11) |
| $S_u = -\frac{\mu}{P_e} \vec{u}$ | (8.12) |
| $S_i(CL_c) = -\frac{M_i J_c}{n_e F}$ | (8.13) |
| $S_i(CI_{a_{H2},a_{CO}}) = -\frac{M_i J_{a_{H2},a_{CO}}}{n_e F}$ | (8.14) |
| $S_i(GDL_a) = + \frac{j_{i,perm} A_{cell} M_i}{V_{cell}}$ | (8.15) |
| $S_i(ref) = \sum_j M_i v_{i,j} r_j - \frac{j_{i,perm} A_{cell} M_i}{V_{cell}}$ | (8.16) |
| $S_T(PBI_{mem}) = \left\|\nabla \varphi_m\right\|^2 \sigma_m^{eff}$ | (8.17) |
| $S_T(GDL, BPP) = \left\|\nabla \varphi_s\right\|^2 \sigma_s^{eff}$ | (8.18) |
| $S_T(CL_c) = \left\|\frac{j_{cat}}{2F}\right\|(T\Delta S) + \left\|\eta\, j_{cat}\right\| + \left\|\nabla \varphi_s\right\|^2 \sigma_s^{eff} + \left\|\nabla \varphi_m\right\|^2 \sigma_m^{eff}$ | (8.19) |
| $S_T(CL_a) = \left\|\eta\, j_{ano}\right\| + \left\|\nabla \varphi_s\right\|^2 \sigma_s^{eff} + \left\|\nabla \varphi_m\right\|^2 \sigma_m^{eff}$ | (8.20) |
| $S_T(MSR) = \sum_{i=1}^{N} \left( \Delta H_{k,298} + \sum_i v_i \int_{298}^{T} Cp_i dT \right)(r_k)$ | (8.21) |
| $J_{a,H_2} = a i_{0,a} \theta_{H_2} \left\{ \exp\left( \frac{\alpha_a}{RT} F \eta_a \right) - \exp\left( -\frac{\alpha_c}{RT} F \eta_a \right) \right\}$ | (8.22) |
| $J_c = -a i_{0,c} \left( \frac{C_{O_2}}{C_{O_2}^{ref}} \right) \left\{ \exp\left( \frac{\alpha_a}{RT} F \eta_c \right) - \exp\left( -\frac{\alpha_c}{RT} F \eta_c \right) \right\}$ | (8.23) |
| $J_{a,CO} = a i_{0,CO} \theta_{CO} \exp\left( \frac{\alpha_{CO}}{RT} F \eta_a \right)$ | (8.24) |

The volumetric exchange current densities ($J_c$, $J_{a(H2)}$ and $J_{a(CO)}$) calculated using the Butler-Volmer equation, considers the over-potentials in anode ($\eta_a$) and cathode ($\eta_c$),

the exchange current density of the anode ($ai_{0,a}$) and cathode ($ai_{0,c}$) and the charge transfer coefficient of the anode ($\alpha_a$) and cathode ($\alpha_c$); the values of the parameters are summarized in Table 8.4. The electro-oxidation of CO, despite the small effect in the overall current density, is also considered in the model (Eq. 8.24), thus, $\alpha_{i0,CO}$ and $\alpha_{CO}$ are the exchange current density and charge transfer coefficient for CO, respectively. The Butler-Volmer equation for the anode (Eq. 8.22) was modified to consider the CO poisoning in the electrochemical reaction rate, therefore the hydrogen coverage ($\theta_{H2}$) was included in the equation. The $\theta_{H2}$ depends on the adsorption, desorption and electrochemical oxidation of the adsorbed species on the catalyst surface (more details about the CO poisoning model can be found elsewhere [10, 41, 42]).

**Table 8.3** Physical and transport properties [10, 41, 42]

| Property | Value | |
|---|---|---|
| Diffusivity of gas the species, ( $m^2 \cdot s^{-1}$) | $D_i^T = D_i^{ref}\left(\frac{T}{333.15}\right)^{1.5}\left(\frac{101325.0}{P}\right)$ | (8.25) |
| | $D_{H_2}^{ref} = 1.055\times10^{-4}$ | |
| | $D_{O_2}^{ref} = 2.652\times10^{-5}$ | |
| | $D_{CO_2}^{ref} = 3.2348\times10^{-5}$ | |
| | $D_{CO}^{ref} = 3.2348\times10^{-5}$ | |
| | $D_{H_2O(anode,MSR)}^{ref} = 1.055\times10^{-4}$ | |
| | $D_{H_2O(cathode)}^{ref,} = 2.982\times10^{-5}$ | |
| | $D_{CH_3OH}^{ref} = 3.2348\times10^{-5}$ | |
| Viscosity of the gas species ($kg \cdot m^{-1} \cdot s^{-1}$) | $\mu_{H_2}^T = 3.205\times10^{-3}\left(\frac{T}{293.85}\right)^{1.5}\left(\frac{1}{T+72}\right)$ | (8.26) |
| | $\mu_{H_2O}^T = 7.512\times10^{-3}\left(\frac{T}{291.15}\right)^{1.5}\left(\frac{1}{T+120}\right)$ | (8.27) |
| | $\mu_{O_2}^T = 8.46\times10^{-3}\left(\frac{T}{292.85}\right)^{1.5}\left(\frac{1}{T+127}\right)$ | (8.28) |
| | $\mu_{Others}^T = 8.46\times10^{-3}\left(\frac{T}{292.85}\right)^{1.5}\left(\frac{1}{T+127}\right)$ | (8.29) |
| Water saturation pressure, (bar) | $p_{sat} = 0.68737\times T^3 - 732.39\times T^2 + +263390\times T - 31919000$ | (8.30) |
| Relative Humidity | $RH = \begin{cases} \frac{x_{H_2O}p}{p_{sat}} \text{(in CL)} \\ \frac{Rh_{CL(ano)} + Rh_{CL(cat)}}{2} \text{(in membrane)} \end{cases}$ | (8.31) |

| | |
|---|---|
| Specific heat capacities ($J \cdot kg^{-1} \cdot K^{-1}$) | $Cp_{p,H_2} = 14283$; $Cp_{O_2} = 919.31$; $Cp_{H_2O} = 2014$<br>$Cp_{N_2} = 1042$; $Cp_{CO_2} = 919.31$ $Cp_{CO} = 919.31$<br>$Cp_{CH_3OH} = 919.31$ |
| Thermal conductivities ($W \cdot m^{-1} \cdot K^{-1}$) | $\lambda_{H_2} = 0.1672$; $\lambda_{O_2} = 0.0246$; $\lambda_{H_2O} = 0.0261$ |
| Change in Entropy ($J \cdot mol^{-1} \cdot s^{-1}$) | $\Delta S = -44.500$ |

**Table 8.4** Electrochemical parameters

| Parameter | Anode | Cathode |
|---|---|---|
| Over-potential, $\eta$ (V) | $\eta = \varphi^s - \varphi^m$ (8.32) | $\eta = \varphi^s - \varphi^m$ (8.33) |
| Equilibrium-potential, $U_0$ (V) | $U_0 = 1.1669\text{-}2.4\text{x}10^{-4}(T\text{-}373.15)$ (8.34) | |
| Specified exchange current density, $ai_0$ ($A \cdot m^{-3}$) | $ai_{0,a}^{ref} \exp\left[-1400\left(\frac{1}{T} - \frac{1}{353.15}\right)\right]$ $ai_{0,a}^{ref} = 1\times10^8$ (8.35) | $ai_{0,c}^{ref} \exp\left[-7900\left(\frac{1}{T} - \frac{1}{353.15}\right)\right]$ $ai_{0,c}^{ref} = 70$ (8.36) |
| Ref. concentrations, $C_i^{ref}$ ($mol \cdot m^{-3}$) | 40.88 | 40.88 |
| Transfer coefficients, $\alpha_{H2}$ | 1 | 0.97 |

*Boundary and Initial condition*

The boundary conditions considered for the PBMR-C/HT-PEMFC device are:

- the mass fluxes at the cathode inlet were determined based on oxygen stoichiometry for the defined current density;
- the mass flux in the reformer was calculated based on the space-time-ratio ($m_{cat}/F_{MeOH}$);
- the water/methanol mixture and cathode gas stream are fed in counter current;
- at the outlets, the pressure was considered to be constant and equal to a specified value;
- at the walls the flow obeys to the no slip condition;
- at the interfaces between bipolar plate, channels, GDL, CL, fuel cell membrane, Pd-Ag membrane the boundaries were coupled for the electronic potential and temperature;

- potentiostatic boundary conditions were imposed at the surfaces of the bipolar plates (terminal surface). The electric potential of the cathode and anode was assumed $\emptyset_s = 0$ and $\varphi_s = U_0 - V_{cell}$, respectively.

### 8.3.3. Numerical Procedure

The 3-dimensional model for the PBMR-C/HT-PEMFC was developed in commercial software Fluent, a platform that uses the finite-volume method to solve the differential equations. The source terms, physical properties and boundary conditions were implemented by developing User Defined Functions (UDF) written in C++, compiled and loaded in FLUENT. The electric potential equations were implemented developing User Defined Scalars (UDS). The governing equations were discretized with a second-order spatial and temporal schemes. The under relaxation was also adjusted to handle the convergence problems. The simulations were carried step-wise to avoid divergence, first solving the reformer equations, then the permeation and finally the fuel cell related equation. In all simulations, strict convergence criteria with residuals of $10x10^{-7}$ were chosen for all variables. The computational grid used for modelling the 3D straight channel PBMR-C/HT-PEMFC has approximately $5x10^5$ grid cells.

## 8.4. Experimental

*Pd-Ag membrane preparation*

Pd-Ag membranes were deposited by magnetron sputtering (QPrep400 from Mantis Deposition®). The target was a 75/25 wt. % Pd/Ag disc with 100 mm diameter and a purity of 99.95 %. The depositions were carried out at 0.1 mbar of base pressure controlled by a throttle valve of 0.002 mbar and using an argon flow of 25 $cm^3 \cdot min^{-1}$. The sputtered films were deposited onto smooth, thermally oxidized 10.15 cm (diameter) silicon wafer (Microchemicals GmbH) at room temperature in a static deposition. The power applied during the deposition was 60 W with a voltage of 277 V and a current of 0.22 A, generating a deposition rate of ca. 0.23 $nm \cdot s^{-1}$.

*Assembly and characterization of the Pd-Ag membrane*

The coated wafers were manually peeled out of the silicon wafer as self-supported membranes. This step is a very delicate procedure that may generate pin holes in the film. After the peel out, the film was characterized by field emission scanning electron microscopy (SEM) to determine the thickness and to assess the membrane quality. The Pd-Ag membrane permeability was assessed using a microchannel device made of polished 316 stainless steel gold plated (Fig. 8.3).

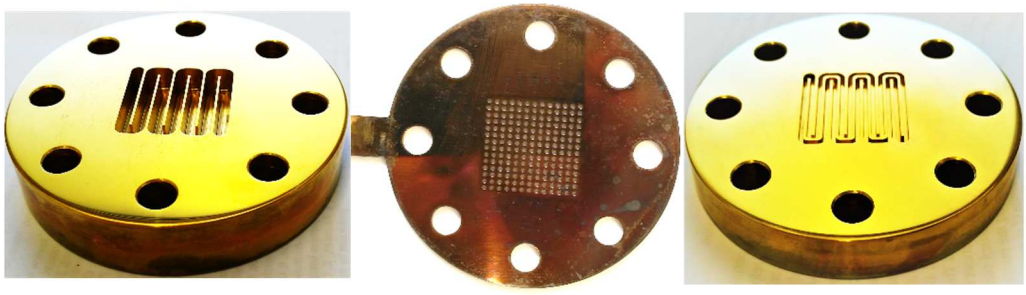

(a) (b) (c)

**Fig. 8.3** Membrane testing cell; (a) feed microchannel plate, (b) perforated plate, (c) permeate microchannel plate.

The Pd-Ag membrane was placed between the feed microchannel plate (Fig 8.3a) and the perforated plate ((Fig 8.3b). The feed microchannel plate (Fig 8.3a) consists on single serpentine channel with an inlet and outlet to feed and to collect the retentate gas, respectively. The perforated plate (Fig. 8.3b) was designed to provide mechanical support to the membrane and comprehends 156 holes of 1 mm in diameter with a total area of 1.43 $cm^2$. The permeate microchannel plate (Fig. 8.3c) has a double serpentine channel geometry with two outlets to collect the permeate gas. The cell was tightened using 8 bolts with a torque of 3.5 N·m. No gasket was used for sealing. The microchannel testing device was then placed in an oven and heated to the target temperature in an inert atmosphere of $N_2$, before $H_2$ was introduced. The feed gas flow and pressure was controlled by pressure flow meter (HORIBA STEC UR-Z712M-B). The permeated hydrogen flow was determined using a high precision film flow meter (HORIBA STEC SF) with a two volumetric units of different ranges, 0.2 – 10 $cm^3 \cdot min^{-1}$ (Film Flow Meter VP-1U)

and 20 – 1000 $cm^3 \cdot min^{-1}$ (Film Flow Meter VP -3U). During experiments with pure hydrogen no sweep gas was used, only pressure and temperature was varied. The testing conditions applied are summarized in Table 8.5.

The membrane selectivity towards hydrogen was determined considering a gas mixture fed to the retentate with volume fractions of 50 % of $H_2$ and 50 % of $N_2$ and a flow rate of 200 $cm^3 \cdot min^{-1}$. The permeated composition was determined by GC (Dani GC 1000 equipped with a thermal conductivity detector (TCD)).

**Table 8.5** Experimental conditions used in the permeation testes for two *in-house* produced membranes.

| Membrane | Heat treatment (activation) | Temperature (K) | Feed Pressure (bar) | Pressure permeate (bar) |
|---|---|---|---|---|
| M1 | 673 K during 24h with hydrogen | 523; 573 | 1 – 4 | 1 |
| M2 | – | 473; 523 | 1 – 4 | 1 |

## 8.5. Results and Discussion

### 8.5.1. Pd-Ag membrane SEM analysis

Before the permeation tests, the Pd-Ag membrane were analysed by SEM (Fig. 8.4). A dense and pinhole-free surface can be observed in Fig. 8.4a and 8.4b, corresponding respectively to the bottom and top views of the membrane; a dense pinhole-free surface is crucial for obtaining high permeation selectivity to hydrogen [44]. Fig. 8.4c shows the cross section of the Pd-Ag membrane evidencing a 4 µm average thickness. Fig. 8.4d highlights the conceptual microstructure of the sputtered palladium-silver membrane. The first layer is characterized by small metal grains corresponds to the nucleation side, which morphology is difficulty to observe even at high magnifications (Fig. 8.4a). The top view shows larger grains, also organized and defect-free (Fig. 8.4b). A smooth substrate and optimized deposition parameters are crucial to obtain of a dense and pinhole-free membrane, as described elsewhere [37, 38].

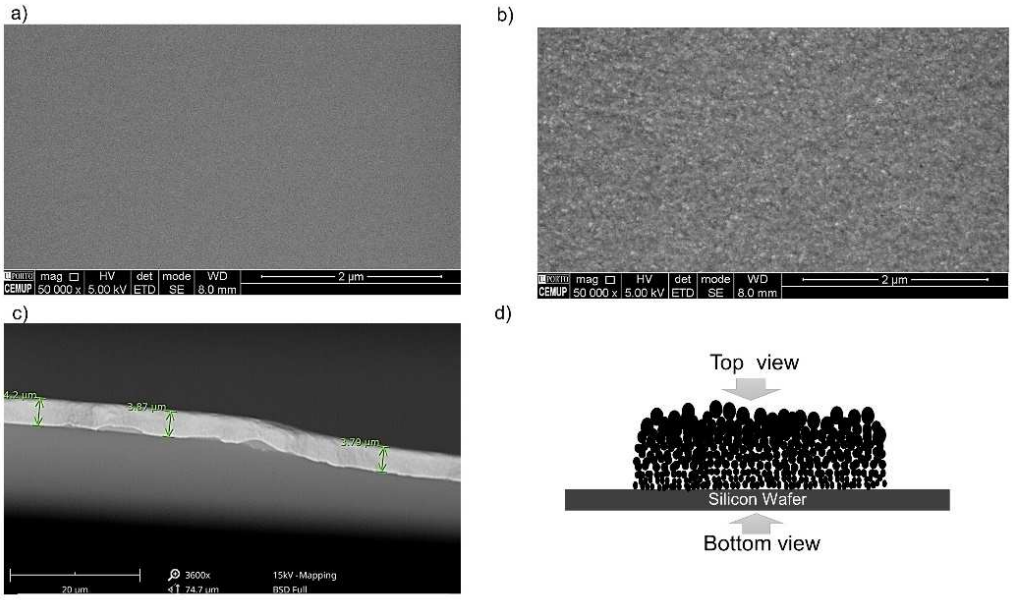


**Fig. 8.4** SEM micrographs from Pd/Ag membrane deposited by magnetron sputtering onto silicon wafer; a) bottom view from membrane; b) top view from membrane; c) cross-section view of the membrane and d) conceptual microstructure of the membrane.

### 8.5.2. Pd-Ag membrane permeability

Pd-Ag membrane M1 was inserted in the microchannel device and left for 24 h at 673 K with a hydrogen flow rate pf 30 $cm^3 \cdot min^{-1}$ – activation procedure. The membrane permeability was then obtained at temperatures between 523 K and 573 K. At constant temperature, the hydrogen permeation flux is given by:

$$J_i = \frac{P_e}{\delta}\left(p_{i,ret}^{1/n} - p_{i,perm}^{1/n}\right) \tag{37}$$

where $J_i$ is the molar flux of species *i*, $P_e$ is the membrane permeability, $\delta$ is the membrane thickness and $p_{i,ret}$ and $p_{i,perm}$ are the partial pressure in the retentate and permeate sides, respectively. The *n-value* (Eq. 37) is an estimation the rate controlling steps. The hydrogen permeation through thick Pd and Pd-alloy membranes (>10 µm) is commonly assumed to be limited by the hydrogen diffusion through the bulk of the membrane [44]. In this case, the membrane permeation follows the Sieverts-Fick law, where the *n-value is* typically equal to two. Reducing the thickness makes the diffusion

transport through the membrane faster; the control step of the hydrogen permeation becomes then the hydrogen dissociation and recombination, at the membrane surfaces [45, 46]. In this case, an n < 2 is expected. For membrane M1 at 573 K nearly straight fitting lines are observed for all *n-values* ranging from 1 to 2, with the best fitting occuring with *n* = 1.25 (Fig. 8.5). The membrane permeability was $4.9\times10^{-6}$ mol·m·s$^{-1}$·m$^{-2}$·bar$^{-0.8}$ at 573 K considering n = 1.25.

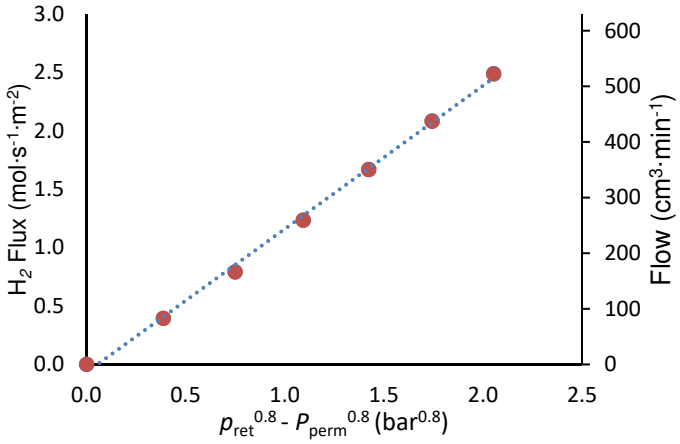


**Fig. 8.5** Hydrogen flux and flow rate through the membrane M1 as a function of the difference of partial pressures between retentate and permeate sides with *n*= 1.25 (no sweep gas) at 573 K; activated during 24 h at 673 K under hydrogen atmosphere – activation procedure.

The selectivity was determined considering pure nitrogen in the retentate side and measuring the permeated flow rate using a high precision film flow meter (range 0.2-10 cm$^3$·min$^{-1}$). The $H_2/N_2$ selectivity was also evaluated considering a $H_2/N_2$ mixture in the retentate side, where the permeated stream composition was analysed by gas chromatography. The first procedure does not provide a precise value, but it gives the magnitude of the $H_2/N_2$ selectivity. At 573 K and for a feed pressure of 4 bar, no permeated nitrogen was detected, resulting in $H_2/N_2$ selectivity > 2500. The GC measurements confirmed a $H_2/N_2$ selectivity of *ca.* 3800.

Pd-Ag membrane M2 was inserted in the permeation cell and heated in an inert atmosphere of $N_2$ till of 473 K and the membrane permeability to hydrogen was then obtained at 473 K and at 523 K. Fig. 8.6 shows the permeated hydrogen flux and flow rate through the membrane M2 as a function of the partial pressure difference with *n*

=1.25, at 473 K. The permeability at 473 K was $2.94\times10^{-6}$ mol·m·s$^{-1}$·m$^{-2}$·bar$^{-0.8}$ with a $H_2/N_2$ selectivity of *ca.* 5800. Only a few studies report the permeability of Pd-alloy membranes at temperatures lower than 573 K. Nayebossadri *et al.* [47] obtained a permeability of $3.2\times10^{-6}$ mol·m·s$^{-1}$·m$^{-2}$·bar$^{-0.5}$ for a $Pd_{46.6}Cu_{53.4}$ of 40 □m at 473 K. Remarkably, these authors report hydrogen permeation even at 373 K, with a permeability of *ca.* $6.3\times10^{-7}$ mol·m·s$^{-1}$·m$^{-2}$·bar$^{-0.5}$.

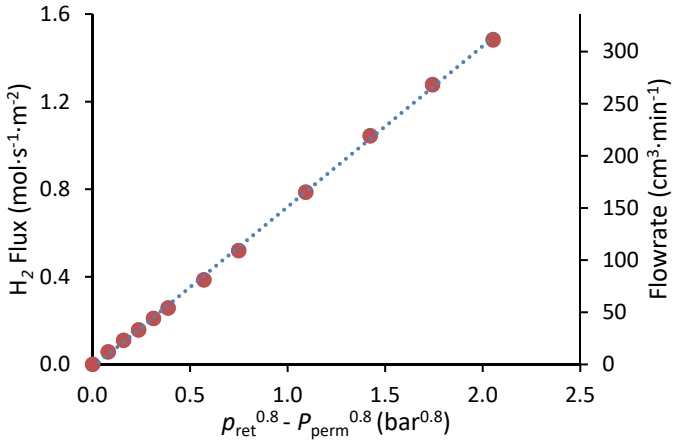


**Fig. 8.6** Hydrogen flux and flow through the membrane M2 as a function of the partial pressure difference between retentate and permeate sides with *n* = 1.25 (no sweep gas) at 473 K.

Fig. 8.7 compares the hydrogen flux as a function of the difference of partial pressures with n=1.25, for membranes M1 and M2 at 523 K. Membrane M1 shows higher performance than M2, indicating that the activation treatment of M1 has a positive effect on the membrane permeability. The activation treatment has been reported to increase the surface roughness, area and grain size [47]. The subject is not consensual in the literature, some authors claiming that the grain growth reduces the hydrogen flux through the membrane due to a reduction in the grain boundary volume fraction, which reduces the hydrogen diffusion along the grain boundaries [48,49] while other claim that the grain growth has neutral [50] or positive effect in the membrane permeability [51]. In this work, the heat treatment of M1 at 673 K indicates a positive effect on the permeability especially at high pressure difference between permeate and retentate.

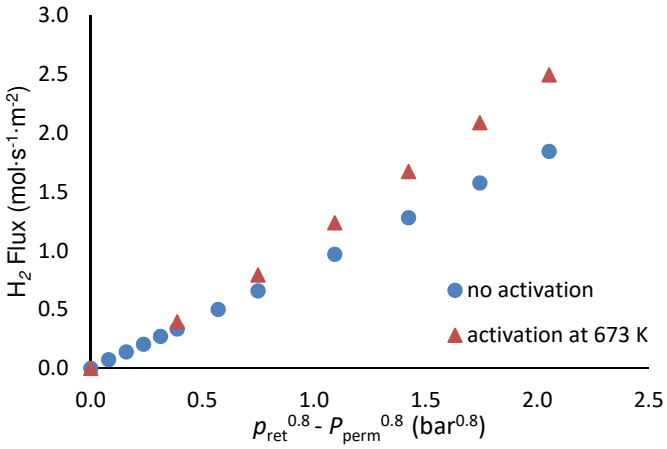


**Fig. 8.7** Hydrogen flux and flow rate through M1 and M2 as a function of the difference of partial pressures between retentate and permeate sides with n= 1.25 (no sweep gas) at 523 K.

### 8.5.3.Model validation

The MSR and HT-PEMFC models were successfully implemented and validate by the authors in a previous work [10, 19]. The implementation of the permeation model was validated considering the experimental work reported by Mejdell *et al.* [52]. The authors measured the hydrogen permeation flow rate thought a 1.4 m thick Pd-Ag membrane with a permeance of 5.4 $mol \cdot s^{-1} \cdot m^{-2} \cdot bar^{-0.5}$ at 573 K with $H_2$:$N_2$ gas mixture (molar ratio of 1:1) in the feed side. Fig. 8.8 shows the experimental and simulated results for the hydrogen flow rate (permeate side) as a function of absolute feed pressure (retentate) of a 1:1 $H_2$:$N_2$ mixture, at different feed flow rates of retentate and without using sweep gas. The simulation results are in good agreement with the experimental data for the studied operating conditions. It is clear that increasing the feed pressure and feed flow rate the hydrogen permeation increases. For a hydrogen feed flow rate of 200 $cm^3 \cdot min^{-1}$, hydrogen permeation flow rate stabilizes at *ca.* 80 $cm^3 \cdot min^{-1}$. Increasing the pressure above 6 bar has small effect on the permeation; this fact is attributed to the hydrogen transport being more rapidly through the membrane than through the polarization gas layer (concentration polarization), reducing the concentration gradient across the membrane and consequently the membrane permeation [53].

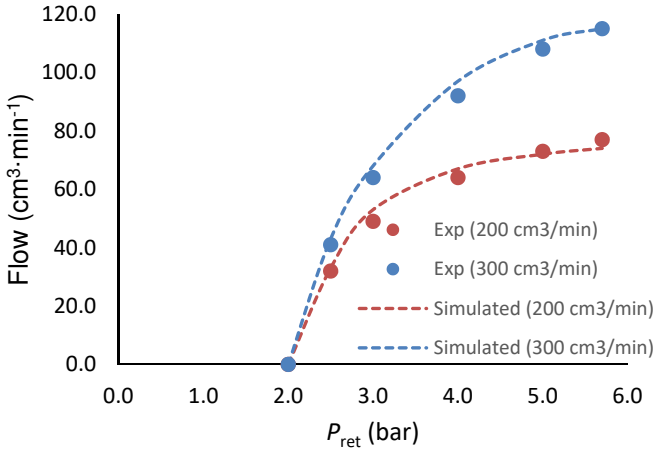


**Fig. 8.8** Experimental (full symbols, from [52]) and simulated results (dotted lines) of hydrogen flow rate at 573 K as a function of the total retentate pressure for a 1:1 $H_2$:$N_2$ molar feed mixture with different flow rates (200 and 300 $cm^3 \cdot min^{-1}$), with no sweep gas in the permeate side.

### 8.5.4. Performance of the PBMR-C/HT-PEMFC

*Methanol conversion*

The Pd-Ag membrane permeability and selectivity towards hydrogen considered in the PBMR-C/HT-PEMFC model was $2.9 \times 10^{-6}$ $mol \cdot m \cdot s^{-1} \cdot m^{-2} \cdot bar^{-0.8}$ and 5800 at 473 K, respectively (data obtained for M2). It is well known that the methanol conversion is enhanced when hydrogen is selectively removed from the reaction bulk; this enhancement is typically assigned to the partial suppression of the backward methanol steam reforming reaction and increase on the reactants residence time [28, 43]. Fig. 8.9 shows the methanol conversion as a function of the space-time ratio in a Pd-Ag membrane reactor for different permeate pressures; as limiting case, the membrane was considered impermeable. As expected, the enhancement in the methanol conversion increases as the permeate pressure decreases. In the PBMR-C/HT-PEMFC arrangement, the hydrogen consumed by the electrochemical reaction can reduce the permeate pressure below 1 bar, forcing the hydrogen to permeate faster through the membrane. This effect can be described as electrochemical hydrogen pumping. Hydrogen partial pressures of *ca*. 0.25 bar - 0.6 bar (typical hydrogen partial pressures present in reformate streams) do

not affect significantly the HT-PEMFC performance. The PBMR-C shows several advantages compared to a normal packed bed reactor, namely higher methanol conversion and production of a pure hydrogen stream even at low methanol conversions.

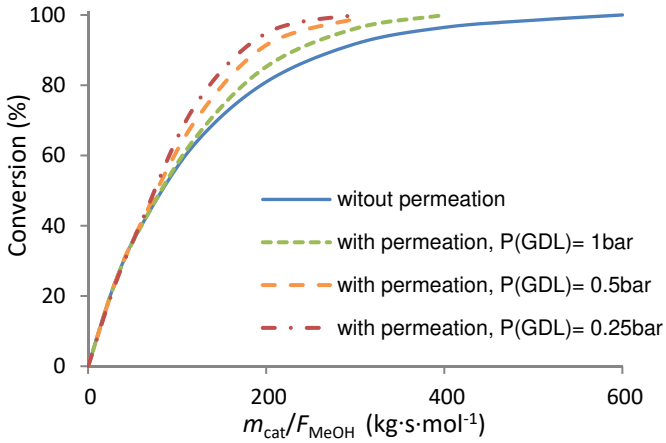


**Fig. 8.9** Simulated methanol conversion as a function of space-time for a Pd-Ag membrane reactor, at 473 K, $P_{ret}$ = 3 bar, S/C = 1.5.

*I-V curves*

The water/methanol flow rate used in the PBMR-C/HT-PEMFC was adjusted considering full methanol conversion and hydrogen stoichiometry of 1.2. Fig. 8.10 shows the simulated polarization curves obtained with the HT-PEMFC fed with pure hydrogen and the HT-PEMFC coupled with the PBMR-C at 473 K. The results obtained with PBMR-C/HT-PEMFC are similar to the ones obtained for HT-PEMFC fed with hydrogen (Fig. 8.10); indicating a high methanol conversion at the MSR and a very high hydrogen permeability of the Pd-Ag membrane matching the hydrogen consumption rate of the HT-PEMFC. It should be emphasised that only hydrogen permeates through the Pd-Ag membrane; unreacted methanol, $CO_2$ or CO do not reach the fuel cell avoiding then anode electrocatalyst poisoning or phosphoric acid leaching/evaporation/diffusion. The high electric conductivity of the Pd-Ag membrane improves the electric contact between the GDL and bipolar plate affecting positively the anode electrochemical reaction. Actually, for a typical FC, the electric contact between the GDL and the bipolar plate is carried through the ribs of the bipolar pate and high reaction rates are found in the vicinity between rib and

the channel, indicating the relevance of the GDL/bipolar plate electrical conductivity [54].

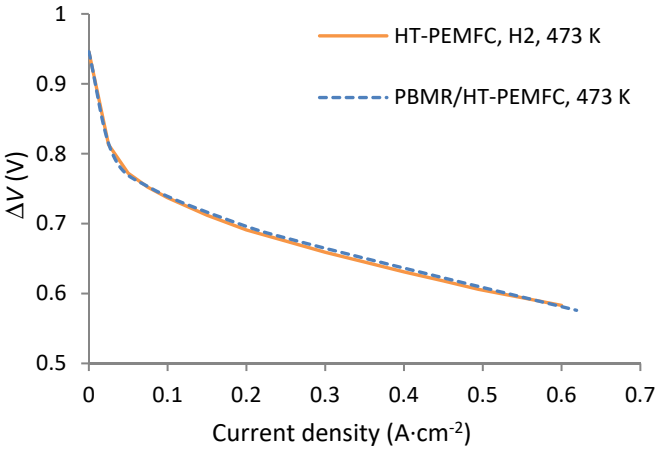


**Fig. 8.10** Simulated electric potential difference as function of the current density for the HT-PEMFC fed with pure hydrogen at 473 K and PBMR-C/HT-PEMFC device ($P_{ret}$ = 3 bar), at 473 K.

*Hydrogen permeation*

Fig. 8.11a shows contours of the hydrogen mass fraction in the PBMR-C/HT-PEMFC at 0.6 A·cm$^{-2}$. Hydrogen is produced by the MSR reaction in the reformer, permeating through the Pd-Ag membrane towards the anode catalyst layer where it is consumed. The highest hydrogen mass fraction is found at in the first third of the reformer length and not at the outlet, as typically is observed for PBR. The low hydrogen mass fraction at the reformer inlet and outlet affects severely the hydrogen permeation. Fig. 8.11b shows the permeating flux along the channel length. At $z$ = 0 m, the hydrogen partial pressure in the reformer is close to zero, therefore hydrogen permeates from the anode GDL/CL to the reformer. At $z$ = 0.015 m the permeating flux inverts direction, reaching a maximum hydrogen permeation flux of *ca*. 0.11 mol·s$^{-1}$·m$^{-2}$ (at $z$ = 0.05 m), reducing afterwards. As result, at the inlet region, the Pd-Ag membrane should be replaced by an impermeable and less expensive material.

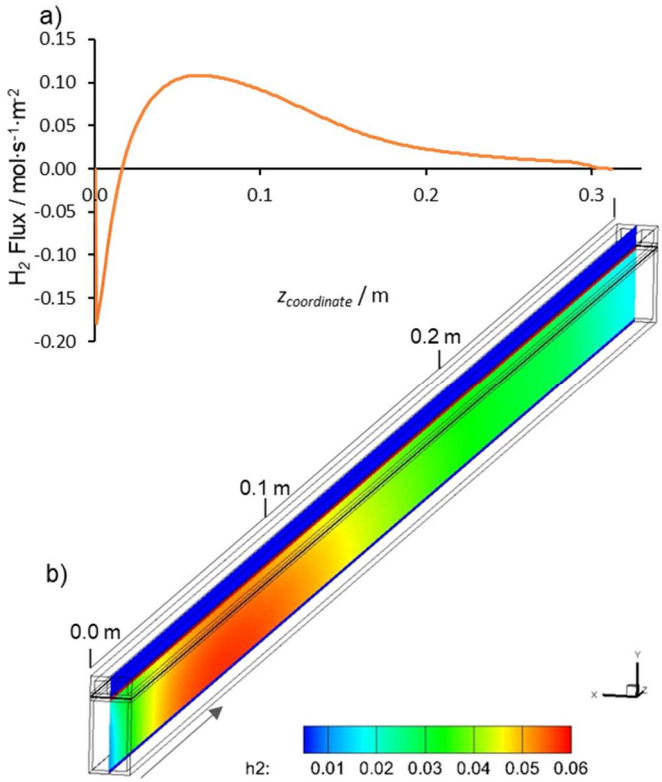


**Fig. 8.11** a) $H_2$ permeation flux through the membrane as function of the *z* coordinate and b) Hydrogen mass fraction contours for PBMR-C/HT-PEMFC (channel length) at 0.6 A·cm$^{-2}$ and 473 K, $P_{ret}$ = 3 bar and $m_{cat}/F_{MeOH}$ = 600 kg·mol$^{-1}$·s.

*Heat integration*

The advantages of the PBMR-C/HT-PEMFC are the heat integration, energy efficiency and compactness. The heat generated by HT-PEMFC, due to the electrochemical reaction and Joule effect (ohmic losses at the electrolyte), is higher than the heat consumed on the water/methanol mixture evaporation/heating and MSR reaction. Most of fuel cell applications require complex solutions such as heat exchangers and thermal fluids to transport the heat produced at the HT-PEMFC [8, 9]. Fig. 8.12 shows the temperature distribution on the PBMR-C/HT-PEMFC at a current density of 0.6 A·cm$^{-2}$. The PBMR-C/HT-PEMFC unit is thermally sustainable; at 0.6 A·cm$^{-2}$, the unit releases *ca.* 7.5 W of heat through the walls (for a 15 cm$^2$ unit without considering the evaporation/heating of reagents). The temperature profile along the reformer channel is mostly related to the MSR reaction, which is endothermic. A temperature drop is observed close

to the reformer channel inlet, caused by the high concentration of reagents that leads to a high MSR reaction rate. At the reformer, the temperature increases along the channel reaching a temperature of 474 K at the reformer outlet. In the cathode channel of the fuel cell the temperature also increases, reaching 474.5 K at the outlet. An efficient way to control the temperature of the PBMR-C/HT-PEMFC is controlling the flow rate of the inlet gases, specially the air at the cathode, as reported in literature [9, 10].

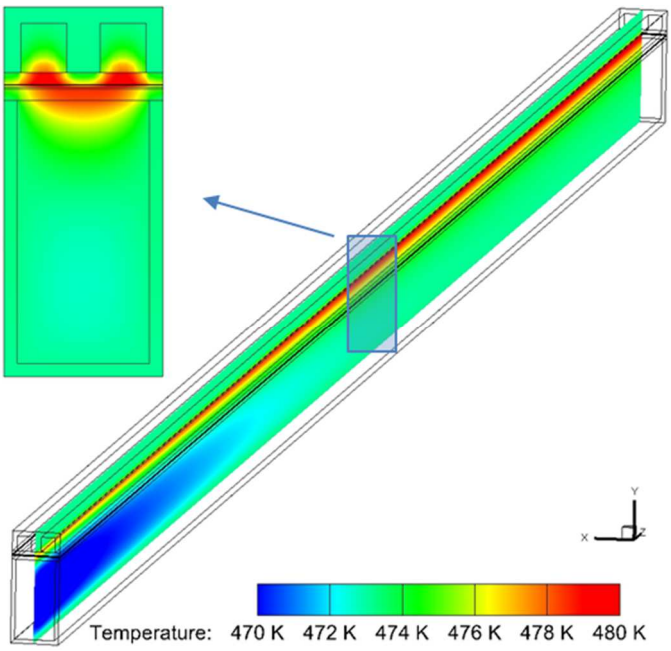


**Fig. 8.12** Temperature profiles of the PBMR-C/HT-PEMFC unit operating at 0.6 A·cm$^{-2}$ and considering the end plates at 473 K.

*Size of the combined unit*

The results presented in Fig. 8.10 – 8.12 were obtained considering a reformer with a channel depth of 8 mm, making the combined unit considerably thick. The PBMR-C/HT-PEMFC should provide a compact solution; therefore, the reformer channel depth was reduced. The unit was simulated considering a reformer with three different channel depths, 8 mm, 5 mm and 2.5 mm. Fig. 8.13 shows the fuel cell current density (at $\Delta V$ = 0.58 V) and methanol conversion as a function of the reformer channel depth. The channel depth reduction has minor effect on the current density, despite the drop on the methanol conversion, as observed in Fig. 8.13. It should be noted that reducing the

depth of the reformer channel also reduces the reforming catalyst mass; changing the depth from 8 mm to 2.5 mm decreases the catalyst mass from 13 g to 4 g. The methanol conversion obtained with the reformer of 2.5 mm channel was *ca.* 89 %; while, the methanol conversion for the same reformer at the same operating conditions (473 K and $m_{cat}/F_{MeOH}$ = 187 kg·mol$^{-1}$·s) without hydrogen permeation was *ca*. 75 % (Fig. 8.9).

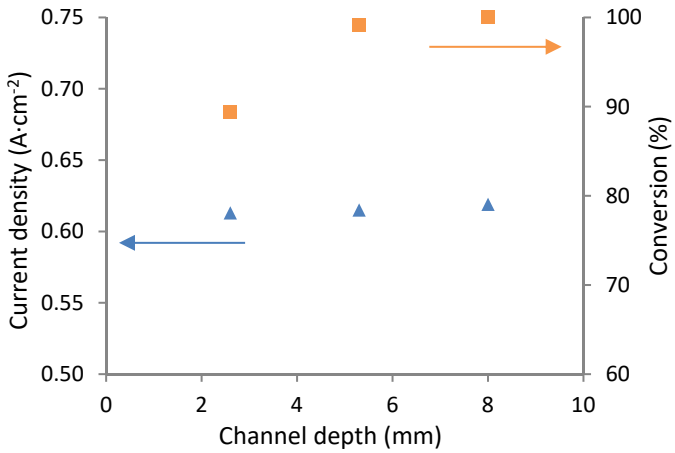


**Fig. 8.13** Simulated the PBMR-C/HT-PEMFC unit current density and methanol conversion as a function of the reformer channel depth at 473 K and $\Delta V$= 0.58 V, $P_{ret}$ = 3 bar.

*Feasibility of the combined unit*

The simulated PBMR-C/HT-PEMFC unit showed very promising results, but some simplifications made in the model should be discussed. The presence of carbon monoxide, carbon dioxide and unreacted methanol in the reformer can decrease the Pd-Ag membrane permeation especially at temperatures lower than 498 K [55]. Carbon monoxide can adsorb reversibly [56] on the membrane surface blocking the adjacent sites and increase the activation energy for hydrogen dissociation. The carbon monoxide concentration in the reformer at 473 K is *ca.* 0.3 %, therefore a slight drop in hydrogen permeation is expected [55,56]. At lower temperatures, such *ca.* 453 K, the carbon monoxide poisoning effect on the Pd-Ag membrane should be less noticeable since the reformer produces less than 0.1 % of carbon monoxide. Methanol can also adsorb on the

Pd-Ag membrane surface affecting the hydrogen permeability [56]. Near to the inlet region of the reformer, low hydrogen permeation is expected, due to high methanol concentrations and low hydrogen availability. On the other hand, palladium nanoparticles can catalyse the methanol steam reforming reaction, methanol decomposition and water-gas-shift [57]; in fact the methanol decomposition has already been reported over Pd-Ag membranes [55]. The effect of carbon dioxide and water on the Pd-Ag membrane permeability should be considered minor; some authors suggested that these species can adsorb on the membrane surface [55,58], while others have claimed the opposite [56, 59]. The accumulation of impurities in the anode side that may permeate through the Pd-Ag membrane or through the PBI membrane can result in the anode total pressure build up. Actually, the hydrogen permeation is not affected by the presence of contaminantes since it is just proportional to the hydrogen partial pressure difference; on the other hand, the total pressure would increase, requiring a dynamic operation to relief the pressure [60, 61].

The Pd-Ag membrane in the PBMR-C/HT-PEMFC configuration avoids the phosphoric acid leaching at the anode side during starts and stop cycles. Nevertheless, the membrane stability can be affected by the phosphoric acid presence. Pd films show high stability under corrosive environments such as phosphoric acid solutions [62], but to the best of the authors' knowledge, a similar study for Pd-Ag films has never been reported.

The palladium membrane can also promote the electro oxidation of hydrogen and methanol [63, 64]. To occur the electro-oxidation of hydrogen in the Pd-Ag membrane should contact directly with the CL (the GDL must be removed), to transport the formed protons at the Pd-Ag membrane surface. The high cost of the Pd-Ag membrane could be the major limitation for the PBMR-C/HT-PEMFC unit and a deeper analysis should be performed, balancing the strengths and weakness to understand the feasibility of this technology. The PBMR-C/HT-PEMFC prototype unit is being developed by the authors; this is an ambitious technological and fundamental research challenge requiring the combined development of tailored materials.

## 8.6. Conclusions

An integrated unit, comprising a Pd-Ag membrane reactor (PBMR-C) and a HT-PEMFC, was studied by simulation. A 3-dimensional non-isothermal model for a PBMR-

/HT-PEMFC combined unit was successfully developed and validated with experimental data. 4 □m thick Pd-Ag membranes were prepared by magnetron sputtering and hydrogen permeability and selectivity were determined. The prepared membranes showed a $H_2/N_2$ molar selectivity of *ca*. 5800 and a permeability to hydrogen of $2.94\times10^{-6}$ $mol\cdot m\cdot s^{-1}\cdot m^{-2}\cdot bar^{-0.8}$ at 473 K without activation treatment. The simulated PBMR-C/HT-PEMFC unit showed very high performance, similar to the one obtained with a HT-PEMFC fed with pure hydrogen at the anode side. The device allowed efficient heat integration, where the heat produced in the electrochemical process was used to perform the MSR reaction. The fuel cell efficiency was not affected when thin cellular reformers were considered. Several concerns were raised about Pd-Ag membrane stability and costs; however, the PBMR-C/HT-PEMFC showed very promising results that should prompt further investigation.

## 8.7. References

[1] D. Ipsakis, M. Ouzounidou, S. Papadopoulou, P. Seferlis, S. Voutetakis, Dynamic modeling and control analysis of a methanol autothermal reforming and PEM fuel cell power system, Applied Energy, 208 (2017) 703-718

[2] G. Kolb, Review: Microstructured reactors for distributed and renewable production of fuels and electrical energy: Chemical Engineering and Processing 65 (2013) 1-44

[3] V. Jaggi, S. Jayanti, A conceptual model of a high-efficiency, stand-alone power unit based on a fuel cell stack with an integrated auto-thermal ethanol reformer, Applied Energy 110 (2013) 295-303.

[4] R.Y. Chein, Y.C Chen, C.M. Chang, J.N. Chung, Experimental study on the performance of hydrogen production from miniature methanol–steam reformer integrated with Swiss-roll type combustor for PEMFC, Applied Energy 105 (2013) 86-98.

[5] T. Kim, Micro Methanol Reformer Combined with a Catalytic Combustor for a PEM Fuel Cell, International Journal of Hydrogen Energy, 34 (2009) 6790-6798.

[6] J.D. Holladay, Y. Wang, E. Jones, Review of developments in portable hydrogen production using microreactor technology, Chemical Reviews, 104 (2004) 4767-4790.

[7] I. Uriz, G. Arzamendi, P.M. Diéguez, F.J. Echave, O. Sanz, M. Montes, L.M. Gandía, a CFD analysis of the effects of the flow distribution and heat losses on the steam reforming of methanol in catalytic (Pd/ZnO) microreactors Chemical Engineering Journal 238 (2014) 37–44

[8] S.L. Sahlin, S.J. Andreasen, S. K. Kær, System model development for a methanol reformed 5 kW high temperature PEM fuel cell system, International journal of hydrogen energy, 40 (2015) 13080-13089

[9] G. Schuller, F. Vidal Vázquez, W. Waiblinger, S. Auvinen, P. Ribeirinha, Heat and fuel coupled operation of a high temperature polymer electrolyte fuel cell with a heat exchanger methanol steam reformer, Journal of Power Sources 347 (2017) 47–56.

[10] P. Ribeirinha, M. Abdollahzadeh, J.M. Sousa, b, M. Boaventura, A. Mendes, Modelling of a high-temperature polymer electrolyte membrane fuel cell integrated with a methanol steam reformer cell, Applied Energy 202 (2017) 6–19.

[11] A. Lotric, M. Sekavcnik, S. Hocevar Effectiveness of heat-integrated methanol steam reformer and polymer electrolyte membrane fuel cell stack systems for portable applications, Journal of Power Sources 270 (2014) 166-182

[12] A. H. Mamaghani, B. Najafi, A. Casalegno, F. Rinaldi, Predictive modelling and adaptive long-term performance optimization of an HT-PEM fuel cell based micro combined heat and power (CHP) plant, Applied Energy 192, 2017, 519–529

[13] A. Arsalis, S. K. Kær, M. P. Nielsen, Modeling and optimization of a heat-pump-assisted high temperature proton exchange membrane fuel cell micro-combined-heat-and-power system for residential applications, Applied Energy, 147, 2015, 569-581

[14] C. Pan, R.H. He, Q.F. Li, J.O. Jensen, N.J. Bjerrum, H.A. Hjulmand, A.B. Jensen, Integration of high temperature PEM fuel cells with a methanol reformer, Journal of Power Sources, 145 (2005) 392-398.

[15] G. Avgouropoulos, T. Ioannides, J.K. Kallitsis, S. Neophytides, Development of an internal reforming alcohol fuel cell: Concept, challenges and opportunities, Chemical Engineering Journal, 176 (2011) 95-101.

[16] S.R Samms, , R.F Savinell, Kinetics of methanol-steam reformation in an internal reforming fuel cell, Journal of Power Sources 112(1) (2002)s 13–29

[17] F. Weng, C. Chenga, K. Chen, Hydrogen production of two-stage temperature steam reformer integrated with PBI membrane fuel cells to optimize thermal management, International Journal of Hydrogen Energy 38 (2013) 6059-6064

[18] P. Ribeirinha, I. Alves, F. Vidal Vázquez, G. Schuller, M. Boaventura, A. Mendes, Heat integration of methanol steam reformer with a high-temperature polymeric electrolyte membrane fuel cell, Energy 120 (2017) 468–477

[19] P. Ribeirinha, G. Schuller, M. Boaventura, A. Mendes, Synergetic integration of a methanol steam reforming cell with a high temperature polymer electrolyte fuel cell, International Journal of Hydrogen Energy, 42(19) (2017) 13902-13912

[20] Q. Li, D. Aili, H.A. Hjuler, J.O. Jensen, High temperature polymer electrolyte membrane fuel cells, Springer Switzerland (2016) 459-484

[21] G. Avgouropoulos, A. Paxinou, b, S. Neophytides In situ hydrogen utilization in an internal reforming methanol fuel cell, International Journal of Hydrogen Energy, 39(31) 2014 18103–18108.

[22] K. M. K. Yu, W. Tong, A. West, K. Cheung, T. Li, G. Smith, et. al, Non-syngas direct steam reforming of methanol to hydrogen and carbon dioxide at low temperature Nature Communications 3 (2012) 1230

[23] A. Lotric, M. Sekavcnik, A. Pohar, B. Likozar, S. Hocevar, Conceptual design of an integrated thermally self-sustained methanol steam reformer e High-temperature PEM fuel cell stack manportable power genera-tor, International Journal of Hydrogen Energy 42 (2017) 16700-16713

[24] P. Ribeirinha, C. Mateos-Pedrero, M. Boaventura, J. Sousa , A. Mendes, CuO/ZnO/Ga2O3 catalyst for low temperature MSR reaction: Synthesis, characterization and kinetic model. Applied Catalysis B: Environmental 221 (2018) 371-379

[25] A. Iulianelli , P. Ribeirinha, A. Mendes, A. Basile, Methanol steam reforming for hydrogen generation via conventional and membrane reactors: A review Renewable and Sustainable Energy Reviews 29, 2014, 355–368

[26] Shu J., Grandjean B. P. A., Van Neste A., Kaliaguine S., Catalytic palladium-based membrane reactors: A review, Canadian Journal of Chemical Engineering. 69(5) (1991) 1036–1060

[27] A. Basile, F. Dalena, J. Tong, T. N. Veziroğlu (eds.), Hydrogen Production, Separation and Purification for Energy, IET 2017

[28] Basile A., Iulianelli A., Tong J., Membrane reactors for the conversion of methanol and ethanol to hydrogen, Membrane Reactors for Energy Applications and Basic Chemical Production, Woodhead Publishing Series in Energy 2015, 187-208

[29] G.Q. Lu, J.C. D. Costa , M. Duke ,S. Giessler ,R. Socolow , R.H. Williams et al., Inorganic membranes for hydrogen production and purification: A critical review and perspective, Journal of Colloid and Interface Science 314 (2007) 589–603

[30] Z. Y. Li, H. Maeda, K. Kusakabe, S. Morooka, H. Anzai, S. Akiyama,Preparation of palladium-silver alloy membranes for hydrogen separation by the spray pyrolysis method, Journal of Membrane Science 78 (3) (1993) 247-254

[31] S. Uemiya, T. Matsuda, E. Kikuchi, Hydrogen permeable palladium-silver alloy membrane supported on porous ceramics, J. Membr. Sci. 56 (1991) 315–325.

[32] E. Kikuchi, S. Uemiya, Preparation of supported thin palladium-silver alloy membranes and their characteristics for hydrogen separation, Gas Separation & Purification 5(4) (1991) 261-266.

[33] S. Yan, H. Maeda, K. Kusakabe, S. Morooka, Thin Palladium Membrane Formed in Support Pores by Metal-Organic Chemical Vapor Deposition Method and Application to Hydrogen Separation Ind. Eng. Chem. Res., 33(3) (1194) 616–622

[34] G. Xomeritakis, Y.S. Lin, CVD synthesis and gas permeation properties of thin palladium/alumina membranes, American Institute of Chemical Engineers. 44 (1998) 174–183.

[35] V. Jayaraman, Y.S. Lin, M. Pakals, R.Y. Lin, Fabrication of ultrathin metallic membranes on ceramic supports by sputter deposition, Journal of membrane science 99 (1995) 89–100

[36] B. McCool, G. Xomeritakis, Y.S. Lin, Composition control and hydrogen permeation characteristics of sputter deposited palladium–silver membranes, Journal of Membrane Science 161 (1999) 67–76.

[37] H. Klette, R. Bredesen, Sputtering of very thin palladium-alloy hydrogen separation membranes, Membrane Technology 2005(5) 2005 7-9

[38] Bredesen R., Klette H., Method of manufacturing thin metal membranes, US Patent, 6,086,729, 2000.

[39] Boeltken T., Belimov M., Pfeifer P., Peters T.A., Bredesen R., Dittmeyer R., Fabrication and testing of a planar microstructured concept module with integrated palladium membranes Chemical Engineering and Processing: Process Intensification, 67, 2013, 136–147

[40] Chen W., Hsia M., Chi Y., Lin Y., Yang C. Polarization phenomena of hydrogen-rich gas in high-permeance Pd and Pd–Cu membrane tubes Applied Energy, 113, 2014, 41-50

[41] K. Jiao, IE. Alaefour, X .Li, Three-dimensional non-isothermal modeling of carbon monoxide poisoning in high temperature proton exchange membrane fuel cells with phosphoric acid doped polybenzimidazole membranes, Fuel 90 (2011) 568-582

[42] K. Oh, J .Gisu, E. Cho, W. Kim, H.Ju, A CO poisoning model for high-temperature proton exchange membrane fuel cells comprising phosphoric acid-doped polybenzimidazole membranes, International Journal of Hydrogen Energy 39 (2014) 21915-21926

[43] P. Ribeirinha, M. Abdollahzadeh, M. Boaventura, A. Mendes H2 production with low carbon content via MSR in packed bed membrane reactors for high-temperature polymeric electrolyte membrane fuel cell, Applied Energy, 188 (2017) 409–419.

[44] C.H. Kim, J.Y. Han, N.C. Kim, S.K. Ryi, D.W. Kim, Characteristics of dense palladium alloy membranes formed by nano-scale nucleation and lateral growth, Journal of Membrane Science 502 (2016) 57–64

[45] N. Vicinanza, I.H. Svenum, L. N. Næss, T. A. Peters, R. Bredesen, A. Borg, H. J. Venvik, Thickness dependent effects of solubility and surface phenomena on the hydrogen transport properties of sputtered Pd77%Ag23%
thin film membranes, Journal of Membrane Science 476 (2015) 602–608

[46] A.L. Mejdell, H. Klette, A. Ramachandran, A. Borg, R. Bredesen, Hydrogen permeation of thin, free-standing Pd/Ag23% membranes before and after heat treatment in air, Journal of Membrane Science 307 (2008) 96–104

[47] S. Nayebossadri, J. Speight, D. Book, Effects of low Ag additions on the hydrogen permeability of Pd–Cu–Ag hydrogen separation membranes, Journal of Membrane Science 451 (2014) 216–225.

[48] U. Stuhr, T. Striffler, H. Wipf, H. Natter, B. Wettmann, S. Janssen,R. Hempelmann, H. Hahn, An investigation of hydrogen diffusion in nanocrystalline Pd by neutron spectroscopy, Journal of Alloys and Compounds 253–254 (1997) 393-396

[49] H. Natter,B.Wettmann, B. Heisel, R. Hempelmann, Hydrogen in nanocrystalline palladium, Journal of Alloys and Compounds 253–254 (1997) 84-86

[50] S. Heinze, B. Vuillemin, J.C. Colson, Relation between grain size and hydrogen diffusion coefficient in an industrial Pd–23% Ag alloy, Solid State Ionics 121 (1999) 51

[51] B.A. McCool, Y.S. Lin, Nanostructured thin palladium–silver membranes: effects of grain size on gas permeation properties, J. Mater. Sci. 36 (2001) 3221-3227.

[52] A.L. Mejdell, M. Jøndahl, T.A. Peters, R. Bredesen, H.J. Venvik, Experimental investigation of a microchannel membrane configuration with a 1.4mm Pd/Ag23 wt.% membrane—Effects of flow and pressure, Journal of Membrane Science 327 (2009) 6–10

[53] M. Mulder, Basic Principles of Membrane Technology, 2nd ed. Kluwer Academic Publishers, Netherlands1996

[54] D.H. Jeon, S.Greenway, S.Shimpalee J.W.Van Zee, The effect of serpentine flow-field designs on PEM fuel cell performance, Int. J. Hydrogen Energy 33(3) (2008) 1052-1066

[55] S. H. Israni and M. P. Harold, Methanol Steam Reforming in Pd-Ag Membrane Reactors: Effects of Reaction System Species on Transmembrane Hydrogen Flux, Ind. Eng. Chem. Res. 49 (2010) 10242–1025

[56] T. H. Nguyen , S. Mori, M. Suzuki, Hydrogen permeance and the effect of $H_2O$ and CO on the permeability of Pd0.75 Ag0.25 membranes under gas-driven permeation and plasma-driven permeation, Chemical Engineering Journal 155 (2009) 55–61

[57] C.S.R. Azenha, C. Mateos-Pedrero, S. Queirós, P. Concepción, A. Mendes, Innovative ZrO2-supported CuPd catalysts for the selective production of hydrogen from methanol steam reforming, Applied Catalysis B: Environmental 203l (2017) 400–407.

[58] A. Unemoto, A. Kaimai, K. Sato, T. Otake, K. Yashiro, J. Mizusaki, et al., Surface reaction of hydrogen on a palladium alloy membrane under co-existence of H2O, CO, CO2, CH4. Int. J. Hydrogen Energy 32 (2007) 4023–4029.

[59] Galluci, F.; Chiaravalloti, F.; Tosti, S.; Drioli, E.; Basile, A. The. Methanol steam reforming in single- effect of mixture gas on hydrogen permeation through a palladium membrane: Experimental study and theoretical approach. Int. J. Hydrogen. Energy 32 (2007) 1837–1845.

[60] Chen et al., Optimization of purge cycle for dead-ended anode fuel cell operation. Int. J. Hydrogen Energy, 38 (2013).

[61] J-H. Jang, W-M Yan, H-C Chiu, J-Y Lui, Dynamic cell performance of kW-grade proton exchange membrane fuel cell stack with dead-ended anode, Applied Energy 142 (2015) 108-114

[62] J. Tang, Y. Zuo, Study on corrosion resistance of palladium films on 316L stainless steel by electroplating and electroless plating Corrosion Science, 50(10) (2008) 2873-2878

[63]R. Pattabiraman ,Electrochemical investigations on carbon supported palladium catalysts, Applied Catalysis A: General 153 (1997) 9-20

[64] Mi. Shao, Palladium-based electrocatalysts for hydrogen oxidation and oxygen reduction reactions, Journal of Power Sources 196 (2011) 2433-2444

# Chapter 9:

# Conclusions and future work

To achieve the thermal integration of a methanol steam reformer with a HT-PEMFC, these devices should operate at the same temperature. However, currently the methanol steam reforming is performed at 513 – 533 K, while HT-PEMFCs operate at 433 K and should not exceed 453 K. To perform the methanol steam reforming at lower temperature, a novel and highly active $CuO/ZnO/Ga_2O_3$ catalyst was synthesized by the research team and fully characterized within this thesis (Chapter 2). The physicochemical study conducted over the $CuO/ZnO/Ga_2O_3$ catalyst indicated very small and highly dispersed copper particles. The synthesized catalyst showed a methanol conversion *of ca.* 2.2 times higher than two commercial $CuO/ZnO/Al_2O_3$ catalysts, levelling out to *ca.* 1.7 times after 80 h of time-on-stream. The two kinetic models, power-law and mechanistic, used to describe the MSR reaction over a novel catalyst, presented a good agreement with the experimental values. The following studies were conducted using commercial $CuO/ZnO/Al_2O_3$ catalysts, since the laboratory has no capacity to produce large amonts of $CuO/ZnO/Ga_2O_3$ catalyst.

The reformer design affects the methanol conversion; therefore, three different methanol reformer designs (multi-channel, radial and tubular) were thoroughly studied experimentally and by CFD simulation (Chapter 3). The multi-channel design showed high methanol conversion and low-pressure drop; the narrow channels and the high metallic surface area in the multi-channel provided an efficient heat transfer from the wall to the bulk. Moreover, the multi-channel showed a good flow distribution with a small coefficient of variation in flow velocity between channels. Among the studied designs, the multi-channel demonstrated to be the best approach for thermal integration with a HT-PEMFC; however, other solutions that reduce the pressure drop, maximize the heat transfer and show even flow distribution could also be considered.

An integrated unit, combining a MSR-C and HT-PEMFC, was developed and operated at 453 K and 463 K using MEAs from Advent TPS (Chapter 4). The combined unit showed at 453 K a current density of 0.5 $A \cdot cm^{-2}$, with a slightly drop of potential (30 mV) when compared to the HT-PEMFC fed directly with hydrogen. After several hours of operation, the degradation of the MEA was noticeable, both at 453 K than at 463 K, because of the low methanol conversion (<90 %). The electrochemical impedance spectroscopy analysis showed an increase in the anode resistance when fed with reformate, due to the catalyst activity loss and lower hydrogen partial pressure; the cathode resistance also increased when fed with reformate, due to methanol crossover from the anode to the cathode. The self-thermal sustainability of the combined device was not reached due to the poor thermal insulation of the combined reactor. The MEAs from Advent TPS compared to PBI-doped ones showed lower power density and stability.

In the second attempt for combining a MSR-C with HT-PEMFC (Chapter 5), a new bipolar plate made of gold plated aluminium was developed and the unit was operated between 453 K and 473 K using a PBI-doped MEA (Celtec P2200N) from BASF. The reformer showed a performance similar to a differential reactor loaded with the commercial catalyst; moreover, the water/methanol vaporisation process was optimized allowing an increasing of the methanol conversion from 93 % to 96 %. The combined MSR-C/HT-PEMFC system displayed a remarkable performance at 453 K with a power output close to the HT-PEMFC fed directly with hydrogen. A stability test of the combined unit (*ca.* 700 h at 0.2 $A \cdot cm^{-2}$ and temperatures of 453 and 463 K), revealed that using reformate as fuel had no significant influence on the MEA degradation compared to hydrogen.

The operation of the combined unit was studied by simulation; therefore, a 3-dimensional non-isothermal model and simulator were developed. The model considers the most significant chemical/physical processes that occur at the HT-PEMFC, including CO poisoning. The simulator indicated that the combined unit to achieved thermal equilibrium at low current densities (0.1 $A \cdot cm^{-2}$) would require a thermal insulation with a minimum of 3 cm thick glass wool. Additionally, it showed that the device temperature control could be managed by feeding air to the cathode at the room temperature and adjusting the airflow rate. The proposed integrated MSR/HT-PEM stack could operate without any external heat source for currents between 4.5 A (0.1 $A \cdot cm^{-2}$) and 54 A (1.2 $A \cdot cm^{-2}$).

The hydrogen production and purification using packed bed membrane reactors for HT-PMFCs applications was assessed by simulation. A 3-dimensional isothermal PBMR model was developed considering a Pd-Ag membrane selective to hydrogen, an ILs membrane selective to carbon dioxide, and a conventional packed bed reactor (PBR), this last as reference. The selective hydrogen removal from the reaction bulk results in a methanol conversion enhancement assigned to the partial suppression of the backward methanol steam reforming reaction and an increase on the residence time. The selective carbon dioxide removal originates a smaller methanol conversion enhancement than when using a hydrogen selective membrane. The results indicated that only very selective and fast membranes, > 1 x $10^{-1}$ mol·s $^{1}$·$m^{-2}$·$bar^{-1}$ at 473 K with ideal selectivity >200, can effectively be used in a PBMR for hydrogen purification. The $CO_2$-PBMR showed to be more energy efficient than $H_2$-PBMR especially for high hydrogen recoveries. Despite the great efforts of the scientific community in developing selective carbon dioxide membranes, they do not have yet the characteristics required for hydrogen purification in PBMRs.

An integrated unit, combining a Pd-Ag membrane reactor (PBMR-C) and a HT-PEMFC, was studied by simulation. To obtain a valid permeation model, two Pd-Ag membranes with 4 μm thick and defect-free, were prepared by magnetron sputtering. The prepared membranes showed a $H_2/N_2$ molar selectivity above 1500 and a permeability to hydrogen at 473 K of 2.94×$10^{-6}$ mol·m·$s^{-1}$·$m^{-2}$·$bar^{-0.5}$ without activation treatment. The simulation results showed that the PBMR-C/HT-PEMFC unit has similar performance to the one obtained with a HT-PEMFC fed with pure hydrogen, the device allowed an efficient heat integration and very thin cellular reformers. The stability and costs of Pd-Ag membranes standout as the main limitation of this technology.

As a future work, it would be important to test experimentally and prove the concept of the combined PBMR-C/HT-PEMFC unit. This task is being carried out in the host laboratory. In a different configuration of the combined unit, the palladium-alloy membrane should be placed in direct contact with platinum particles of the electro-catalyst layer; this way the hydrogen atoms that diffuse through the palladium membrane could oxidize to form the protons jumping the hydrogen association step. This facilitated transport/reaction was never described in the literature, but it should affect both permeation and electro-catalytic reaction.

The prepared $CuO/ZnO/Ga_2O_3$ catalyst was not yet tested in the combined unit; however, a company using this catalyst recipe is currently upscaling its production. When commercially available, this catalyst should be tested in both configurations of the combined unit (MSR-C/HT-PEMFC and PBMR-C/HT-PEMFC)

Solid acids are a type of proton conducting electrolytes studied for fuel cell applications that operate at temperature between 473 and 573 K. Operating the integrated unit at high temperature would have several advantages: higher methanol conversions and thinner reformers, higher tolerance of the electro-catalytic system to contaminants (CO, methanol), lower activation over-potentials, use of non-precious metal catalyst and cogeneration. A combined unit equipped with solid acid membrane should be studied.

Finally, the model developed for the MSR-C/HT-PEMFC and PBMR-C/HT-PEMFC should be improved, incorporating the effect of contaminants (CO, methanol, water) on the palladium membranes as on the fuel cell electro catalytic system. Additionally, an extended experimental study is required, since limited data is available in literature considering the effect of contaminants on palladium membranes and fuel cell electro-catalytic system in the temperature range of 453 – 473 K.